Model-Supported Lithium-Ion Battery Diagnostics for Knowledge-Based Cell Optimization

Zur Erlangung des akademischen Grades eines
Doktors der Ingenieurwissenschaften (Dr.-Ing.)
von der KIT-Fakultät für Elektrotechnik und Informationstechnik des
Karlsruher Instituts für Technologie (KIT)

angenommene
Dissertation
von

Daniel Witt, M. Sc.

Tag der mündlichen Prüfung:	08. November 2024
Hauptreferentin:	Prof. Dr.-Ing. Ulrike Krewer
Korreferent:	Prof. Dr. Gregory J. Offer

Kurzfassung

Lithium-Ionen-Batterien sind von zentraler Bedeutung für ein breites Spektrum von Anwendungen, von Smartphones über Elektrofahrzeuge bis hin zu stationären Energiespeicherlösungen. Mit der schnell wachsenden Nachfrage nach diesen Batterien wird die effiziente Verarbeitung von teuren Rohstoffen in langlebige Zellen mit überlegenen Leistungsmerkmalen immer wichtiger.

In dieser Arbeit wird physikochemische Modellierung auf zwei grundlegend leistungs- und kostenbestimmende Phasen in der Herstellung von Lithium-Ionen-Batterien angewandt: Zelldesign und Zellproduktion. Zunächst werden anhand einer modellbasierten Designstudie die Herausforderungen optimalen anwendungsspezifischen Zelldesigns aufgezeigt. Dabei wird die Bedeutung der seltener untersuchten Ladeleistung in den Fokus gestellt, da diese für eine ganzheitliche Optimierung eines Zelldesigns entscheidend ist. Anschließend wird der Formierungsprozess, einer der teuersten Prozessschritte in der Batterieproduktion, analysiert. Dieser umfasst das erste Laden und Zyklisieren einer Lithium-Ionen-Batterie, welches eine kontrollierte Bildung der Solid Electrolyte Interphase (SEI) auf dem Anodenaktivmaterial gewährleistet. Trotz intensiver Forschung sind die initiale Bildung der SEI und ihr Effekt auf die Zelldegradation und -leistungsfähigkeit noch nicht vollständig verstanden. Aus diesem Grund wird ein Zell- und SEI-Modell entwickelt, das eine zerstörungsfreie Charakterisierung dieses komplexen Oberflächenfilms für verschiedene Formierungsprozeduren ermöglicht. Dabei stellt die gemeinsame Parametrierung mit Entladungsmessungen und elektrochemischen Impedanzspektren sicher, dass die ermittelten Parameter zuverlässige Einblicke in das Zellverhalten ermöglichen. Mit diesem Ansatz kann schließlich der Zellzustand unmittelbar nach der Formierung ermittelt und seine Veränderung im Laufe der Alterung untersucht werden.

Zusammenfassend zeigt diese Arbeit die Bedeutung eines ganzheitlichen Ansatzes für Zelldesign und -diagnostik. Ohne ein gutes Verständnis der Entlade- und Ladeeigenschaften einer Zelle ist eine eindeutige Identifizierung überlegener Zelldesigns für spezifische Anwendungen nicht möglich. Die gemeinsame Analyse experimenteller C-Ratentests und Impedanzdaten ist entscheidend für eine zuverlässige Differenzierung zwischen Zelleigenschaften auf Partikel- und Elektrodenebene. Mit diesem Ansatz konnten die Leistungsunterschiede nach verschiedenen Formierungsprozeduren detailliert untersucht werden. Die Ergebnisse deuten darauf hin, dass sich unterschiedliche Oberflächenfilme in der Anode und der Kathode ausbilden, die im Zusammenhang mit signifikanten mikrostrukturellen Änderungen in den Elektroden stehen.

Abstract

Lithium-ion batteries power an increasingly broad spectrum of applications, from smartphones to electric vehicles and stationary energy storage solutions. With the rapidly growing demand for these batteries, the efficient transformation of expensive raw materials into long-lasting cells with superior performance characteristics becomes increasingly important.

In this thesis, physicochemical modeling is used to advance the understanding of two fundamentally performance- and cost-defining phases in the creation of a lithium-ion battery: cell design and cell production. First, a model-based design study is used to exemplify the challenges of optimal cell design, providing a guideline for application-tailored electrode design optimization. Here, the importance of the seldom-reported charge performance is highlighted, which is crucial for a holistic cell design optimization. Secondly, the cell formation process, one of the most expensive process steps in battery production, is analyzed. This process comprises the first charging and cycling of a lithium-ion battery, which ensures a controlled formation of the so-called solid electrolyte interphase (SEI) on the anode active material. Despite intensive research, the initial SEI formation and its impact on cell degradation and performance are still not fully understood. For this reason, a physicochemical cell and SEI model is developed, which enables a non-destructive characterization of this intricate surface film for different formation procedures. Here, the joint parameterization with discharge curves and electrochemical impedance spectra ensures that the parameter estimates provide meaningful insights into the experimentally observed cell behavior. Eventually, this approach can be used to analyze the cell state immediately after formation, as well as the evolution of this state during aging.

In summary, the results in this thesis underline the importance of a holistic approach toward cell design and cell diagnostics. A clear identification of truly superior cell designs for specific applications is impossible without a good understanding of a cell's discharge and charge characteristics. Likewise, the joint analysis of experimental C-rate tests and impedance data is crucial for a reliable differentiation between electrode- and particle-level cell properties, providing rapid yet non-destructive insights into performance-sensitive cell properties. This approach was used to investigate the origin of performance improvements for variations in the formation process. The results indicate that the chosen procedure affects the surface film formation in both the anode and cathode, which is associated with significant microstructural changes in the electrodes.

Preface and Acknowledgments

This thesis was written during my time in the research group of Prof. Dr.-Ing. Ulrike Krewer at the Institute of Energy and Process Systems Engineering at the Technische Universität Braunschweig and the Institute of Applied Materials – Electrochemical Technologies at the Karlsruhe Institute of Technology. Large parts of the manuscript are adopted verbatim from prior scientific publications with significant contributions from my side (see Appendix A).

First, I want to thank Prof. Dr.-Ing. Ulrike Krewer for the opportunity to research at the intersection of battery modeling, electrochemical characterization, and cell optimization. Thank you for your support and guidance, the critical discussions, and your valuable feedback on both science and personal growth. Furthermore, I would like to thank Prof. Dr. Gregory J. Offer for being my second examiner. Thanks also to Prof. Dr.-Ing. Mike Barth for chairing my examination board and to Prof. Dr.-Ing. Martin Doppelbauer and Prof. Dr. rer. nat. Wilhelm Stork for being part of my examination board.

I would like to thank the German Federal Ministry for Economic Affairs and Energy for support through the "DaLion 4.0" project (03ETE017A), and the Friedrich and Elisabeth Boysen Foundation (BOY-174). Their funding enabled my research and its presentation to the scientific community. I would also like to thank the DaLion 4.0 team and the student assistants Frauke Stamereilers, Caroline Willuhn, Ruth Witzel, Leon Schmidt, and Julia Hilbig for their invaluable support during experimental studies.

I would also like to thank my colleagues for the enriching journey, the intense discussions, and the non-academic endeavors. In particular, I would like to thank Prof. Dr.-Ing. Fridolin Röder as my group leader in Braunschweig for the numerous discussions on physicochemical modeling and numerical methods, Dr.-Ing. Vincent Laue for his advice on model parameterization and sharing his in-depth experience in project work, Dr.-Ing. Lars Bläubaum for his help with and his invaluable perspective on the design and execution of experimental studies, Dr.-Ing. Florian Baakes as my group leader in Karlsruhe for the numerous scientific discussions and his in-depth feedback on publications and project proposals, Walter Cistjakov for valuable discussions on the application of numerical methods in battery modeling, and Ruth Witzel and Tobias Goosmann for their insightful feedback on the clarity and comprehensibility of various illustrations.

Finally, my gratitude goes to my parents, family, and friends for their encouragement and support during this time. The joint activities, be it long-distance cycling or petrol-powered road trips, refueled my enthusiasm for discovery and creation, offering a welcome balance to the long-term goal of this thesis.

Braunschweig, November 2024 *Daniel Witt*

Contents

1 Introduction

The quest for zero-emission transportation and the heightened awareness of energy security will continue to drive demand for sustainably produced batteries, boasting ever-improving performance and degradation characteristics. With expected compounded annual growth rates in global battery production capacity of about 20% and an even faster scale-up in Europe, any immediately implemented improvement in cell quality and cost will have a huge impact [1]. In addition to fundamental material development, two other phases in the creation of a lithium-ion battery offer significant potential for cost savings and quality improvements, namely cell design and cell production. This thesis offers a perspective on the value of detailed physicochemical modeling for both cell design optimization and in-depth yet non-destructive cell diagnostics.

1.1 Motivation

Climate change is a long-term global problem with substantial economic, political, and social challenges. Changes in local average and maximum temperature have a pronounced effect on agriculture, freshwater availability, and natural ecosystems [2]. The more frequent occurrence of extreme weather events and rapidly melting polar ice caps remind us of our responsibility to reduce greenhouse gas emissions as fast as possible. To limit the extent and impact of climate change, humanity's growing hunger for energy must be satisfied in an increasingly sustainable way. Two approaches can make meaningful contributions to realize the ulterior vision of zero-carbon emissions in the future. First, a more efficient energy utilization immediately reduces the demand for both fossil fuels and sustainably produced energy. Second, the availability of scalable energy storage technologies facilitates the utilization of comparably cheap but volatile renewable energies [3]. Lithium-ion battery technology is in the unique position to offer a solution for both approaches due to its high energy efficiency along with its high energy and power density [4].

At first sight, reducing global energy consumption with lithium-ion batteries seems counterintuitive. However, the potential for meaningful energy savings becomes obvious when looking at battery- versus gasoline- or diesel-powered vehicles. Road transport accounts for about 12% of the global greenhouse gas emissions, with 60% of this number originating from passenger travel [5, 6]. Common combustion engines can achieve peak efficiencies of roughly 30% for gasoline

and 40% for diesel [7]. Importantly, these tank-to-wheel efficiencies can only be realized for low loads of about 20%. They drop sharply for smaller power demands and also decline for higher ones. This deteriorates the fuel economy, especially in urban and local driving conditions [8]. In contrast, battery-powered vehicles can offer peak efficiencies beyond 80%, and they can do so over a much broader performance range [7]. As a result, the energy demand for transportation could be cut at least in half by leveraging the higher tank-to-wheel efficiency of battery-powered vehicles. In fact, these vehicles could reduce overall greenhouse gas emissions by at least 68% compared to gasoline-powered vehicles, even when using the European electricity mix with its reliance on fossil fuels [9].

For grid-scale energy storage, using electricity for producing storable energy carriers, like hydrogen or synthetic gasoline, is inherently attractive as it allows to compensate for multi-day or even seasonal fluctuations in renewable energy production. However, the conversion efficiencies from electricity to chemically stored energy are only about 67% for hydrogen [10] and 50% for liquid hydrocarbons [11, 12]. Combined with the conversion losses to electricity in a fuel cell or internal combustion engine, this storage approach presents a significant challenge: relying predominately on sustainably produced energy carriers would amplify humanity's need for clean electricity. Lithium-ion batteries come with a different disadvantage as their capacity is directly linked to the amount of expensive raw materials. Their economic viability for large-scale energy storage depends heavily on the average storage duration and the arbitrage between charged and discharged energy. However, specific use cases, such as peak power shaving in industry, can offer substantial savings even for higher storage costs since energy consumption and peak power demand are billed separately [13]. Large-scale commercialization of low-cost energy storage technologies such as sodium-ion and nickel-hydrogen batteries would expand the range of economically-viable energy storage applications [14]. Ultimately, a combination of different technologies will be required to realize a reliable, economical, yet zero-carbon energy supply.

For the widespread adoption of lithium-ion batteries in transportation, convenience and cost are two major factors. Consequently, low production costs, superior performance, and slow aging are critical. In addition, the fast charge capability is often vital as it allows for an almost uninterrupted utilization of battery-powered vehicles.

To enable an efficient optimization of cell design or production process parameters, the identification of performance-limiting physical processes within a lithium-ion cell is crucial. For instance, bottlenecks may arise from transport of lithium ions in the electrolyte phase or from reaction kinetics at the active material particle surface. Pinpointing these limitations facilitates targeted cell design or process adjustments for iterative improvements in cell quality. In the context of application-tailored cell performance, physicochemical battery modeling can help identify promising cell designs and provide design guidelines without the need for extensive experimental parameter screening [15]. However, a seemingly straightforward change in design parameters,

such as electrode thickness and porosity, inherently requires production process adjustments, which may have an unexpected effect on electrode properties and cell performance. This introduces uncertainty into performance predictions and design recommendations from physicochemical battery models. Uncertainty is especially relevant when these recommendations are far extrapolated from the experimental cell used for the underlying model parameterization. A pragmatic balance between experimental studies and model-based recommendations is needed to minimize the overall time and effort required for a successful cell design optimization.

A direct experimental separation of performance-limiting cell properties across the electrode to the particle level is often challenging. This is further complicated by the formation of an anode-side surface film during the cell formation process, i.e., the first cycling of a lithium-ion battery in cell production. The quality of this surface film, known as the solid electrolyte interphase (SEI), is crucial for superior cell lifetime and performance. However, its experimental characterization, particularly in terms of structure and composition, commonly requires cell disassembly and provides only limited insight into the effect of this surface film on cell performance. Physicochemical modeling enables cell state estimations based on non-destructive electrochemical measurements [16]. This approach offers insights into performance limitations caused, e.g., by reaction kinetics at the interface of this surface film or by transport processes in the electrolyte phase. Furthermore, such model-based cell diagnostics enable the identification of changes in these processes due to aging, although they do not directly explain why these changes occur. The formation process, as one of the most cost-intensive and quality-critical process steps in battery production, presents a unique opportunity for worthwhile improvements. A deeper understanding of the intricate relationship between the chosen cell formation process, the initial surface film formation, and cell performance could facilitate knowledge-driven process improvements [17].

1.2 Scope of the Thesis

Considering the potential impact of lithium-ion battery technology on global energy use, the primary goal of this thesis is to investigate optimization potentials in the context of application-tailored cell design and fast cell formation.

The foundation of a well-performing cell is a sound design of its underlying electrodes for the desired use case. As a universal electrode design optimum is unrealistic, this thesis will address challenges and provide guidelines for the model-based design of cells with a high areal capacity, using two-layer electrodes. Beyond optimal cell design, detailed cell diagnostics are crucial for identifying and subsequently addressing performance bottlenecks in experimental cells. Given the importance of the SEI for cell quality, this thesis introduces a physicochemical cell and SEI

model to analyze changes in the state of an NMC622|Graphite cell along aging, using a commercial three-electrode setup. Afterward, this model is used to decipher the intricate interplay between cell formation conditions, cell performance, and performance-limiting cell properties. This provides valuable insights into the origin of performance improvements in lithium-ion cells after cost-efficient fast formation.

Chapter 2 begins with fundamentals of lithium-ion battery technology. Afterward, state-of-the-art cell design and cell production are addressed. Here, a particular focus is on the time-consuming and cost-intensive cell formation process, which inherently affects the formation of the SEI. Finally, battery modeling is discussed with a focus on physicochemical modeling, which forms the basis for all studies in this thesis. In Chapter 3, the fundamental challenges of optimal cell design are illustrated by a model-based study on two-layer electrodes with a high areal capacity. It provides a perspective on the importance of the chosen evaluation criterion and benchmark for the outcome of any cell quality assessment, ranging from cell design to production process optimizations. In Chapter 4, a physicochemical cell model is extended by a detailed SEI model. The combined model is then used for an exemplary cell state estimation along aging. In Chapter 5, an experimental study is shown, which provides a comprehensive picture of formation-induced changes in cell behavior. The subsequent application of the earlier developed cell and SEI model allows for detailed insights into the effect of the formation process on performance-limiting cell properties. Finally, Chapter 6 concludes this dissertation with a review of its major findings. Furthermore, an outlook on future developments in the convergence area between battery production, diagnostics, and prognostics is given.

2 Fundamentals and State of the Art

In Section 2.1, the basics of lithium-ion batteries and standard methods for electrochemical cell characterization are introduced. Section 2.2 starts with a brief discussion of the interrelation between individual cell properties and their effect on cell performance. Afterward, the path of a lithium-ion battery from its initial design to the end of cell production is addressed. Finally, Section 2.3 discusses different approaches toward lithium-ion battery modeling for both predictive cell design and in-depth cell diagnostics. Herein, the focus is on physicochemical models that enable a good understanding of performance-limiting cell properties, whether for a model-based design study or the analysis of differently processed cells.

2.1 Basics of Lithium-Ion Batteries

This section offers a basic understanding of lithium-ion batteries and their electrochemical characterization. In general, the commonly used term *battery* can refer to a single lithium-ion cell or an interconnection of multiple cells. For simplicity, the term *battery* is used synonymously for a single cell in this work. Furthermore, lithium-ion battery electrodes are regularly named as *anode* and *cathode* based on the discharge direction, referring to the negative and positive electrode, respectively.

2.1.1 Cell Chemistry and Structure

A state-of-the-art lithium-ion battery consists of four fundamental components: anode, separator, cathode, and electrolyte. The active components of both anode and cathode are commonly coated onto copper and aluminium current collectors, respectively.[1] They enable the transfer of electrons between the anode and cathode via an external electric circuit. The electrolyte allows for the corresponding transport of lithium ions within the cell. Finally, the separator prevents an electric short circuit between the electrodes but allows for lithium-ion transport.

[1] These materials provide sufficient electrochemical stability for the operating potentials of each electrode [18].

State-of-the-art lithium-ion batteries use a "rocking chair" mechanism, i.e., lithium ions are shuffled from anode to cathode without a transition to its metallic form at any time [19].[2] A common active material for the anode is graphite, which enables the intercalation of lithium ions within its layered structure. Lithium-metal anodes are intensively researched for their promise of a higher energy density, but they still struggle with requirements like cell safety and lifetime [21]. The same promise explains the broad range of research on silicon-based anodes. Here, major challenges include significant volume expansion during lithiation, poor electrical conductivity, unstable surface films, and gassing during slurry preparation [22, 23]. On the cathode side, lithium iron phosphate and nickel manganese cobalt oxide (NMC) are common choices. The cobalt content in NMC-based active materials has decreased significantly over recent years and is expected to decrease further [24]. Besides geopolitical, social, environmental, and economic considerations, this trend toward nickel-rich NMC is driven by its higher mass-specific capacity [25]. Overall, the governing electrochemical reactions at the active material particle surfaces are given by

$$\mathrm{LiC_6} \rightleftarrows \mathrm{Li_{1-x}C_6} + x\mathrm{e^-} + x\mathrm{Li^+} \tag{2.1}$$

for a graphite-based anode and by

$$\mathrm{LiNMC} \rightleftarrows \mathrm{Li_{1-x}NMC} + x\mathrm{e^-} + x\mathrm{Li^+} \tag{2.2}$$

for an NMC-based cathode. These reactions can be summarized for the full cell as:

$$\mathrm{LiC_6} + \mathrm{Li_{1-x}NMC} \rightleftarrows \mathrm{Li_{1-x}C_6} + \mathrm{LiNMC}. \tag{2.3}$$

Common liquid electrolytes use lithium hexafluorophosphate ($\mathrm{LiPF_6}$) as the conductive salt in combination with aprotic organic solvents like ethylene carbonate (EC) and ethyl methyl carbonate (EMC). Importantly, the electrolyte is not involved in the main electrochemical reaction in contrast, e.g., to a lead-acid battery, which shows a decreasing acidity during discharge. Nonetheless, the aggressive electrochemical conditions within a lithium-ion battery result in side reactions with the electrolyte, especially on the anode side [26]. The deposition of the corresponding reaction products on the active material surface during the first charging and cycling increasingly suppresses these side reactions. As such, the solid electrolyte interphase is essential for the long-term function and stability of a lithium-ion battery. The current understanding of the SEI as a functional surface film will be discussed in detail in Section 4.1.

Commercial lithium-ion batteries can have different form factors. Fundamentally, cells can be distinguished between cylindrical, prismatic, and pouch formats. For instance, the standard types

[2] Aggressive fast charge procedures and low operating temperatures can trigger the deposition of metallic lithium on the anode side. It is highly undesirable in terms of aging and operational safety of lithium-ion batteries [20].

18650 and 21700 refer to a cylindrical format with a diameter of 18 mm / 21 mm and a length of 65 mm / 70 mm, respectively. Here, the trend toward the larger 21700-format reduces the impact of the cell housing on the energy density and lowers production cost, but it comes with challenges in terms of temperature control [27]. Further challenges arise in terms of the housing material. Hardcase cylindrical or prismatic cells offer superior mechanical rigidity, but they lack the flexibility of pouch cells, which use lightweight aluminium laminated films [28].

2.1.2 Electrochemical Characterization Methods

A holistic understanding of lithium-ion battery performance and degradation is crucial for the final integration of a cell into a larger system. Furthermore, it provides the basis for knowledge-driven cell design and production process adjustments.

A standard characterization method is a C-rate test, i.e., a constant-current measurement until the lower or upper cutoff cell voltage is reached. Herein, the C-rate is an often-used parameter that allows comparing discharge curves between cells of different capacities. This is realized by normalizing the applied electric current with the cell capacity. In practical terms, a discharge current corresponding to a C-rate of C/10 would theoretically discharge a cell within 10 h and a C-rate of 2C would take 0.5 h. Although these estimates are only valid for negligible voltage losses within the cell, the C-rate enables a quick categorization of the applied electric load independent of the cell format. Eventually, elevated C-rates can provide insights into transport limitations within both the active material particles and the electrolyte-filled pore volume of the electrodes. At low C-rates, transport losses and reaction kinetics become almost negligible, i.e., the anode and cathode half-cell potentials approach equilibrium. In this context, the differential voltage analysis can be a valuable tool to estimate the loss of lithium inventory and active material [29].

Electrochemical impedance spectroscopy (EIS) differs from a C-rate test in terms of both measurement complexity and resemblance to common load scenarios. Herein, a small sinusoidal excitation signal, e.g., a current, is applied, and the corresponding voltage response is measured to obtain the frequency-dependent impedance of a cell. A fundamental requirement for meaningful EIS data is a time-invariant and linear system response. This implies the need for a sufficient relaxation time before the impedance measurement and a sufficiently small galvanostatic or potentiostatic excitation signal. Ultimately, EIS allows to distinguish processes based on their respective time constants. For instance, the contact resistances between the current collector and coating composite can be expected above 1 kHz, reaction kinetics on the order of 10 Hz – 100 Hz, and solid diffusion below 1 Hz [30, 31].

Overall, C-rate tests and EIS provide complementary information about the inner state of a cell. If such characterization experiments are repeated along cycle-induced or calendar aging, they

can help to gain a deeper understanding of cell degradation and performance, providing supplementary information beyond the often-used capacity retention along cell aging.[3] Combined with model-based cell diagnostics, these experimental data can be reduced to several model parameters. This enables a straightforward comparison of different cells. Depending on the chosen model, these parameters can provide direct insights into the electrode- or even particle-level origin of performance limitations.

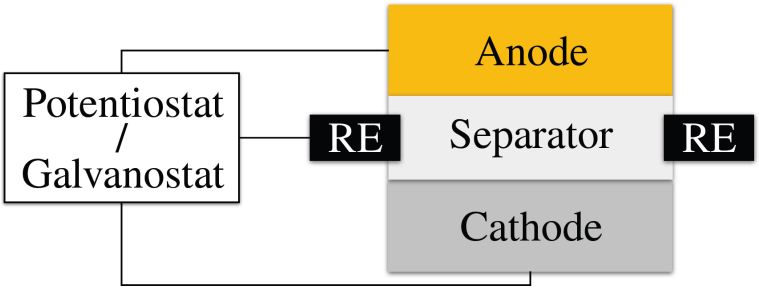

Figure 2.1: Schematic illustration of a three-electrode setup consisting of a potentiostat/galvanostat that is connected to an anode, a cathode, and a reference electrode (RE). For the experiments in this work, the reference electrode consists of lithium metal coated on a stainless steel ring, which is placed around the separator.

Commercial lithium-ion cells have one contact for the anode and one for the cathode. Although this is sufficient for regular battery operation, it complicates detailed cell diagnostics by superimposing anode- and cathode-side contributions. This problem can be solved for laboratory-scale experiments by introducing a reference electrode into the cell. A schematic of such a three-electrode setup is shown in Figure 2.1. Notably, the location, geometry, and material of the reference electrode can significantly impact the quality of impedance measurements [32]. With a ring-shaped lithium-metal reference, the effect of geometric asymmetry on the half-cell impedance response can already be reduced [33]. Mesh reference electrodes with lithium-iron-phosphate or lithium-titanium-oxide coatings can further reduce artifacts, but they increase transport losses in the electrolyte phase [34]. As a compromise between minimal distortions in the impedance and discharge behavior, all experiments in this work use a ring-shaped reference electrode. Ultimately, three-electrode measurements enable a more holistic and reliable identification of performance-limiting cell properties. This knowledge can then be used to optimize cell design, production, and even operating strategies of cells without reference electrodes.

[3] The capacity retention refers to the relative decline of the discharge capacity as a function of cycle number.

2.2 From Cell Design to Production

This section aims to provide a fundamental understanding of the major influencing factors of cell quality and cost. The performance and aging characteristics of a lithium-ion battery are defined mainly by its design, production, and final utilization. First, a brief overview of the inherent link between cell performance and electrode- to particle-level properties is provided. Second, the process of cell design optimization and available cell design options are presented. Third, the individual process steps of state-of-the-art cell production are introduced. Here, the focus is on a general understanding of the impact of individual process steps on cell quality and cost. As one of the major cost drivers, the cell formation process is discussed in more detail.

2.2.1 Cell Properties, Performance, and Aging

The performance characteristic of a lithium-ion battery is governed by lithium-ion transport in the active material particles, ionic transport in the electrolyte phase, electrical transport in the electrodes, and reaction kinetics at the interface between active material and electrolyte. At sufficiently low C-rates, these processes do not have a significant impact on the cell voltage and the corresponding half-cell potentials. As such, the usable capacity is driven by the chosen cutoff voltages and the initial or maximum lithium inventory of the respective electrodes. At elevated C-rates, any of the mentioned processes can significantly contribute to overpotentials.

Fast transport of lithium ions within the active material is essential for a good utilization of the available lithium inventory. It can be affected by the solid diffusion coefficient and the particle size. For the exemplary insertion of lithium ions into a cathode active material particle, poor transport properties could result in substantial concentration gradients and a high concentration, i.e., a low potential, at the particle surface. Although the core of the active material may still be able to accommodate more lithium ions, the low half-cell potential could trigger a premature end of discharge. Smaller particles could help in this case by reducing the diffusion length.

Another major factor for good active material utilization throughout the electrode is a fast transport of lithium ions in the electrolyte phase. The electrolyte defines the upper transport limit in terms of lithium-ion diffusivity, ionic conductivity, and transference number. However, state-of-the-art electrodes are porous particle systems infiltrated with electrolyte. As such, the effective transport properties in the electrolyte phase also depend on the microstructure of an electrode. Two critical metrics for the assessment of electrolyte transport are porosity and tortuosity. The former parameter can be measured, e.g., with mercury intrusion porosimetry [35]. A low porosity translates into a small pore volume available for lithium-ion transport. The tortuosity is a measure for the increase of the effective transport length within the pore network compared to

the shortest path, i.e., the electrode thickness. As such, the tortuosity must be equal to or higher than one. In literature, different methods for tortuosity estimation are described, comprising the analysis of microstructure reconstructions or the utilization of impedance data from symmetrical cells with a blocking, i.e., a non-intercalating, electrolyte [36, 37].

In this work, the tortuosity will be estimated with a homogenized battery model. Herein, the tortuosity describes the effective transport properties within the electrolyte-filled pore volume.[4] Ultimately, a low tortuosity in combination with a sufficiently high porosity will enable superior performance at elevated C-rates. This also explains the performance benefit that originates from a vertical alignment of graphite particles during coating [40, 41]. Essentially, it avoids long transport pathways around these high-aspect-ratio particles, which facilitates lithium-ion transport into the depth of the electrode.

The electrical conductivity of an electrode is another parameter that can have a pronounced impact on the active material utilization. This is especially relevant for the cathode due to the poor bulk conductivity of the active material. Here, conductive additives must be used to ensure low-resistance electron transport. Otherwise, high potential gradients throughout the electrode would result in a preferential active material utilization close to the current collector, which features electron transport with minimal ohmic losses. This is in contrast to the effect of a high tortuosity and a low porosity, which would favor the active material utilization close to the separator.

The electrochemical reaction at the interface between the electrolyte and active material finally brings lithium ions and electrons together. Besides reaction kinetics, the overpotential for a given current depends on various aspects. One essential factor is the electrochemically active surface area of the particles within the electrode. For instance, a larger surface area directly translates into a lower current density at the interface between active material and electrolyte, effectively reducing the overpotential for a given current. Apart from this, the availability of lithium ions in the electrolyte phase is crucial for an intercalation reaction. The required overpotential would increase significantly if there were a local depletion of lithium ions. Eventually, this could trigger a premature end of charge, which explains the importance of fast lithium-ion transport in the electrolyte phase. Besides these two aspects, the direction of the reaction can have a notable impact on reaction kinetics. For instance, the intercalation of lithium ions into graphite is slower than their deintercalation. This may be explained by an accumulation of lithium ions close to the interface during intercalation [42]. Furthermore, particle surface modifications can alter kinetics for the de-/solvation process and the de-/intercalation reaction of lithium ions [43].

[4] For the sake of simplicity, the term *tortuosity* is used throughout this work instead of the term *tortuosity factor*. Strictly, the former relates to the geometric definition, i.e., the effective path length compared to the direct path length through a porous medium, and the latter refers to a scaling parameter, e.g., for the effective ionic conductivity in the pore volume [38]. The Bruggeman relation is often used to correlate porosity and tortuosity factor [39].

Given the complex interrelation between lithium-ion transport, electron conduction, and kinetics, it is no surprise that a change within one electrode can impact the behavior of the other electrode. For this reason, a holistic approach toward cell characterization is crucial. The earlier introduced three-electrode setup can help to reduce uncertainty in data interpretation and analysis by separating anode- and cathode-side contributions. Section 4.3 addresses this point in the context of electrode-specific parameter identification as a fundamental challenge of model-based cell diagnostics.

As discussed before, transport limitations can result in a partial utilization of the electrodes. This intensifies the stress of the used part of the electrodes, eventually leading to faster cell degradation. In consequence, the chosen cell design can have a direct impact on the cell aging behavior. A brief overview of aging mechanisms is provided in the following.[5]

High current densities increase the mechanical stress on the active material, which in turn increases the probability of particle cracking [46]. Such mechanical degradation can be responsible for irreversible volume expansion and eventually a dry-out of the electrode due to a lack of excess electrolyte volume [47]. Particle cracking can further result in a loss of usable active material due to loss of electrical contact with the conductive network throughout the electrode [44]. Additionally, loss of lithium inventory can occur due to rapid film formation on the new surface created at the fracture site of the particle. Cathode active material coatings can help to prevent particle cracking by suppressing side reactions at highly reactive grain boundaries [48].

The application of high C-rates presents another challenge, specifically for fast charging. At low anode potentials, plating of metallic lithium can occur, which competes with the intended intercalation reaction. Two major problems arise from this. First, lithium plating is a safety concern regarding i) dendrite formation, possible separator penetration, and short-circuiting of the cell, and ii) a lower onset temperature for a thermal runaway [20]. Second, the stripping of plated lithium may not be reversible during discharge due to the detachment of a dendrite, known as dead lithium. Under standard conditions, lithium plating becomes possible below $0\,\mathrm{V}$ vs. $\mathrm{Li}/\mathrm{Li}^{+}$. Local lithium-ion depletion in the electrolyte phase and sluggish reaction kinetics or a small specific surface area induce higher overpotentials, i.e., critically low anode potentials. This renders plating-free fast charging in transport-limited electrodes challenging. At low temperatures, slower reaction kinetics and deteriorated lithium-ion transport in the electrolyte exacerbate this issue [49, 50]. Aging due to lithium plating at low temperatures and accelerated lithium-consuming side reactions at high temperatures illustrate the challenges of aging-optimal fast charging [51]. However, recent work on graphite active material coating could demonstrate a massive improvement in capacity retention under fast-charge conditions by preventing the formation of natural SEI and delaying the onset of lithium plating [52].

[5] For comprehensive overviews of cell aging and its modeling, the reader is referred to [44] and [45].

2.2.2 Cell Design[6]

Optimizing the cell design of lithium-ion batteries involves navigating a complex landscape of cell design options and potentially conflicting goals. While some optimization objectives may align synergistically, others may require a careful trade-off. In the end, a well-designed cell must strike a balance between various performance-limiting processes, such as mass transport and reaction kinetics, while also considering specific application requirements like volumetric energy density and production costs.

Figure 2.2 gives a simplified overview of the cell design workflow. The first step toward any optimization problem should be the holistic definition of optimization objectives along with a corresponding benchmark system for a meaningful evaluation of the optimization progress. In the next step, state-of-the-art and novel cell design options must be evaluated with respect to their relevance to the optimization problem. Finally, an optimization method must be chosen, which combines the optimization objective and the selected cell design options. Here, a fine-grained screening of a broad parameter space, i.e., a brute-force optimization, will likely be too expensive and time-consuming from an experimental perspective and potentially also from a modeling point of view. For this reason, methods for an efficient exploration and exploitation of the parameter space, like design of experiments or direct mathematical optimization, are crucial. For an optimal utilization of available resources, a particular focus should be on the synergistic combination of experimental studies, model-based cell diagnostics for the identification of performance bottlenecks, and model-based design recommendations. Possible pathways toward optimal electrode design are discussed in detail in Section 3.1.

Despite the wide range of possible optimization objectives, electrode design is commonly regarded in the context of improved discharge characteristics. Although a broad body of literature elaborates on the challenges of fast charging [20, 53, 54], the focus commonly is not on optimal cell design for fast charging but rather on other crucial aspects, such as beneficial material properties [55–58], charging protocol optimization [59–62], cell aging [63–66], and temperature-related lithium plating mitigation strategies [67, 68]. Some studies consider the effect of electrode structure. Tanim et al. highlight the importance of tight production tolerances for structural properties, such as electrode composition, porosity, and tortuosity, to avoid an early onset of cell aging due to local electrode inhomogeneities [63]. Vishnugopi et al. investigated the interrelation between electrode porosity, performance, and lithium plating at various temperatures [69]. In contrast to electrode design optimizations for discharge, a fundamental study on ideal electrode design for both charge and discharge is yet unavailable in literature. However, most applications demand a

[6] Parts of this subsection have been published in Witt, Wilde, Baakes, Belkhir, Röder, Krewer, Energy Technol., 9(6):2000989, 2021 (doi: 10.1002/ente.202000989, CC BY 4.0 [15]).

minimal recharge time to enable an almost uninterrupted mobile power supply. The continuous discharge requirements are often much lower.

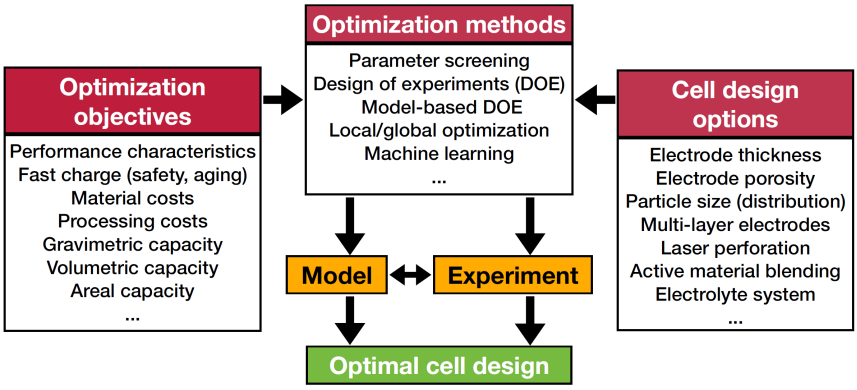

Figure 2.2: Overview of possible optimization objectives for lithium-ion batteries along with possible cell design options and optimization methods. To identify an optimal cell design, either a battery model (physicochemical or data-driven), an experiment, or a synergistic combination of both can be used.

When considering available cell design options, multiple decisions are required to reduce the number of design parameters to a manageable level. One of the most critical decisions is the selection of a suitable cell chemistry for the targeted application. Primarily, this comprises the selection of the anode and cathode active materials and the electrolyte system. Besides aspects, such as million-mile cycle life of a cell chemistry [70] and material costs [71], the choice of the active material inherently defines a theoretical limit to the maximum achievable energy density [72]. In terms of cell performance, the selected electrolyte system significantly impacts mass transport within the electrode. The transport properties of standard electrolytes are a key bottleneck for achieving superior fast-charge capability [56]. However, even without significant improvements in electrolyte formulation, fast charging at elevated cell temperatures benefits from enhanced lithium-ion transport [68].

Besides common electrode formulations with a single active material, a blend of multiple active materials can help to optimize the overall electrode properties. For instance, adding silicon to a graphite anode notably increases its capacity, which allows for thinner electrodes. However, challenges arise from the higher reactivity of silicon compared to graphite. This can complicate slurry mixing due to gassing [23] and induce rapid cell degradation if it is not addressed properly, e.g., via coatings of the active material and electrolyte additives like fluoroethylene carbonate [22]. In addition, lithium can be trapped in silicon due to i) sluggish lithiation/delithiation kinetics, which hinders the extraction of lithium during discharge, and ii) pulverization of the active material due to huge volume changes >300% [73].

After the choice of a suitable cell chemistry, the electrode properties can be tailored to different use cases. Basic electrode design options comprise the porosity and thickness of an electrode, as well as the size of the utilized active material particles. A reduced electrode porosity generally leads to an increase in volumetric capacity. However, for NMC cathodes to perform well at elevated C-rates, intermediate porosities are preferred as they strike a balance between electrical conductivity and effective ionic conductivity [74, 75]. The effective electrical conductivity benefits from a lower electrode porosity, which facilitates the formation of a percolation network with conductive additives. This is less important for graphite-based anodes due to the high intrinsic conductivity of the active material. In contrast, the effective ionic conductivities of both anode and cathode benefit from a higher porosity, which shortens transport pathways and reduces concentration gradients in the electrolyte phase. As long as the electrode is not limited by transport in the electrolyte phase, increasing the electrode thickness can increase the volumetric capacity by reducing the proportion of passive components, such as the separator and current collectors [76, 77]. In terms of particle size, smaller particles inherently feature shorter solid diffusion pathways and a higher specific surface area, which can improve the rate capability of an electrode [78]. However, for graphite-based anodes, medium-sized particles are recommended to mitigate accelerated side reactions associated with small particles and the increased risk of lithium plating with larger ones [79].

Electrodes with high areal capacity are prone to severe transport limitations in the electrolyte phase, but they are favorable in terms of production throughput and volumetric capacity. However, optimizing basic electrode parameters, such as electrode porosity and active material particle size, may be insufficient to simultaneously achieve a high volumetric capacity and good performance at high C-rates. To overcome this conflict of objectives, advanced structuring methods can be employed. Laser ablation is a technique that can be used to create regular patterns, such as linear channels [80] or holes [81], in an electrode. This facilitates lithium-ion transport into the depth of an electrode, which can notably improve performance.

Multi-layer electrode coating is another approach that promises to improve the performance of thick electrodes. In general, creating a homogeneous electrode composition and structure is a fundamental challenge in the production of single-layer electrodes with high mass loading. It was observed that fast drying of the coated wet film leads to notable gradients in the binder concentration throughout a single-layer electrode [82]. This migration of binder to the electrode surface during drying reduces the adhesive force between the coating and the current collector, while also degrading cell performance [83]. Using a simultaneous two-layer slot die coating process allows to address this problem by using a slurry formulation with a lower binder content in the top layer [83]. However, a more homogeneous binder distribution and improved performance may also be achieved by fine-tuning the mixing and drying process, favoring gentle mixing to maintain the agglomeration of conductive additives and binder and lower drying rates to reduce

the driving force for binder migration [77]. If layering is performed sequentially by coating a second layer on top of an already dried layer, the electrical conductivity at the interface between the two layers emerges as an additional challenge [84].

Besides addressing the issue of binder migration, multi-layer electrode coating enables the creation of layers with different characteristics, e.g., regarding active material type and particle size [85]. Furthermore, the discharge performance generally benefits from a higher porosity toward the electrode surface, which facilitates lithium-ion transport in the electrolyte phase [86]. Multiple simulation studies support this general structuring recommendation [87–89].

Ultimately, experimental and model-based studies on electrode design are inherently heterogeneous due to the variety of design options. In addition, they differ in terms of their optimization objectives and benchmark systems, which can lead to different reported benefits for similar design variations [87, 88]. This complicates the selection of the most suitable electrode design for a specific application. Furthermore, the common focus on discharge characteristics impedes a holistic understanding of recommended cell designs. Chapter 3 will address this issue and provide a perspective on two-layer electrode design for charge and discharge. It starts with a critical analysis of available approaches for electrode design optimization. Afterward, two model-based case studies are discussed that illustrate the challenges of optimal cell design and showcase the importance of a robust design optimum in the context of production uncertainties.

2.2.3 Cell Production[7]

Deviations in intermediate product properties, such as coating thickness and porosity of an electrode, are accepted within predefined tolerances to optimize production costs in terms of consistent product quality and low scrap rate. Given the significant impact of process-product interdependencies in battery production on the final cell behavior, a well-defined electrode design alone cannot ensure superior performance characteristics [90, 91]. For the identification of meaningful optimization potentials in cell production regarding cell quality and cost, a basic understanding of the individual production steps is necessary.

Figure 2.3 gives a simplified overview of cell production.[8] The first series of processes concerns the production of the required electrodes. This involves dry and wet mixing of the materials, coating the slurry on the current collectors, calendering of the electrode web, slitting the electrode web to the desired width, and final vacuum drying. Afterward, the electrodes are cut into single electrodes that can be stacked or winded to fit the desired cell format. After contacting, enclosing,

[7] Parts of this subsection have been published in Witt, Bläubaum, Baakes, Krewer, Batteries Supercaps, e202400023, 2024 (doi: 10.1002/batt.202400023, CC BY 4.0 [17]).

[8] For a detailed review and perspective on battery production technologies, the reader is referred to [72, 92, 93].

and electrolyte filling, the cell is ready for cell formation, i.e., the first charging or rather cycling within its lifetime. Subsequent degassing ensures that gaseous side reaction products from the formation process do not remain in the cell, potentially displacing electrolyte and thus rendering an electrode partially inactive. Finally, a so-called aging process is performed to enable cell maturation and quality assurance.

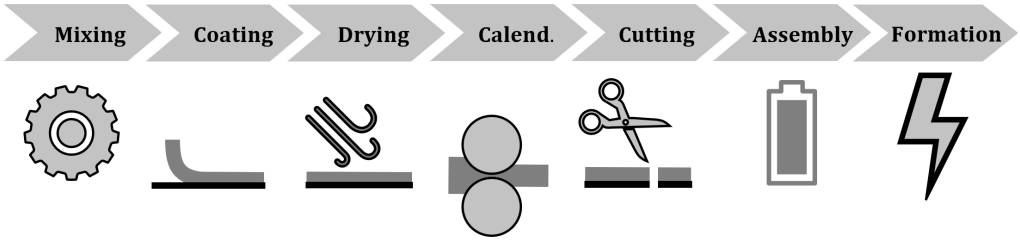

Figure 2.3: Flowchart of lithium-ion cell production.

The total cost of a lithium-ion battery can be divided into roughly 75% material costs and 25% production costs, comprising both operational and capital expenditure [92, 94]. To facilitate meaningful innovations in battery production, a thorough understanding of cost, time demand, and energy consumption of state-of-the-art production processes is crucial. The cell formation and the subsequent cell aging combined are currently the most cost-sensitive process steps toward the end of battery production, accounting for roughly 30% of the production cost of lithium-ion batteries [92, 93, 95]. For comparison, electrode coating and drying contribute about 15% to the total production cost, while enclosing and electrolyte filling constitute about 13% [93, 95].

Nonetheless, the final cell quality is the result of all process steps and the quality of their intermediate products. For instance, the mixing process has a notable effect on the microstructure of an electrode, which influences lithium-ion transport in the electrolyte phase and, consequently, performance at elevated C-rates [96]. The calendering process, which is applied after electrode coating and drying, compresses an electrode to a target porosity [97]. This increases the theoretical volumetric capacity and facilitates the formation of a percolation network with conductive additive particles. Especially for cathode coatings, this percolation network can increase the electrical conductivity well beyond the intrinsic conductivity of the active material [75]. However, excessive compression impedes transport in the electrolyte phase, counteracting the benefit of a higher electrical conductivity.

Regarding production throughput, the formation and aging processes are a clear bottleneck with process times up to multiple days for formation and multiple weeks for aging [98]. This also explains the large number of battery cyclers and the substantial floor space requirements of up to 25% of the entire production facility, presenting a unique opportunity for meaningful optimizations [98]. In terms of energy consumption, cell formation is less critical due to the recycling

of discharged energy, resulting in a share of about 1% to 5% [93, 99, 100]. Electrode drying and solvent recovery offer a much more significant potential for energy savings with a share of roughly 47% and dry room operation with about 29% [93].

The time requirement of the cell formation process is related to the commonly applied low current densities, which are intended to create a well-protective solid electrolyte interphase. This surface film formation is inevitable due to the large voltage window of lithium-ion batteries in contrast to the much smaller stability window of standard electrolyte systems [101]. Once established, the SEI suppresses ongoing side reactions, ensures a high coulombic efficiency, and results in a reliable and stable battery performance [26, 102]. Without a sufficiently passivating SEI, side reactions would continue to consume cyclable lithium and, as a side effect, ongoing SEI growth would deteriorate transport in an increasingly less porous electrode. Both aspects decrease the practical capacity and energy density of the cell. For this reason, a sound understanding of the impact of formation conditions, like current density, voltage range, and temperature, on performance-limiting and degradation-related cell properties is crucial for knowledge-based optimizations. Chapter 5 elaborates in more detail on cell formation. It combines an experimental formation variation with detailed model-based cell diagnostics to reveal formation-induced changes within the cells.

After formation, an aging procedure is applied with two main goals: i) facilitate the naturally occurring restructuring of the SEI after its initial formation [103, 104] and ii) enable a classification of the final cells, commonly based on their self-discharge over multiple weeks [92, 105]. To the best of the author's knowledge, a dedicated study on the impact of this process on the fast charge/discharge and aging characteristic of a cell is not yet available. Thus, the actual optimization potential for meaningful time savings without a compromise in terms of cell quality remains unclear. However, different approaches have been patented to enable a substantially faster quality classification, e.g., by measuring a self-discharge current over hours rather than a self-discharge voltage over weeks [106] or by estimating self-discharge via calorimetry [107].

Overall, the above analysis of meaningful optimization potentials is based on state-of-the-art cell production with a liquid electrolyte and separate electrode production lines for anode and cathode. In perspective, further cost savings may be possible by eliminating entire production steps. For instance, all-solid-state cells with lithium-metal anodes promise to enable an anode-free cell production [108, 109]. Similar to a graphite-based anode, the lithium inventory of the final cell originates from the cathode active material. The difference is that the anode does not need any coating with active material. Instead, the first charging results in lithium metal deposition on the anode current collector. This could eliminate half of the electrode production, which in turn reduces the production complexity, costs, and energy consumption.

Besides optimizing individual production processes, the chosen cell design also affects the cost and sustainability of the overall cell production. For instance, a higher coating thickness can increase the throughput of produced cell capacity with the same equipment [94]. However, this adjustment is limited by the performance requirements of the targeted application. In the context of process uncertainties, the scrap rate at the end of the production line may be reduced by choosing a robust electrode design that provides relatively stable cell characteristics [91, 110]. These aspects will be considered in detail in Chapter 3.

2.3 Lithium-Ion Battery Modeling

The choice of an adequate cell modeling framework is critical for both model-based cell design and diagnostics. It needs to combine sufficient model complexity, i.e., the ability to describe the actual cell behavior, with reasonable computational cost, i.e., minimal time for design optimization and parameter estimation. This section starts with a brief overview of available modeling approaches, ranging from behavioral to physicochemical models. Here, the pseudo-two-dimensional (P2D) cell model is introduced, which forms the basis for all studies in this thesis. Afterward, specific challenges for cell design and diagnostics are discussed.

2.3.1 From Behavioral to Physicochemical Modeling[9]

The behavior of lithium-ion batteries has been studied extensively in literature. Depending on the use case, different modeling approaches can be used. The following overview starts with the computationally least demanding ones and advances to 3D microstructure-resolved models.

Empirical models are a valid option for applications that need an accurate representation of known cell behavior but do not need valid simulation results beyond the underlying calibration data. This makes them useful for applications like real-time control systems or performance prediction under known aging conditions [111]. However, their validity range depends on the scope of potentially time-consuming and expensive experimental data for model calibration, as they lack a physical basis for meaningful extrapolations. Deeper insights into performance-limiting processes on the electrode or particle level should generally not be expected.

Equivalent circuit models (ECM) also aim to describe the cell behavior without necessarily describing the underlying transport processes or reaction kinetics directly. They use electronic components, like resistors and capacitors, to mimic the overall voltage response of a lithium-ion

[9] Parts of this subsection have been published in Witt, Röder, Krewer, Batteries Supercaps, 5(7):e202200067, 2022 (doi: 10.1002/batt.202200067, CC BY 4.0 [16]).

battery. As such, they may be regarded as empirical models with predefined building blocks. ECMs are widely used for impedance analysis and system control due to their easily adjustable level of complexity and low computational cost [112, 113]. However, this versatility can also lead to ambiguities in model-based cell diagnostics. If the elements within an ECM are not backed by a physics-based analogy, this complicates the interpretation of their parameters [114]. Although ECMs commonly employ electronic components, they can also be used as a general framework to structure physicochemical models. When the electrical elements are translated into their electrochemical analogs, e.g., a Butler-Volmer equation instead of a reaction resistance, an ECM can provide the same level of insight as a physicochemical model [115].

Physicochemical models overcome the limitations of empirical models and simple ECMs. For cell design and diagnostics, they offer two major advantages. First, they enable a straightforward physical interpretation of limiting processes and process changes. All model parameters have a physically meaningful interpretation, including electrode tortuosity, diffusion coefficients, and reaction rate constants. This facilitates a direct comparison with dedicated experiments and simulations on properties like lithium-ion diffusion coefficients in the active material [116] or electrolyte phase [50]. Furthermore, they can provide insights into local overpotentials or even concentration profiles throughout a cell. Second, they feature a better extrapolation capability. This results from modeling physicochemical processes rather than providing only an imitation of the observed cell behavior. However, the level of detail can vary significantly, increasing from a single particle model (SPM) over a P2D model to 3D microstructure-resolved models.

At the lower end of the complexity range, SPMs can be used to analyze quasi-steady state data, i.e., measurements at low C-rates and EIS [117, 118]. Such models simplify the structure of a lithium-ion battery significantly by homogenizing an electrode to one representative active material particle or a particle size distribution [119]. This is valid if concentration and potential gradients throughout an electrode are negligible. As a result, the model accuracy is best for relatively thin and porous electrodes.

The P2D model may be considered the general-purpose tool of physicochemical lithium-ion battery modeling. Although 3D microstructure-resolved battery models are likely to capture the electrochemical cell behavior better, their computational cost currently still prohibits their utilization for broad cell design studies and model-based cell diagnostics [120]. Additionally, the measurement of the electrode microstructure, e.g., via synchrotron [77] or FIB/SEM tomography [121], results in additional effort and infrastructure requirements. The P2D model promises to resemble the accuracy of a 3D model but with moderate computational cost on the order of minutes or even seconds. The major difference to a 3D microstructure-resolved model is the homogenization of the electrodes. The effect of the pore connectivity and carbon-binder domain on the overall cell behavior is typically described by effective transport properties like the effective electrical and ionic conductivity. Similar to the SPM, particles are represented as

spheres. All studies in this thesis are based on the P2D model introduced by Doyle et al. [122], which is extended by an electrochemical double-layer to enable realistic cell dynamics [123].

Although the P2D model can be used for both model-based cell design and diagnostics, their requirements differ substantially. For example, a cell design model should ideally include a realistic representation of microstructure properties over a wide range of design parameters. In contrast, a model-based cell state estimation does not need this prediction capability, although it could help to reduce the number of unknown model parameters. Vice versa, accurate modeling of the SEI is deemed essential for holistic cell diagnostics. However, a cell formation model that is valid over a wide range of cell designs and process parameters is yet to be developed. As long as predictive cell formation models are computationally expensive and not verified for multiple electrode designs, a meaningful incorporation of the SEI into the design process does not seem feasible [124]. For this reason, the specific modeling details are given separately for the cell design study without SEI in Chapter 3 and for the model-based cell state estimation with SEI in Chapter 4, which is later also used in Chapter 5.

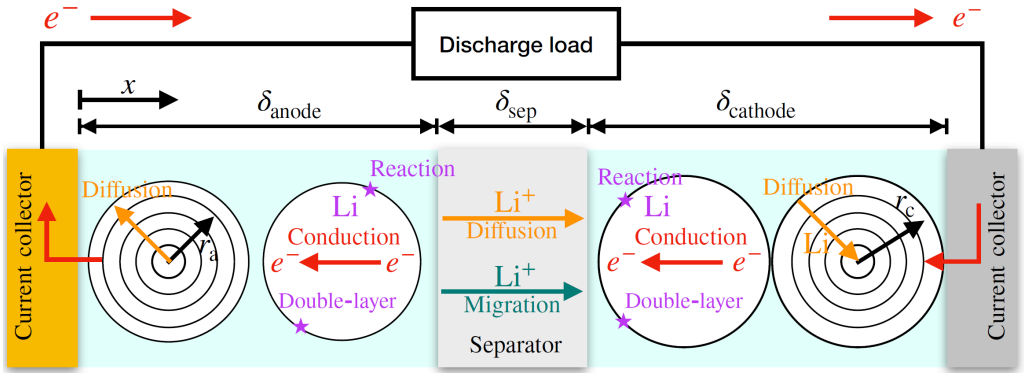

Figure 2.4: Schematic representation of the basic P2D cell model (figure style inspired by [125]). The coordinate x is used for the cell-level discretization of anode, separator, and cathode with thicknesses δ_a, δ_{sep}, and δ_c. The radial coordinate r is used for the particle-level discretization of the active material particles.

The basic equations of the P2D model and its boundary conditions are given in Table 2.1. They enforce mass and charge conservation in the solid and electrolyte phase. Figure 2.4 presents a schematic representation of the basic P2D model, illustrating the governing processes during discharge. Changes in the local lithium concentration c_s in the active material particles are driven by diffusion, which is described by Fick's second law. Here, the flux of lithium ions at the surface of the spherical active material particles matches the faradaic current of the electrochemical reaction. At the particle center, the diffusion flux must be zero. The potential in the solid phase Φ_s is governed by Ohm's law. Charge transport in the solid phase is coupled to the electrolyte phase by an electrochemical double-layer. Here, the total flux of electrons is the sum of the contributions

from the electrochemical reaction and the capacitive effect of the electrochemical double-layer. To ensure charge conservation, the flux of electrons leaving the anode current collector equals the flux of electrons entering the cathode current collector during discharge. As the separator is an electrical insulator, the electrical fluxes at its interfaces are zero. Changes in the local concentration of lithium ions in the electrolyte phase c_e are driven by migration and diffusion. These processes are modeled with the Nernst-Planck equation, assuming negligible convection. As transport of lithium ions through the current collectors is not possible, the concentration gradients at the interfaces between the current collectors and the electrolyte phase are zero. Finally, gradients in the electrolyte potential Φ_e and the lithium-ion concentration drive charge transport in the electrolyte phase. The total flux of lithium ions is the sum of the contributions from the electrochemical reaction and the capacitive effect of the electrochemical double-layer. The gradients in the electrolyte potentials at the current collectors are zero.

Table 2.1: Basic equations of the utilized P2D cell model [122, 123]. L_cell denotes the full-cell thickness. δ_a and δ_c describe the coating thickness of the anode and cathode, respectively.

Variable	Partial differential equation	Boundary condition
c_s	$\begin{cases} \varphi_\mathrm{s}(r) = -D_\mathrm{s}\dfrac{\partial c_\mathrm{s}(r)}{\partial r} \\ \dfrac{\partial c_\mathrm{s}(r)}{\partial t} = \dfrac{1}{r^2}\dfrac{\partial}{\partial r}\left(D_\mathrm{s} r^2 \dfrac{\partial c_\mathrm{s}(r)}{\partial r}\right) \end{cases}$	$\begin{cases} \varphi_\mathrm{s}(0) = 0 \\ \varphi_\mathrm{s}(R_\mathrm{s}) = \dfrac{j^\mathrm{Li}(x)}{a_\mathrm{s} F} \end{cases}$
Φ_s	$\begin{cases} J_\mathrm{s}(x) = -\sigma_\mathrm{s,eff}\dfrac{\partial \Phi_\mathrm{s}(x)}{\partial x} \\ \dfrac{\partial J_\mathrm{s}(x)}{\partial x} = -j^\mathrm{Li}(x) - j^\mathrm{DL}(x) \\ j^\mathrm{DL}(x) = a_\mathrm{s} C_\mathrm{DL}\dfrac{\partial\left(\Phi_\mathrm{s}(x) - \Phi_\mathrm{e}(x)\right)}{\partial t} \end{cases}$	$\begin{cases} J_\mathrm{s}(0) = -\dfrac{I_\mathrm{cell}(t)}{A_\mathrm{cell}} \\ J_\mathrm{s}(\delta_a) = 0 \\ J_\mathrm{s}(L_\mathrm{cell} - \delta_\mathrm{c}) = 0 \\ J_\mathrm{s}(L_\mathrm{cell}) = \dfrac{I_\mathrm{cell}(t)}{A_\mathrm{cell}} \end{cases}$
c_e	$\left\{\varepsilon_\mathrm{e}\dfrac{\partial c_\mathrm{e}(x)}{\partial t} = \dfrac{\partial}{\partial x}\left(D_\mathrm{e,eff}\dfrac{\partial c_\mathrm{e}(x)}{\partial x}\right) + (1-t_\mathrm{p})\dfrac{j^\mathrm{Li}(x)}{F}\right.$	$\begin{cases} \dfrac{\partial c_\mathrm{e}}{\partial x}(0) = 0 \\ \dfrac{\partial c_\mathrm{e}}{\partial x}(L_\mathrm{cell}) = 0 \end{cases}$
Φ_e	$\begin{cases} J_\mathrm{e}(x) = -\sigma_\mathrm{e,eff}(x)\dfrac{\partial \Phi_\mathrm{e}(x)}{\partial x} - \sigma_\mathrm{De,eff}(x)\dfrac{\partial \ln\left(c_\mathrm{e}(x)\right)}{\partial x} \\ \dfrac{\partial J_\mathrm{e}(x)}{\partial x} = j^\mathrm{Li}(x) + j^\mathrm{DL}(x) \end{cases}$	$\begin{cases} \dfrac{\partial \Phi_\mathrm{e}}{\partial x}(0) = 0 \\ \dfrac{\partial \Phi_\mathrm{e}}{\partial x}(L_\mathrm{cell}) = 0 \end{cases}$

2.3.2 From Modeling to Predictive Cell Design[10]

Considering the variety of possible cell design configurations, a purely experimental identification of the most suitable one is a resource-intensive, if not unrealistic, endeavour. Physicochemical models can aid the design process by providing insights into performance bottlenecks or even by recommending an optimized cell design configuration for a targeted experimental evaluation. For this purpose, the chosen model must be able to accurately capture the electrochemical behavior of a real cell. Furthermore, the model must consider the intricate effect of design parameters, such as electrode porosity and particle size, on effective electrode properties, such as tortuosity, electrical conductivity, and electrochemically active surface area [75]. In addition, the effect of the carbon-binder domain must be considered, as it can reduce the active surface area, which affects reaction kinetics and elongates diffusion pathways [120]. The accurate modeling of these complex structure-property relationships is crucial for realistic cell design recommendations. Importantly, this does not comprise the effect of significant changes in the electrode production, such as different slurry mixing equipment and intensity [96], different drying rates [77], or different cell formation conditions [17, 126]. A fully integrated process and performance model that is valid over a wide range of process and cell design parameters is not available yet.

In terms of model selection, 3D microstructure-resolved models can directly capture the effect of electrode microstructure on transport pathways in the solid and electrolyte phase, as well as its effect on the electrochemically active surface area [120]. This enables a detailed analysis of the effect of the spatial position of the carbon-binder domain on cell performance [127, 128]. The required electrode microstructures can be generated virtually by microstructure models [129, 130] or they can be obtained experimentally using X-ray tomography [131–133], focused ion beam scanning electron microscopy [134, 135], or a synergistic combination of both [136].

The earlier introduced P2D model does not inherently consider the effect of electrode microstructure on cell performance. Instead, the electrodes are homogenized and assigned effective properties, such as an effective electrical conductivity and active surface area. Especially for far-extrapolated design recommendations, the relationships between design parameters and effective properties of the resulting electrode microstructure should not be ignored. In fact, neglecting these structure-property relationships would limit the ability of the model to provide reliable insights when exploring a broad range of design parameter configurations. This would undermine the key advantage of the P2D model compared to 3D microstructure-resolved models: its low computational cost, which enables rapid sensitivity analyses and design optimizations.

[10] Parts of this subsection have been published in Witt, Wilde, Baakes, Belkhir, Röder, Krewer, Energy Technol., 9(6):2000989, 2021 (doi: 10.1002/ente.202000989, CC BY 4.0 [15]).

To overcome the limited prediction capability of the basic P2D model and enable broad cell design studies, insights from stochastic 3D microstructure simulations can be incorporated into the modeling framework [75, 137]. Figure 2.5 illustrates the value of this approach. It compares the effective electrical and ionic conductivity of a simulated NMC111 cathode as a function of porosity, derived either from a stochastic 3D microstructure simulation or calculated with the often used Bruggeman relation [75]. The results clearly show that the microstructure-derived electrical conductivity improves by multiple orders of magnitude as the porosity decreases. This originates from the formation of a percolation network with conductive additives, which features a much higher conductivity than the active material. In contrast, the Bruggeman relation cannot capture this effect. For the ionic conductivity, the 3D microstructure- and Bruggeman-derived values are in good agreement at high porosities. However, the effect of blocked pores at lower porosities can only be captured by the stochastic 3D microstructure simulation. The Bruggeman relation simplifies the structure-property relationship to a power-law dependence of the effective ionic conductivity on porosity, which results in an overestimation of effective ionic conductivity at lower porosities.

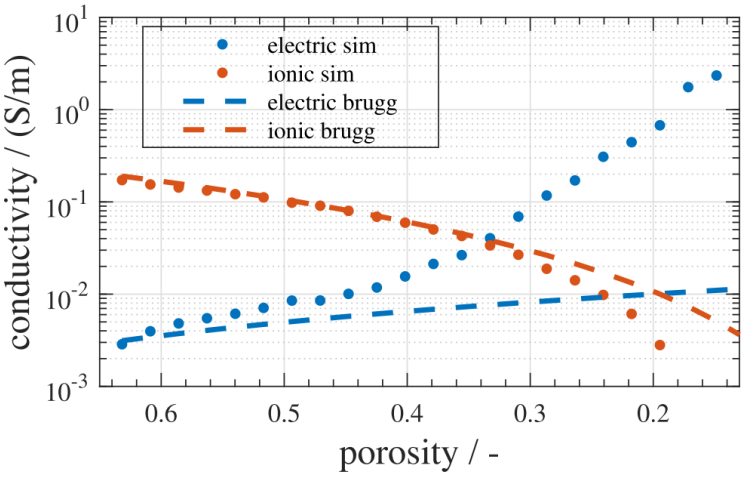

Figure 2.5: Comparison of predicted effective electrical (blue) and ionic (orange) conductivity versus porosity for two modeling approaches: 3D microstructure simulation (dots) and Bruggeman relation (dashed lines). The volume ratio between the NMC111 cathode active material and carbon black is kept constant at 4.4/1. Reprinted from [75], Copyright 2019, with permission from Elsevier.

2.3.3 From Experimental to Model-Based Diagnostics[11]

The state of health of a lithium-ion battery can be evaluated by various criteria like its capacity loss [138] or its change in internal resistance [139]. However, these experimental metrics inextricably summarize the effects of likely different underlying changes at the electrode and particle level. Advanced model-based cell diagnostics can help to improve the understanding of fundamental degradation-related and performance-limiting processes. These insights can then be used to introduce knowledge-based electrode design and production process adjustments, facilitating the realization of available optimization potentials in terms of reduced cost, improved performance, and extended cycle life [72].

For a holistic cell diagnosis, the solid electrolyte interphase is particularly important as it affects cell performance and degradation [102, 140]. The earlier discussed substantial process duration for its initial formation is another strong incentive for a detailed SEI characterization to facilitate knowledge-driven process optimizations. Notably, the composition, thickness, and structure of the SEI are not static after the initial formation. When electrochemically less stable SEI components degrade or soluble components dissolve in the electrolyte, interfacial and bulk properties of the SEI can change [26]. In addition, the volume changes of the active material during cycling can trigger fractures in the SEI, promoting additional SEI growth and irreversible capacity loss [141]. As a result, the formation of an initial SEI with favorable mechanical, chemical, interfacial, and conductive properties is of significant interest.

Available approaches for the characterization of the SEI can be divided into two categories: direct experimental and model-assisted methods. Experimental methods generally require a special cell preparation that may not be representative of commercial cells anymore. Furthermore, these methods are commonly performed post-mortem, complicating their utilization for broad experimental studies. However, they can offer a valuable understanding of SEI composition and structure. For instance, Luchkin et al. used in-situ atomic force microscopy to observe SEI nucleation and growth and assess its electrical and mechanical properties [142]. Leißing et al. analyzed gas composition and volume after cell formation to draw conclusions about governing side reactions as a function of formation current [143]. Stenzel et al. provide a comprehensive review of chromatographic techniques for the analysis of changes within the liquid electrolyte after formation or along aging [144]. Huang et al. have shown the first cryogenic electron microscopy of the SEI on a carbonaceous anode, which helps to understand the structure of the SEI, including its fragile components [145]. Nonetheless, parameters such as the anode tortuosity after cell formation, i.e., including the contribution of the SEI, are experimentally difficult to measure. Symmetric EIS measurements with a non-intercalating electrolyte could provide an

[11] Parts of this subsection have been published in Witt, Röder, Krewer, Batteries Supercaps, 5(7):e202200067, 2022 (doi: 10.1002/batt.202200067, CC BY 4.0 [16]).

estimate of this parameter [36]. However, the extraction and preparation of the electrodes from a full cell would likely remove at least part of the SEI. Furthermore, monitoring the evolution of such parameters in the same cell during cycling would not be possible.

Model-assisted approaches can provide insights into the current cell and SEI state based on non-destructive electrochemical measurements like C-rate tests and EIS. In principle, a cell diagnosis with a physicochemical lithium-ion battery model could utilize a wide range of measurements. However, most models focus only on one measurement data type like C-rate test [146, 147] or EIS measurement [118, 148]. Such a restricted diagnosis is disadvantageous for multiple reasons. For example, a double-layer capacitance is likely better identifiable from EIS measurements than C-rate tests, whereas a solid diffusion coefficient may be better accessible from discharge curves [149, 150]. Notably, there are also parameters, like reaction rate constants, that influence both C-rate and EIS data. Without a model for the joint analysis of both measurement types, a robust and unambiguous cell diagnosis cannot be ensured [149, 151]. Furthermore, SEI-related insights from aging models that use only cycling data are commonly limited to the loss of cyclable lithium, which is attributed to SEI growth [147, 152]. With an EIS-based cell state estimation, changes in interfacial SEI properties, like process kinetics and double-layer capacitance, become accessible [118]. However, the interrelation with the discharge behavior remains unclear. Chapter 4 will introduce a physicochemical cell and SEI model that enables a holistic cell diagnosis based on both discharge and impedance data.

3 Importance of Cell Design and Production Uncertainties[1]

As briefly introduced in Section 2.2, both the initial cell design and the subsequent cell production have a significant impact on the final performance of a lithium-ion cell. The starting point for any holistic cell design optimization is a comprehensive definition of the targeted application scenario, which serves as the cornerstone of a well-performing cell design and is essential to successfully navigate the variety of available design choices. These comprise i) material selection, regarding active materials, binders, and conductive additives, ii) electrode parameters, such as active material particle size, coating thickness, and porosity, and iii) electrode structuring concepts, like single-layer or multi-layer electrode coatings, laser perforation, and vertical alignment of non-spherical active material particles.

In general, the intricate relationship between a desired cell design configuration, the required process parameters, and the resulting electrode properties introduces uncertainty into the expected performance of far-extrapolated cell design recommendations. This is especially critical if notable process adjustments are required to realize the desired cell design. For instance, binder migration during the drying process of ultra-thick cathodes can significantly influence their microstructure [77]. Similarly, an adjustment of the slurry mixing equipment and intensity can notably influence the microstructure and fast charge capability of a graphite-based anode [96]. As such, a sound understanding of the process-product interdependencies is important for both experimental and model-supported design recommendations. To enable realistic performance predictions, the electrochemical simulations in this chapter utilize an empirical surrogate model by Laue et al. to capture the relationship between electrode porosity and microstructure properties, like tortuosity and effective electrical conductivity [75].

The goal of this chapter is to provide actionable insights into holistic cell design optimization with a special focus on the value of model-based studies for a computational rather than experimental exploration of vast parameter ranges. It begins with an overview of optimization

[1] Parts of this chapter have been published in Witt, Wilde, Baakes, Belkhir, Röder, Krewer, Energy Technol., 9(6):2000989, 2021 (doi: 10.1002/ente.202000989, CC BY 4.0 [15]).

approaches and overall challenges of electrode design. Afterward, two model-based case studies are defined. The first study investigates the performance characteristics of more than 5,000 cells with two-layer electrodes and a high theoretical capacity of 5 $\mathrm{mAh\,cm^{-2}}$ at C-rates of C/10 and 1C in charge and discharge direction. The second study investigates a two-layer cathode half-cell with a fine-grained parameter variation, offering insights into the importance of the parameter space surrounding a chosen electrode design. Based on these studies, the effects of the parameter screening granularity, the chosen evaluation criterion, i.e., areal versus volumetric and charge versus discharge capacity, and the chosen benchmark system are discussed and recommendations are derived.

3.1 Pathways Toward Optimal Electrode Design

This section begins with a discussion of optimization objectives, benchmark systems, and optimization methods. Afterward, a perspective on opportunities and challenges of electrode design optimization is provided.

3.1.1 Optimization Approaches

The diversity of optimization objectives and the broad range of benchmark electrodes is an inherent consequence of the variety of possible application requirements. Published studies on electrode design mirror this diversity and illustrate its complexity. In the following, the topic of optimization objectives and corresponding benchmark systems is discussed in more detail as it is crucial for the solution of any design problem. Furthermore, available optimization methods are presented that enable the translation of an objective into an optimal electrode design.

In general, a universal formulation of an electrode design problem is everything but straightforward. Depending on the desired application, the focus could be on the performance characteristic of a cell at a given C-rate or over a specific C-rate range [153]. The targeted performance characteristic may be the areal capacity [76, 77, 87], the gravimetric [77, 88] or volumetric energy density [74, 88], or the volumetric power density [74]. Other targets may comprise a minimum mean overpotential in an electrode and a minimum spatial deviation from its mean value, resulting in a more homogeneous mechanical stress throughout the electrode [89]. This list of optimization objectives does not aim to be comprehensive. However, there are a few fundamental aspects of quantifying performance that need to be discussed. In the first step, these are areal, volumetric, and gravimetric metrics. The difference between capacity, energy, and power will be discussed in the second step.

Areal performance metrics, like the areal capacity, are unambiguous due to their independence of coating thickness and mass or volume of passive materials like separator and current collectors. In contrast, volumetric and gravimetric metrics require a precise definition of the considered materials within the cell. For example, if one study investigates the capacity per active material mass, and another study provides the capacity per total electrode mass, the results are hardly comparable without additional information. However, with different optimization objectives, like a high active material utilization or a mass-constrained application, both definitions are reasonable.

As a performance metric, capacity is universally applicable to the investigation of charge and discharge. If the energy density was chosen as an evaluation criterion, a high energy density during charge could either indicate high ohmic losses, i.e., a low charging efficiency, or a high charged capacity. However, this is also the strength of the energy density as it enables the assessment of the energy conversion efficiency by considering both voltage and capacity. Power characteristics may be seen as a different category as they combine energy density and rate capability. This is crucial, e.g., in the context of electric vehicles with a high discharge power demand for acceleration and a high charge power requirement for short charging times. On the downside, the power density does not enable an assessment of the actually usable capacity or energy.

Similar to the universal definition of an optimization problem for all application scenarios, the question for the one true single-layer benchmark electrode cannot be answered. Depending on the optimization objective, different benchmarks are required to evaluate the optimization progress objectively. In this context, the utilization of arbitrary benchmark systems seems unfavorable but especially for experimental studies likely unavoidable due to the extensive design parameter space. A more general assessment of the merits and limitations of an electrode design concept would require an optimized state-of-the-art benchmark electrode. From the perspective of electrode production, this would help to answer the question if the necessary process development and equipment establishment for a structured electrode are well invested. The work by Dai et al. highlighted this aspect by comparing an optimized homogeneous electrode to an optimized electrode with varying porosity at multiple C-rates [88]. Their estimated benefit from a varying porosity across the cathode was relatively small compared to studies with non-optimized benchmark electrodes. As a result, a study without an optimized benchmark can only assess trends within the investigated parameter space. An optimized benchmark enables a more general evaluation of an electrode design concept, such as a two-layer electrode coating.

An experimental parameter screening is the most basic approach to solving an optimization problem. Considering the required equipment, personnel, and operational costs, such experimental studies most likely have to focus on estimating a local optimum. A battery model that is validated over a wide range of measurement data can go beyond local optima and approximate the global optimum, using global mathematical optimization algorithms like particle swarm optimization,

genetic algorithm, and Bayesian optimization [154]. Here, the latter method can provide confidence intervals for the optimized parameters, enabling a first evaluation of parameter sensitivity.

Even without a battery model, an equidistant experimental parameter screening may not be necessary. With design of experiments (DOE), a statistics-based minimum number of experiments can be defined that still allows for an effective reconstruction of the relationship between the optimization target and the chosen design parameters. For instance, Su et al. used DOE to identify the most relevant factors for capacity degradation in lithium-ion batteries [155]. Rynne et al. developed a guideline for the application of DOE to the problem of electrode formulation [156]. A further reduction of required experiments may be achieved via model-based design of experiments. It is commonly used for the definition of experiments that are most suitable and efficient for parameter identification [157–160]. In contrast to the purely statistics-based DOE, it enables a knowledge-based definition of the most insightful experiments before a comprehensive experimental study is conducted.

Especially in material design and discovery, model-based high-throughput instead of mathematical optimization approaches are used to identify the best possible solution within a broad parameter space [161, 162]. This has been done extensively with density functional theory simulations for applications, like solid-state lithium-ion conductors [163, 164]. However, to the best of the author's knowledge, there are no experimental studies on high-throughput lithium-ion battery electrode design, comprising both highly adaptable electrode production and electrochemical characterization. In contrast, model-based studies are limited primarily by their validity range and only secondarily by the available computational resources.

Using machine learning is another approach to improve the understanding and eventually enable an optimization of process parameters for their effect on the final electrode properties. Such data-driven models can correlate large amounts of input data, like process parameters or electrochemical characterization measurements, with output data, like performance or aging characteristics. This is especially valuable if a good physical understanding of the underlying processes is unavailable. In general, data-driven approaches are an option, especially if high-quality data is already available or can be generated easily. For instance, Cunha et al. used machine learning algorithms to investigate the interrelation between slurry manufacturing parameters and final cathode mass loading and porosity [165]. Considering electrode design-specific aging characteristics, data-driven approaches may also help to extend the scope of electrode design and manufacturing optimization to battery aging. In the context of cell characterization, Severson et al. used machine learning for the prediction of battery lifetime based only on the first few cycles [166]. Attia et al. performed a closed-loop optimization of fast-charging protocols by iteratively defining the following experiments based on a data-driven lifetime prediction model [60].

Physicochemical models can provide insights into internal and not directly measurable cell properties that aid in identifying and mitigating performance-limiting processes. In a slightly different context, a machine learning-based surrogate model was created from a P2D model to enable a fast end-of-line cell characterization [167]. This kind of surrogate modeling could also help to reduce the computational cost of physicochemical battery models for rapid cell diagnostics and design optimizations. Merits and limitations of the combination of physicochemical modeling with machine learning are discussed in detail by Dawson-Elli et al. [168].

Schmidt et al. investigated the effect of production uncertainties on the volumetric energy density with a standard P2D model [110]. With a Monte-Carlo approach, cell configurations were sampled from the probability distributions of production uncertainties, including electrode thickness, porosity, and tortuosity. Here, different parameter sensitivities lead to an uneven performance distribution, especially at high C-rates due to more pronounced voltage losses [110, 169]. From an electrode design perspective, this emphasizes the necessity to consider production uncertainties for the design of electrodes. Robust optimization can help to identify a cell design that delivers similar performance characteristics despite uncertainties in the production process. To the best of the author's knowledge, the application of robust optimization to the problem of electrode production is yet unavailable. However, in the context of process engineering, efficient frameworks for robust optimization have already been established [170, 171].

3.1.2 Opportunities and Challenges of Electrode Design Optimization

Researchers in the field of electrode design can build upon a wide range of experimental and simulation studies that explore the effects of different material properties, like particle size distribution, and structuring concepts, like multi-layer electrodes. 3D microstructure models can be used to investigate the effect of structural inhomogeneities on cell performance or even local lithium plating. P2D modeling approaches lack this detailed local insight, but they are computationally less expensive while enabling a reasonably accurate representation of experimental data. However, for a truly predictive cell design tool that includes modeling of slurry production, as well as electrode coating and drying, 3D models may be a better choice for directly utilizing microstructural features from process simulations, as opposed to averaging for homogenized models like the P2D model. Considering the rapid increase in computational resources, it may soon be feasible to use 3D models for cell design optimizations.

Apart from physicochemical battery modeling, machine learning can be a valuable tool that facilitates the understanding and thus optimization of the complex interrelations between process parameters and final cell properties. Applications range from slurry production for electrode

coating over electrode calendering to aging prediction. Considering the importance of battery lifetime, a data-driven aging and performance prediction based on production process parameters seems highly relevant for process optimization. Furthermore, future studies on electrode design should make uncertainties a fundamental part of the optimization process. This would enable not only superior performance characteristics, but it would also enable a more sustainable electrode production with lower scrap rates. Here, large experimental screening studies and thus purely data-driven approaches would likely be too expensive compared to a direct optimization with a validated battery model. Currently, however, a model cannot be adequately parameterized, nor can the resulting model-based design recommendation be verified without experiments.

Despite the broad coverage of electrode design in literature, the selection of the most suitable electrode design for a specific application is everything but straightforward. Different study objectives and often arbitrary benchmark systems complicate the comparison between studies and conceal the benefit of a specific electrode design for a different application. However, some studies recognized this problem and used optimized benchmark systems. This is a step in the right direction. A model-based design optimization can support an experimental study by providing a prediction for such an optimal benchmark electrode. Nonetheless, different application requirements and thus optimization objectives will inevitably complicate the comparison between different studies. The choice of a benchmark system tailored to the optimization objective enables a less biased assessment of an electrode design concept, such as single-layer versus two-layer electrode coatings. Furthermore, it seems critical to provide not only the investigated performance characteristic but also other characteristics, like the fast charge behavior, that may be more relevant to other application scenarios.

Finally, estimated design advantages from half-cell studies should be interpreted with caution. The neglected interaction with a realistic counter electrode may distort the achieved improvements. Concentration profiles throughout an electrode are likely less favorable with a state-of-the-art porous composite electrode than a solid lithium-metal counter electrode.

3.2 Case Study: Model-Based Optimization of Two-Layer Electrodes

Electrode optimization can utilize many design concepts to fulfill specific application requirements. For the investigation of these concepts, physicochemical battery models are available with various levels of detail, ranging from simple single particle models to microstructure-resolved simulations that enable a differentiated local assessment of limiting processes within an electrode (see Section 2.3). Considering their computational cost, the long-established and extensively used P2D model nowadays still seems to offer the best compromise between model

fidelity and computational cost. Consequently, the two case studies in this work use a P2D model, upgraded with insights from 3D microstructure simulations and extended for two-layer electrodes to enable broad electrode design screenings with insightful structuring trends.

As discussed earlier, studies on electrode design commonly focus on discharge performance while using a wide range of benchmark systems. In the following, two model-based electrode design studies are defined to create a better understanding of optimal cell designs for charge or discharge. The first model-based study resembles an experimental parameter screening for a full-cell setup with two-layer electrodes. It investigates general design principles for discharge and charge at C/10 and 1C. Furthermore, the influence of the parameter screening granularity and the chosen benchmark system on the study outcome is investigated. However, ten design parameters allow only for coarse screening. Therefore, the second case study features a fine-grained parameter variation for a two-layer cathode half-cell in a significantly constricted parameter space. With only two design parameters, it provides a perspective on the importance of the scope of a study for its implied benefit from electrode structuring. In addition, the high resolution of the parameter space allows for an evaluation of the impact of production uncertainties on robust cell performance.

3.2.1 Model Setup and Parameterization

The P2D model by Doyle et al. is chosen as a starting point to enable broad parameter variations with reasonable computational cost [122, 172]. Empirical polynomials from 3D microstructure simulations from Laue et al. are used to integrate knowledge on the microstructure-parameter relationships into the P2D model [75]. The governing model equations, including an electrochemical double-layer, were already summarized in Table 2.1. The reaction kinetics are described with a Butler-Volmer equation and a constant exchange current density. These and other complementary model equations are summarized in Table B.1 in the Appendix.

To enable the simulation of two-layer electrodes, the basic model is extended. The schematic full-cell structure in Figure 3.1 shows the geometric structure parameters for a full-cell setup with two-layer electrodes. Each of the four electrode layers has three parameters that may be changed: the active material volume fraction ε, the particle radius R, and the layer thickness d. Consequently, derived parameters, like the electrolyte volume fraction, the tortuosity, and the effective electrical conductivity, may differ in each layer. The governing equations for solid diffusion, solid potential, electrolyte potential, and electrolyte diffusion are extended to the additional layer within each electrode. Taleghani et al. provide a detailed summary of applicable boundary conditions in a P2D model for a two-layer versus a single-layer electrode [173]. For all simulations, the electrode- and particle-level discretization of each electrode layer is fixed to five and four, respectively. Simulations of configurations that do not converge and exceed 15 minutes

of simulation time compared to a typical simulation time of less than 1 minute are terminated, and the results are discarded. All simulations were performed with MATLAB version 2019a or newer, using the solver ode15s.

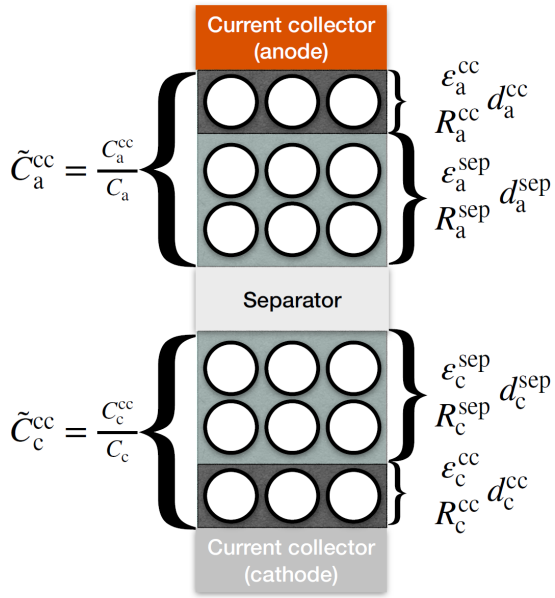

Figure 3.1: Lithium-ion battery cell with two layers of different properties in each electrode. Three structure parameters can be changed per layer: the active material volume fraction ε, the particle radius R, and the layer thickness d. The parameter $\tilde{C}^{\mathrm{cc}}$ describes the ratio between the theoretical capacity in the layer adjacent to the current collector C^{cc} (dark grey layer) and the total theoretical capacity C (dark + light grey layer).

The parameter set for the P2D model is largely adopted from Laue et al. and summarized in Table B.2 in the Appendix [75]. To enable a realistic representation of transport properties as a function of the electrode structure, Laue's effective polynomials from 3D microstructure simulations for the active surface area, the effective ionic conductivity, and the electrical conductivity of the cathode are used. Equally, the volume ratio between active material (AM) and carbon-binder domain for the cathode of 4.4/1 is adopted. It is defined for the anode at a higher value of 10/1 due to the good electrical conductivity of graphite. In general, the 3D microstructure simulations by Laue et al. were performed for a particle size of 5.5 µm. An adjustment of the polynomials based on additional microstructure simulations for the later defined particle size variations is out of the scope of this work. Nonetheless, a quantitative design recommendation for an experimental study would require this adjustment and a validation with experimental data.

In Laue's work, the empirical polynomials were derived only for the cathode. Considering the relatively high electrical conductivity of the anode active material, a polynomial is not deemed

necessary for this parameter. Instead, its effective electrical conductivity is scaled with the AM volume fraction. For calculating the effective ionic conductivity and diffusivity within the electrolyte phase, the tortuosity is described via the Bruggeman equation along with a Bruggeman exponent β of 1.5, which describes perfect spheres [38]. The active surface area is commonly calculated based on the assumption of ideal spherical particles with a linear dependence on the active material volume fraction. However, this approximation is not valid for very high AM volume fractions since the active surface area cannot be highest in a material without any pore volume. To circumvent this unrealistic behavior and despite potentially different particle shapes, the effective polynomial for the cathode active surface area is also used for the anode.

The concentration-dependent ionic conductivity and diffusivity of the 1M $LiPF_6$ EC:EMC 3:7 (w:w) electrolyte system are described by empirical polynomials that were fitted to experimental data by Landesfeind et al. [50]. The anode and cathode open circuit potentials are described with empirical expressions as a function of the state of charge [75].

For the second parameter study, a two-layer cathode half-cell is investigated. In contrast to the full-cell model, the graphite-based anode is replaced with a lithium counter electrode that is modeled as a boundary condition, i.e., it provides the amount of lithium ions corresponding to the externally applied current density. This ensures an interaction-free evaluation of the cathode design for lithium intercalation, but it inherently also limits its value for the direct estimation of the performance of a such optimized cathode in a full-cell setup. Apart from different parameter variations, the same equations are used for the cathode in the full- and half-cell study.

3.2.2 Case Study Definition

3.2.2.1 Full-Cell Parameter Study

The first step toward electrode design optimization is defining an optimization objective. For this study, four application scenarios are defined, i.e., discharge and charge at C/10 and 1C. The high and low C-rate will enable an assessment of transport limitations as a function of the applied load. To enable a direct comparison between discharge and charge performance, the voltage-independent capacity is used as the evaluation metric. For a mathematical design optimization, it would be required to choose between areal, volumetric, and gravimetric capacity or to incorporate multiple objectives into a then more complex optimization process. Such a trade-off is obsolete for a parameter study with predefined parameter variations. The simulation data can be analyzed with respect to areal, volumetric, and gravimetric capacities at all investigated C-rates. As the theoretical capacity, i.e., the mass loading of each electrode, is fixed as

a boundary condition in this study, the gravimetric and areal capacities are qualitatively equivalent. To enable a more intuitive comparison with the volumetric capacity, the areal capacity is chosen instead of the gravimetric capacity. Here, the volumetric capacity inherently includes a trade-off between electrode volume and mass transport losses in porous electrodes compared to the volume-independent areal capacity. In summary, the chosen optimization targets for the parameter studies in this work are the areal and volumetric discharge and charge capacity at C-rates of C/10 and 1C with cutoff cell voltages of 2.9 V and 4.2 V. The diversity of these application scenarios will enable an in-depth understanding of structure recommendations for application-optimal cell performance.

For the calculation of the volumetric capacity, double-sided coated electrodes are assumed. As a result, the full thickness of the separator (20 µm) but only half the cathode (20/2 µm) and half the anode (10/2 µm) current collector thickness are considered. The theoretical capacities of the anode and cathode are balanced $1.1/1$ such that the anode capacity is 10% higher than the cathode capacity. This is a common design choice to mitigate lithium plating [20, 56]. As this is an electrode design study focusing on capacity improvements, sophisticated charging protocols, e.g., to prevent lithium plating, are not considered.

The parameter variations for the full-cell parameter screening of two-layer electrodes are defined based on the schematic cell structure in Figure 3.1. Importantly, a fine-grained evaluation of the whole parameter space is infeasible due to the resulting combinatorial explosion with twelve examined geometric structure parameters: layer thickness, active material volume fraction, and particle radius for each of the four layers. The theoretical cathode capacity is fixed to $5\,\mathrm{mAh\,cm^{-2}}$, which is roughly between an ultra-high and a state-of-the-art mass loading [77]. This ensures diverse performance characteristics with poor performance at 1C for overly dense electrodes and reasonable performance for well-designed electrodes. The theoretical capacity is calculated based on the maximum lithium concentration within the AM of anode and cathode.

The fixed cell capacity of $5\,\mathrm{mAh\,cm^{-2}}$ already reduces the degrees of freedom to ten design parameters. However, this still results in $3^{10} = 59{,}049$ full-cell configurations for just three variations per design parameter. With the focus on investigating general electrode design principles for both charge and discharge, the number of simulations is reduced by investigating two instead of three different particle radii. Here, 3 µm and 9 µm represent typical particle sizes [75, 174].

A variation of the cathode AM volume fraction has a pronounced effect on i) mass transport in the electrolyte phase that deteriorates with decreasing porosity and ii) electrical conductivity of the solid phase that is highly sensitive around the percolation threshold. For this reason, three variations are defined, leading to effective electrical conductivities that differ by one order of magnitude each. On the anode side, ohmic losses are less of an issue due to the high electrical

conductivity of the graphite AM. Nonetheless, mass transport in the electrolyte phase still deteriorates nonlinear with decreasing porosity. For this reason, the same AM volume fractions are chosen for the anode and cathode.

For the last two degrees of freedom, a dimensionless parameter $\tilde{C}^{cc}$ is introduced for both anode and cathode. It describes the ratio between the theoretical capacity in the layer adjacent to the current collector and the total electrode capacity. This enables a better understanding of the capacity provided by each layer within a two-layer electrode. Two variations are defined for $\tilde{C}^{cc}$ with either 25% or 75% of the electrode capacity provided by the layer adjacent to the anode and cathode current collector, respectively. This results in 5,184 cell configurations for the full-cell parameter screening with four simulations each to cover charge and discharge at C/10 and 1C. Table 3.1 summarizes the chosen parameter values for the model-based full-cell design screening.

Table 3.1: Definition of the parameter variations for the rapid full-cell electrode design screening, comprising the active material volume fraction ε, the particle radius R, and the ratio $\tilde{C}^{cc}$, which compares the theoretical capacity of the layer at the current collector to the total electrode capacity.

Parameters	Low value	Medium value	High value
ε_a^{cc} / -	0.45	0.55	0.65
ε_a^{sep} / -	0.45	0.55	0.65
ε_c^{sep} / -	0.45	0.55	0.65
ε_c^{cc} / -	0.45	0.55	0.65
R_a^{cc} / µm	3	-	9
R_a^{sep} / µm	3	-	9
R_c^{sep} / µm	3	-	9
R_c^{cc} / µm	3	-	9
$\tilde{C}_a^{cc}$ / %	25	-	75
$\tilde{C}_c^{cc}$ / %	25	-	75

The full-cell design screening is repeated with a slight modification to evaluate the effect of lithium plating prevention during 1C charge on optimal electrode design. In this case, the charging operation can also be terminated if the local anode potential falls below 0 V vs. Li/Li^+.

Finally, a suitable benchmark system must be defined for the four application scenarios. For this purpose, the performance of the best structured cell for a specific application is compared to the best single-layer cell configuration within the predefined parameter space. This resembles an experimental parameter screening, which may not have access to an optimized benchmark system and must resort to one of the investigated cell configurations for comparison.

Overall, the first case study provides a rough overview of the parameter space with its coarse-grained parameter screening. However, with only two or three values per design parameter, the study does not provide an insight into how sensitive the result is to small changes in these

parameters. Such a more detailed analysis can be done by evaluating significantly more values for each parameter. This is the subject of the second case study described in the following.

3.2.2.2 Half-Cell Parameter Study

This case study is limited to a cathode half-cell to enable a closer look at the design parameter space for a two-layer electrode. Here, the cathode is deemed more insightful than the anode due to the poor electrical conductivity of the cathode active material that depends strongly on the percolation network formed by the carbon-binder domain. To allow for an intuitive graphical visualization, typically only two parameters are varied [88, 89, 110]. With a fixed theoretical capacity of $5\,\mathrm{mAh\,cm^{-2}}$, the design parameter space contains five degrees of freedom and will be further reduced to two design parameters. The full-cell parameter screening will reveal a low sensitivity of cell performance to cathode particle size for the utilized parameter set. Consequently, the AM particle radius is fixed to $3\,\mu\mathrm{m}$. Further, a fixed average AM volume fraction of 55% is chosen, which is the medium value used for the parameter variations in the full-cell parameter screening. With a constant theoretical capacity, the combined coating thickness of both cathode layers is $133.4\,\mu\mathrm{m}$.

The remaining degrees of freedom are the AM volume fraction in the layer at the separator and the thickness of this layer. Hence, a decrease in the AM volume fraction in one layer must be compensated by an increase in the AM volume fraction in the other layer. The cathode AM volume fraction at the separator varies between 45% and 65%, consistent with the full-cell study. The thickness of the layer at the separator is varied between 10% and 90% of the total coating thickness. Both parameters are changed in steps of 0.5 percentage points. Parameter configurations requiring an AM volume fraction beyond the investigated minimum and maximum value are discarded and assigned a zero capacity. As a result of the fixed coating thickness and theoretical capacity, a single-layer benchmark electrode is already defined and may be regarded as an optimized benchmark. This enables a critical assessment of the benchmark definition in the full-cell study that uses the best homogeneous electrodes from the parameter screening instead of an optimized system.

As the lithium counter electrode is implemented as a boundary condition, only the intercalation into the cathode, i.e., the full-cell discharge process, can be studied consistently. For the deintercalation, i.e., the charge direction in a full-cell setup, the electrolyte concentration could drop below zero due to the concentration-independent implementation of the counter electrode. The cell performance at C/10 can be expected to be almost independent of the electrode structure. For this reason, only intercalation at 1C is investigated.

3.3 Results and Discussion

First, the full-cell parameter screening results are discussed with respect to i) general electrode design guidelines for optimal performance during discharge and charge, and ii) the expected benefit of two-layer electrodes when compared to the best-in-class single-layer cell configurations in the parameter study. Subsequently, the relevance of lithium plating during charge at 1C for cell design is analyzed. In the second part, the benefit of electrode structuring is evaluated from the perspective of the fine-grained cathode half-cell parameter study. Here, a particular focus is on the importance of the parameter space surrounding an electrode design point for robust electrode production. Finally, the results from the full- and half-cell study are compared.

3.3.1 Full-Cell Parameter Study

The discussion of the full-cell parameter screening is broken down into four parts. First, an overview of the more than 5,000 simulated cell configurations is provided. Second, the best-performing cells for charge and discharge at 1C and C/10 are identified and analyzed in more detail. Here, also the difference between areal and volumetric capacity is discussed regarding their effect on favored cell designs for best performance. Finally, the occurrence of lithium plating during 1C charge is investigated in the best cells for 1C discharge and charge, respectively.

3.3.1.1 Parameter Screening Overview

Figure 3.2 shows the charge and discharge performance of all simulated full-cell configurations at C-rates of C/10 and 1C. The parameter variations are sorted by their volumetric discharge capacity at 1C. This reveals three fundamental aspects. First, many simulated cell configurations lead to cells with poor discharge and charge performance at 1C while delivering a similar capacity at C/10. Second, the discharge capacity at 1C is not directly related to the charge capacity, i.e., a cell with a lower discharge capacity may feature a higher charge capacity and vice versa. This holds for both single-layer and two-layer cell configurations. This finding underlines the necessity to consider both discharge and charge performance for a holistic cell design optimization. While some parameter variations may show a direct correlation between charge and discharge performance, inferring charge performance from discharge performance is generally not advised. Third, apart from cells with best-in-class performance for a specific application, some cell configurations among the more than 5,000 samples show similar performance for charge and discharge at 1C. For an overview of possible performance characteristics, it is thus worthwhile to conduct a coarse-grained parameter screening as presented here.

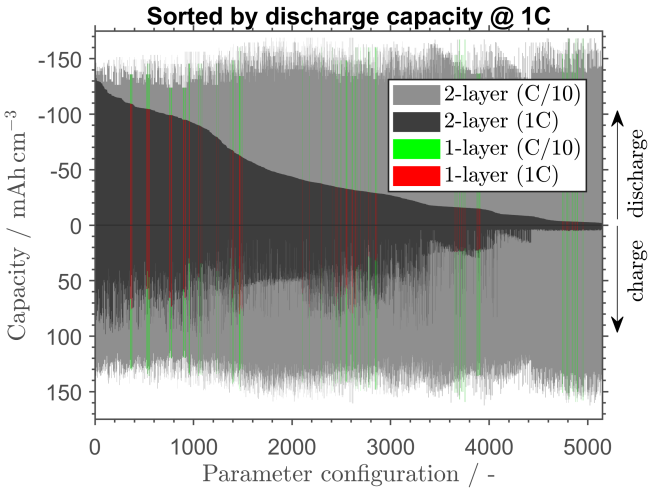

Figure 3.2: Performance comparison of all investigated parameter variations for cells with two-layer electrodes, sorted in descending order by their volumetric discharge capacity at 1C. Discharge is shown with negative values, charge with positive values.

3.3.1.2 Implications of Performance Metrics for Cell Design

Figure 3.3 shows the best cell configurations for the four operating modes, i.e., discharge and charge at C/10 and discharge and charge at 1C. The best single-layer cell configuration for each application is shown for comparison with thin, colored bars. In the following, the performance characteristics and corresponding electrode structures of the best-in-class cell configurations are discussed in terms of the areal capacity in Figure 3.3a and the volumetric capacity in Figure 3.3b.

As a first observation, the best cell configurations for charge and discharge at 1C feature almost the same areal capacities at C/10 as those explicitly tailored for C/10 applications. This would suggest that cells can be optimized directly for 1C discharge or charge without any worries about their performance at C/10. There is also no significant benefit of using two-layer versus single-layer cells if both are tailored for charge or discharge at C/10 since the cell voltage is only slightly affected by transport processes at such a low C-rate. In contrast, the areal capacities of the best two-layer cells for discharge and charge at 1C are notably higher than the best single-layer cell configurations with an improvement of 20% and 28%, respectively.

It should be noted that the observed performance improvement of up to 28% with two-layer electrodes may originate from the coarse parameter screening, which underlies this study. A finer grid for the parameter screening would probably enable a better trade-off between transport losses in the electrolyte and solid phase of single-layer electrodes. However, for most practical design problems, direct mathematical optimization should be preferred due to a more efficient parameter space exploration. Coarse experimental and model-based parameter studies alike can

only reflect improvements over an arbitrary benchmark cell or over the best homogeneous cell configuration determined by the studies themselves. In contrast, an optimized homogeneous benchmark system would presumably result in a less significant performance benefit from two-layer electrodes.

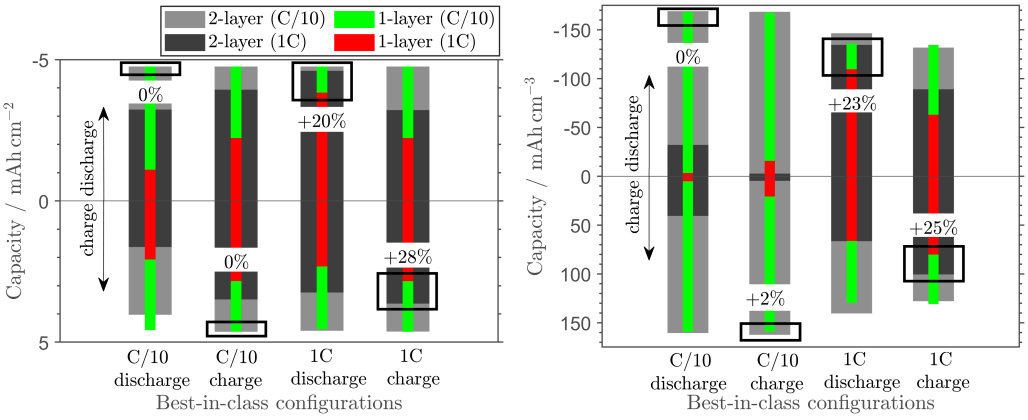

Figure 3.3: Comparison of performance of best-in-class cell configurations with single-layer (thin bars) and two-layer electrodes (wide bars) for discharge at C/10, charge at C/10, discharge at 1C, and charge at 1C. The best-in-class cell configurations from the full-cell study are selected (a) for the areal capacity and (b) for the volumetric capacity. Black boxes highlight the performance focus of the cells. Percentage performance gains indicate the increase in capacity when comparing two-layer and single-layer electrodes.

In the following, the above-mentioned performance benefit of two-layer over single-layer electrodes is discussed with respect to the actual electrode structures. Tables 3.2 and 3.3 summarize the specific structural properties of the best two-layer and single-layer cell configurations for highest areal capacity.

For discharge at 1C, the best cell employs a cathode that provides 25% of the capacity in a medium porous layer at the current collector (55% active material volume fraction) and 75% of the capacity in a highly porous layer at the separator (45% AM volume fraction). This ensures good electrical conductivity near the current collector while facilitating mass transport into the deeper electrode structure by the more porous layer at the separator. In contrast, the best homogeneous cell configuration cannot make this trade-off. Instead, it employs a cathode with an AM volume fraction of 55%. This leads to an overall deteriorated discharge performance at 1C because of an increased mass transport resistance that the improved electrical conductivity cannot compensate. On the anode side, the layer at the current collector provides 75% of the total anode capacity with an AM volume fraction of 45 %. The layer adjacent to the separator has an AM volume fraction of 55%. This seems to enable a more homogeneous active material utilization throughout the anode.

Table 3.2: Identified parameter values in the full-cell parameter study for highest areal capacity for the four different operating modes with two-layer electrodes.

Parameters	Discharge @ C/10	Charge @ C/10	Discharge @ 1C	Charge @ 1C
ε_a^{cc} / -	0.65	0.45	0.45	0.45
ε_a^{sep} / -	0.55	0.45	0.55	0.45
ε_c^{sep} / -	0.45	0.45	0.45	0.45
ε_c^{cc} / -	0.55	0.65	0.55	0.55
R_a^{cc} / µm	9	3	3	3
R_a^{sep} / µm	3	3	3	9
R_c^{sep} / µm	3	9	3	9
R_c^{cc} / µm	3	9	3	9
$\tilde{C}_a^{cc}$ / %	75	25	75	75
$\tilde{C}_c^{cc}$ / %	75	25	25	75

Table 3.3: Identified parameter values in the full-cell parameter study for highest areal capacity for the four different operating modes with single-layer electrodes.

Parameters	Discharge @ C/10	Charge @ C/10	Discharge @ 1C	Charge @ 1C
ε_a / -	0.55	0.45	0.55	0.45
ε_c / -	0.45	0.55	0.55	0.55
R_a / µm	9	3	3	3
R_c / µm	3	9	3	9

For charge at 1C, mass transport seems to be the most relevant issue on the anode side, favoring the smallest AM volume fraction in both layers. On the cathode side, the AM volume fraction in the layer at the current collector is still 55% and at the separator 45%. However, in contrast to discharge at 1C, the highly porous layer at the separator accounts for only 25% instead of 75% of the total cathode capacity, favoring a higher electrical conductivity over a lower transport resistance for charge at 1C. Overall, the performance benefit of the best structured compared to the best homogeneous cell seems to originate from a better trade-off between sluggish transport in the electrolyte phase of too-dense electrodes and low electrical conductivity in the solid phase of too-porous electrodes.

For applications without volume constraints, the areal capacity seems to be a reasonable evaluation metric that allows cell design optimization to focus on the performance at 1C. However, the volumetric capacity in Figure 3.3b shows a different picture. Here, the cell configurations tailored to 1C applications cannot deliver the same volumetric capacity at C/10 as the ones explicitly tailored to C/10 charge and discharge. This is the result of higher transport losses at 1C, which favors more porous electrodes and leads to the lower volumetric capacity at C/10.

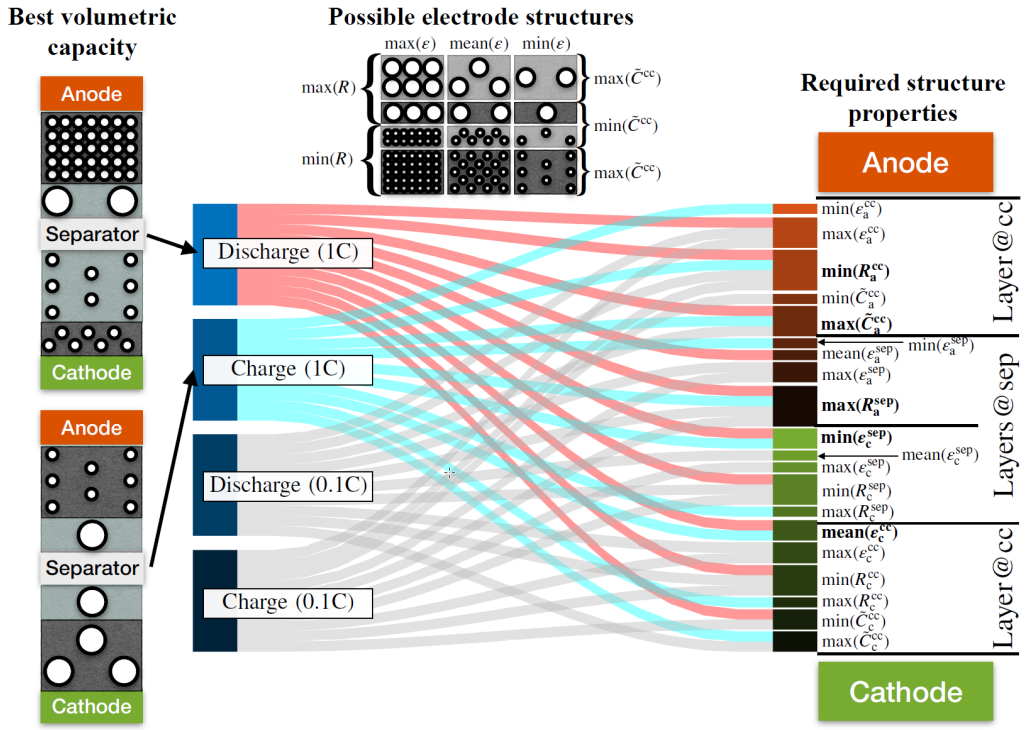

Figure 3.4: Sankey diagram with application scenarios on the left side and required structure properties on the right side. The desired application focus, i.e., discharge or charge at C/10 or 1C, is translated through the flows into the individually required structure properties for highest volumetric capacity. Structure properties required for both charge and discharge at 1C are printed in bold to facilitate the comparison with the C/10 application scenarios. The best cell structures for discharge (red flows) and charge (turquoise flows) at 1C are schematically shown on the left side. A legend for the relationship between varied parameters and schematic electrode structures is shown at the top. The Sankey diagram was created with MATLAB code from Wang [175].

When comparing the best-in-class cells for discharge and charge at 1C, the difference between the best two-layer and the best single-layer cell configurations is significant with 23% and 25%, respectively. This benefit of electrode structuring is in the same range as for the areal capacity. The identified best structure parameters for all four operating modes with the volumetric capacity as the performance metric are summarized in Table B.3 and Table B.4 in the Appendix for the two-layer and single-layer cell configurations, respectively. For the two-layer electrodes, the parameters are visualized by a Sankey diagram in Figure 3.4. Here, the flows link the four application scenarios on the left side to the required structure parameters for best-in-class volumetric capacity on the right side. Structure properties used for charge and discharge at 1C are highlighted. Due to almost negligible mass transport losses for C/10 charge and discharge, the recommended structures are mostly dense and feature the highest active material volume fraction. Only for discharge at C/10, a thin cathode layer at the separator with a medium AM volume

fraction of 55% is required. Compared to the cell configurations for a high areal capacity at C/10, these relatively dense structures have a devastating effect on the performance at 1C (see Figure 3.3b). Again, there is no significant benefit of two-layer over single-layer cell configurations for discharge at C/10 and only a 2% improvement for charge at C/10.

For both charge and discharge at 1C, it seems essential that the anode provides most of the capacity (75%) with small particles at the current collector and the remainder of the capacity (25%) with large particles at the separator. This design resembles the continuous particle radius profile in the model-based study by Golmon et al. [87]. However, they did not investigate charging. Although small particles may be expected to provide better performance due to a larger surface area with enhanced reaction kinetics and a reduced solid diffusion length, the results indicate that larger particles at the separator improve the volumetric charge capacity by about 11%. For discharge, the design principle is the same: small particles at the current collector to minimize the overpotential and large particles at the separator to achieve a more homogeneous active material utilization throughout the electrode. However, the benefit of large over small particles is only 1%. For the cathode, the particle size is insensitive for the employed parameter set due to fast reaction kinetics and solid diffusion.

On the cathode side, the lowest and medium active material volume fractions are favored at the separator and current collector, respectively. This structure provides decent electrical conductivity toward the current collector while maintaining sufficiently fast lithium-ion transport through the porous layer at the separator into the deeper electrode structure. The highest cathode AM volume fraction is only relevant with a focus on C/10 applications. This trend toward denser cathodes for lower C-rates is in good agreement with the experimental study by Schmidt et al. and highlights the challenge of proper cathode design [74]. On the one hand, a high porosity is required to facilitate mass transport. On the other hand, a higher densification, i.e., a smaller porosity, is needed for adequate electrical conductivity. Without proper consideration of these two relations on the modeling side, e.g., with approximations from microstructure simulations, a model-based design optimization could leave the validity range of the underlying model early on, potentially providing poor design recommendations.

3.3.1.3 Cell Design for Lithium Plating-Free Charging

Apart from the pronounced benefit of two-layer electrodes for 1C applications in this case study, the results strongly suggest that the best-in-class charge and discharge characteristic at 1C cannot be achieved with the same electrode structures. The performance improvement of a cell tailored to charge at 1C compared to one tailored to discharge at 1C is about 51%. Vice versa, the improvement is coincidentally also 51%. This underlines that proper optimization has to find a trade-off between cell design for charge and discharge requirements.

It should be noted that the earlier case study used a constant current for charge and discharge without any safety- or aging-related considerations. However, safety-critical effects, like lithium plating, can easily be studied with the employed battery model [20]. Figure 3.5 addresses this point and compares the 1C charge performance of the best-in-class cell for 1C discharge to the best-in-class cell for 1C charge in the context of lithium plating. For the two bars on the left side, charging was terminated upon reaching the upper cutoff cell voltage of 4.2 V, equivalent to Figure 3.3. For the two bars on the right side, the charge simulations could additionally be terminated upon reaching a local anode potential below 0 V vs. Li/Li$^+$, which could result in lithium plating. Interestingly, the structure of the best cell without the possibility of lithium plating is the same as for the already discussed parameter screening, which did not control for lithium plating. Due to a comparable interpretation for both homogeneous and structured cell configurations, the following discussion will focus on the better-performing structured cells.

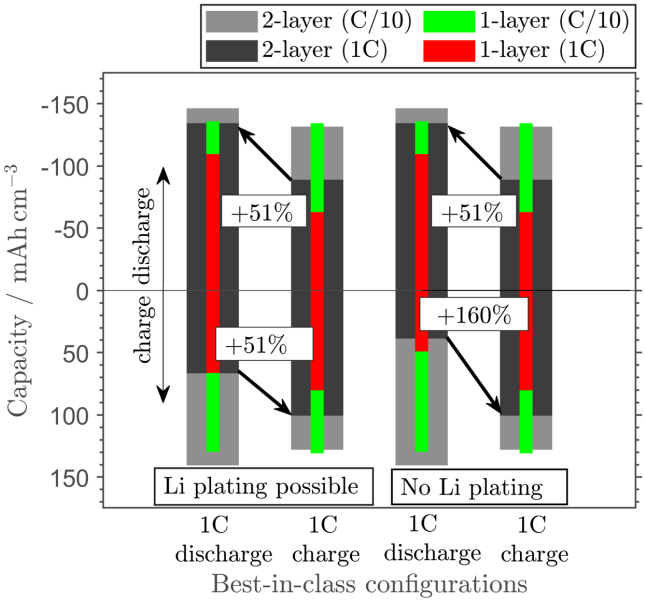

Figure 3.5: Comparison of volumetric capacity of best-in-class electrode configurations for single-layer (thin bars) and two-layer electrodes (wide bars) from the full-cell parameter study for discharge and charge at 1C. For the two bars on the left side, charge simulations were terminated upon reaching 4.2 V cell voltage. For the two bars on the right side, charge simulations were terminated upon reaching 4.2 V or upon reaching a local anode potential below 0 V vs. Li/Li$^+$. Percentage performance gains indicate the increase in capacity when comparing the structured cell tailored to charge to the one tailored to discharge at 1C and vice versa.

With the described lithium plating prevention measure in place, the 1C charge capability of the best cell configuration for 1C discharge significantly deteriorates. The cell tailored for 1C charge has a 160% higher charge capacity than the one designed for 1C discharge. This finding highlights the necessity to tailor a cell not only to the discharge requirements of a given application

but also to the required charge performance. Future studies may consider incorporating additional aspects besides lithium plating into the cell design optimization. For instance, Golmon et al. incorporated an upper limit for the mechanical stress on the active material particles into the design optimization [176]. This may be further extended to the long-term growth of the SEI [152, 177], as well as the mechanical degradation of the active material [46].

Overall, the presented coarse-grained parameter screening should be seen as a valuable tool for identifying basic trends. Due to the large design parameter space with ten degrees of freedom, the screening is likely too coarse-grained to locate the global optimum. Such an analysis requires a higher resolution of the parameter space. Considering that even more than 5,000 simulations cannot provide a comprehensive understanding of the whole design parameter space, a sufficiently broad experimental study seems infeasible without an automated high-throughput production and testing system. Even with DOE, experimental studies will have to focus on selected cell designs. These may be derived from experimental observations and experience or model-based predictions. Independent of the selected cell configurations, it is recommended to consider both discharge and charge direction in practically relevant performance ranges to provide a more holistic understanding and faster adoption of the investigated process or electrode design improvements.

3.3.2 Half-Cell Parameter Study

In this section, the results from the fine-grained cathode half-cell study are discussed. The significantly reduced design parameter space with only two degrees of freedom allows for a higher resolution than the full-cell design screening. This enables a good approximation of the optimal electrode structure. Furthermore, it allows for a detailed assessment of the correlation between design parameters and usable capacity in proximity to the optimal electrode structure. As already discussed, the full-cell parameter study was not designed to provide this level of detail. The contrast between the coarse full-cell screening and this highly discretized half-cell study will help to put the roughly 20% performance benefit of two-layer electrodes from the full-cell study into perspective.

Due to the definition of a constant particle radius, theoretical capacity, and average active material volume fraction, the cathode structure can be defined by two parameters: the thickness of the layer at the separator and the active material volume fraction in this layer. This implies that a lower AM volume fraction at the separator directly results in a higher AM volume fraction at the current collector and vice versa. Due to the constant coating thickness, the areal and volumetric capacity are directly proportional. For this reason, Figure 3.6 shows the cathode parameter study with the more intuitive areal capacity as a performance metric.

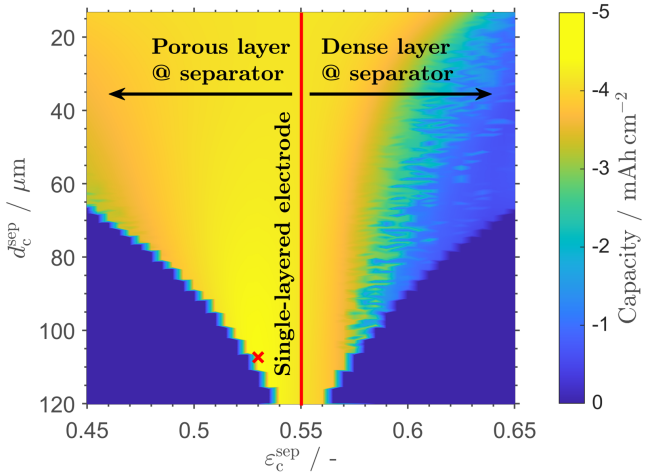

Figure 3.6: Parameter study for a two-layer cathode with a fixed theoretical capacity of 5 mAh cm^{-2} and a fixed average active material volume fraction of 55%, corresponding to a coating thickness of 133.4 µm. The red line represents single-layer electrode configurations. The color scale describes the areal capacity for intercalation, i.e., full-cell discharge, at 1C. The optimum is highlighted with a red cross. Configurations with an active material volume fraction in one layer below 45% or above 65% are shown with 0 mAh cm^{-2}.

The results indicate that a 5.9% higher capacity is obtained with a slightly more porous layer at the separator compared to the layer at the current collector. This general structuring recommendation is in good agreement with the prior full-cell study. It also resembles findings from other studies for both half-cell and full-cell design [87–89, 178].

For a holistic cell design, the large capacity plateau located around the single-layer electrode could be even more important than a slight capacity increase. The plateau suggests that the active material distribution and thus the porosity distribution within the two-layer cathode could vary over a wide parameter range without significantly altering its performance. For a design point in the center of such a plateau, small production variations could be expected to have a negligible effect on the final electrode performance. However, the capacity can deteriorate significantly for large production deviations or a disadvantageous electrode design selection.

Considering the homogeneous electrode as the baseline, the center of mass of the higher discharge capacities is on the side of the electrodes with the more porous layers at the separator. Notably, the capacity also does not decline as fast for a more porous layer at the separator. However, it should be noted that this capacity plateau may look different or be non-existent when looking at a full-cell instead of a half-cell configuration or when changing the fixed parameters, such as the theoretical capacity, the average AM volume fraction, or the particle size.

Overall, knowledge of the parameter space surrounding a chosen electrode design can help to minimize the detrimental effect of production uncertainties on consistent cell performance. To

enable a more sustainable and robust electrode production, future studies on electrode design should consider using robust optimization approaches. This would enable a reasonable trade-off between optimal performance and minimal production-related performance variance.

3.3.3 Comparison of Half- and Full-Cell Study

When comparing the full-cell and half-cell study, the estimated benefit from electrode structuring is significantly reduced from roughly 20% to 6%. This highlights the inherent difficulty in comparing i) studies with a realistic (full-cell study) and a non-limiting counter electrode (half-cell study), ii) studies with a similar benchmark, i.e., single-layer electrodes, but with variable versus fixed electrode thickness, and iii) studies with a substantially different resolution of the parameter space. Here, the latter aspect is critical since the benchmark system in both studies is defined as the best single-layer electrode configuration within the parameter space. The coarse full-cell screening cannot ensure to find the global optimum for the single-layer benchmark cell. The same holds true for the best two-layer cell configurations. Ultimately, the coarse full-cell parameter screening is a computationally expensive brute-force optimization. It should be seen primarily as a tool to identify promising trends within a parameter space. It does not allow for a universal evaluation of the concept of multi-layer electrodes if the single-layer benchmark system is not truly optimized. In contrast, the half-cell study has a well-defined single-layer benchmark electrode and indicates that electrode structuring is of minor importance. Nonetheless, it also does not allow for a general assessment of the concept of multi-layer electrodes due to the focus on only a small fraction of the theoretically available design parameter space.

An unbiased estimation of the benefit of multi-layer electrodes for a well-defined optimization objective may be possible with both an optimized single-layer benchmark system and an optimized multi-layer electrode. However, the result would still depend on the chosen design parameters and the optimization objective. In the end, multi-layer electrodes are just one concept within the electrode design toolbox. Their generalized classification as beneficial or unnecessary would contradict the diversity of possible application scenarios. However, with a well-motivated choice of values and assumptions, trends and conclusions can be made, which hold in the range of interest.

3.4 Concluding Remarks

To facilitate the selection of the best-suitable electrode design from published studies, researchers are encouraged to report performance characteristics that go beyond their primary optimization

objective and include areal and volumetric metrics, as well as charge and discharge characteristics. This approach can help mitigate the challenge of navigating the variety of investigated electrode designs along with their diverse optimization objectives and benchmark systems.

The shown model-based full-cell parameter study provides a first systematic analysis of two-layer electrodes for both discharge and charge at C/10 and 1C. As expected, the difference between cell designs for charge and discharge and the advantage of two- over single-layer electrodes is almost negligible at C/10 due to generally small overpotentials. For 1C charge and 1C discharge, the best-in-class cells with two-layer electrodes perform about 20% better. However, this notable benefit is partially the result of the coarse parameter screening, which does not allow for an optimal trade-off between volumetric capacity and transport limitations with single-layer electrodes. In terms of a universal cell design optimum, the 1C charge performance of a cell tailored for 1C charge was found to be 51% higher compared to a cell tailored for 1C discharge and, coincidentally, also 51% vice versa. If the charging process could additionally be terminated to prevent lithium plating, the 1C charge performance of a cell designed for this purpose is 160% higher compared to a cell designed for 1C discharge. This divergence of performance characteristics underlines the importance to analyze and report both discharge and charge performance for practically relevant C-rates as part of any electrode design study, whether experimental or model-based. It further highlights that there is no universal electrode design for all application scenarios, pointing to the necessity of a holistic definition of requirements.

The cathode half-cell parameter study was performed with only two design parameters and a high resolution to allow for a detailed understanding of the interrelation between cell performance and electrode structure. The roughly 20% capacity improvement at 1C over the best homogeneous electrode in the full-cell study compares to a 6% gain in the half-cell study. Thus, the estimated benefit of multi-layer electrodes depends on the chosen design parameters, the screening granularity, and the benchmark system. Furthermore, the half-cell study revealed a significant capacity plateau for cathodes that deviate in porosity only slightly from a homogeneous electrode, accompanied by a steep capacity decline for a less-porous layer at the separator. In the context of production uncertainties, the parameter space surrounding an electrode configuration should be considered during electrode design to ensure robust electrode quality. This could be realized either by a retrospective correlation of experimental production and electrochemical test data, a stochastic model-based study, or a model-based robust optimization.

The performed model-based parameter screenings comprised thousands of simulations. From an experimental perspective, this raises the question of whether expensive and limited production capacities are well invested in parameter screening or if these resources are better utilized in combination with battery models. In the end, a battery model can provide a design recommendation, but it can hardly be validated without experiments. In turn, an experimental study may find a better cell configuration compared to a specific benchmark. Still, it cannot reasonably investigate

the whole parameter space in the quest for an optimal electrode design. Here, physicochemical battery models can aid the experimental electrode design optimization i) by evaluating the expected benefit from different structuring concepts compared to an optimized benchmark system, ii) by recommending electrode designs for different application scenarios, and iii) by enabling a knowledge-based rather than a retrospective assessment of the effect of production uncertainties on the final cell performance variance.

4 Holistic Cell Diagnosis via SEI and Cell Modeling[1]

This chapter shifts the perspective from model-supported cell design to cell diagnostics. While cell design requires an accurate prediction of cell behavior for the design parameters of interest, a battery model for diagnostics does not have to be predictive in nature. Instead, the focus is on the current cell state, accessible from experimental data by optimizing model parameters. Here, the ability to reproduce experiments accurately is critical to provide meaningful parameter estimates for a deeper understanding of cell behavior.

As briefly introduced in Section 2.2, the formation of the solid electrolyte interphase affects the cost and quality of lithium-ion batteries. For a better understanding of its effect on cell performance and aging, fast and economically scalable SEI diagnostics are indispensable. Especially for repeated inspections along aging, a detailed diagnosis based on non-destructive measurements is highly preferred as this significantly reduces the overall experimental effort. Physicochemical battery models promise to extract hardly accessible interfacial and bulk properties of the SEI from electrochemical impedance spectra and C-rate tests. However, the typical analysis of only one measurement impedes a precise localization of degradation-related and performance-limiting processes. The following work will demonstrate that an SEI-extended cell model can reproduce both measurement types and provide detailed insights into the initial cell state after formation with clear changes in SEI and cell properties during aging.

This chapter starts with a discussion of the understanding and modeling of processes at the interfaces of the SEI and charge transport through the SEI. Subsequently, the integration of the SEI model into a P2D modeling framework is elaborated. Afterward, an iterative model parameterization strategy is described, which exploits parameter sensitivities in different measurements for meaningful parameter estimates. In the next step, an experimental aging study is introduced. Finally, these experimental data are analyzed with the proposed model parameterization strategy to gain insights into the initial cell state and its changes during aging.

[1] Parts of this chapter have been published in Witt, Röder, Krewer, Batteries Supercaps, 5(7):e202200067, 2022 (doi: 10.1002/batt.202200067, CC BY 4.0 [16]).

4.1 SEI Understanding and Modeling

To allow for insightful modeling of the SEI that adds value to model-based cell diagnostics, a good understanding of its properties, transport mechanisms, and interfacial processes is crucial. An et al., Peled and Menkin, and Wang et al. provide comprehensive reviews on the SEI, covering its initial formation [26], current and future challenges of SEI-dependent battery systems [102], and relevant modeling approaches [101]. It is generally accepted that the SEI is a complex composite structure built of various degradation products with different electrochemical and mechanical stability and transport properties. Here, inorganic products, like Li_2CO_3 and LiF, form a dense layer on the anode active material surface, which is covered by a porous organic outer layer. Organic SEI components, such as lithium ethylene dicarbonate (LEDC), are typically less stable and more prone to secondary reactions. In terms of cell safety, the predominately organic SEI in new cells contributes to a lower self-heating temperature, whereas a transition toward a thicker and more inorganic SEI in aged cells results in a notable increase in this temperature [179]. Polymeric species, derived from film-forming electrolyte additives like vinylene carbonate (VC), can enhance the mechanical stability of the multi-component SEI [180]. For the modeling of the SEI, its multi-component nature and multi-layer structure raise fundamental questions about the optimal level of detail for model-based cell diagnostics. Furthermore, processes and reactions at the interfaces of the SEI, as well as lithium-ion transport between them, must be considered.

It is still under discussion whether a porosity of the SEI should be modeled. In this context, Single et al. proposed a continuum model for the electrochemical formation of the SEI on graphite [181]. Based on the suggested competition between electron conduction and solvent diffusion, a non-zero SEI porosity was predicted. Li et al. investigated the SEI on a lithium-metal anode in a detailed simulation study [182]. It is pointed out that only the inner layer of the anode surface film, i.e., the densely packed inorganic layer, should be considered an effective passivation film that prevents further side reactions. The outer porous layer is not considered passivating due to liquid electrolyte in its pores. In this work, only the dense inner layer of the surface film is modeled, which will be referred to as the SEI for simplicity.

Apart from the multi-layer structure of the SEI, it must be decided on the modeling of its multi-component nature. There are two archetypes of component alignment: serial connection and parallel connection. A two-layer structure with one ionically almost isolating component, like LiF, on top of a better conductive component, like Li_2CO_3, would result in a different overall transport loss compared to a side-by-side arrangement. Based on simple EIS measurements and C-rate tests, an insightful deconvolution of the overall SEI-related transport losses into individual SEI components and their average alignment throughout the anode is unrealistic. Significant synergistic effects between components with individually unfavorable transport characteristics

add a further level of complexity and uncertainty [183]. Given these two aspects, i.e., component orientation in the film and synergistic effects, an explicit modeling of the local SEI properties would necessitate complex ex-situ measurements to reveal the local arrangement of different SEI components. Nonetheless, experimental limitations would still leave some open questions, e.g., regarding the effect of SEI morphology and composition on ion transport [184]. Considering the desired SEI characterization based on fast and non-destructive measurements, an effective SEI ionic conductivity is used in this work.

In the following, charge transfer at the SEI interfaces, lithium-ion transport between the electrolyte and the active material phase, and the potential profile over the SEI thickness are discussed. Models on SEI-related cell degradation often consider only the ohmic properties of the SEI while using a classic Butler-Volmer expression for the intercalation reaction [147, 152]. To enable an accurate representation of cell dynamics, and thus be able to simulate realistic impedance spectra, a more differentiated look at the involved reaction mechanism is necessary. In this context, Lück and Latz presented a model for an electrochemical double-layer between a planar electrode and a liquid electrolyte, which was used to study intercalation reactions [185, 186]. Based on experimental observations from lithium-ion batteries, they considered a two-step intercalation mechanism that comprises i) the lithium-ion de-/adsorption at the interface between solid and electrolyte phase and ii) the de-/intercalation into the active material. For simplicity, they projected the spatial resolution of the double-layer on the interface between electrode and electrolyte. The interface was coupled to the transport in bulk electrode and bulk electrolyte. They concluded that the charging of the electrochemical double-layer is the driving force for charge transfer across the interface. However, their work did not consider a surface film between the active material and the electrolyte phase.

In a previous work, continuum P2D cell modeling and a kinetic Monte Carlo method were combined to analyze the growth of the SEI during cell formation [124]. Here, lithium-ion transport through the SEI was described as a combination of three process steps: i) adsorption of a solvated lithium ion at the interface of the SEI with the liquid electrolyte, ii) transport through the SEI to its inner interface, and iii) intercalation into the active material. Heinrich et al. used a similar setup for the analysis of impedance spectra along cell aging [118]. Both studies assumed single-ion conductor properties for the SEI, i.e., pure ionic conduction. For the sake of model simplicity, the transfer of an adsorbed lithium ion into the SEI and its intercalation into the active material were treated as a homogeneous multi-step reaction [118, 124, 187]. The three-step charge transfer mechanism is adopted in this work, but the three steps are considered individually rather than lumped together. Individual electrochemical double-layers and species balances are considered for both SEI interfaces [118, 124].

Regarding transport through the SEI, the assumption of a single-ion conductor is well supported by research. For instance, Borodin et al. investigated lithium-ion transport in LEDC, a common organic SEI component [188]. They suggested that LEDC acts as a single-ion conductor. Shi et al. used density functional theory to reveal the mechanism of lithium-ion transport in the inorganic SEI component Li_2CO_3 [189, 190]. They suggested that lithium ions are transported rapidly by pore diffusion in the porous outer organic SEI layer and by knock-off diffusion, i.e., displacement of neighboring lattice sites rather than direct-hopping through empty spaces, of interstitial Li^+ in the inner inorganic SEI layer. They confirmed their results with estimated SEI resistances from impedance data and other measurements like transmission electron microscopy, X-ray photoelectron spectroscopy, and time-of-flight secondary ion mass spectrometry. With only one main diffusion carrier, this points to a single-ion conductor behavior. From the perspective of impedance modeling, Single et al. also investigated transport within the SEI [148]. In the first step, they modeled it similarly to transport in the electrolyte phase with migration and diffusion. In the next step, they parameterized their model with experimental data. Here, they could only accurately reproduce the experimental impedance spectra with a transference

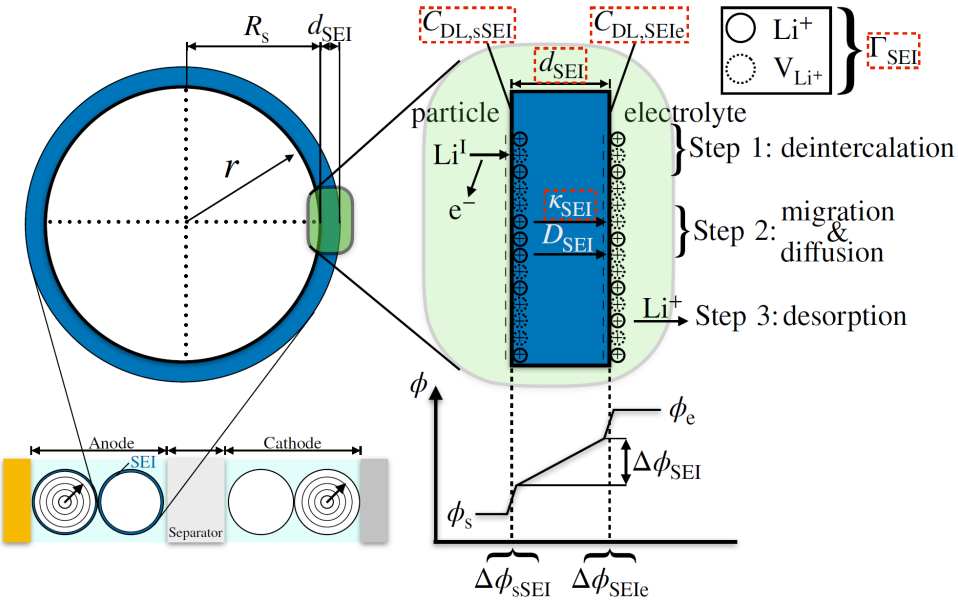

Figure 4.1: Graphical summary of the SEI model for the anode side, illustrating the potential profile at the interfaces of the SEI with electrochemical double-layers at both interfaces. The arrows at the magnified SEI on the right side indicate the pathway of a lithium ion from the solid into the electrolyte phase. The interfaces provide a limited number of surface sites Γ_{SEI} for occupation by lithium ions. Here, vacant surface sites are shown as dotted circles and occupied ones as solid circles. SEI-related parameters, which are updated along cell aging, are surrounded by dashed, red boxes.

number close to one, which suppors the assumption of a single-ion conductor. However, the investigated symmetric cell with planar lithium-metal electrodes, i.e., non-intercalation electrodes, and a Li-TFSI electrolyte in a tetraglyme solution may not be directly comparable to lithium-ion batteries with graphite-based anodes. For this reason, the diffusion process is kept in this work's model to assess its necessity for reproducing experimental EIS and C-rate data. The estimated SEI transference number of 0.97 is adopted from Single et al. [148].

Figure 4.1 shows the translation of the discussed SEI understanding into a schematic representation of the SEI model, which is used in this work. It shows one representative anode active material particle covered by an SEI within a P2D cell model. Here, relevant processes and the potential profile through the SEI are illustrated. This comprises the deintercalation from the active material into the active material-SEI interface, the transport through the SEI via diffusion and migration, and the final desorption at the SEI-electrolyte interface. Henceforth, the interface between active material particle and SEI is indicated by the index sSEI; the interface between SEI and electrolyte is indicated by the index SEIe. For visual clarity, the surface sites are only shown on one side of each interface. Furthermore, the surface sites and thus the electrochemical double-layers are shown with a non-zero spatial expansion, which would be expected in reality. In the model, this spatial resolution is eliminated, resulting in a potential-step at the interfaces.

4.2 Model Development

With the ambition of fast yet in-depth model-based cell diagnostics, an adequate cell modeling framework is crucial. This necessitates two fundamental trade-offs: i) necessary model complexity for accurate reproduction of experimental data versus computational cost, and ii) detailed modeling of physicochemical processes versus a potentially larger number of difficult-to-identify model parameters.

Equivalent circuit models are commonly used to analyze electrochemical impedance spectra, but they can also be used to describe a cell's charge/discharge behavior [112, 113, 191, 192]. Still, ECMs rely on state-of-charge-dependent resistances that would need to be translated into diffusion coefficients or reaction rate constants for a detailed understanding of cell behavior changes. Physicochemical models, like the P2D model, directly describe the underlying processes like diffusion, migration, and concentration-dependent reaction kinetics. Here, considering a particle size distribution would improve the model accuracy, but it would also increase the computational cost [120]. As a result, this work uses a P2D modeling framework with one representative particle size for each electrode as the basis for the SEI modeling. Nonetheless, advances in available computational power and the utilization of surrogate modeling could make microstructure-resolved battery models a great extension of the here presented SEI modeling [193].

In the following sections, the P2D cell model itself and the implementation of the SEI into this model are discussed in detail. In the end, the dynamics at the anode and cathode current collector are briefly described.

4.2.1 Basic P2D Cell Modeling Framework

A summary of the basic equations for lithium-ion transport in the active material particles, in the electrolyte phase, and transfer between these phases was already given in Table 2.1. The kinetics on the anode side are described with non-ideal activities [194, 195]. The detailed equations are provided in the following section. The kinetics on the cathode side are described with a Butler-Volmer expression, representing a single rate-limiting process. For the concentration-dependent exchange current density, the activities in the active material and the electrolyte phase are obtained by normalization of the lithium-ion concentrations to the maximum solid concentration and the reference electrolyte concentration, respectively. A summary of these and other complementary model equations is given in Table C.1 in the Appendix. Figure 4.2 presents a schematic of the SEI-extended P2D model, illustrating the governing processes during discharge. The depicted modeling of the anode-side SEI, as well as dynamics related to the anode and cathode current collectors are discussed in the following sections. Due to less pronounced and typically not performance-limiting surface film formation on the cathode side, this electrode is modeled SEI-free [59, 196].

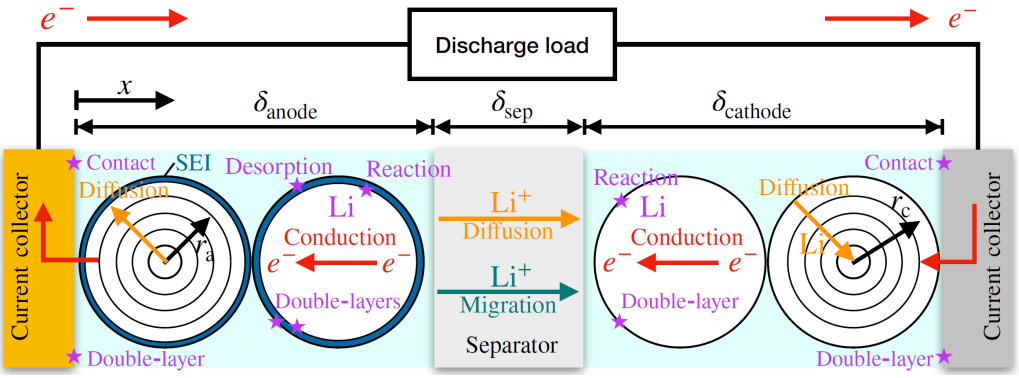

Figure 4.2: Schematic representation of the employed P2D cell model with the SEI on the anode active material particles shown as a dark blue surface layer (figure style inspired by [125]). The coordinate x is used for the cell-level discretization of anode, separator, and cathode with thicknesses δ_a, δ_{sep}, and δ_c. The radial coordinate r is used for the particle-level discretization of the active material particles. The kinetics of the anode are governed by a deintercalation reaction at the inner interface of the SEI and a desorption process at its outer interface. The kinetics of the cathode are driven by an insertion reaction. At the anode and cathode current collectors, dynamics arising from contact resistances and electrochemical double-layers are considered.

All simulations use a cell discretization of twelve representative particles for both anode and cathode side with a four-fold discretization of each particle. The separator is discretized with thirteen volume elements. The simulations were performed with MATLAB version 2020b, using the solver ode15s.

4.2.2 Implementation of the SEI in a P2D Cell Model

This section addresses the implications of a second interface between active material and electrolyte for determining the solid and electrolyte phase potential. Afterward, the equations for the intercalation reaction, the adsorption process, and the transport through the SEI are introduced. Finally, the necessary equations for the potentials at the two electrochemical double-layers of the SEI and its interfacial surface coverages are shown.

The original Doyle-Fuller-Newman model does not consider a surface film between active material and electrolyte phase [122]. Without the SEI, the solution of the solid phase potential ϕ_s and electrolyte phase potential ϕ_e at the location x within the cell is straightforward. With the electrochemical double-layer between solid and electrolyte phase, the total volumetric current of lithium ions j^tot from electrical conduction in the active material

$$j^\mathrm{tot}(x) = \frac{\partial}{\partial x}\left[\sigma_\mathrm{s,eff}\frac{\partial \phi_\mathrm{s}(x)}{\partial x}\right] \tag{4.1}$$

with conductivity $\sigma_\mathrm{s,eff}$ can be equated with the total lithium-ion current from migration and diffusion in the electrolyte phase

$$j^\mathrm{tot}(x) = -\frac{\partial}{\partial x}\left[\sigma_\mathrm{e,eff}(x)\frac{\partial \phi_\mathrm{e}(x)}{\partial x}\right] - \frac{\partial}{\partial x}\left[\sigma_\mathrm{De,eff}(x)\frac{\partial \ln\left(c_\mathrm{e}(x)\right)}{\partial x}\right] \tag{4.2}$$

with the effective ionic electrolyte conductivity $\sigma_\mathrm{e,eff}$, the effective diffusive ionic conductivity $\sigma_\mathrm{De,eff}$, and the electrolyte concentration c_e. The finite volume method can offer a numerical solution to this problem. In the classical P2D model, the desired potentials ϕ_s and ϕ_e can be obtained via the electrochemical potential at the double-layer

$$\Delta\phi_\mathrm{DL} = \phi_\mathrm{s} - \phi_\mathrm{e}. \tag{4.3}$$

In an SEI-extended P2D cell model, the two SEI interfaces with their individual electrochemical double-layers result in four instead of two relevant potentials. As a starting point, the potentials at the double-layers at both the inner and the outer SEI interface, i.e., $\Delta\phi_\mathrm{sSEI}$ and $\Delta\phi_\mathrm{SEIe}$, are

initialized at the equilibrium potential of the active material vs. Li/Li^+ and 0 V vs. Li/Li^+, respectively. Then, the potential difference between solid and electrolyte phase is given by

$$\phi_s - \phi_e = \Delta\phi_{sSEI} + \Delta\phi_{SEI} + \Delta\phi_{SEIe} \tag{4.4}$$

with the potential drop $\Delta\phi_{SEI}$ over the SEI thickness. The charge transport through the SEI is described with the Nernst-Planck equation [197] according to

$$j^{tot} = \frac{a_s \kappa_{SEI}}{d_{SEI}} \left(\frac{RT(1-2t_{p,SEI})}{F} \ln\left(\frac{\theta_{sSEI}}{\theta_{SEIe}}\right) - \Delta\phi_{SEI} \right) \tag{4.5}$$

with the SEI ionic conductivity κ_{SEI}, the specific surface area a_s of the spherical active material particles, the universal gas constant R, the temperature T, the transference number in the SEI $t_{p,SEI}$, the Faraday constant F, the interfacial lithium-ion coverage at the inner and outer interface of the SEI θ_{sSEI} and θ_{SEIe}, respectively, and the SEI thickness d_{SEI}. Combined with Equation 4.1 and Equation 4.2, this allows for the calculation of the total volumetric lithium-ion current in the presence of the SEI along with the corresponding solid and electrolyte phase potentials. In the following, all equations for lithium-ion transport and transfer between anode active material and electrolyte phase are derived. They are introduced starting with the deintercalation, going on with the transport through the SEI, and ending with the solvatization of a lithium ion and its desorption at the outer SEI interface.

In the first step, intercalated lithium Li(s) is transferred to a vacant surface site V_{Li} at the sSEI-interface while leaving a vacancy and an electron in the active material, according to the following equation:

$$Li(s) + V_{Li}(sSEI) \rightleftharpoons Li^+(sSEI) + V_{Li}(s) + e^-(s). \tag{4.6}$$

The reaction rate coefficients for the forward reaction $k_{f,s/sSEI}$

$$k_{f,s/sSEI} = k_{0,s/sSEI} \exp\left(-\frac{E_{a,s/sSEI}}{RT}\right) \exp\left(\frac{\alpha\Delta\phi_{sSEI}F}{RT}\right) \tag{4.7}$$

and the backward reaction $k_{b,s/sSEI}$

$$k_{b,s/sSEI} = k_{0,s/sSEI} \exp\left(-\frac{E_{a,s/sSEI} - \Delta G^0_{s/sSEI}}{RT}\right) \exp\left(-\frac{(1-\alpha)\Delta\phi_{sSEI}F}{RT}\right) \tag{4.8}$$

are defined based on the Arrhenius equation, with the reaction rate constant $k_{0,s/sSEI}$, the standard Gibbs free energy $\Delta G^0_{s/sSEI}$, the activation energy $E_{a,s/sSEI}$, and the electrochemical potential at

the interface between active material and SEI $\Delta\phi_{\mathrm{sSEI}}$. For this reaction, the standard Gibbs free energy is defined as

$$\Delta G^0_{\mathrm{s/sSEI}} = \mu^0_{\mathrm{Li(sSEI)}} + \mu^0_{\mathrm{V_{Li}(s)}} + \mu^0_{\mathrm{e^-}} - \mu^0_{\mathrm{Li(s)}} - \mu^0_{\mathrm{V_{Li}(sSEI)}} \tag{4.9}$$

with the standard chemical potentials μ^0 listed in Table C.2 in the Appendix. Finally, the overall volumetric reaction rate $r_{\mathrm{s/sSEI}}$ at the sSEI-interface is described as an elementary charge-transfer reaction [194]. It depends on the forward and backward reaction rate constants k_{f} and k_{b}, the ratio between the number of occupied and total surface sites, i.e., the surface coverages θ_{sSEI} and θ_{SEIe}, the surface site density Γ_{SEI}, the activity of lithium ions a in their respective states, and the specific surface area a_{s}:

$$r_{\mathrm{s/sSEI}} = a_{\mathrm{s}}\Gamma_{\mathrm{SEI}}\left[a_{\mathrm{Li(s)}}\left(1-\theta_{\mathrm{sSEI}}\right)k_{\mathrm{f,s/sSEI}} - a_{\mathrm{V_{Li}(s)}}\theta_{\mathrm{sSEI}}k_{\mathrm{b,s/sSEI}}\right]. \tag{4.10}$$

The required activities of lithium in the active material are obtained with a Redlich-Kister approach [194]. In this work, the surface site density is the same for both SEI interfaces. As a result, the de-/intercalation reaction and the de-/adsorption process are influenced by this parameter. Future studies may use different values for the inner and the outer SEI interface as a function of its local composition and surface structure or roughness.

The volumetric reaction rate of the generic reaction i can be transformed into the corresponding volumetric lithium-ion current with

$$j^{\mathrm{Li}}_{\mathrm{i}} = r_{\mathrm{i}}\mathrm{F}. \tag{4.11}$$

The lithium-ion transport $\dot{n}_{\mathrm{sSEI/SEIe}}$ between the inner (sSEI) and outer (SEIe) interface of the SEI is driven by potential and concentration gradients, i.e., migration and diffusion, respectively [148, 197]. For the sake of simplicity, the curvature of the SEI is neglected due to its small thickness compared to the underlying particle radius [198]. This allows to use the same specific surface area a_{s} for the inner and outer interface of the SEI. The earlier discussed transference number for lithium ions in the SEI $t_{\mathrm{p,SEI}}$ accounts for deviations from a single-ion conductor. This results in:

$$\dot{n}_{\mathrm{sSEI/SEIe}} = -D_{\mathrm{Li,SEI}}\Gamma_{\mathrm{SEI}}a_{\mathrm{s}}^2\frac{\theta_{\mathrm{SEIe}}-\theta_{\mathrm{sSEI}}}{d_{\mathrm{SEI}}} + \frac{t_{\mathrm{p,SEI}}j^{\mathrm{tot}}}{F}. \tag{4.12}$$

A spatial discretization was omitted to reduce the computational burden of the SEI implementation. This is valid if transport through the SEI is fast and gradients within this thin surface film are small.

The final process step, i.e., the solvatization and desorption of lithium ions at the SEIe-interface, is defined analogously to the deintercalation reaction at the sSEI-interface in Equations 4.6–4.10. During the desorption process, a lithium ion from the SEIe-interface is transferred into the electrolyte phase while leaving a vacant surface site according to

$$\mathrm{Li^+(SEIe)} \rightleftharpoons \mathrm{V_{Li}(SEIe)} + \mathrm{Li^+(e)}. \tag{4.13}$$

The forward reaction rate is given by

$$k_{\mathrm{f,SEIe/e}} = k_{\mathrm{0,SEIe/e}} \exp\left(-\frac{E_{\mathrm{a,SEIe/e}}}{\mathrm{R}T}\right) \exp\left(\frac{\alpha \Delta\phi_{\mathrm{SEIe}} \mathrm{F}}{\mathrm{R}T}\right) \tag{4.14}$$

and the backward reaction rate by

$$k_{\mathrm{b,SEIe/e}} = k_{\mathrm{0,SEIe/e}} \exp\left(-\frac{E_{\mathrm{a,SEIe/e}} - \Delta G^0_{\mathrm{SEIe/e}}}{\mathrm{R}T}\right) \exp\left(-\frac{(1-\alpha)\,\Delta\phi_{\mathrm{SEIe}} \mathrm{F}}{\mathrm{R}T}\right). \tag{4.15}$$

The standard Gibbs free energy is obtained via

$$\Delta G^0_{\mathrm{SEIe/e}} = \mu^0_{\mathrm{V_{Li}(SEIe)}} + \mu^0_{\mathrm{Li(e)}} - \mu^0_{\mathrm{Li(SEIe)}}. \tag{4.16}$$

The volumetric de-/adsorption rate of lithium ions is defined based on power-law kinetics [118]:

$$r_{\mathrm{SEIe/e}} = a_{\mathrm{s}} \Gamma_{\mathrm{SEI}} \left[\theta_{\mathrm{SEIe}} k_{\mathrm{f,SEIe/e}} - a_{\mathrm{Li(e)}} \left(1 - \theta_{\mathrm{SEIe}}\right) k_{\mathrm{b,SEIe/e}}\right]. \tag{4.17}$$

Here, the activities for solvated lithium ions in the electrolyte phase are obtained by normalization to a reference concentration of $1\,\mathrm{mol\,L^{-1}}$. The volumetric reaction rate can be converted into the corresponding volumetric current density of lithium ions with Equation 4.11.

The two following species balances describe the time dependence of the surface coverage at the interface between active material and SEI

$$a_{\mathrm{s}} \Gamma_{\mathrm{SEI}} \frac{\partial \theta_{\mathrm{sSEI}}}{\partial t} = r_{\mathrm{s/sSEI}} - \dot{n}_{\mathrm{sSEI/SEIe}} \tag{4.18}$$

and at the interface between SEI and electrolyte phase

$$a_{\mathrm{s}} \Gamma_{\mathrm{SEI}} \frac{\partial \theta_{\mathrm{SEIe}}}{\partial t} = \dot{n}_{\mathrm{sSEI/SEIe}} - r_{\mathrm{SEIe/e}} \tag{4.19}$$

with the corresponding interfacial reaction rates r_{i} and the transport through the SEI $\dot{n}_{\mathrm{sSEI/SEIe}}$.

Finally, the charge balances for the electrochemical double-layers at the two SEI interfaces are introduced. It is assumed that the double-layer capacitance C_{DL} is constant with respect to potential and local lithium-ion concentration. The charge balances are given by

$$C_{\mathrm{DL,sSEI}} \frac{\partial \left(\Delta\phi_{\mathrm{sSEI}}\right)}{\partial t} = \frac{j^{\mathrm{tot}} - j^{\mathrm{Li}}_{\mathrm{sSEI}}}{a_{\mathrm{s}}} \tag{4.20}$$

for the interface between the active material and the SEI and by

$$C_{\mathrm{DL,SEIe}} \frac{\partial \left(\Delta\phi_{\mathrm{SEIe}}\right)}{\partial t} = \frac{j^{\mathrm{tot}} - j^{\mathrm{Li}}_{\mathrm{SEIe}}}{a_{\mathrm{s}}} \tag{4.21}$$

for the interface between the SEI and the electrolyte phase with the potentials at the double-layers $\Delta\phi_{\mathrm{sSEI}}$ and $\Delta\phi_{\mathrm{SEIe}}$, respectively.

4.2.3 Dynamics Related to the Current Collectors

For an improved understanding of the SEI, it is important to differentiate between SEI-related and contact-related impedance contributions. Here, Gaberscek et al. shaped the commonly accepted impedance interpretation by investigating the origin of the high-frequency impedance arc in lithium-ion batteries beyond 1 kHz [199]. They demonstrated that this impedance contribution must be related to the contact between the electrode coating and the underlying metallic substrate, i.e., the current collector. For a meaningful physicochemical cell diagnosis, this should not be confused with the SEI and its reported characteristic frequency on the order of 250 Hz [30, 200]. For this reason, the anode and cathode contact resistances are included in the model.

The potentials at the double-layers at the anode $(\Delta\phi_{\mathrm{a,cc}})$ and cathode $(\Delta\phi_{\mathrm{c,cc}})$ current collector with the contact resistances $R_{\mathrm{a,cc}}$ and $R_{\mathrm{c,cc}}$ and the electric current I_{cell} are described with

$$C_{\mathrm{DL,a,cc}} \frac{\mathrm{d}\left(\Delta\phi_{\mathrm{a,cc}}\right)}{\mathrm{d}t} = \left(\frac{I_{\mathrm{cell}}(t)}{A_{\mathrm{cell}}} - \frac{\Delta\phi_{\mathrm{a,cc}}}{R_{\mathrm{a,cc}}} \right) \tag{4.22}$$

and

$$C_{\mathrm{DL,c,cc}} \frac{\mathrm{d}\left(\Delta\phi_{\mathrm{c,cc}}\right)}{\mathrm{d}t} = \left(-\frac{I_{\mathrm{cell}}(t)}{A_{\mathrm{cell}}} - \frac{\Delta\phi_{\mathrm{c,cc}}}{R_{\mathrm{c,cc}}} \right). \tag{4.23}$$

Both potentials at the double-layers are initialized at 0 V vs. $\mathrm{Li/Li^+}$. Eventually, the cell voltage can be calculated with

$$V_{\mathrm{cell}} = \phi_{\mathrm{c}}\left(L_{\mathrm{cell}}\right) + \Delta\phi_{\mathrm{c,cc}} - \phi_{\mathrm{a}}(0) - \Delta\phi_{\mathrm{a,cc}}. \tag{4.24}$$

4.3 Parameterization Strategy

As discussed before, the central purpose of the proposed SEI-extended P2D cell model is to enable a holistic cell diagnosis based on multiple measurement types for an in-depth understanding of the state of a lithium-ion battery and its changes during aging. Inevitably, this requires a sound parameterization strategy to avoid ambiguous and thus potentially misguiding parameter estimates. For this reason, a multi-step parameterization procedure is used, which exploits individual parameter sensitivities that differ between the measurement techniques. Figure 4.3 provides a condensed summary of the strategy for both the initial model parameterization and the later parameter update during cell aging.

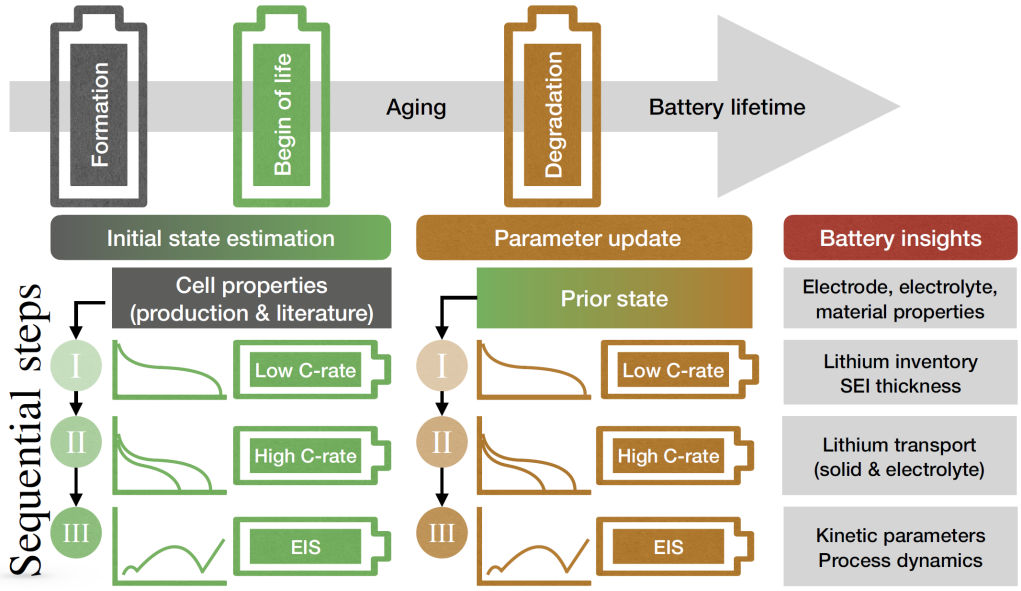

Figure 4.3: Schematic representation of the multi-step parameterization strategy for a model-based cell diagnosis with the SEI-extended P2D cell model and three-electrode measurements. Before any mathematical optimization is applied, properties from electrode production, like electrode thickness, porosity, and active material volume fraction, are fixed. Other properties, like the ionic conductivity of the utilized electrolyte system, may be adopted from literature. Afterward, three parameterization steps are executed sequentially for both the initial model parameterization after cell formation and the parameter update along cell cycling. The parameter update of aging-sensitive parameters always uses the prior cell state, i.e., either the initial or an already updated parameter set from an earlier characterization snapshot.

The basic parameterization procedure is similar to the work by Laue et al. [149]. It highlighted that the commonly chosen approach for P2D cell model parameterization based on discharge curves cannot ensure good parameter identifiability. Although the experimental data may be represented accurately, a non-unique parameter set could lead to wrong conclusions with respect to limiting processes in the cell. To overcome this problem, a multi-step parameter estimation approach was employed, using quasi-static discharge and dynamic EIS measurements in a three-electrode setup. To account for the SEI, this parameterization strategy is adjusted.

Table 4.1 summarizes the extracted parameters in each parameterization step from Figure 4.3. It specifies the already known parameters and the exploited measurement data for the parameter estimation, starting with low C-rate discharge for lithium-ion concentrations in the active materials (step I), moving on to high C-rate discharge for mass transport-related parameters (step II), and advancing to EIS data for kinetic parameters (step III). The corresponding objective functions are detailed in Section C.2 in the Appendix. The identifiability of the initial parameters and the parameter changes due to aging are discussed in the Appendix in Sections C.3 and C.4, respectively. For the EIS analysis, only the medium frequencies between 1 kHz and 5 Hz are used. In this range, the reaction kinetics and SEI-related processes take place, for which parameters are identified [30, 191, 200]. Importantly, this frequency range is not accessible with a standard discharge measurement, which underlines the importance of a joint analysis of C-rate and EIS data for a holistic cell diagnosis.

Table 4.1: Summary of the parameterization steps including the extracted parameters and the utilized (experimental) data sources for both the initial model parameterization and the update of aging-sensitive model parameters during cycling. The experiments comprise anode and cathode half-cell data.

Step	Data	Parameters (initial)	Parameters (update)
Cell properties	Production, supplier data	d_a, d_s, d_c, $\varepsilon_{e,a}$, $\varepsilon_{e,s}$, $\varepsilon_{e,c}$, $\varepsilon_{s,a}$, $\varepsilon_{s,c}$	-
	Literature	Electrolyte properties	-
	OCP measurement	Activities, chemical potentials	-
	1st formation cycle	d_{SEI}	-
I	C/10 discharge	$c_{a,0}$, $c_{c,0}$, $c_{a,max}$, $c_{c,max}$	d_{SEI}, $D_{s,c}$
II	1C, 2C discharge	τ_a, τ_c, $D_{s,a}$, $D_{s,c}$	τ_a, $D_{s,c}$
III	EIS	$k_{0,s/sSEI}$, $k_{0,SEIe/e}$, $k_{0,c}$, $C_{DL,sSEI}$, $C_{DL,SEIe}$, $C_{DL,c}$, $\sigma_{s,c}$, $\sigma_{s,a}$, κ_{SEI}, $R_{a,cc}$, $R_{c,cc}$, $C_{DL,a,cc}$, $C_{DL,c,cc}$	Γ_{SEI}, $k_{0,c}$, $C_{DL,sSEI}$, $C_{DL,SEIe}$, $C_{DL,c}$, κ_{SEI}

4.3.1 Initial Model Parameterization

As the first step in any model parameterization, all already known or easily accessible parameters should be fixed. In this work, the electrode and separator thicknesses, the electrode porosity ε_e, and the active material volume fraction ε_s are known. Other parameters, like electrolyte conductivity and diffusivity, may require tailored experiments, which are often already available in literature. For this work, the electrolyte properties are approximated with empirical polynomials for 1M $LiPF_6$ in EC:EMC 3:7 (w:w) by Landesfeind et al. [50]. The anode and cathode open circuit potentials are described with a Redlich-Kister expansion. The corresponding Redlich-Kister coefficients are extracted from half-cell discharge data at a C-rate of C/50 after cell formation via nonlinear least-squares fitting (see Appendix, Table C.3).

Although not directly measurable, the initial SEI thickness after cell formation is calculated based on the initial capacity loss in the first formation cycle. In contrast to a mathematical optimization, this circumvents ambiguous results due to strong correlations with parameters like the SEI ionic conductivity. Model-based studies on SEI growth commonly use available image analysis data to estimate the SEI thickness or directly calculate it from the initial capacity loss during cell formation [118, 147, 152]. This work uses the latter approach and estimates the SEI thickness based on the difference between charge and discharge capacity during the first formation cycle. Importantly, only a part of the observed capacity loss during formation is attributed to irreversible SEI growth. The apparent capacity loss at high anode potentials is related to a reversible shift in the lithiation degree of the anode (see Appendix, Section C.1).

Generally, a wide range of SEI growth reactions is possible within a $LiPF_6$ EC:EMC electrolyte system with a small amount of VC as a formation additive [26]. Intertwined reaction pathways between these components and their intermediate reaction products further complicate the estimation of the exact SEI composition and its related lithium consumption [201]. The formation data alone do not provide enough features for a proper differentiation between SEI growth reactions and resulting SEI components. To enable a clear estimation of the SEI thickness, all SEI growth is attributed to the inorganic SEI component lithium carbonate, similar to the EIS-focused study by Heinrich et al. [118]. The EC-related film thickness for the reaction [101]

$$\mathrm{EC} + 2\mathrm{Li}^+ + 2\mathrm{e}^- \rightarrow \mathrm{Li_2CO_3} + \mathrm{C_2H_4} \tag{4.25}$$

is calculated from the irreversible initial capacity loss Q_{ICL} along with the molar volume of lithium carbonate $\tilde{V}_{\mathrm{Li_2CO_3}}$:

$$d_{\mathrm{SEI}} = \frac{Q_{\mathrm{ICL}}}{2\mathrm{F}} \tilde{V}_{\mathrm{Li_2CO_3}} a_{\mathrm{s}}^{-1}. \tag{4.26}$$

It is assumed that the SEI forms homogeneously throughout the anode. Taking into account the SEI volume, the anode porosity is adjusted:

$$\varepsilon_{\mathrm{a,e}}^{\mathrm{adjusted}} = \varepsilon_{\mathrm{a,e}}^{\mathrm{init}} - d_{\mathrm{SEI}} a_{\mathrm{s}}. \tag{4.27}$$

4.3.2 Parameter Update during Aging

To determine how the cell and the SEI change during cycling, aging-sensitive parameters are identified and updated after 50 and 100 aging cycles (see Table 4.1). The starting points for these mathematical parameter optimizations are the initial parameter set after formation and the updated parameter set after 50 aging cycles, respectively. Importantly, the parameters in this work were chosen based on their ability to capture the observed changes in the experiments. A reassessment of the selected aging-sensitive parameters is highly recommended for different cell designs, cell chemistries, or aging conditions.

In the first step, the SEI thickness d_{SEI} is updated with discharge data at a C-rate of C/10 to capture the observed loss of lithium inventory. Here, the complete capacity loss is attributed to SEI growth and not loss of active material. This assumption is supported by a differential voltage analysis of the experimental half-cell data, which does not show substantial changes in peak separation at low state of charge on the anode side. In any other case, the parameterization would have to consider the deactivation of (partially) lithiated active material. In the second step, the anode tortuosity τ_{a} and the cathode solid diffusion coefficient $D_{\mathrm{s,c}}$ are adjusted based on 1C and 2C discharge data. These two parameters were crucial to reproduce the observed changes in the respective half-cell potentials. In the final parameterization step, the EIS measurement is used to update the ionic conductivity of the SEI κ_{SEI}, its surface site density Γ_{SEI}, and its two distinct double-layer capacitances $C_{\mathrm{DL,sSEI}}$ and $C_{\mathrm{DL,SEIe}}$. These parameters enable a lateral shift of the anode half-cell impedance, a direct manipulation of its kinetics via the surface site density, and a shift of its characteristic frequencies via the two capacitances. It is assumed that changes in the kinetics are related to the available surface site density. However, a change in the reaction and adsorption rate constant, e.g., due to an altered interfacial composition, would have the same effect on the cell behavior. Additional studies would be needed to decide on the physically more reasonable change. The SEI diffusion coefficient is not adjusted due to a lack of corresponding features in the experimental data. On the cathode side, the reaction rate constant $k_{0,\mathrm{c}}$ and the double-layer capacitance $C_{\mathrm{DL,c}}$ are updated.

4.4 Experimental

The following experimental study is used for the model-based state estimation of a new cell directly after the formation process and along aging. Herein, the initial cell state will help to assess the effect of individual SEI properties on the cell performance at elevated C-rates and the impedance behavior. The subsequent analysis of cell behavior changes during aging via a parameter update will help to understand degradation or rather transformation processes within the cell.

The electrodes for the aging study in this work were produced in the Battery LabFactory Braunschweig. Both the graphite anode and the NMC622 cathode have an active material content of 93%. The electrode porosities and other parameters that were measured, known from production, or obtained from the initial model parameterization are summarized in Table C.4 in the Appendix.

For the electrochemical cell characterization, a commercial PAT-Cell three-electrode setup by EL-Cell GmbH was used. The electrodes were punched to a diameter of 18 mm for the EL-Cell PAT-Cell, weighed, and dried at 120 °C under high vacuum. Afterward, they were transferred into an argon-filled glovebox for cell assembly. Here, the cathode was assembled as the bottom electrode in the PAT-Cell. To enable three-electrode studies, a PP fiber/PE membrane separator by EL-Cell GmbH with an integrated lithium-metal reference electrode was used (ECC1-00-0210-V/X). The test cells were filled with 100 µL electrolyte, which is composed of 1M $LiPF_6$ conducting salt in a 3:7 (v:v) solvent mixture of EC and EMC with 2 wt% VC as a formation additive. Cell formation and cycling were done with an automated MACCOR series 4000 test system. The EIS measurements were performed with a Gamry Reference 3000 potentiostat/galvanostat. All measurements were performed at 20 °C in an ESPEC SU-641 temperature chamber.

The cell formation procedure is performed with currents based on the theoretical capacity of the cathode. After formation, a capacity test at a C-rate of C/10 is applied to determine the usable capacity of the cell. This value is used to set the currents for the respective C-rates during cell characterization and aging. The employed measurement routine for cell formation, cell characterization, and cell aging is given in Table C.5 in the Appendix. In brief, after wetting and cell formation, a characterization procedure is applied, which comprises an EIS measurement and a C-rate test at various C-rates. Afterward, a cell aging procedure is applied with 50 charge-discharge cycles between 2.9 V and 4.2 V. These two procedures are repeated for a total of three characterization snapshots along 100 aging cycles. Based on this measurement routine, two cells were assembled and tested. Due to similar results, one cell was selected for the following model-based cell diagnosis.

4.5 Results and Discussion

This section first discusses how well the model can reproduce experimental discharge curves and impedance spectra and what insight can be gained from the identified parameters. Subsequently, the changes in cell behavior during aging are analyzed along with the corresponding changes in model parameters.

4.5.1 Model-Based Insight into the Initial Cell State

In the first step, the capability of the model to reproduce experimental data is discussed. Afterward, the identified SEI properties and their implications for cell performance are investigated.

Figure 4.4 shows the initial battery state with experimental full-cell and half-cell discharge data and impedance spectra (solid lines) and compares them with the simulation results (dashed lines).

The full-cell discharge curves in Figure 4.4a show a good agreement between experiment and simulation for all investigated C-rates, comparable to other studies in the field [77, 147]. However, an underestimation of the cell voltage becomes visible in the upper voltage regime for C-rates at and above 1C. The half-cell discharge data in Figure 4.4c indicate that this observed underestimation of the cell voltage should mainly be attributed to the cathode side. Literature in this context suggests that this deviation may be related to a sequential particle-by-particle charging and discharging mechanism rather than a homogeneous concentration increase in all particles [202]. Another study proposed an activity-based correction of the solid phase diffusion coefficient, which could improve the representation of experimental charge and discharge curves [195]. It was also shown that mechanical-electrochemical volume changes of the active material can have a substantial effect on cell performance [203, 204]. Furthermore, the utilization of the median anode and cathode particle sizes rather than their respective particle size distributions likely also contributes to the observed deviations in the discharge behavior [119, 120, 205].

Figure 4.4b shows the experimental full-cell EIS measurement and the corresponding simulated impedance spectrum, which are in excellent agreement, as evident from the highlighted frequencies. At frequencies below 0.1 Hz, an almost linear slope can be observed, which is commonly attributed to diffusion in the active material. At higher frequencies between 1 Hz and 1 kHz, a non-ideal, i.e., depressed, semicircle can be seen. These frequencies are commonly attributed to charge transfer between active material and electrolyte as well as transport through the SEI [30]. Based on the SEI understanding described in this work, a differentiation between SEI and charge transfer is not reasonable. The two dynamic processes are attributed to the SEI interfaces. As such, the SEI is inherently bound to the charge transfer, but the bulk SEI is not responsible for the observed dynamics.

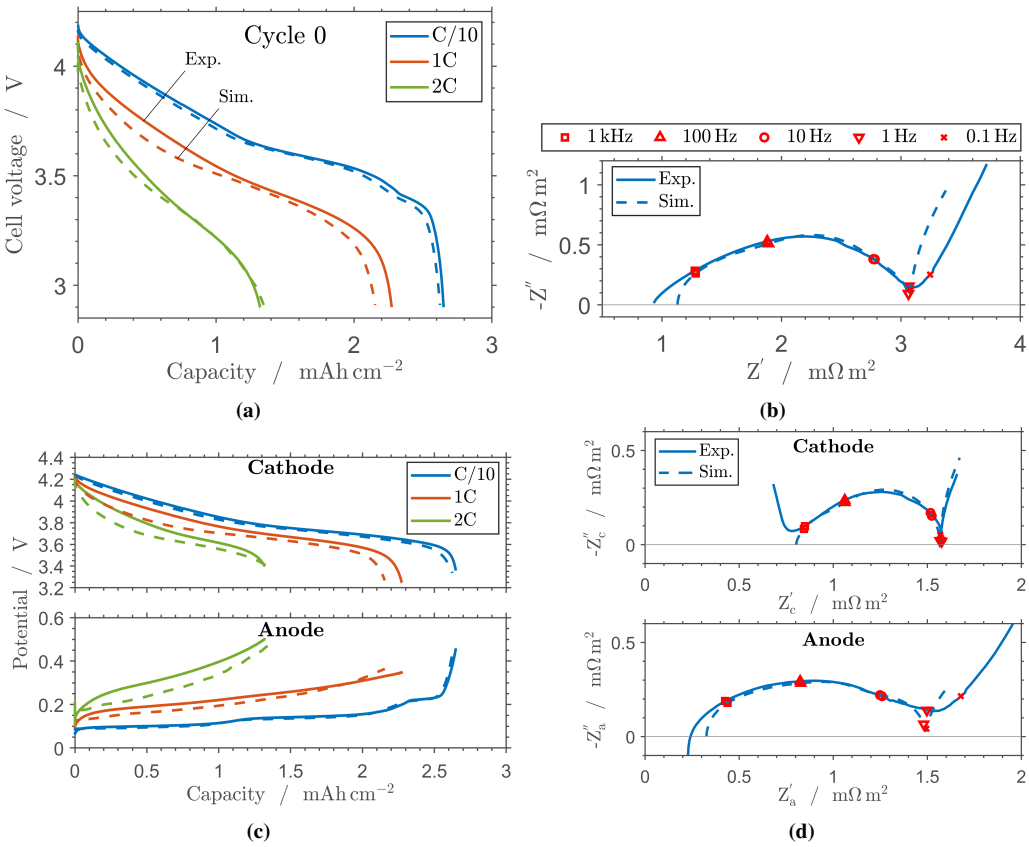

Figure 4.4: Simulations with the parameterized model (dashed line) and the experimental data (solid line) for (a) full-cell and (c) half-cell discharge curves at C/10, 1C, and 2C, and (b) full-cell and (d) half-cell impedance spectra at 3.7 V. Five frequencies are highlighted with red markers: 1 kHz (□), 100 Hz (Δ), 10 Hz (○), 1 Hz (∇), and 0.1 Hz (×).

For the interpretation of the half-cell impedance data in Figure 4.4d, it is essential to be aware of the limitations of the utilized three-electrode setup, which can sometimes show clear artifacts, like loops, in the half-cell impedance spectra [33, 34].[2] Nonetheless, the half-cell responses at medium frequencies between 1 kHz and 5 Hz are still valuable. They were used for the parameterization to distinguish between anode and cathode processes. As a result, this frequency range is reproduced very well, which indicates a successful identification of process dynamics. The

[2] Besides possible issues with electrical contacts, artifacts can originate from an inhomogeneous current distribution within the electrolyte [33, 34]. The used 220 µm thick separator helps to reduce the effect of geometric asymmetry, e.g., due to electrode misalignment. Regarding electrochemical asymmetry, the placement of the ring-shaped reference electrode around the cell assembly combined with a different impedance of anode and cathode inevitably induces a frequency-dependent distortion of the reference potential.

relatively poor representation of the lower frequency range in the full-cell and especially anode half-cell impedance suggests that the solid diffusion may not be captured accurately. The wide range of reported diffusion coefficients as a function of the intercalation degree also prevents the direct utilization of literature values, which depend on graphite type, electrode microstructure, and measurement technique [205].

The significantly depressed semicircle for the anode half-cell impedance in Figure 4.4d suggests the superposition of at least two dynamic processes. This supports modeling two independent anode processes (de-/intercalation, de-/adsorption). In contrast, the cathode half-cell impedance shows an almost perfect semicircle, which suggests one characteristic process. Here, the nearly linear impedance increase between 1 kHz and 100 Hz is related to the superposition of the dynamic response of multiple cathode particles. On the anode side, this theoretically also occurs but it is less significant due to the much higher electrical conductivity of the active material. Finally, above 1 kHz, the interface between electrode coating and current collector dominates the cell dynamics [113, 199]. However, a distinct feature for these dynamics cannot be seen in the impedance data. This renders the corresponding model parameters in this study less insightful.

Overall, the results show that the proposed model can adequately reproduce EIS measurements and discharge curves up to 2C. Consequently, the obtained parameter values are representative for this wide operational range and thus inherently more insightful than single-measurement estimates. In the following, the identified SEI parameters are discussed in detail.

The estimated SEI thickness is roughly 90 nm. This is within the range of other simulation studies on SEI growth. In a previous multiscale modeling study on SEI formation, its thickness increased to roughly 40 nm to 60 nm, depending on the applied formation current [124]. Aging studies commonly start with SEI thicknesses below 50 nm and predict SEI growth during aging beyond 100 nm [152], 300 nm [206], or even 600 nm [147]. Experimental studies commonly report values between roughly 3–100 nm [26, 102, 189]. This divergence between experiments and aging-focused simulation studies also becomes visible in the later discussed parameter estimates along aging and most likely has a systematic origin.

Model-based studies commonly resort to an approximation of the specific surface area of the active material, which is based on the assumption of perfectly spherical particles (see Appendix, Table C.1). The experimental study by Nowak et al. gives an idea of the validity of this simplification. They estimated the mass-specific surface area of different particle size distributions via the Brunauer-Emmett-Teller theory [35]. Depending on the median particle size of the sample, the estimated specific surface area is roughly three to nine times higher than the corresponding approximation with spherical particles. Such an underestimation would result in a proportional overestimation of the SEI thickness, which would explain the difference to experiments. For a quantitative parameter comparison between cells with the same electrode, this is not a problem,

as the initial microstructure is the same. With different electrodes, a comparison between SEI parameter estimates should be made with caution unless realistic surface area measurements or model-based approximations are available.

The estimated ionic conductivity of the SEI is roughly $830\,\mu S\,m^{-1}$. Practical simulation studies that target the discharge characteristics along cell aging use ionic conductivities ranging from $100\,\mu Sm^{-1}$ to $10{,}000\,\mu Sm^{-1}$ [147, 206]. Compared to studies that focus on transport properties of individual SEI components, these values are relatively high. For instance, Borodin et al. investigated lithium-ion transport in LEDC, a common organic SEI component for electrolytes containing ethylene carbonate [188]. From molecular dynamics simulations and experiments, they estimated an ionic conductivity on the order of $0.1\,\mu Sm^{-1}$. Shi et al. discussed defect thermodynamics in lithium carbonate, investigating its implications for charge transport in the SEI over a wide voltage range [190]. For the anode side, their simulations provide a potential-dependent conductivity of roughly $0.01 - 1\,\mu S\,m^{-1}$.

Clearly, the conductivity of these pure SEI components is significantly lower than the estimated ionic conductivity in this work. However, due to the multi-component nature of the SEI, the observed ohmic resistance will not be the result of just one component. Zhang et al. found that the poorly conductive LiF has a significant positive effect on the ionic conductivity of Li_2CO_3 [183]. They suggested an improvement of this parameter by two orders of magnitude. Maibach et al. investigated potential gradients at the SEI interfaces using photoelectron spectroscopy [207]. Ongoing SEI formation did not change their results significantly, suggesting a minimal potential gradient over the SEI thickness, i.e., a high ionic conductivity. Considering both the underestimation of the active surface area, i.e., the overestimation of the SEI thickness and its ionic conductivity, and the synergistic effect between different SEI components, the estimated ionic conductivity of $830\,\mu S\,m^{-1}$ points at a multi-component SEI.

Finally, the diffusion coefficient of lithium ions in the SEI was adopted from density functional theory simulations for Li_2CO_3 by Shi et al. [189]. They suggested a diffusion coefficient of roughly $10^{-11}\,m^2s^{-1}$ at 300 K. This value worked well to reproduce the experimental data in this work and did not necessitate an adjustment. However, the following parameter study reveals that this may differ for cells with other SEI properties.

4.5.2 Impact of SEI on EIS and C-Rate Performance

To gauge the importance of individual SEI properties for the overall cell behavior, a sensitivity analysis is performed for the SEI thickness, ionic conductivity, diffusion coefficient, and surface site density. In real batteries, a complex combination of multiple parameter effects is expected. For instance, not only the SEI thickness may change upon cell aging but also its composition and

structure. Similarly, different formation procedures or electrolyte additives would be expected to alter all SEI-related properties. To understand their individual contributions to the cell behavior, the four SEI parameters are analyzed separately. This also enables a rough estimation of parameter changes in experimental data without a detailed model-based analysis.

Figure 4.5 and 4.6 show the effect of these parameters on the full-cell discharge and impedance behavior, respectively. The medium values correspond to the estimated initial battery state from the previous section. The SEI thickness was found to have a relatively high sensitivity. Thus, this parameter is varied by roughly $\pm 50\,\mathrm{nm}$, whereas the other ones are varied more widely by a factor of 0.2 and 5.

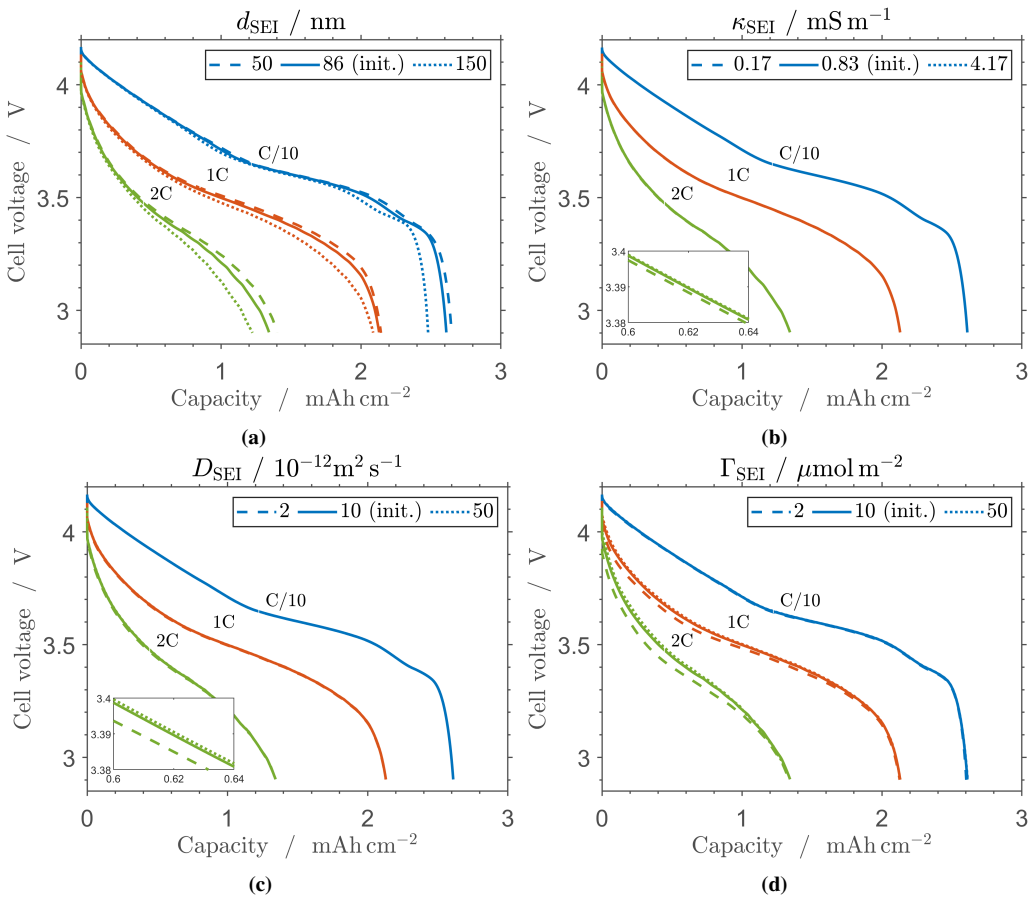

Figure 4.5: Simulated discharge curves for C/10, 1C, and 2C for variations of (a) SEI thickness, (b) ionic conductivity of the SEI, (c) diffusion coefficient of lithium ions in the SEI, and (d) SEI surface site density. The simulation of the initial battery state is shown as a reference in each plot (solid line). The simulations are performed with the same conditions as the experiments.

The SEI thickness in Figure 4.5a shows a clear effect on all investigated C-rates from C/10 to 2C. Primarily, this is due to the direct relation between SEI growth and lithium loss. In addition, SEI growth impacts mass transport in the electrolyte phase via a reduced electrode porosity, which leads to an increased tortuosity based on the Bruggeman relation. For the two SEI thickness variations of 50 nm and 150 nm, this translates into a tortuosity decrease of roughly -5% and an increase of about +9% compared to the initial state, respectively. In contrast, a significant contribution of the SEI ionic conductivity and its diffusion coefficient can be ruled out. The corresponding discharge curves in Figure 4.5b and 4.5c are almost indistinguishable even at higher C-rates without the aid of the insets. Finally, the variations of the SEI surface site density in Figure 4.5d have an effect on the cell voltage, especially at higher C-rates. The influence of this parameter on kinetics is visible right from the beginning of discharge. As such, it can be easily differentiated from the SEI thickness, which has a more pronounced effect toward the end of discharge. This delayed effect is related to mass transport limitations in the electrolyte phase and a reduced lithium inventory.

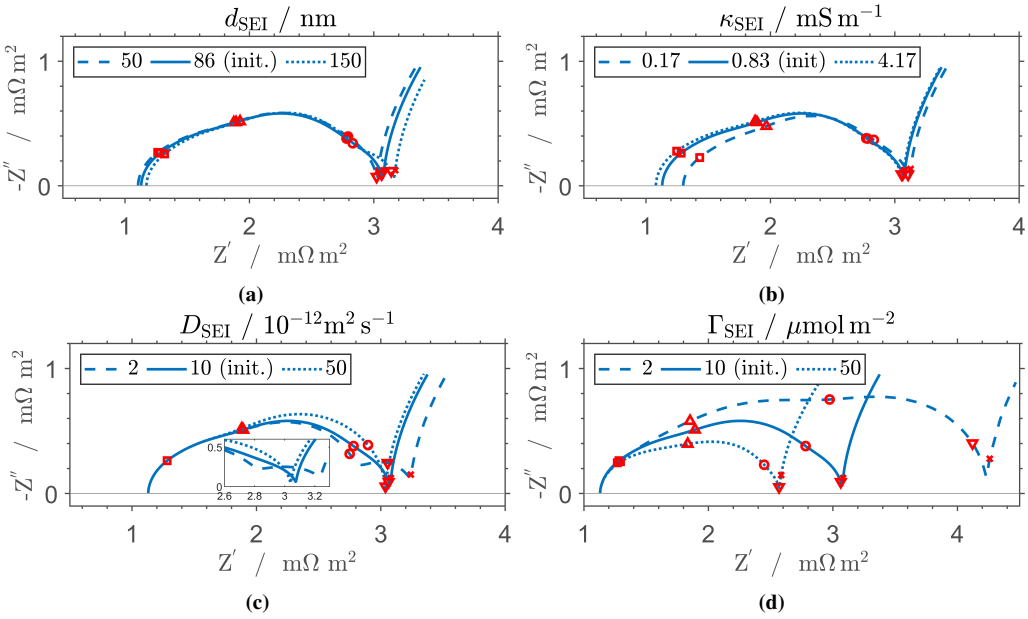

Figure 4.6: Simulated full-cell impedance spectra at 3.7 V with the parameterized model for variations of (a) SEI thickness, (b) ionic conductivity of the SEI, (c) diffusion coefficient of lithium ions in the SEI, and (d) SEI surface site density. The simulation of the initial battery state is shown as a reference in each plot (solid line). The simulations are performed with the same conditions as the experiments. Five frequencies are highlighted with red markers: 1 kHz (□), 100 Hz (Δ), 10 Hz (○), 1 Hz (∇), and 0.1 Hz (×).

In Figure 4.6a, the influence of the SEI thickness on the impedance response is analyzed. It can be seen that it mainly yields a higher impedance at the Z'-axis intercept at high frequencies and a parallel shift of the whole spectrum. This is related to its effect on the ohmic resistance of the surface film and thus the overall ohmic resistance of the cell. For comparison, equivalent circuit models commonly differentiate between the dynamics of the SEI, the dynamics of the anode charge transfer, and the ohmic resistance of the cell [113, 191, 208]. In these studies, the SEI resistance likely refers to its ohmic properties. However, it could also refer to a reaction resistance at its interface. For the model in this work, the distinction is clear: the bulk SEI does not have a capacitance. As such, its ionic conductivity does not significantly alter interfacial kinetics for reasonably chosen values.

Figure 4.6b shows the effect of the SEI ionic conductivity. Here, a lower value mostly affects the Z'-axis intercept at high frequencies without a proportional shift of the low-frequency impedance toward higher resistances. This behavior likely originates from the implementation of the SEI as a combination of two interfacial processes and one transport process across the SEI. Its conductivity affects the potentials in both the active material and the electrolyte phase (see Equation 4.4). As a result, an adjustment of this parameter inherently alters the conditions for both the intercalation reaction and the adsorption process. Common equivalent circuit models do not consider this kind of overarching effect of the SEI on adjacent processes. As discussed before, they rather separate charge transfer and SEI into two separate resistor-capacitor elements.

In Figure 4.6c, the variation of the SEI diffusion coefficient reveals a possible additional semicircle around a frequency of 1 Hz upon a decrease of this parameter. At the same time, this shifts the impedance response below 0.1 Hz to higher ohmic values. When the diffusion coefficient is increased, the time constant of the diffusion process decreases. The additional semicircle disappears. In this case, the shape of the impedance spectrum between roughly 100 Hz and 10 Hz changes and becomes less depressed, i.e., it approaches the form of a perfect semicircle. This suggests that a higher diffusion coefficient causes an overlap with kinetics. In this work, this parameter was not optimized based on experimental data but rather adopted from literature. If experiments show an additional feature around 1 Hz, an update of this parameter may become necessary [118].

Finally, Figure 4.6d shows the variation of the SEI surface site density for occupation by lithium ions. Here, a lower value creates a larger but still significantly depressed semicircle, composed of three visually distinguishable processes: cathode insertion, anode deintercalation at the solid-SEI interface, and desorption at the SEI-electrolyte interface. Here, especially the dynamic at the outer SEI interface, i.e., the de-/adsorption process, contributes to the impedance increase. A higher surface site density substantially decreases the impedance response. This is expected as this parameter has a direct effect on the interfacial reaction and process kinetics (see Equations 4.10 and 4.17).

In summary, the performed parameter study highlights that the ionic conductivity and the diffusion coefficient of the SEI have an almost negligible effect on the discharge behavior but a notable effect on the impedance spectra. In contrast, the SEI thickness and the surface site density can influence the overall cell behavior. Nonetheless, the interfacial properties of the SEI remain much more sensitive in the EIS simulations. This indicates that the interfacial and bulk properties of the SEI are less relevant for optimizing a cell's discharge performance. However, these parameters may be the key to better understanding cell aging.

The results further illustrate the importance of a multi-step parameterization strategy similar to previous works [149, 209]. For instance, the SEI thickness can be extracted from a discharge curve at a low C-rate without significant parameter interactions. If this parameter was instead extracted from an EIS measurement, the similar effect of the SEI ionic conductivity would complicate an accurate parameter estimation.

4.5.3 Impact of Aging on Cell State and SEI Properties

The results from the model-based cell diagnosis during cell aging provide in-depth insights into the underlying reasons for cell behavior changes. Understanding these degradation mechanisms lays the foundation for better aging predictions and could help to mitigate rapid cell degradation. In the following, the experimental data for aging cycles 50 and 100 are analyzed. Subsequently, the updated model parameters are discussed with respect to their contribution to the observed cell behavior changes.

Figure 4.7a and 4.7b show the experimental and the simulated discharge curves for cycles 50 and 100. The performance at cycle 0 is shown for comparison (black lines). It can be seen that the capacity at C/10 decreases significantly during the first 50 aging cycles (-5.5%). The additional capacity loss during the subsequent 50 cycles is relatively small (-1.5%). In contrast, the performance at 2C improves during the first 50 aging cycles (+5.8%) and even further during the subsequent 50 cycles (+4.7%).

The simulations capture the capacity decline at C/10 very well. The performance improvement at 2C is reproduced qualitatively by the simulation, although the total improvement is moderately underestimated. In the model, the capacity loss at low C-rates is attributed to SEI growth (see Figure 4.5a). However, a pure thickness increase would result in lower capacities also at higher C-rates, which is not observed in the measurements. The surface site density of the SEI may have increased, but the effect on the discharge capacity was small in Figure 4.5d. The remainder of the performance improvement may be attributed to improved transport in both anode and cathode.

The comparison between the full-cell EIS measurements and simulations at aging cycles 50 and 100 are shown in Figure 4.7c and 4.7d, respectively. The experimental impedance spectrum

directly after cell formation, i.e., aging cycle 0, is provided for comparison in both figures. It can be seen that the full-cell impedance decreases substantially within the first 50 aging cycles. Between cycles 50 and 100, the spectrum changes less significantly. The semicircle between roughly 1 kHz and 1 Hz only shrinks slightly, which points to kinetic improvements.

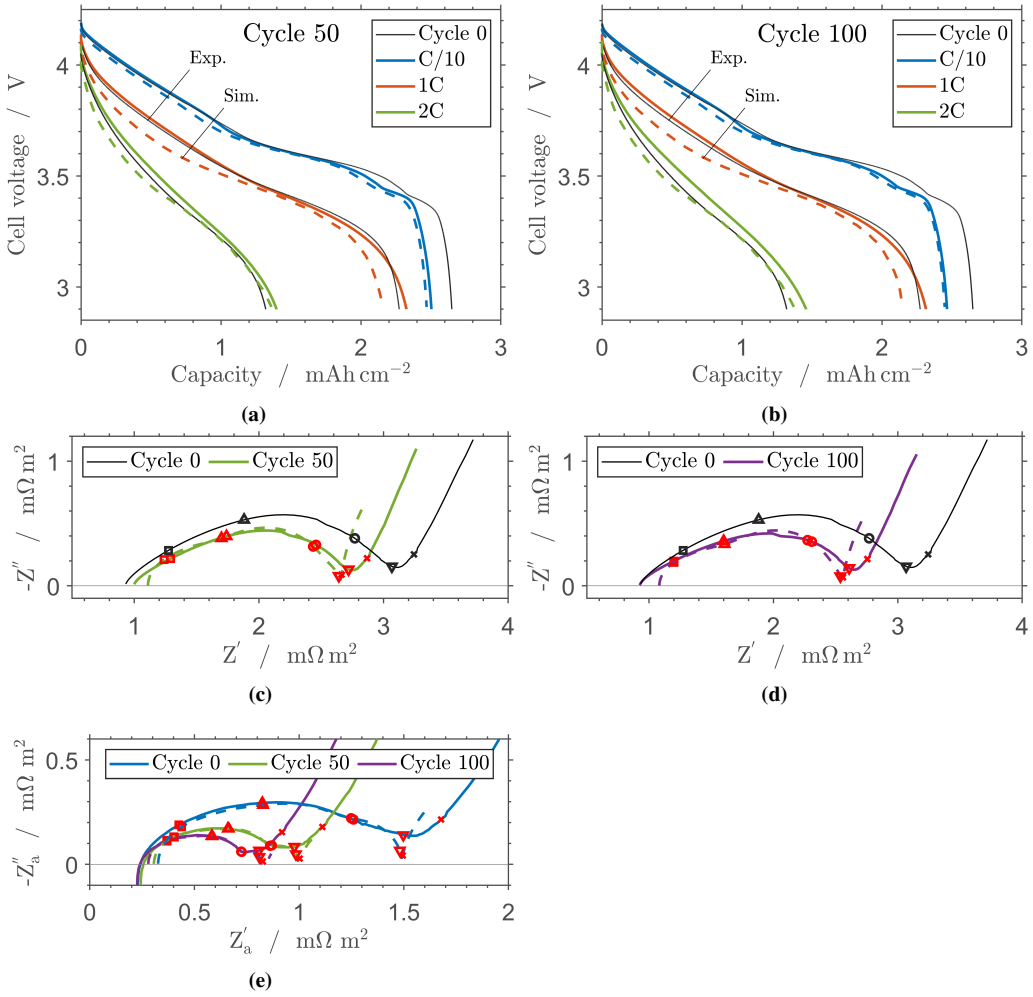

Figure 4.7: Comparison of experimental discharge curves (solid lines) and simulations after the model-based cell diagnosis (dashed lines) for (a) cycle 50 and (b) cycle 100. Experimental data for cycle 0 is shown for comparison (solid black lines). Experimental impedance spectra at 3.7 V (solid line) are compared with corresponding simulations (dashed line) for (c) cycle 50 and (d) cycle 100. The experimental data for cycle 0 is again shown with a solid black line for comparison. (e) Experimental and simulated anode half-cell impedance spectra for cycles 0, 50, and 100. Five frequencies are highlighted with red markers: 1 kHz (□), 100 Hz (Δ), 10 Hz (○), 1 Hz (∇), and 0.1 Hz (×).

To identify the origin of the impedance decline, Figure 4.7e shows the anode half-cell impedance along aging. It reveals that the anode impedance between cycles 0 and 50 decreases more rapidly than the full-cell impedance, which implies a simultaneous rise of the cathode impedance. On the anode side, the significant impedance reduction upon cycling points to substantial improvements in kinetics. A similarly strong decline of the anode half-cell impedance was observed in literature in the context of manganese poisoning of the SEI, which alters its interfacial properties [210]. However, this work uses NMC622 rather than lithium manganese oxide as the cathode active material so that manganese dissolution on the cathode side should be less of an issue [25]. Another explanation may be an evolution of its interfacial composition and structure due to the decomposition of less stable SEI components. Regarding the slight increase of the cathode impedance during cycling, both the formation of a surface layer and a surface reconstruction of the active material seem reasonable [196, 211]. A precise identification of the actual degradation mechanism would require additional experiments, like X-ray diffraction, to elucidate changes in the active material crystal structure. Although out of the scope of this work, this kind of targeted experiment cannot be substituted with a model-based cell diagnosis based on simple measurements yet.

Figure 4.8 shows the evolution of the model parameters along cell aging. As already expected based on the experimental discharge data, there is ongoing but significantly decelerating SEI growth. This explains the substantial capacity decline during the first 50 aging cycles, followed by a marginal additional decline during the subsequent 50 cycles. This trend is in good agreement with research on SEI-related capacity fade [152, 212].

The ionic SEI conductivity shows a moderate increase after 50 cycles and an even more significant rise by cycle 100. On the chemical level, the identified conductivity increase of the SEI may be related to i) a change in the SEI composition due to the decomposition of less stable and also less conductive components, like LEDC [188], or ii) a performance-enhancing doping of the SEI with synergistic components, like LiF [183].

The surface site density increases almost linearly during aging. This improves kinetics and yields a decline in anode impedance. A possible explanation for a higher surface site density is an increased surface roughness. Due to the multi-component nature of the SEI, a partial decomposition of less stable components could likely alter its structure and create a rougher surface with more available surface sites. Furthermore, the mechanical stress on the SEI due to the volume expansion of the anode active material during cycling can induce cracks in the surface film [141, 213]. Although these cracks would heal by rapidly forming new SEI, this would alter its surface structure. Alternatively, the observed improvement in kinetics could also relate to a change in interfacial species that may facilitate, e.g., electrolyte stripping [214]. As such, the increased surface site density may refer to either a larger active surface area, faster kinetics at the same surface sites, or most likely a combination of both. Again, additional experiments, like

depth profiling [215], spatial resistivity mapping [216], or imaging of the SEI [26, 217, 218], could help to identify the underlying reason for this parameter change by providing a better understanding of SEI structure and composition.

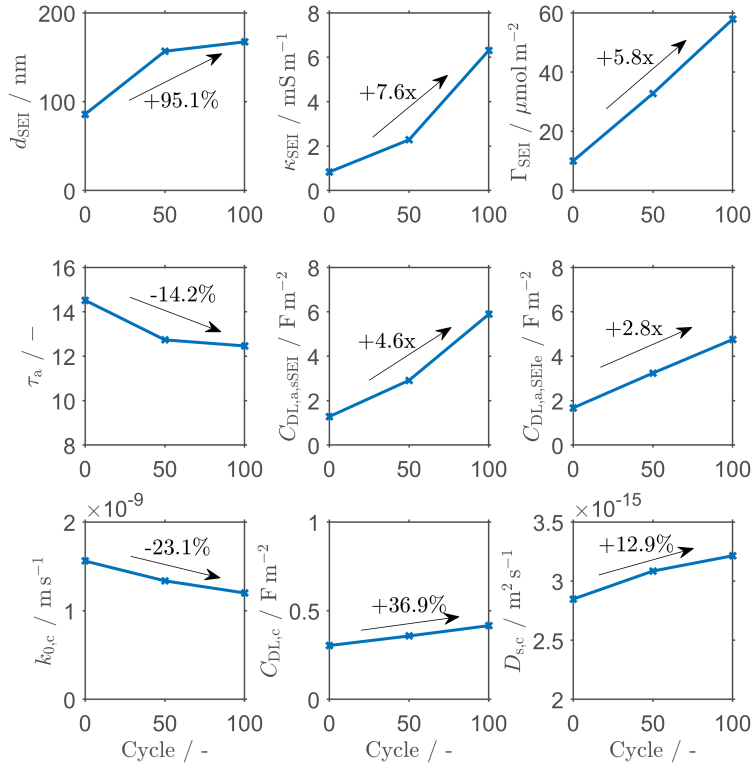

Figure 4.8: Parameter estimates from the model-based cell diagnosis along the first 100 cycles. The first row shows the evolution of the SEI thickness, its ionic conductivity, and its surface site density. The second row shows the anode tortuosity, as well as the active material-side and the electrolyte-side double-layer capacitance of the SEI. The third row shows the cathode reaction rate constant, its double-layer capacitance, and the cathode solid diffusion coefficient. The indicated relative parameter changes compare cycle 100 to cycle 0.

The anode tortuosity decreased by 14.1% during aging, suggesting improved transport in the electrolyte phase. There is a substantial decline by cycle 50 (-12.3%) and a further decline by cycle 100 (-1.8%). The SEI thickness-related reduction of the anode pore space compensates only little of this mass transport improvement. There are multiple possible explanations for the tortuosity decrease, i.e., the improvement of the effective transport properties in the anode electrolyte phase. This change may originate from i) gaseous species that are trapped within the cell and that escape over time [219], ii) a partial decomposition of less stable SEI components [26], or iii) a change in the transport properties of the electrolyte as a result of dissolved reaction products from the SEI formation. The first option could be investigated by using a different cell format,

which allows for degassing after cell formation. Changes in the microstructural properties of the anode could be explored via mercury intrusion porosimetry [35] or X-ray nano-tomography [132], which may help to detect a shift in the incremental pore volume distribution. However, maintaining the formed SEI structure during the sample preparation would be challenging. Also, the swelling of the binder upon contact with liquid electrolyte could not be considered.

Furthermore, the cell formation process may change the effective transport properties in the electrolyte phase. In this context, Ushirogata et al. proposed a near-shore aggregation mechanism based on density functional theory simulations to explain SEI formation [220]. Within this mechanism, reaction products do not directly become part of a solid surface film. Instead, they desorb, diffuse into the electrolyte phase, and form aggregates. These aggregates finally coalesce and complete the SEI formation upon contact with the electrode. However, some reaction products may still be present in the bulk electrolyte phase after the end of the cell formation process. Whereas some reaction products may only remain temporarily in the electrolyte phase until further reaction or aggregation [221, 222], others, like lithium butylene dicarbonate, may not precipitate on the electrode surface at all due to their high solubility [223]. As a result, a long-term effect of these species on lithium-ion transport in the electrolyte phase may be expected. An experimental analysis of the electrolyte after cell formation could help to pinpoint the fundamental cause for changes in the effective transport properties in the electrolyte phase.

The double-layer capacitance at the interface between SEI and electrolyte increases by a factor of about three during aging. Evaluated on its own, this would shift the time constant of the adsorption process toward higher values. However, the surface site density increases even more significantly during aging, i.e., the process resistance decreases (see Figure 4.7e). This is surprising, as capacitance is the product of surface area and specific capacitance. As a result, a proportional change in surface site density and capacitance would have been expected. It can be concluded that the specific capacitance and with it the physical nature of the double-layer, i.e., the permittivity of the SEI, must have changed.

Similar to the outer SEI interface, the double-layer capacitance at the inner interface between anode active material and SEI also increases along aging. However, it changes by a factor of about four instead of three, indicating a different SEI composition at its two interfaces. This is in good agreement with the experimentally observed two-layer structure of the SEI [215].

Finally, the cathode-related parameters are discussed. As a reminder, the cathode-side processes at the active material particle surface were simplified to one effective process, similar to common ECMs [113, 224]. A brief look at the anode and cathode half-cell impedance in Figure 4.4d underlines that this is a valid assumption for the investigated cell. The cathode impedance between 0.1 Hz and 100 Hz resembles an almost perfect semicircle, corresponding to one dynamic process. The more linear stretch at higher frequencies originates from the spatial distribution

of particle relaxations in the electrode and partially from an overlap with the contact resistance. Nonetheless, the model could be easily extended by a cathode surface film. This would be necessary, e.g., if the impedance had more similarity with a depressed semicircle, suggesting the superposition of more than one dynamic process.

As expected based on the experimental impedance data, cathode reaction kinetics deteriorate with cycling. Although the degradation decelerates slightly from cycle 50 (-14.3%) to cycle 100 (-8.8%), the trend suggests ongoing aging similar to the study by Heinrich et al. [118].

The double-layer capacitance on the cathode side increases by 17.7% from cycle 0 to cycle 50 and an additional 19.2% by cycle 100. This indicates changes in the nature of the interface between active material and electrolyte. In addition, the often discussed mechanical degradation of the active material particles may contribute to the capacitance increase via a rise in the active surface area [25, 46, 196].

The solid diffusion coefficient in the cathode active material was found to affect mainly the end of discharge. It increased by 8.3% by cycle 50 and by an additional 4.6% by cycle 100. A possible reason for this could be the formation of cracks in the active material, shortening solid diffusion pathways. However, the electron transport distance would increase at the same time, rendering the overall impact of microcracks on cell performance unclear [225]. It was also reported that a coating with Al_2O_3 during active material production improves both charge transfer and apparent solid diffusion [226]. Although this specific surface species cannot explain the estimated diffusion improvement in this work, it illustrates the possible impact of any surface film on the apparent diffusion coefficient. To determine the actual cause of this parameter change, an experimental examination of the particles' structure and surface composition would be necessary.

4.6 Concluding Remarks

This chapter presented the first physicochemical lithium-ion battery and SEI model that reproduces EIS data and discharge curves, making it suitable for detailed battery state analysis. Within this model, the SEI understanding comprises two interfacial processes connected by the bulk SEI via migration and diffusion. This explicit modeling allows to identify limiting processes and trace back changes in cell behavior to distinct cell and SEI properties.

The performed analysis highlights that SEI growth does not inevitably lead to an impedance rise. In most equivalent circuit models, the SEI resistance represents one dynamic process, lumping together the effect of SEI thickness, conductivity, and interfacial process kinetics. This prevents a precise localization of performance limitations and degradation processes. The presented model

reasonably explains a shrinking anode impedance despite ongoing SEI growth by considering changes in its interfacial processes.

The SEI thicknesses found in this and other simulation studies are systematically overestimated compared to experiments. In battery models, the specific surface area is commonly calculated for a representative spherical particle. Measurements of the specific surface area from other studies reveal much larger values, which originate from both non-uniform particle size distributions and non-spherical particle shapes. To make SEI parameter values comparable between different electrode designs, a measurement or a reliable approximation of the specific surface area is recommended.

The model-based aging analysis offers a perspective on the evolution of SEI properties after formation. It could be shown that SEI growth with its consumption of cyclable lithium and a change in electrode porosity significantly affects a cell's discharge behavior. The ionic conductivity of the SEI was found to be relatively high compared to pure SEI components, suggesting significant synergistic effects. This also means that fine-tuning the bulk SEI composition in the examined cell could not improve the discharge performance. In contrast, the interfacial characteristic of the SEI, i.e., its surface site density, significantly influences the impedance response, but it also has a distinct effect on the overpotential during discharge. Its substantial increase along aging suggests fundamental changes in the interfacial composition and structure of the SEI. Such significant changes could serve as a predictor for cell aging or even enable a better understanding of the cell formation process.

5 Effect of Fast Formation on Cell Performance[1]

The proposed model-based cell state estimation in the previous Chapter 4 enables the identification of critical cell and SEI properties with respect to cell performance and aging. As such, it is a valuable tool that can help to advance the understanding of the expensive cell formation process, i.e., the first cycling of a lithium-ion battery during cell production (see Section 2.2). Here, the common use of relatively low current densities results in long process times. In terms of cost optimization, the major challenge is to reduce the formation time without sacrificing cell quality. Various experimental studies have already shown that slow formation may neither be necessary nor beneficial for cell lifetime and performance [126, 227]. However, the fundamental cause of performance improvements after moderately fast cell formation remains unclear.

To close the knowledge gap between industry and academia, systematic research on the intricate interplay between cell formation, cell performance, and performance-defining cell properties is needed. The goal of this chapter is a better understanding of the physical effects that formation procedures have on the cell and SEI state. Specifically, an experimental formation study is performed, which is inspired by recommendations from literature. For deeper insights into the effect of formation temperature on cell performance, all formation procedures are investigated at 20 °C, 35 °C, and 50 °C. In contrast to other studies, both the fast discharge and the fast charge capability are analyzed to obtain a more comprehensive picture of the effect of cell formation. Focusing on the best-performing cell, the physicochemical cell and SEI model from Chapter 4 is utilized to identify formation-induced changes in electrode- and particle-level cell properties.

5.0.1 Cell Formation Approaches

Due to their huge impact on cell lifetime and performance, commercially used cell formation procedures and electrolyte compositions are well-protected corporate secrets [98]. Schomburg

[1] Parts of this chapter have been published in Witt, Bläubaum, Baakes, Krewer, Batteries Supercaps, e202400023, 2024 (doi: 10.1002/batt.202400023, CC BY 4.0 [17]).

et al. provide a comprehensive review on the cell formation process, highlighting the rarity of systematic variations of this cell quality-defining process step in scientific literature [228].

Various studies achieve improved cell characteristics with different formation procedures but, at first sight, surprisingly similar explanations. For example, An et al. proposed shallow formation cycling above 3.9 V, essentially avoiding full depth-of-discharge cycles and focusing on the high cell voltage regime, i.e., low anode potentials [227]. Müller et al. found a clear benefit for the constant-voltage charging step during formation, ensuring low anode potentials over an extended time [229]. Mao et al. investigated formation protocols with various C-rates [126]. They found that the best cell characteristics could be achieved neither with the fastest formation due to lithium plating nor the slowest procedure. Röder et al. investigated surface film formation at different C-rates by coupling a continuum pseudo-two-dimensional cell model with a stochastic SEI growth model [124]. They found that medium C-rates offer a trade-off between the spatial heterogeneity of the SEI at higher C-rates and the prevailing stochastic effects on SEI composition and structure at lower C-rates. Drees et al. used an equivalent circuit model to minimize the formation time while maintaining similar aging characteristics compared to a slower formation [192]. For their optimization, they considered a lower limit for the anode potential of 10 mV vs. Li/Li^+ to prevent lithium plating. Overall, these studies mirror the general understanding within the battery community that a well-protective, dense, and stable SEI is predominately formed at low anode potentials below 0.5 V or even 0.25 V vs. Li/Li^+ [103, 230, 231]. Here, fast formation seems generally favorable as long as substantial lithium plating is prevented.

Apart from production economics, which is closely related to formation time, the final cell quality must be evaluated. The capacity retention and the impedance rise along aging are often used for benchmarking different formation procedures [126, 192, 227, 229, 232]. Some studies also report the rate performance of the cells, but do not see substantial differences in discharge capacity [126, 227]. Although most applications demand a minimal recharge time to enable an almost uninterrupted mobile power supply, the fast charge capability is only rarely reported.

5.0.2 SEI Formation and Evolution

Forming a stable SEI is challenging as it is influenced by various aspects like formation conditions (current density profile, temperature, pressure), electrolyte composition, active material, and particle surface modifications [105, 233]. In general, the formation of the SEI on carbonaceous anode active material particles originates from the reductive decomposition of the electrolyte. Commonly observed SEI components after cell formation comprise inorganic species, like lithium fluoride and lithium carbonate, close to the particle surface and organic species, like lithium ethylene dicarbonate, in a more porous secondary layer [26]. However, a study on reaction products with the common electrolyte component ethylene carbonate detected only LEDC

and no lithium carbonate [234]. A complementary analysis of the SEI component LEDC revealed that its degradation leads to a more complex SEI composition and structure, including Li_2CO_3 and various organic salts [235]. Eventually, elevated formation currents could also alter the SEI composition and structure, e.g., due to concentration depletion of low-concentration electrolyte additives at the particle surface. This could trigger a transition between different SEI growth reactions.

The initially formed SEI has various vulnerabilities and weak points. It is commonly agreed upon the occurrence of further SEI growth during cell aging [118, 147, 236]. This is attributed to slowly progressing side reactions [152, 237], mechanical degradation of the surface film with a subsequent rapid SEI reformation [46], transition metal deposition in the SEI from the cathode [238], and crossover of electrolyte oxidation products from the cathode side, which degrade first the conductive salt $LiPF_6$ [239] and afterward the SEI [240]. This adds to the complexity of possible reasons for an evolution of the SEI composition and its effective properties along aging.

Elevated cell temperatures further strain the stability of the SEI and the electrolyte system. Parimalam et al. demonstrated that elevated temperatures of only 55 °C already result in the decomposition of lithium carbonate and $LiPF_6$ into CO_2, LiF, and F_2PO_2Li [241]. They repeated the study with LEDC instead of lithium carbonate and observed an even higher reactivity. The reaction products also became much more diverse in this case, including phosphates, fluorophosphates, and oligoethylene oxides. In the context of cell formation, such a thermal SEI decomposition could interfere with the formation of a robust SEI structure at elevated formation temperatures. This is not only important for the choice of an optimal formation temperature. It also suggests that large temperature gradients within a cell during formation may result in a location-dependent SEI composition and structure.

5.1 Experimental

5.1.1 Cell Setup

The cells in this work use graphite and NMC622 as the anode and cathode active materials, respectively. The electrodes were produced in the Battery LabFactory Braunschweig. They have an active material content of 93% with a final electrode porosity of 37% for the anode and 24% for the cathode [16]. All experiments were performed with the commercial PAT-Cell three-electrode setup by EL-Cell GmbH. For this setup, the electrodes were punched to a diameter of 18 mm, weighed, and dried at 120 °C under high vacuum. The subsequent cell assembly was done in an argon-filled glovebox. A polypropylene fiber/polyethylene membrane separator by

EL-Cell GmbH with an integrated lithium-metal reference electrode was used (ECC1-00-0210-V/X) to complete the three-electrode setup. The cells were filled with 100 µL electrolyte, i.e., 1 M $LiPF_6$ conducting salt in a 3:7 (v:v) solvent mixture of ethylene carbonate and ethyl methyl carbonate with 2 wt% vinylene carbonate.

5.1.2 Formation Process Variations

A complete infiltration of the porous cell structure with electrolyte is crucial for a successful cell formation. Otherwise, SEI growth and current density distribution could be highly inhomogeneous throughout the cell, leading to unpredictable cell characteristics and potential cell failure [242]. For this reason, all formation variations are preceded by a 12 h rest time. Afterward, two formation cycles are applied. All variations of formation procedure and temperature are summarized in Table 5.1. The formation with a C-rate of C/10, named F@C/10, and a temperature of 20 °C is used as a reference. The faster formation procedure, F@C/2, and the literature-inspired formation with a lower cutoff voltage of 3.7 V in the first cycle, F@C/$2_{3.7\,V}$, are added to distinguish the impact of higher formation currents and the effect of low anode potentials over an extended time, respectively [227]. Besides 20 °C, elevated formation temperatures of 35 °C and 50 °C are used to study the effect of faster reaction kinetics and transport processes on SEI formation. The higher temperatures essentially emulate notable self-heating in large-format cells without active cooling. The omission of the constant-voltage charging step could provoke the formation of an insufficiently protective SEI [229]. For this reason, all formation variations include this step in charge direction.

Table 5.1: Variations of the cell formation process regarding applied C-rate and temperature. In charge direction, a constant-voltage step with a cutoff C-rate of C/20 is added. The cutoff voltages for charge and discharge are 4.2 V and 2.9 V, respectively. The variation F@C/$2_{3.7\,V}$ without full depth of discharge uses a lower cutoff voltage of 3.7 V in the first formation cycle.

Formation procedure	**F@C/10**	**F@C/2**	**F@C/$2_{3.7\,V}$**
Temperature / °C	20, 35, 50	20, 35, 50	20, 35, 50
Charge rate in 1st cycle	C/10	C/2	C/2
Discharge rate in 1st cycle	C/10	C/2	$C/2 \geq 3.7\,V$
Charge rate in 2nd cycle	C/10	C/2	C/2
Discharge rate in 2nd cycle	C/10	C/2	C/2

5.1.3 Electrochemical Characterization

Cell formation and cycling were done with an automated MACCOR series 4000 test system. EIS measurements were conducted with a Gamry Interface 5000E potentiostat/galvanostat. All measurements were carried out in an ESPEC SU-641 temperature chamber at 20 °C or, for formation at elevated temperatures, at 35 °C and 50 °C. The C-rates for cell formation and the subsequent cell cycling are defined based on the theoretical capacity of the cathode, i.e., the weight of the individual electrodes. Two cells were assembled and tested for each formation variation.

After formation, a capacity test at a C-rate of C/10 is applied to determine the practical capacity of the cell, which is used to estimate the initial capacity loss and to approximate the initial SEI thickness. Subsequently, a characterization procedure is applied, which comprises an EIS measurement and a C-rate test at various C-rates. Afterward, the cells undergo 50 charge-discharge cycles between 2.9 V and 4.2 V, followed by the same characterization procedure as before. This combination of cycling and characterization procedure is repeated for a total of 100 cycles and three detailed electrochemical characterizations. The measurement procedure is summarized in Table D.1 in the Appendix.

5.2 Computational Methods

5.2.1 Model Setup

As shown in Chapter 4, the analysis of a broad range of operational modes is crucial for a proper parameter estimation in a P2D cell model including the SEI. The estimated parameters within the physicochemical cell and SEI model are inherently more insightful as they are valid for the discharge and impedance behavior. This ensures that processes and their impact on performance can be reliably identified, differentiating between charge transfer kinetics, SEI properties, and transport in the solid and electrolyte phase. To reveal the root cause of formation-related performance improvements, the cell and SEI model from Chapter 4 is utilized [16]. As the overall impact of cathode-side surface layer formation is generally less pronounced, it is modeled SEI-free [26].

The SEI thickness d_{SEI} is again linked to the specific surface area of the anode active material and the loss of lithium inventory. For this study, the required initial capacity loss for the calculation of the initial SEI thickness is estimated based on the charged capacity in the first formation cycle compared to the discharge capacity in the third cycle, i.e., the first cycle after cell formation. In contrast to Chapter 4, the discharge capacity in the first formation cycle cannot be used as also a formation procedure without full depth of discharge is investigated.

5.2.2 Parameterization Strategy

For a meaningful model-based cell diagnosis, the three-step parameterization strategy from the previous chapter in Section 4.3 is largely adopted for the initial cell state estimation and the parameter update along aging [16]. This strategy takes advantage of different parameter sensitivities in discharge curves and EIS measurements, using a three-electrode setup. As the same electrodes are used for all formation process variations, the electrical conductivities of the anode and the cathode are estimated once for F@C/10 at 20 °C and kept constant for all further analyses. The parameters for the dynamics at the current collectors are adopted from the study in the previous chapter.

Table 5.2: Summary of the parameterization steps, including estimated model parameters and utilized experiments for the initial model parameterization for cycle 0 and the update of aging-sensitive model parameters for cycles 50 and 100.

Step	Data	Parameters (initial)	Parameters (update)
Direct calculation	Lithium loss during formation	d_{SEI}	-
I	C/10 discharge	$c_{\mathrm{a},0}$, $c_{\mathrm{c},0}$, $c_{\mathrm{a,max}}$, $c_{\mathrm{c,max}}$	d_{SEI}, $D_{\mathrm{s,c}}$
II	1C, 2C discharge	τ_{a}, τ_{c}, $D_{\mathrm{s,c}}$	τ_{a}, τ_{c}, $D_{\mathrm{s,c}}$
III	EIS	κ_{SEI}, Γ_{SEI}, $C_{\mathrm{DL,sSEI}}$, $C_{\mathrm{DL,SEIe}}$, $k_{0,\mathrm{c}}$, $C_{\mathrm{DL,c}}$	κ_{SEI}, Γ_{SEI}, $C_{\mathrm{DL,sSEI}}$, $C_{\mathrm{DL,SEIe}}$, $k_{0,\mathrm{c}}$, $C_{\mathrm{DL,c}}$

Table 5.2 summarizes the parameters and experimental data that are considered in each parameterization step. First, the available lithium inventory after cell formation is extracted from C/10 discharge curves, comprising the SEI thickness d_{SEI} and the initial and maximum lithium concentrations in the anode ($\mathrm{c}_{0,\mathrm{a}}$, $\mathrm{c}_{\mathrm{max,a}}$) and cathode active materials ($\mathrm{c}_{0,\mathrm{c}}$, $\mathrm{c}_{\mathrm{max,c}}$). Here, the initial cell state estimation based on cycle 0 is unique as it can also use cell formation data. This enables a direct calculation of d_{SEI} based on the initial capacity loss. Higher C-rates of 1C and 2C provide insights into effective transport properties in the solid and electrolyte phase, comprising the tortuosity of anode τ_{a} and cathode τ_{c}, as well as the cathode solid diffusion coefficient $D_{\mathrm{s,c}}$. The anode solid diffusion coefficient is adopted from the study in Chapter 4 as it did not show notable sensitivity [16]. Finally, kinetic parameters and process dynamics are extracted from half-cell impedance spectra between 1 kHz and 10 Hz, including the ionic conductivity of the SEI κ_{SEI}, its surface site density Γ_{SEI}, which captures anode kinetics, its interfacial double-layer capacitances $C_{\mathrm{DL,sSEI}}$ and $C_{\mathrm{DL,SEIe}}$, the cathode reaction rate constant $k_{0,\mathrm{c}}$, and the cathode double-layer capacitance $C_{\mathrm{DL,c}}$.

The chemical potentials and Redlich-Kister coefficients related to the open circuit potentials of both electrodes are adopted from the study in Chapter 4 (see Appendix, Tables C.2 and C.3). The electrolyte properties are again approximated with empirical polynomials by Landesfeind et al. for 1 M $LiPF_6$ in EC:EMC 3:7 (w:w) [50]. The basic parameter set that is used for the simulation of all cells is given in Table C.4 in the Appendix. The adjusted model parameters for one cell each of the formation procedures F@C/10, F@C/2, and F@C/$2_{3.7\,V}$ at 20 °C are summarized in Table D.2 in the Appendix for cycles 0, 50, and 100.

All simulations were performed with MATLAB version 2021b, using the solver ode15s. The cell discretization comprises twelve representative active material particles for the anode and cathode. Each particle consists of four volume elements. The separator is divided into thirteen volume elements.

5.3 Results and Discussion

The following analysis of the cell formation study is divided in three parts. First, the effect of the applied cell formation procedure and temperature on the cell performance is analyzed. Afterward, the experimental data of the best-performing cell is analyzed in more detail to better understand the origin of the formation-induced performance improvement compared to the reference, i.e., the C/10 formation at 20 °C. Finally, model-based cell and SEI modeling is used to identify the key cell properties that lead to this enhanced cell performance.

5.3.1 Effect of Formation on Cell Performance

Figure 5.1a shows the C/10 discharge, and Figure 5.1b the 2C discharge and charge capacities for formation procedures F@C/10, F@C/2, and F@C/$2_{3.7\,V}$ and formation temperatures of 20 °C, 35 °C, and 50 °C. The slow formation F@C/10 at 20 °C is used as a reference to facilitate the comparison between the different formation variations. The discussion of higher C-rates is omitted, as charge capacities at 3C already fall below 20% of their theoretical values (see Appendix, Figure D.8). Part of this performance drop at high C-rates can be attributed to the utilized 220 µm separator in the three-electrode setup.

For C/10 discharge, it can be seen that the applied formation procedure and temperature have only a small effect on the initial capacity. For instance, the shallow formation cycling F@C/$2_{3.7\,V}$ at 20 °C shows the highest capacity in the formation study (+6%). However, the same procedure applied at 50 °C features the lowest capacity (-3%). A general trend between capacity and formation temperature independent of formation procedure cannot be observed.

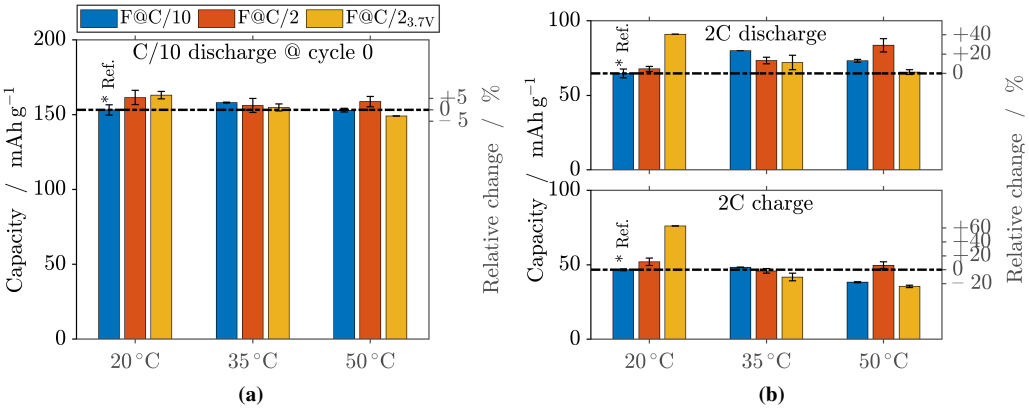

Figure 5.1: Comparison of (a) C/10 discharge and (b) 2C discharge and 2C charge capacities directly after formation as a function of formation procedure and formation temperature. The indicated standard deviations are based on two cells for each formation variation. The dashed-dotted line indicates the performance of the formation F@C/10 at 20 °C directly after formation, which is used as the reference (marked by *).

For 2C discharge, the performance differences due to formation are much more significant. Any formation variation matches or exceeds the capacity of the reference procedure. In fact, the reference procedure F@C/10 applied at formation temperatures of 35 °C and 50 °C can already offer a 24% and 13% higher capacity, respectively. However, this clearly lags behind F@C/2$_{3.7\,V}$ at 20 °C, which shows a discharge capacity improvement of 41%. Interestingly, F@C/2 at 20 °C resembles more the performance characteristics of the reference formation F@C/10. This indicates that the omission of the full depth of discharge between the first and second formation cycle is critical for superior fast discharge capability. Vice versa, the shallow formation cycling F@C/2$_{3.7\,V}$ at 50 °C just meets the reference capacity. Here, the full depth of discharge in F@C/2 seems to be beneficial, resulting in a 29% performance improvement compared to the reference.

For 2C charge, only F@C/2$_{3.7\,V}$ at 20 °C can substantially outperform the reference formation. Elevated formation temperatures seem to be disadvantageous. Some cells even perform significantly worse than the reference case. For instance, the shallow formation F@C/2$_{3.7\,V}$ at 50 °C underperforms by 24%. The slow formation F@C/10 at 50 °C shows similar losses. In contrast, the shallow formation procedure applied at 20 °C can outperform the reference formation by 63%. Similar to 2C discharge, cycling in the upper cell voltage regime seems critical. Again, F@C/2 with a full depth of discharge does not show this significant improvement. It offers only an 11% increase.

Overall, the results show that elevated formation temperatures of 35 °C and 50 °C can boost the 2C discharge performance by up to 29% while maintaining a comparable C/10 discharge capacity. Although this cannot match the 41% capacity improvement for 2C discharge of F@C/2$_{3.7\,V}$ at 20 °C, it suggests that elevated formation temperatures, e.g., by external temperature control

or self-heating in large-format cells, can offer discharge performance improvements over the slow reference formation at 20 °C. However, when the fast charge behavior is also considered, increased formation temperatures become less appealing as discharge improvements do not necessarily translate into better charge performance. This demonstrates again that the discharge capacity alone is not a reliable indicator of charge performance. Cells with similar discharge characteristics can have a strongly different fast charge capacity as shown in Chapter 3. As a result, a comprehensive understanding of the effect of cell formation is not possible based on the commonly reported discharge capacity along aging.

When An et al. reported a benefit of shallow formation cycling compared to the standard full depth-of-discharge cycling, they observed an improvement in capacity retention for cycling at 1C along 1,300 cycles and a major reduction in cell formation time [227]. To assess the onset of cell behavior changes, Figure 5.2 shows the cell characteristics for all formation variations after 100 cycles. For simplicity, this cycle count omits all cycles from the applied cell characterization procedure.

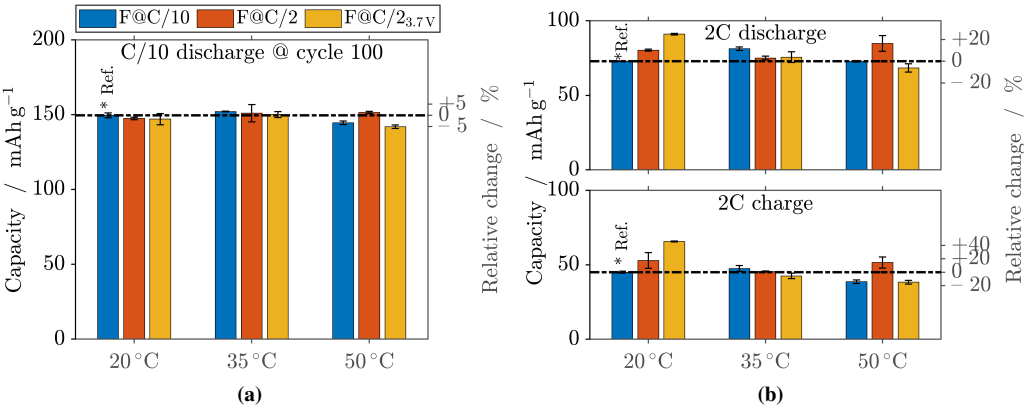

Figure 5.2: Comparison of (a) C/10 discharge and (b) 2C discharge and 2C charge capacities after 100 cycles as a function of formation procedure and formation temperature. The indicated standard deviations are based on two cells for each formation variation. The dashed-dotted line indicates the performance of the formation F@C/10 at 20 °C after 100 cycles, which is used as the reference (marked by *).

For C/10 discharge, the capacities of all cells decrease and approach roughly the same value for formation temperatures of 20 °C and 35 °C. As a result, the initially higher capacity for F@C/2$_{3.7V}$ at 20 °C is lost over the first 100 cycles. For formation at 50 °C, F@C/10 and F@C/2$_{3.7V}$ experience an even faster capacity loss and underperform the reference formation by roughly 5%.

Similar to the cell characteristics directly after cell formation, the shallow formation cycling F@C/2$_{3.7V}$ at 20 °C still outperforms for 2C discharge and charge by 25% and 46%, respectively.

Compared to the cell behavior directly after formation, the total capacity remains roughly the same for the discharge direction. However, the relative benefit is reduced because the reference performed better after 100 cycles than immediately after formation. For the charge direction, the relative benefit decreased due to an absolute decline in capacity.

Eventually, the results show that F@C/$2_{3.7\,V}$ at 20 °C is unique in delivering substantial performance benefits for both fast discharge and fast charge. Due to the overall impaired cell performance at elevated formation temperatures, the following analysis will focus on the origin of performance differences for formation at 20 °C. Possible reasons for the performance disadvantages at elevated formation temperatures are analyzed in the Appendix, Sections D.1.2 and D.1.3, considering anode half-cell potentials during formation and EIS data.

5.3.2 Detailed Experimental Analysis of Best-Performing Cell

The following discussion focuses on the best-performing cell, i.e., the cell after the shallow formation cycling F@C/$2_{3.7\,V}$ at 20 °C. Here, the comparison with the formation F@C/10 and F@C/2 at 20 °C allows to assess the effect of the applied C-rate and the depth of discharge, respectively.

Figure 5.3 shows the C-rate dependence of the cathode and anode half-cell potentials for all formation procedures. Although this does not allow for a direct quantification of differences in performance-limiting processes, it still enables a qualitative assessment of the formation impact. Importantly, the 220 µm thick separator, while reducing geometry-induced artifacts in the half-cell EIS data, is about one order of magnitude thicker than commercially relevant separators [33, 34]. This deteriorates cell performance at elevated C-rates due to extended transport pathways. The additional potential drop between the reference electrode and the anode causes an offset in the measured anode half-cell potential from the true potential at the anode surface, which is indicative of lithium plating [243]. The canonical threshold of 0 V vs. Li/Li^+ is also only a first indicator of lithium plating, considering its concentration dependence [49]. As such, the negative anode potential during 1C and 2C charge in Figure 5.3b cannot be clearly identified as lithium plating without further experiments.

The discharge capacity at C/10 in Figure 5.3 changes with formation procedure, indicating either a formation-dependent loss of lithium inventory, a change in the usable active material, or likely a combination of both. This is supported by a differential voltage analysis of the C/10 discharge data (see Appendix, Figure D.2). Herein, the characteristic features are the same for all formation procedures. However, they are visible at shifted positions, which suggests a change in the accessible active material of anode and cathode [29, 139].

For 2C discharge, notable differences in the anode and cathode half-cell potentials can be observed between the investigated formation procedures. The anode half-cell potential is notably lower and the cathode half-cell potential is significantly higher for F@C/$2_{3.7\,V}$. This suggests changes in mass transport or reaction kinetics in both electrodes.

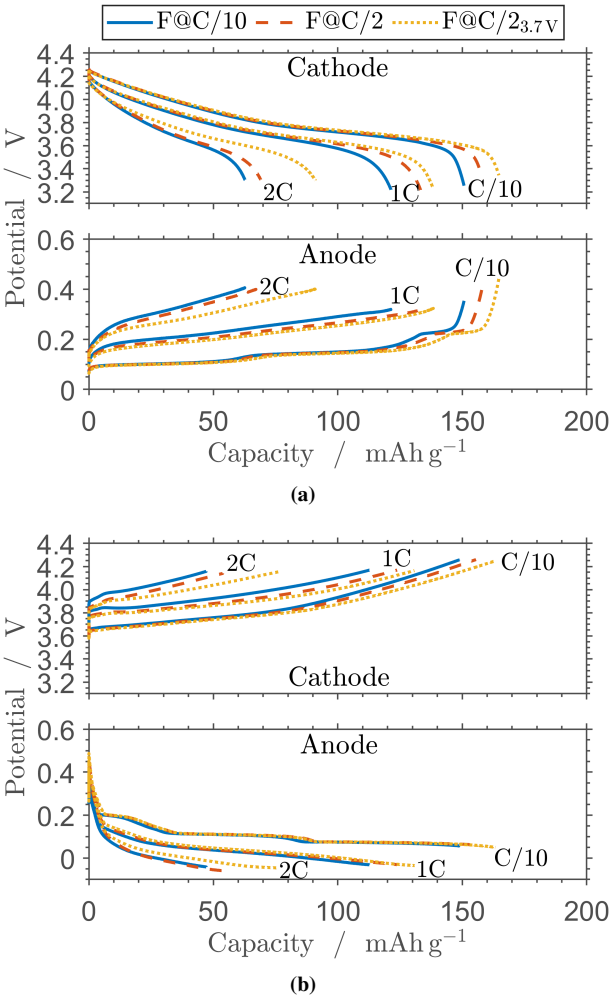

Figure 5.3: Cathode and anode half-cell data from the C-rate test directly after formation for all three formation procedures at 20 °C. The half-cell potentials are shown for C-rates of C/10, 1C, and 2C in (a) discharge and (b) charge direction.

Figure 5.3b shows the cathode and anode half-cell potential for the charge direction at C-rates of C/10, 1C, and 2C. At the lowest investigated C-rate of C/10, the deviations between the formation procedures can be seen again. At higher C-rates, differences in the cathode overpotential become

obvious. In combination with the observed differences between the formation procedures in Figure 5.3a for the discharge direction, this strongly suggests that both the anode and the cathode must have been affected by the applied formation procedure in terms of mass transport, reaction kinetics, or a combination of both.

Figure 5.4a shows the anode potential during cell formation at 20 °C as a function of time. The shallow formation cycling F@C/2$_{3.7\,V}$ takes roughly 6 h. F@C/2 features a process duration of about 8.5 h. The reference formation F@C/10 requires about 37 h. It can also be seen that the best-performing shallow formation cycling F@C/2$_{3.7\,V}$ maintains a low anode potential $<$ 200 mV for an extended time. There are multiple reasons why this potential range could be beneficial. Although SEI growth continues in the discharge direction, it is less pronounced than in the charge direction [237, 244]. By avoiding a complete discharge, SEI formation can continue at a low anode potential, which likely leads to a more dense and stable SEI [103, 230, 231]. Partially discharging reduces volume changes of the active material, and thus also mechanical stress on the newly formed SEI. This can help minimize the SEI and particle fracture probability, limiting subsequent SEI growth at such exposed surface sites [141]. Furthermore, molecular dynamics simulation studies have shown that the electrode potential significantly influences the composition of the electrolyte close to the graphite surface [245]. This likely contributes to the critical importance of the anode potential during cell formation for a well-protective yet not performance-inhibiting SEI.

Apart from SEI growth and its effect on cell performance, none of the formation variations in Figure 5.4a shows an anode potential notably below 0 V vs. Li/Li$^+$, avoiding safety-critical lithium plating [20]. However, a recent study found that small amounts of plated lithium during formation have no significant effect on thermal cell safety and capacity retention during cycling [246]. Eventually, this provides headroom for a further reduction of formation time, e.g., via a model-based fast charge optimization [192].

The anode half-cell impedance spectra in Figure 5.4b are very similar for all three formation procedures at 20 °C. Such similarity indicates a rather small effect of the formation procedure on the interfacial and bulk properties of the SEI. Yet, the cell performance was impacted by the applied formation variation. This points to formation-induced differences in effective transport properties for lithium-ions. Notable changes in anode and cathode half-cell potentials during 2C charge and discharge (see Figure 5.3), along with negligible changes in anode impedance and quite similar full-cell impedance (see Appendix, Figure D.1), support the claim of formation-induced differences in transport properties.

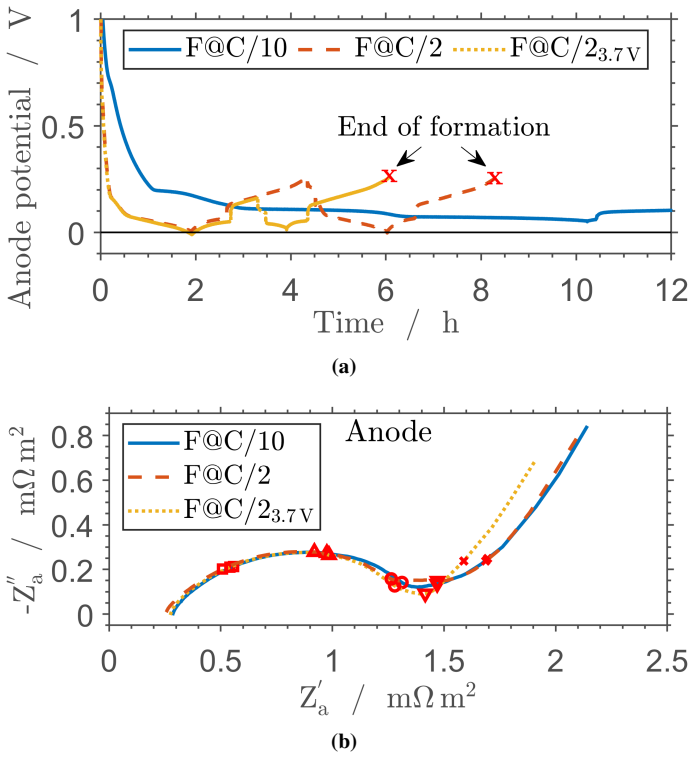

Figure 5.4: Detailed insights into different formation procedures at 20 °C. (a) Anode half-cell potentials during formation. The end of the formation procedures F@C/2 and F@C/$2_{3.7\,V}$ is highlighted with red markers. For F@C/10, the cell formation takes more than 37 hours. (b) Anode half-cell impedances at a cell voltage of 3.7 V after formation. Five frequencies are highlighted with red markers: 1 kHz (□), 100 Hz (Δ), 10 Hz (○), 1 Hz (∇), and 0.1 Hz (×).

5.3.3 Model-Based Analysis of Performance-Enhancing Cell Properties

Model-based cell diagnostics is valuable for gaining detailed insights into physically meaningful cell properties from non-destructive measurements. However, mere parameter values and their evolution along aging do not provide an intuitive understanding of why a cell behaves differently. The following discussion will start with a brief assessment of performance-sensitive model parameters. Afterward, the actual parameter values and their trend along aging are analyzed, focusing on the best-performing cell after formation F@C/$2_{3.7\,V}$ at 20 °C.

The parameters in the employed cell and SEI model can be broadly divided into five categories: i) active material-related, i.e., initial and maximum lithium concentrations, ii) transport-related, i.e., solid diffusion in the active material and transport in the electrolyte phase, iii) charge-transfer-related, i.e., kinetics at the particle and SEI surface, iv) SEI-related, i.e., SEI thickness and ionic

conductivity, and v) dynamics-related, i.e., double-layer capacitances. The earlier introduced parameterization procedure contains model parameters from all five categories. It is important to differentiate between model parameters that can be identified based on the available measurement data and those that can also explain differences in the discharge behavior. For instance, a double-layer capacitance can significantly influence the cell voltage during rapid dynamic operation in the range of 1 Hz to 100 Hz. Thus, it can be identified from EIS, but it has no impact on the 2C discharge capacity. A sensitivity analysis (see Appendix, Section D.2.1) provides a deeper understanding of the effect of individual model parameters on the discharge behavior. The following discussion will focus on those ten parameters that are notably performance-sensitive. The identified parameter values, including the ones that are not performance-sensitive, are given in Table D.2 in the Appendix. First, the initial and maximum lithium concentrations in the cathode and anode active material are analyzed. Afterward, the initial cell state and its evolution during aging are examined in terms of SEI thickness d_{SEI}, anode tortuosity τ_{a} and cathode tortuosity τ_{c}, cathode solid diffusion $D_{\mathrm{s,c}}$, and anode and cathode reaction kinetics, represented by Γ_{SEI} and $k_{0,\mathrm{c}}$, respectively.

The initial and maximum lithium concentrations in the anode and cathode active material are adjusted directly after formation based on C/10 discharge data. The estimated ratio of initial and maximum concentrations, i.e., the lithiation degrees at the beginning of discharge, is fairly similar for all formation procedures: they deviate no more than $\pm 1.6\%$ from the reference F@C/10. However, the maximum concentrations for the anode and cathode active material for F@C/$2_{3.7\,\mathrm{V}}$ are estimated to be 6.6% and 10.9% higher compared to the reference formation F@C/10, respectively. This can explain mainly the about 6% higher C/10 discharge capacity, with a similar relative improvement at higher C-rates (see Appendix, Figure D.9). As such, these parameters alone cannot explain the 41% increase in 2C discharge capacity for F@C/$2_{3.7\,\mathrm{V}}$. On the electrode level, these parameter changes suggest that more active material and thus also more lithium inventory seem to be accessible. This is supported by the differential voltage analysis of the half-cell potentials during C/10 discharge (see Appendix, Figure D.2).

In general, a smaller maximum lithium concentration in either anode or cathode active material may be related to an increased amount of active material that is isolated from the electronic or ionic network, e.g., due to blocked pores by side reaction products. However, a change in the lithiation-dependent solid diffusivity and especially its decline for high lithiation levels [247] or a change in reaction kinetics [113] could also contribute to an apparent change in the available active material. A differential voltage analysis at notably lower C-rates than C/10 would allow to reduce the effect of these processes. Additional characterization measurements, like the galvanostatic intermittent titration technique for the analysis of solid diffusivity [248], and inductively coupled plasma optical emission spectroscopy for the investigation of average cathode lithiation or even its distribution across single cathode particles [249], could help to reach a definitive

conclusion regarding the change in accessible active material. In any case, the parameter estimates highlight that both the anode and cathode are affected positively by the shallow formation procedure F@C/$2_{3.7\,\mathrm{V}}$ compared to both F@C/10 and F@C/2.

Figure 5.5 shows the six performance-sensitive model parameters for the initial and aged cell states. First, the initial cell states are explored, as understanding these will provide deeper insights into the observed formation-induced performance differences. Herein, the initial SEI thickness d_{SEI} differs among the three formation procedures, with a 20% thinner SEI for the shallow formation cycling F@C/$2_{3.7\,\mathrm{V}}$ compared to the reference F@C/10. Differences in the SEI thickness have two implications: an initial capacity loss and a change in anode porosity due to a different total SEI volume. Nonetheless, the initial differences in this parameter cannot explain a notable part of the 41% increase in 2C discharge capacity (see Appendix, Figure D.11a).

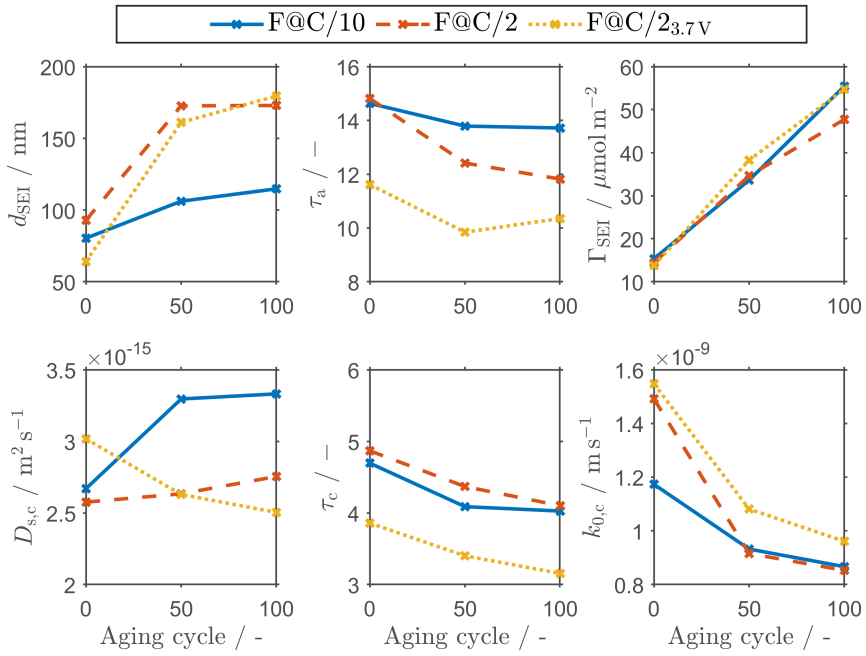

Figure 5.5: Performance-sensitive parameter estimates from the model-based cell diagnosis for all three formation procedures at 20 °C along the first 100 cycles. The first row shows the evolution of the SEI thickness d_{SEI}, the anode tortuosity τ_{a}, and the surface site density of the SEI Γ_{SEI}. Notably, τ_{a} serves as a scaling factor for effective transport properties within the anode electrolyte phase, while Γ_{SEI} maps anode reaction kinetics. The second row shows the cathode solid diffusion coefficient $D_{\mathrm{s,c}}$, the cathode tortuosity τ_{c}, which serves as a scaling factor for effective transport properties within the cathode electrolyte phase, and the cathode reaction rate constant $k_{0,\mathrm{c}}$.

The anode tortuosity τ_{a}, and thus a transport-related parameter, was found to be about 20% lower, i.e., better, for the shallow formation cycling F@C/$2_{3.7\,\mathrm{V}}$ compared to both F@C/10 and F@C/2.

If the initially formed SEI by F@C/$2_{3.7\,V}$ had either less volume in total, i.e., a higher electrode porosity, or a more favorable structure, i.e., a lower electrode tortuosity, effective transport in the electrolyte phase would improve. As such, formation-induced changes in τ_a may be seen as a secondary effect of surface film formation. Although it is not possible to pinpoint the major cause or distinguish between changes in porosity and tortuosity without additional experiments, it can be clearly stated that the effective transport properties in the anode electrolyte phase are affected by the applied formation procedure.

The anode tortuosity can explain part of the performance difference at elevated C-rates (see Appendix, Figure D.10a). Thus, it is worthwhile to discuss formation-induced tortuosity changes in more detail and relate them to findings in literature. As a surface film, the SEI inherently alters the microstructure of an electrode. For instance, a cryo-TEM study on a carbonaceous electrode found that a thin SEI nucleates at first, evolving into i) a compact SEI with a high ratio of inorganic, well-passivating components and ii) an extended SEI with a thickness of hundreds of nanometers [145]. Nano-resolution X-ray computed tomography revealed substantial microstructural changes in an anode along cycling, featuring 50% less pore volume within a cycle-aged compared to a pristine electrode from a commercial cell [250]. This change was attributed to ongoing SEI growth, i.e., the accumulation of electrolyte decomposition products within the pore volume. In silicon anodes, extensive SEI growth could also be identified as a major limitation for transport within the bulk electrolyte [251]. In graphite-silicon composite electrodes, a highly heterogeneous SEI thickness and a displacement of the carbon-binder domain by the SEI could be observed [252]. For active material with poor electrical conductivity, this may trigger a rapid performance deterioration due to the collapse of the conductive network [253]. Overall, this emphasizes the crucial role of a dense and protective SEI in ensuring consistent cell performance over the long term. If the SEI extends substantially into the bulk electrolyte, it effectively deteriorates lithium-ion transport within the pore volume. The model-based analysis of the electrochemical characterization measurements suggests strongly that the transformation of the microstructure of a pristine electrode already starts during the cell formation process, i.e., before any cycle aging.

The question remains as to why SEI growth could result in a different anode tortuosity τ_a for different formation procedures. The lower tortuosity for the shallow formation cycling F@C/$2_{3.7\,V}$ compared to the full depth-of-discharge cycles in F@C/2 may be related to the extended duration at low anode potentials, which is associated with a more stable and dense SEI [103, 230, 231]. However, minimizing the time at high anode potentials seems insufficient for a beneficial tortuosity change. Otherwise, there should be a significant difference between F@C/2 and the much slower formation procedure F@C/10. In this context, an experimental study demonstrated that the nascent SEI can be partially oxidized during discharge, leading to the decomposition into both gaseous and solid products [254]. This could explain why shallow formation cycles result

in improved cell characteristics. Without substantial oxidation and a subsequent new formation of the SEI, its initial structure could remain largely intact, potentially preventing additional SEI growth and reducing its impact on transport within the pore network. To the same end, the reduced depth of discharge causes less volume change in the active material, which could result in less mechanical stress and a lower fracture probability for the nascent SEI during formation.

The surface site density of the SEI Γ_{SEI}, which maps anode reaction kinetics, deviates slightly between the formation procedures. The parameter is 6% lower for F@C/2 and about 10% lower for F@C/$2_{3.7\,\mathrm{V}}$ compared to the reference formation. However, a deviation of this magnitude has a negligible effect on the discharge performance (see Appendix, Figure D.11c), and thus cannot explain formation-induced performance deviations. This was already expected from the similar anode half-cell impedance in Figure 5.4b. Combined with the differences in anode tortuosity, this supports the common understanding of the SEI as a two-layer structure with a more porous and organic outer layer and a predominately dense and inorganic layer at the particle surface [181, 215, 255]. If the outer SEI layer was sufficiently porous, lithium-ion transport would resemble that of the bulk electrolyte phase. In that case, only the inner layer of the SEI would be visible in EIS measurements as no charge transfer reaction would take place at the outer SEI layer. This could explain differences in electrolyte-level transport and yet allow for similar anode reaction kinetics.

On the cathode side, the solid diffusion coefficient $D_{\mathrm{s,c}}$ is about 13% higher for the shallow formation cycling F@C/$2_{3.7\,\mathrm{V}}$ and about 4% lower for F@C/2 compared to F@C/10. Similar to the anode tortuosity, the critical factor for an improvement does not seem to be the applied C-rate. Otherwise, F@C/2 and F@C/$2_{3.7\,\mathrm{V}}$ should feature similar parameter values. Instead, the omission of the full depth of discharge, and thus an extended uninterrupted duration at high potentials, seems critical for improved solid diffusivity. This could be attributed, e.g., to beneficial changes in the grain boundaries, which are essential for the effective diffusivity inside the active material particles [256], or a change in surface film composition and porosity, which may affect transport into the underlying active material [48, 190]. Mechanical degradation of the active material particles is unlikely to contribute notably to changes in the solid diffusivity as it develops over hundreds of cycles [46, 257]. A clear identification of the primary cause for the diffusion improvement is not possible based on the performed experiments. Nonetheless, this parameter has a notable effect on the observed differences in the 1C and 2C discharge capacity (see Appendix, Figure D.10d). A publication on coated cathode active material used the suitable term "apparent diffusion coefficient", which summarizes well that multiple factors affect its value beyond bulk diffusion [226].

The cathode tortuosity τ_{c} was also affected by the applied formation procedure. The values for F@C/10 and F@C/2 are fairly similar, with a less than 4% higher tortuosity for F@C/2. The shallow formation without full depth of discharge F@C/$2_{3.7\,\mathrm{V}}$ features an 18% lower tortuosity,

which indicates beneficial changes in the microstructure of the cathode. Changes of this magnitude have a significant effect on the discharge performance at 2C but only a small effect at 1C (see Appendix, Figure D.10b). This highlights that cell formation affects not only particle-level transport, i.e., solid diffusivity, but also electrode-level transport, i.e., electrode tortuosity. As the investigated formation procedures comprise only two cycles at moderate C-rates of up to C/2, substantial particle cracking and a corresponding change in electrode microstructure, like during cycle-aging, would not be expected [47]. This points all the more at a different surface film formation on the cathode side. In general, a higher cell voltage promotes electrolyte decomposition and thus surface film formation [258, 259]. However, it has also been reported that the cathode surface film growth during discharge was much more pronounced compared to maintaining a high voltage [260]. This may explain part of the benefit of the shallow formation cycling. Furthermore, cross-talk between anode and cathode may affect the final surface film properties [259]. As such, the improved cathode tortuosity for F@C/2$_{3.7\,\mathrm{V}}$ may be no coincidence, considering the equally beneficial anode tortuosity. In this context, a study on fast charging demonstrated that an artificial SEI on graphite could substantially improve the long-term capacity retention [52]. This also poses the question of whether the improved aging behavior and performance in their study originated only from improved anode properties or also a lack of cross-talk between anode and cathode due to the artificial SEI. Eventually, the performed C-rate tests and EIS data in this work cannot answer i) if only the extended uninterrupted duration at high cathode potentials or ii) if also the favorable SEI formation on the anode side causes the significantly improved cathode performance.

The cathode reaction rate constant $k_{0,\mathrm{c}}$ is lowest for the reference formation. It is about 27% and 32% higher for F@C/2 and F@C/2$_{3.7\,\mathrm{V}}$, respectively. This could imply a larger electrochemically active surface area or an altered surface composition. However, parameter differences of this magnitude have only a small effect at elevated C-rates, primarily influencing the cell voltage and not the discharge capacity (see Appendix, Figure D.11d).

Finally, the parameter changes during aging are discussed. The SEI growth continues for cycles 50 and 100, but it seems to decelerate substantially between cycle 50 and 100 for F@C/2 and F@C/2$_{3.7\,\mathrm{V}}$. The slow formation F@C/10 shows a much smaller increase in SEI thickness, which suggests a better passivating SEI. However, this seemingly better passivation capability was achieved with a higher initial capacity loss.

Apart from an increase of the SEI thickness, steady improvements in anode reaction kinetics (Γ_{SEI}) suggest an ongoing transformation of this surface film. However, this improvement has only a marginal effect on the cell voltage during fast discharge, yet it is clearly identifiable from the anode half-cell impedance data. Similar changes take place for the not performance-limiting double-layer capacitances at the inner and outer interface of the SEI ($C_{\mathrm{DL,sSEI}}$, $C_{\mathrm{DL,SEIe}}$), which support the expectation of either an increase in electrochemically active surface area, e.g., due

to particle cracking [261], or a change in SEI composition and structure. Such surface film alterations could originate from the further reduction of SEI components [26] or cross-talk with electrolyte oxidation products from the cathode [240, 262]. A partial surface film decomposition could also explain the decrease of the anode tortuosity for all cells between cycle 0 and 50. Although this trend continues between cycle 50 and 100 for F@C/10 and C/2, the anode tortuosity for F@C/$2_{3.7\,\mathrm{V}}$ already increases slightly. Given the better charge and discharge performance for F@C/$2_{3.7\,\mathrm{V}}$, aspects like the total charge throughput during cycling may contribute to the observed parameter increase. Given the absence of a consistent parameter trend for all formation procedures over 100 cycles, conducting extended cycling experiments becomes even more important to assess the long-term effect of cell formation on dominant aging mechanisms.

The trend for the cathode solid diffusivity $D_{\mathrm{s,c}}$ is unique for each cell. It improves between cycle 0 and 100 by about 25% for F@C/10 and 7% for F@C/2, but it declines about 18% for F@C/$2_{3.7\,\mathrm{V}}$. As already discussed for the initial cell state, the utilized model cannot pinpoint the root cause for changes in the apparent solid diffusivity using discharge curves and impedance data. An in-depth understanding of the long-term effect of cell formation on the aging behavior would require further experiments. A detailed characterization of the surface species [48] and an analysis of the mechanical degradation of the active material particles would be especially relevant [257].

The cathode tortuosity τ_{c} decreases, i.e., improves, by at least 20% for all cells during aging. Similar to the anode tortuosity, imaging techniques, like nano-resolution X-ray computed tomography, could help to advance the understanding of the root cause of this improvement [250]. Furthermore, by using a cross-talk blocking separator, it would be possible to discriminate the impact of electrode cross-talk from the intrinsic effect of the formation process on transport processes within the cathode [263]. A detailed analysis of changes in the electrolyte composition could provide further insights [264].

In contrast to the anode, the cathode reaction rate constant $k_{0,\mathrm{c}}$ deteriorates for all formation procedures during cycling. Independent of the initial value, it seems to asymptotically approach a similar value for all formation procedures after 100 cycles. This suggests that the electrochemically active surface of the cathode particles may have reached a more equilibrated chemical or mechanical state.

Overall, the study revealed a multitude of changes in parameters due to formation but also aging. This raises several intriguing questions about the underlying causes and invites further analysis, as suggested above. Moreover, it is important to note that 100 cycles only mark the beginning of cell aging. Further experiments over the full lifetime and in a commercially-relevant cell format are necessary to verify if, or rather how long, the estimated parameter trends continue and how long the fast charge/discharge benefit of the shallow formation F@C/$2_{3.7\,\mathrm{V}}$ at 20 °C is maintained.

High-precision coulometry could prove to be a valuable tool for the rapid screening of formation protocols to assess aging within weeks instead of months [265].

5.4 Concluding Remarks

In this chapter, a substantial impact of the applied cell formation procedure and temperature on the fast charge/discharge capability of NMC622|Graphite cells was revealed. For elevated formation temperatures of 35 °C and 50 °C, some formation procedures were able to outperform the reference formation F@C/10 at 20 °C in terms of 2C discharge capacity by up to 29%. However, for 2C charge, these formation variations fell short of, let alone exceed, the performance of this reference. This implies that a formation temperature of 20 °C is essential to realize well-balanced performance characteristics with the investigated cell chemistry and design, underscoring the significance of this process parameter.

The experiments revealed that shallow formation cycling F@C/$2_{3.7\,\mathrm{V}}$ at 20 °C can boost the cell performance for 2C discharge and 2C charge by 41% and 63%, respectively. With a full depth of discharge, the formation procedure F@C/2 did not show significant performance gains. This suggests that the extended, uninterrupted time at a low anode potential, a high cathode potential, or a combination of both is critical for superior performance. Eventually, this adds to the reported benefit of the time-efficient shallow formation procedures by An et al., who demonstrated better capacity retention during long-term cycling [227].

The model-based analysis of the best-performing cell after formation with F@C/$2_{3.7\,\mathrm{V}}$ at 20 °C and its differences to the other formation procedures provided deeper insights into potential structural changes within the cell. It could be shown that its performance benefit originated from both the anode and the cathode. Notably, the initial SEI thickness and anode reaction kinetics were similar for all investigated formation procedures. Cathode reaction kinetics improved, but did not substantially alter the 2C discharge capacity. Instead, improved effective transport in the anode and especially the cathode electrolyte phase in combination with an enhanced cathode solid diffusivity were identified as the primary drivers for the superior cell performance.

The anode-side transport improvement may be related to a different structure or composition of the SEI. Here, the shallow formation cycling may allow for SEI growth with a reduced impact on the electrode microstructure: low anode potentials favor the formation of a dense and stable SEI, and incomplete discharge may minimize the mechanical stress and the reported restructuring of the formed SEI. For the cathode, improved effective transport properties in the solid and electrolyte phase may also be attributed to a beneficial surface film formation. Eventually, further research will be necessary to expand the understanding of surface film growth on the cathode side, comprising half- and full-cell studies on cross-talk between anode and cathode for different

formation procedures and electrolyte compositions. Here, using a cross-talk blocking separator may prove insightful [263].

In terms of cell degradation, the model-based cell diagnosis highlighted that some cell properties, like the SEI thickness and anode tortuosity, still evolve after formation but stabilize between cycles 50 and 100. Other parameters, like the surface site density of the SEI, display a fairly steady increase. Utilizing the presented model provided deep and unparalleled insights into formation-induced performance changes, circumventing the necessity for non-electrochemical, destructive measurements. While the model serves as a potent diagnostic aid, it is imperative to recognize the intricate effects of cell formation on both performance and aging. Understanding the long-term impact of different cell formation conditions, coupled with their knowledge-driven optimization, remains a complex endeavor. The sampling efficiency of data-driven optimization approaches might offer an edge in navigating this complexity [60].

6 Conclusion and Outlook

This thesis showcased the value of physicochemical modeling for holistic cell design optimization and non-destructive cell diagnostics. In both cases, the detailed modeling of transport processes and kinetics allows for the identification of performance bottlenecks in a lithium-ion battery, providing a sound basis for targeted improvements. Application-tailored cell design is the first step to enhance the utilization of expensive active materials. While optimal cell design lays the foundation for superior performance, the final cell behavior is notably influenced by cell production. Model-based cell diagnostics can provide deeper insights into the cell state based on non-destructive C-rate tests and EIS data. For instance, this approach allows to analyse the effect of different cell formation conditions on SEI properties and effective transport properties within an electrode, which are embedded in the cell behavior but difficult to measure directly. Although parameter estimates cannot explain the underlying reason for changes in the cell state, they can help to reveal performance bottlenecks. The formation process in particular presents a unique opportunity for improvement as it significantly affects cell quality and cost, and yet, the understanding of its process-product interdependencies is still limited.

The design of optimal electrodes for lithium-ion batteries is a complex task due to the variety of design options, application scenarios, and benchmark systems. Chapter 3 provided a perspective on the myth of a universal electrode design optimum for best-in-class charge and discharge performance. The performed parameter screening demonstrated that best-in-class fast discharge and fast charge performance could not be achieved with the same cell design. Furthermore, it illustrated the challenge of a general assessment of the benefit of two- over single-layer electrodes as the benefit will depend on the parameter screening granularity. This is especially critical for resource-limited experimental studies, highlighting the benefit of combined model-based and experimental cell design exploration and optimization. To facilitate a holistic assessment of the merits of different cell designs, the categorical reporting of both discharge and charge performance for practically relevant C-rates is highly recommended. The results further revealed the possibility of performance plateaus, where broad design parameter ranges yield similar performance characteristics. Considering the cost of tight production tolerances, the effect of production uncertainties on the resulting cell performance variance should already be considered during the cell design phase.

Chapter 4 shifted focus from optimal cell design to detailed cell diagnostics. A pseudo-two-dimensional cell model was extended by an SEI model to gain deeper insights into the effect of this intricate surface film on the cell behavior. The performed cell state estimation for an NMC622|Graphite cell indicated a minor effect of the bulk and interfacial properties of the SEI on the discharge behavior but a significant effect on the impedance response. In contrast, the SEI thickness and the improvement of the anode tortuosity after cycling affected the discharge performance. As such, SEI-induced changes in electrode microstructure and loss of lithium inventory are likely more promising for performance improvements than bulk and interfacial SEI properties. Eventually, model-based cell diagnostics facilitate the interpretation of experimental data by tracing back behavioral changes to individual model parameters. Steady improvements, e.g., in anode reaction kinetics, and a seeming stabilization of other parameters, such as SEI thickness and anode tortuosity, during the first 100 cycles exemplify the potential for a better understanding of cell degradation. At the same time, they illustrate the challenge of predicting long-term cell behavior based on a limited scope of experimental data.

Chapter 5 investigated the effect of different cell formation procedures and temperatures on cell performance. Whereas temperatures of 35 °C and above could offer improved fast discharge performance compared to a standard C/10 formation at 20 °C, their fast charge capability did not improve or even deteriorate. This suggests that fast formation of large-format cells without active cooling may result in suboptimal cell performance due to self-heating. In contrast, shallow formation cycling without full depth of discharge at a C-rate of C/2 and 20 °C improved the 2C discharge and charge capacities by up to 41% and 63%, respectively, while reducing the formation time by over 80%. Formation at a C-rate of C/2 with full depth of discharge could not offer this level of improvement. Consequently, the right combination of formation procedure and temperature was critical for overall cell performance improvements. The subsequent model-based cell diagnosis of the cell formation procedures at 20 °C revealed that the performance improvements are driven by changes in the anode and cathode, comprising improved effective transport properties in the anode and cathode electrolyte phase, a higher cathode solid diffusivity, and a lower initial capacity loss. As such, focusing on the formation of a dense SEI layer in the anode is insufficient for a comprehensive understanding and, ultimately, optimization of the cell formation process.

This thesis highlighted the value of physicochemical modeling in identifying performance bottlenecks in lithium-ion cells. With improvements in computational resources and algorithms, future cell design studies may go beyond homogenized models with their effective electrode properties and directly utilize 3D microstructure-resolved models. Here, integrated simulations of multiple production steps, like electrode coating, drying, and calendering, may evolve into a comprehensive framework for combined cell design and production optimizations [266]. In terms of model-based cell diagnostics, this thesis focused on a better understanding of the effect of the

formation process on cell performance. However, the presented approach is generally agnostic to the underlying process changes. Future experimental studies on other processes, such as mixing and calendering, may find that model-based cell diagnostics can provide valuable insights into how performance bottlenecks shift in response to process changes. Nonetheless, identifying the fundamental reason for changes in the underlying cell properties remains difficult based on electrochemical characterization data. For instance, differences in effective transport properties as a function of cell formation conditions were attributed to changes in surface film formation in Chapter 5. Experimental methods, such as nano-resolution X-ray computed tomography [250] and cryogenic transmission electron microscopy [145], may help to understand the actual effect of surface film formation on electrode porosity and tortuosity. In the end, experimental studies will remain essential until SEI growth models with a broad validity range are available [124, 267]. A rapid and comprehensive optimization of the formation process may be realized, e.g., by combining an early prediction model for cycle life with a Bayesian optimization algorithm [60]. Model-based cell diagnostics could help identify critical parameters for optimization, shedding light also on the potential value of an artificial SEI [52].

Bibliography

[1] G. Bridge and E. Faigen, "Towards the lithium-ion battery production network: Thinking beyond mineral supply chains," *Energy Res. Soc. Sci.*, vol. 89, p. 102659, 2022.

[2] D. J. Wuebbles, D. W. Fahey, K. A. Hibbard, D. J. Dokken, B. C. Stewart, and T. K. Maycock, Eds., *Climate Science Special Report: Fourth National Climate Assessment, Volume I*. Washington, DC, USA: U.S. Global Change Research Program, 2017.

[3] H. Ritchie and M. Roser, "Energy," 2021, accessed September 29, 2022. [Online]. Available: ourworldindata.org/energy

[4] S. Farhad and A. Nazari, "Introducing the energy efficiency map of lithium-ion batteries," *Int. J. Energy Res.*, vol. 43, no. 2, pp. 931–944, 2019.

[5] H. Ritchie, M. Roser, and P. Rosado, "CO_2 and Greenhouse Gas Emissions," 2020, accessed September 28, 2022. [Online]. Available: https://ourworldindata.org/co2-and-other-greenhouse-gas-emissions

[6] IEA, "Transport sector CO_2 emissions by mode in the Sustainable Development Scenario, 2000-2030," Paris, 2022, accessed August 23, 2022. [Online]. Available: https://www.iea.org/data-and-statistics/charts/transport-sector-co2-emissions-by-mode-in-the-sustainable-development-scenario-2000-2030

[7] O. A. Hjelkrem, P. Arnesen, T. Aarseth Bø, and R. S. Sondell, "Estimation of tank-to-wheel efficiency functions based on type approval data," *Appl. Energy*, vol. 276, p. 115463, 2020.

[8] X. Liu, A. Elgowainy, R. Vijayagopal, and M. Wang, "Well-to-Wheels Analysis of Zero-Emission Plug-In Battery Electric Vehicle Technology for Medium- And Heavy-Duty Trucks," *Environ. Sci. Technol.*, vol. 55, no. 1, pp. 538–546, 2021.

[9] M. Prussi, M. Yugo, L. De Prada, M. Padella, and M. Edwards, *JEC Well-To-Wheels report v5*. Luxembourg: Publications Office of the European Union, 2020.

[10] S. Schiebahn, T. Grube, M. Robinius, V. Tietze, B. Kumar, and D. Stolten, "Power to gas: Technological overview, systems analysis and economic assessment for a case study in Germany," *Int. J. Hydrogen Energy*, vol. 40, no. 12, pp. 4285–4294, 2015.

[11] X. Li, P. Anderson, H. R. M. Jhong, M. Paster, J. F. Stubbins, and P. J. Kenis, "Greenhouse Gas Emissions, Energy Efficiency, and Cost of Synthetic Fuel Production Using Electrochemical CO_2 Conversion and the Fischer-Tropsch Process," *Energy Fuels*, vol. 30, no. 7, pp. 5980–5989, 2016.

[12] V. Batteiger, P. Schmidt, K. Ebner, A. Habersetzer, L. Moser, W. Weindorf, and T. Rakscha, "Power-to-Liquids: A scalable and sustainable fuel supply perspective for aviation," 2022, accessed September 29, 2022. [Online]. Available: https://www.umweltbundesamt.de/en/publikationen/power-to-liquids

[13] R. Martins, H. C. Hesse, J. Jungbauer, T. Vorbuchner, and P. Musilek, "Optimal component sizing for peak shaving in battery energy storage system for industrial applications," *Energies*, vol. 11, no. 8, 2018.

[14] W. Chen, Y. Jin, J. Zhao, N. Liu, and Y. Cui, "Nickel-hydrogen batteries for large-scale energy storage," *Proc. Natl. Acad. Sci. U. S. A.*, vol. 115, no. 46, pp. 11 694–11 699, 2018.

[15] D. Witt, D. Wilde, F. Baakes, F. Belkhir, F. Röder, and U. Krewer, "Myth and Reality of a Universal Lithium-Ion Battery Electrode Design Optimum: A Perspective and Case Study," *Energy Technol.*, vol. 9, no. 6, p. 2000989, 2021.

[16] D. Witt, F. Röder, and U. Krewer, "Analysis of Lithium-Ion Battery State and Degradation via Physicochemical Cell and SEI Modeling," *Batteries Supercaps*, vol. 5, no. 7, p. e202200067, 2022.

[17] D. Witt, L. Bläubaum, F. Baakes, and U. Krewer, "Origin of performance improvements in lithium-ion cells after fast formation," *Batteries Supercaps*, p. e202400023, 2024.

[18] P. Zhu, D. Gastol, J. Marshall, R. Sommerville, V. Goodship, and E. Kendrick, "A review of current collectors for lithium-ion batteries," *J. Power Sources*, vol. 485, p. 229321, 2021.

[19] V. S. Bagotsky, A. M. Skundin, and Y. M. Volfkovich, *Electrochemical Power Sources*. Hoboken, NJ, USA: John Wiley & Sons, Inc., 2014.

[20] T. Waldmann, B. I. Hogg, and M. Wohlfahrt-Mehrens, "Li plating as unwanted side reaction in commercial Li-ion cells – A review," *J. Power Sources*, vol. 384, pp. 107–124, 2018.

[21] S. Chen, F. Dai, and M. Cai, "Opportunities and Challenges of High-Energy Lithium Metal Batteries for Electric Vehicle Applications," *ACS Energy Lett.*, vol. 5, no. 10, pp. 3140–3151, 2020.

[22] C. Zhang, F. Wang, J. Han, S. Bai, J. Tan, J. Liu, and F. Li, "Challenges and Recent Progress on Silicon-Based Anode Materials for Next-Generation Lithium-Ion Batteries," *Small Struct.*, vol. 2, no. 6, p. 2100009, 2021.

[23] M.-T. F. Rodrigues, S. E. Trask, I. A. Shkrob, and D. P. Abraham, "Quantifying gas generation from slurries used in fabrication of Si-containing electrodes for lithium-ion cells," *J. Power Sources*, vol. 395, pp. 289–294, 2018.

[24] C. Xu, Q. Dai, L. Gaines, M. Hu, A. Tukker, and B. Steubing, "Future material demand for automotive lithium-based batteries," *Commun. Mater.*, vol. 1, no. 1, p. 99, 2020.

[25] T. Li, X.-Z. Yuan, L. Zhang, D. Song, K. Shi, and C. Bock, "Degradation Mechanisms and Mitigation Strategies of Nickel-Rich NMC-Based Lithium-Ion Batteries," *Electrochem. Energy Rev.*, vol. 3, no. 1, pp. 43–80, 2020.

[26] S. J. An, J. Li, C. Daniel, D. Mohanty, S. Nagpure, and D. L. Wood, "The state of understanding of the lithium-ion-battery graphite solid electrolyte interphase (SEI) and its relationship to formation cycling," *Carbon*, vol. 105, pp. 52–76, 2016.

[27] T. Waldmann, R. G. Scurtu, K. Richter, and M. Wohlfahrt-Mehrens, "18650 vs. 21700 Li-ion cells – A direct comparison of electrochemical, thermal, and geometrical properties," *J. Power Sources*, vol. 472, p. 228614, 2020.

[28] R. Korthauer, Ed., *Handbuch Lithium-Ionen-Batterien*. Berlin, Heidelberg: Springer Berlin Heidelberg, 2013.

[29] M. Lewerenz, A. Marongiu, A. Warnecke, and D. U. Sauer, "Differential voltage analysis as a tool for analyzing inhomogeneous aging: A case study for $LiFePO_4$|Graphite cylindrical cells," *J. Power Sources*, vol. 368, pp. 57–67, 2017.

[30] J. P. Schmidt, T. Chrobak, M. Ender, J. Illig, D. Klotz, and E. Ivers-Tiffée, "Studies on $LiFePO_4$ as cathode material using impedance spectroscopy," *J. Power Sources*, vol. 196, no. 12, pp. 5342–5348, 2011.

[31] U. Krewer, F. Röder, E. Harinath, R. D. Braatz, B. Bedürftig, and R. Findeisen, "Review—Dynamic Models of Li-Ion Batteries for Diagnosis and Operation: A Review and Perspective," *J. Electrochem. Soc.*, vol. 165, no. 16, pp. A3656–A3673, 2018.

[32] R. Raccichini, M. Amores, and G. Hinds, "Critical review of the use of reference electrodes in li-ion batteries: A diagnostic perspective," *Batteries*, vol. 5, no. 1, pp. 1–24, 2019.

[33] M. Ender, J. Illig, and E. Ivers-Tiffée, "Three-Electrode Setups for Lithium-Ion Batteries," *J. Electrochem. Soc.*, vol. 164, no. 2, pp. A71–A79, 2017.

[34] J. Costard, M. Ender, M. Weiss, and E. Ivers-Tiffée, "Three-Electrode Setups for Lithium-Ion Batteries: II. Experimental Study of Different Reference Electrode Designs and Their Implications for Half-Cell Impedance Spectra," *J. Electrochem. Soc.*, vol. 164, no. 2, pp. A80–A87, 2017.

[35] C. Nowak, L. Froboese, M. Winter, T. Placke, W. Haselrieder, and A. Kwade, "Designing Graphite-Based Positive Electrodes and Their Properties in Dual-Ion Batteries Using Particle Size-Adjusted Active Materials," *Energy Technol.*, vol. 7, no. 10, p. 1900528, 2019.

[36] J. Landesfeind, J. Hattendorff, A. Ehrl, W. A. Wall, and H. A. Gasteiger, "Tortuosity Determination of Battery Electrodes and Separators by Impedance Spectroscopy," *J. Electrochem. Soc.*, vol. 163, no. 7, pp. A1373–A1387, 2016.

[37] F. L. E. Usseglio-Viretta, A. Colclasure, A. N. Mistry, K. P. Y. Claver, F. Pouraghajan, D. P. Finegan, T. M. M. Heenan, D. Abraham, P. P. Mukherjee, D. Wheeler, P. Shearing, S. J. Cooper, and K. Smith, "Resolving the Discrepancy in Tortuosity Factor Estimation for Li-Ion Battery Electrodes through Micro-Macro Modeling and Experiment," *J. Electrochem. Soc.*, vol. 165, no. 14, pp. A3403–A3426, 2018.

[38] B. Tjaden, S. J. Cooper, D. J. Brett, D. Kramer, and P. R. Shearing, "On the origin and application of the Bruggeman correlation for analysing transport phenomena in electrochemical systems," *Curr. Opin. Chem. Eng.*, vol. 12, pp. 44–51, 2016.

[39] M. Ebner and V. Wood, "Tool for Tortuosity Estimation in Lithium Ion Battery Porous Electrodes," *J. Electrochem. Soc.*, vol. 162, no. 2, pp. A3064–A3070, 2014.

[40] J. Billaud, F. Bouville, T. Magrini, C. Villevieille, and A. R. Studart, "Magnetically aligned graphite electrodes for high-rate performance Li-ion batteries," *Nat. Energy*, vol. 1, no. 8, p. 16097, 2016.

[41] M. Ebner and M. Kory, "Trockenbeschichtung und selbsttragende Schichten mit ausgerichteten Partikeln," Patent DE 10 2021 108 683 A1, 2022.

[42] E. M. Gavilán-Arriazu, O. A. Pinto, B. A. López de Mishima, D. E. Barraco, O. A. Oviedo, and E. P. Leiva, "Kinetic Monte Carlo applied to the electrochemical study of the Li-ion graphite system," *Electrochim. Acta*, vol. 331, p. 135439, 2020.

[43] J. Asenbauer, T. Eisenmann, M. Kuenzel, A. Kazzazi, Z. Chen, and D. Bresser, "The success story of graphite as a lithium-ion anode material-fundamentals, remaining challenges, and recent developments including silicon (oxide) composites," *Sustain. Energy Fuels*, vol. 4, no. 11, pp. 5387–5416, 2020.

[44] J. M. Reniers, G. Mulder, and D. A. Howey, "Review and Performance Comparison of Mechanical-Chemical Degradation Models for Lithium-Ion Batteries," *J. Electrochem. Soc.*, vol. 166, no. 14, pp. A3189–A3200, 2019.

[45] J. S. Edge, S. O'Kane, R. Prosser, N. D. Kirkaldy, A. N. Patel, A. Hales, A. Ghosh, W. Ai, J. Chen, J. Yang, S. Li, M. C. Pang, L. Bravo Diaz, A. Tomaszewska, M. W. Marzook, K. N. Radhakrishnan, H. Wang, Y. Patel, B. Wu, and G. J. Offer, "Lithium ion battery degradation: what you need to know," *Phys. Chem. Chem. Phys.*, vol. 23, no. 14, pp. 8200–8221, 2021.

[46] A. Tahmasbi and M. Eikerling, "Statistical physics-based model of mechanical degradation in lithium ion batteries," *Electrochim. Acta*, vol. 283, pp. 75–87, 2018.

[47] T. Bond, R. Gauthier, S. Gasilov, and J. R. Dahn, "In-Situ Computed Tomography of Particle Microcracking and Electrode Damage in Cycled NMC622/Graphite Pouch Cell Batteries," *J. Electrochem. Soc.*, vol. 169, no. 8, p. 080531, 2022.

[48] M. J. Herzog, N. Gauquelin, D. Esken, J. Verbeeck, and J. Janek, "Increased Performance Improvement of Lithium-Ion Batteries by Dry Powder Coating of High-Nickel NMC with Nanostructured Fumed Ternary Lithium Metal Oxides," *ACS Appl. Energy Mater.*, vol. 4, no. 9, pp. 8832–8848, 2021.

[49] S. Carelli and W. G. Bessler, "Prediction of Reversible Lithium Plating with a Pseudo-3D Lithium-Ion Battery Model," *J. Electrochem. Soc.*, vol. 167, no. 10, p. 100515, 2020.

[50] J. Landesfeind and H. A. Gasteiger, "Temperature and Concentration Dependence of the Ionic Transport Properties of Lithium-Ion Battery Electrolytes," *J. Electrochem. Soc.*, vol. 166, no. 14, pp. A3079–A3097, 2019.

[51] X. G. Yang and C. Y. Wang, "Understanding the trilemma of fast charging, energy density and cycle life of lithium-ion batteries," *J. Power Sources*, vol. 402, pp. 489–498, 2018.

[52] E. Kazyak, K. Chen, Y. Chen, T. H. Cho, and N. P. Dasgupta, "Enabling 4C Fast Charging of Lithium-Ion Batteries by Coating Graphite with a Solid-State Electrolyte," *Adv. Energy Mater.*, vol. 12, no. 1, p. 2102618, 2022.

[53] S. Ahmed, I. Bloom, A. N. Jansen, T. Tanim, E. J. Dufek, A. Pesaran, A. Burnham, R. B. Carlson, F. Dias, K. Hardy, M. Keyser, C. Kreuzer, A. Markel, A. Meintz, C. Michelbacher, M. Mohanpurkar, P. A. Nelson, D. C. Robertson, D. Scoffield, M. Shirk, T. Stephens, R. Vijayagopal, and J. Zhang, "Enabling fast charging – A battery technology gap assessment," *J. Power Sources*, vol. 367, pp. 250–262, 2017.

[54] W. Xie, X. Liu, R. He, Y. Li, X. Gao, X. Li, Z. Peng, S. Feng, X. Feng, and S. Yang, "Challenges and opportunities toward fast-charging of lithium-ion batteries," *J. Energy Storage*, vol. 32, p. 101837, 2020.

[55] Y. Liu, Y. Zhu, and Y. Cui, "Challenges and opportunities towards fast-charging battery materials," *Nat. Energy*, vol. 4, no. 7, pp. 540–550, 2019.

[56] A. M. Colclasure, A. R. Dunlop, S. E. Trask, B. J. Polzin, A. N. Jansen, and K. Smith, "Requirements for Enabling Extreme Fast Charging of High Energy Density Li-Ion Cells while Avoiding Lithium Plating," *J. Electrochem. Soc.*, vol. 166, no. 8, pp. A1412–A1424, 2019.

[57] E. Logan and J. Dahn, "Electrolyte Design for Fast-Charging Li-Ion Batteries," *Trends Chem.*, vol. 2, no. 4, pp. 354–366, 2020.

[58] N. Kim, S. Chae, J. Ma, M. Ko, and J. Cho, "Fast-charging high-energy lithium-ion batteries via implantation of amorphous silicon nanolayer in edge-plane activated graphite anodes," *Nat. Commun.*, vol. 8, no. 1, pp. 1–10, 2017.

[59] A. Tomaszewska, Z. Chu, X. Feng, S. O'Kane, X. Liu, J. Chen, C. Ji, E. Endler, R. Li, L. Liu, Y. Li, S. Zheng, S. Vetterlein, M. Gao, J. Du, M. Parkes, M. Ouyang, M. Marinescu, G. Offer, and B. Wu, "Lithium-ion battery fast charging: A review," *eTransportation*, vol. 1, p. 100011, 2019.

[60] P. M. Attia, A. Grover, N. Jin, K. A. Severson, T. M. Markov, Y.-H. Liao, M. H. Chen, B. Cheong, N. Perkins, Z. Yang, P. K. Herring, M. Aykol, S. J. Harris, R. D. Braatz, S. Ermon, and W. C. Chueh, "Closed-loop optimization of fast-charging protocols for batteries with machine learning," *Nature*, vol. 578, no. 7795, pp. 397–402, 2020.

[61] M. Xu, R. Wang, B. Reichman, and X. Wang, "Modeling the effect of two-stage fast charging protocol on thermal behavior and charging energy efficiency of lithium-ion batteries," *J. Energy Storage*, vol. 20, pp. 298–309, 2018.

[62] M. Torchio, L. Magni, R. Braatz, and D. Raimondo, "Optimal Health-aware Charging Protocol for Lithium-ion Batteries: A Fast Model Predictive Control Approach," *IFAC-PapersOnLine*, vol. 49, no. 7, pp. 827–832, 2016.

[63] T. R. Tanim, E. J. Dufek, M. Evans, C. Dickerson, A. N. Jansen, B. J. Polzin, A. R. Dunlop, S. E. Trask, R. Jackman, I. Bloom, Z. Yang, and E. Lee, "Extreme Fast Charge Challenges for Lithium-Ion Battery: Variability and Positive Electrode Issues," *J. Electrochem. Soc.*, vol. 166, no. 10, pp. A1926–A1938, 2019.

[64] S. Schindler, M. Bauer, H. Cheetamun, and M. A. Danzer, "Fast charging of lithium-ion cells: Identification of aging-minimal current profiles using a design of experiment approach and a mechanistic degradation analysis," *J. Energy Storage*, vol. 19, pp. 364–378, 2018.

[65] H. Wang, S. Frisco, E. Gottlieb, R. Yuan, and J. F. Whitacre, "Capacity degradation in commercial Li-ion cells: The effects of charge protocol and temperature," *J. Power Sources*, vol. 426, pp. 67–73, 2019.

[66] C. Mao, R. E. Ruther, J. Li, Z. Du, and I. Belharouak, "Identifying the limiting electrode in lithium ion batteries for extreme fast charging," *Electrochem. Commun.*, vol. 97, pp. 37–41, 2018.

[67] X. G. Yang, G. Zhang, S. Ge, and C. Y. Wang, "Fast charging of lithium-ion batteries at all temperatures," *Proc. Natl. Acad. Sci. U. S. A.*, vol. 115, no. 28, pp. 7266–7271, 2018.

[68] X. G. Yang, T. Liu, Y. Gao, S. Ge, Y. Leng, D. Wang, and C. Y. Wang, "Asymmetric Temperature Modulation for Extreme Fast Charging of Lithium-Ion Batteries," *Joule*, vol. 3, no. 12, pp. 3002–3019, 2019.

[69] B. S. Vishnugopi, A. Verma, and P. P. Mukherjee, "Fast Charging of Lithium-ion Batteries via Electrode Engineering," *J. Electrochem. Soc.*, vol. 167, no. 9, p. 090508, 2020.

[70] J. E. Harlow, X. Ma, J. Li, E. Logan, Y. Liu, N. Zhang, L. Ma, S. L. Glazier, M. M. E. Cormier, M. Genovese, S. Buteau, A. Cameron, J. E. Stark, and J. R. Dahn, "A Wide Range of Testing Results on an Excellent Lithium-Ion Cell Chemistry to be used as Benchmarks for New Battery Technologies," *J. Electrochem. Soc.*, vol. 166, no. 13, pp. A3031–A3044, 2019.

[71] L. Mauler, F. Duffner, W. G. Zeier, and J. Leker, "Battery cost forecasting: A review of methods and results with an outlook to 2050," *Energy Environ. Sci.*, vol. 14, no. 9, pp. 4712–4739, 2021.

[72] J. Li, Z. Du, R. E. Ruther, S. J. An, L. A. David, K. Hays, M. Wood, N. D. Phillip, Y. Sheng, C. Mao, S. Kalnaus, C. Daniel, and D. L. Wood, "Toward Low-Cost, High-Energy Density, and High-Power Density Lithium-Ion Batteries," *JOM*, vol. 69, no. 9, pp. 1484–1496, 2017.

[73] Y. Li, X. Zheng, Z. Cao, Y. Wang, Y. Wang, L. Lv, W. Huang, Y. Huang, and H. Zheng, "Unveiling the mechanisms into Li-trapping induced (ir)reversible capacity loss for silicon anode," *Energy Storage Mater.*, vol. 55, pp. 660–668, 2023.

[74] D. Schmidt, M. Kamlah, and V. Knoblauch, "Highly densified NCM-cathodes for high energy Li-ion batteries: Microstructural evolution during densification and its influence on the performance of the electrodes," *J. Energy Storage*, vol. 17, pp. 213–223, 2018.

[75] V. Laue, F. Röder, and U. Krewer, "Joint structural and electrochemical modeling: Impact of porosity on lithium-ion battery performance," *Electrochim. Acta*, vol. 314, pp. 20–31, 2019.

[76] S. Yu, S. Kim, T. Y. Kim, J. H. Nam, and W. I. Cho, "Model prediction and experiments for the electrode design optimization of $LiFePo_4$/graphite electrodes in high capacity lithium-ion batteries," *Bull. Korean Chem. Soc.*, vol. 34, no. 1, pp. 79–88, 2013.

[77] L. S. Kremer, A. Hoffmann, T. Danner, S. Hein, B. Prifling, D. Westhoff, C. Dreer, A. Latz, V. Schmidt, and M. Wohlfahrt-Mehrens, "Manufacturing Process for Improved Ultra-Thick Cathodes in High-Energy Lithium-Ion Batteries," *Energy Technol.*, vol. 8, no. 2, p. 1900167, 2020.

[78] H. Buqa, D. Goers, M. Holzapfel, M. E. Spahr, and P. Novák, "High rate capability of graphite negative electrodes for lithium-ion batteries," *J. Electrochem. Soc.*, vol. 152, no. 2, p. A474, 2005.

[79] L. Bläubaum, F. Röder, C. Nowak, H. S. Chan, A. Kwade, and U. Krewer, "Impact of Particle Size Distribution on Performance of Lithium-Ion Batteries," *ChemElectroChem*, vol. 7, no. 23, pp. 4755–4766, 2020.

[80] N. Dunlap, D. B. Sulas-Kern, P. J. Weddle, F. Usseglio-Viretta, P. Walker, P. Todd, D. Boone, A. M. Colclasure, K. Smith, B. J. Tremolet de Villers, and D. P. Finegan, "Laser ablation of Li-ion electrodes for fast charging: Material properties, rate capability, Li plating, and wetting," *J. Power Sources*, vol. 537, p. 231464, 2022.

[81] V. De Lauri, L. Krumbein, S. Hein, B. Prifling, V. Schmidt, T. Danner, and A. Latz, "Beneficial Effects of Three-Dimensional Structured Electrodes for the Fast Charging of Lithium-Ion Batteries," *ACS Appl. Energy Mater.*, vol. 4, no. 12, pp. 13 847–13 859, 2021.

[82] S. Jaiser, M. Müller, M. Baunach, W. Bauer, P. Scharfer, and W. Schabel, "Investigation of film solidification and binder migration during drying of Li-Ion battery anodes," *J. Power Sources*, vol. 318, pp. 210–219, 2016.

[83] R. Diehm, J. Kumberg, C. Dörrer, M. Müller, W. Bauer, P. Scharfer, and W. Schabel, "In Situ Investigations of Simultaneous Two-Layer Slot Die Coating of Component-Graded Anodes for Improved High-Energy Li-Ion Batteries," *Energy Technol.*, vol. 8, no. 5, pp. 1–7, 2020.

[84] D. Westhoff, T. Danner, S. Hein, R. Scurtu, L. Kremer, A. Hoffmann, A. Hilger, I. Manke, M. Wohlfahrt-Mehrens, A. Latz, and V. Schmidt, "Analysis of microstructural effects in multi-layer lithium-ion battery cathodes," *Mater. Charact.*, vol. 151, pp. 166–174, 2019.

[85] M. Wood, J. Li, Z. Du, C. Daniel, A. R. Dunlop, B. J. Polzin, A. N. Jansen, G. K. Krumdick, and D. L. Wood, "Impact of secondary particle size and two-layer architectures on the high-rate performance of thick electrodes in lithium-ion battery pouch cells," *J. Power Sources*, vol. 515, p. 230429, 2021.

[86] A. Shodiev, M. Chouchane, M. Gaberscek, O. Arcelus, J. Xu, H. Oularbi, J. Yu, J. Li, M. Morcrette, and A. A. Franco, "Deconvoluting the benefits of porosity distribution in layered electrodes on the electrochemical performance of Li-ion batteries," *Energy Storage Mater.*, vol. 47, pp. 462–471, 2022.

[87] S. Golmon, K. Maute, and M. L. Dunn, "A design optimization methodology for Li^+ batteries," *J. Power Sources*, vol. 253, pp. 239–250, 2014.

[88] Y. Dai and V. Srinivasan, "On Graded Electrode Porosity as a Design Tool for Improving the Energy Density of Batteries," *J. Electrochem. Soc.*, vol. 163, no. 3, pp. A406–A416, 2016.

[89] Y. Qi, T. Jang, V. Ramadesigan, D. T. Schwartz, and V. R. Subramanian, "Is There a Benefit in Employing Graded Electrodes for Lithium-Ion Batteries?" *J. Electrochem. Soc.*, vol. 164, no. 13, pp. A3196–A3207, 2017.

[90] H. Bockholt, M. Indrikova, A. Netz, F. Golks, and A. Kwade, "The interaction of consecutive process steps in the manufacturing of lithium-ion battery electrodes with regard to structural and electrochemical properties," *J. Power Sources*, vol. 325, pp. 140–151, 2016.

[91] M. Thomitzek, O. Schmidt, F. Röder, U. Krewer, C. Herrmann, and S. Thiede, "Simulating Process-Product Interdependencies in Battery Production Systems," *Procedia CIRP*, vol. 72, pp. 346–351, 2018.

[92] A. Kwade, W. Haselrieder, R. Leithoff, A. Modlinger, F. Dietrich, and K. Droeder, "Current status and challenges for automotive battery production technologies," *Nat. Energy*, vol. 3, no. 4, pp. 290–300, 2018.

[93] Y. Liu, R. Zhang, J. Wang, and Y. Wang, "Current and future lithium-ion battery manufacturing," *iScience*, vol. 24, no. 4, p. 102332, 2021.

[94] F. Duffner, L. Mauler, M. Wentker, J. Leker, and M. Winter, "Large-scale automotive battery cell manufacturing: Analyzing strategic and operational effects on manufacturing costs," *Int. J. Prod. Econ.*, vol. 232, p. 107982, 2021.

[95] P. A. Nelson, S. Ahmed, K. G. Gallagher, and D. W. Dees, "Modeling the Performance and Cost of Lithium-Ion Batteries for Electric-Drive Vehicles, Third Edition," Argonne National Laboratory (ANL), Argonne, IL (United States), Tech. Rep., 2019.

[96] K. Huber, A. Adam, D. Grießl, and A. Kwade, "Understanding slurry mixing effects on the fast charging capability of lithium-ion battery cells: Methodology and case study," *J. Power Sources*, vol. 536, p. 231455, 2022.

[97] M. Abdollahifar, H. Cavers, S. Scheffler, A. Diener, M. Lippke, and A. Kwade, "Insights into Influencing Electrode Calendering on the Battery Performance," *Adv. Energy Mater.*, vol. 13, no. 40, p. 2300973, 2023.

[98] D. L. Wood, J. Li, and S. J. An, "Formation Challenges of Lithium-Ion Battery Manufacturing," *Joule*, vol. 3, no. 12, pp. 2884–2888, 2019.

[99] S. Davidsson Kurland, "Energy use for GWh-scale lithium-ion battery production," *Environ. Res. Commun.*, vol. 2, no. 1, p. 012001, 2020.

[100] A. Jinasena, O. S. Burheim, and A. H. Strømman, "A flexible model for benchmarking the energy usage of automotive lithium-ion battery cell manufacturing," *Batteries*, vol. 7, no. 1, pp. 1–21, 2021.

[101] A. Wang, S. Kadam, H. Li, S. Shi, and Y. Qi, "Review on modeling of the anode solid electrolyte interphase (SEI) for lithium-ion batteries," *npj Comput. Mater.*, vol. 4, no. 1, p. 15, 2018.

[102] E. Peled and S. Menkin, "Review—SEI: Past, Present and Future," *J. Electrochem. Soc.*, vol. 164, no. 7, pp. A1703–A1719, 2017.

[103] S. Zhang, M. S. Ding, K. Xu, J. Allen, and T. R. Jow, "Understanding solid electrolyte interface film formation on graphite electrodes," *Electrochem. Solid-State Lett.*, vol. 4, no. 12, pp. 10–13, 2001.

[104] I. Rubio Lopez, M. J. Lain, and E. Kendrick, "Optimisation of Formation and Conditioning Protocols for Lithium-Ion Electric Vehicle Batteries," *Batteries Supercaps*, vol. 3, no. 9, pp. 900–909, 2020.

[105] H. H. Heimes, C. Offermanns, A. Mohsseni, H. Laufen, U. Westerhoff, L. Hoffmann, P. Niehoff, M. Kurrat, M. Winter, and A. Kampker, "The Effects of Mechanical and

Thermal Loads during Lithium-Ion Pouch Cell Formation and Their Impacts on Process Time," *Energy Technol.*, vol. 8, no. 2, p. 1900118, 2020.

[106] E. Brorein, M. Vulovic, B. Boswell, and R. Zollo, "Systems and methods for determining a self-discharge current characteristic of a storage cell," Patent US 2018/0 164 363 A1, 2018.

[107] A. Noel and I. Zilberman, "Anordnung zur Messung vorbestimmter Qualitätskriterien von wärmeemittierenden Prüflingen," Patent EP 3 971 544 A1, 2022.

[108] Y.-K. Sun, "Promising All-Solid-State Batteries for Future Electric Vehicles," *ACS Energy Lett.*, vol. 5, no. 10, pp. 3221–3223, 2020.

[109] P. Albertus, V. Anandan, C. Ban, N. Balsara, I. Belharouak, J. Buettner-Garrett, Z. Chen, C. Daniel, M. Doeff, N. J. Dudney, B. Dunn, S. J. Harris, S. Herle, E. Herbert, S. Kalnaus, J. A. Libera, D. Lu, S. Martin, B. D. McCloskey, M. T. McDowell, Y. S. Meng, J. Nanda, J. Sakamoto, E. C. Self, S. Tepavcevic, E. Wachsman, C. Wang, A. S. Westover, J. Xiao, and T. Yersak, "Challenges for and Pathways toward Li-Metal-Based All-Solid-State Batteries," *ACS Energy Lett.*, vol. 6, no. 4, pp. 1399–1404, 2021.

[110] O. Schmidt, M. Thomitzek, F. Röder, S. Thiede, C. Herrmann, and U. Krewer, "Modeling the Impact of Manufacturing Uncertainties on Lithium-Ion Batteries," *J. Electrochem. Soc.*, vol. 167, no. 6, p. 060501, 2020.

[111] X. Jin, A. Vora, V. Hoshing, T. Saha, G. Shaver, O. Wasynczuk, and S. Varigonda, "Applicability of available Li-ion battery degradation models for system and control algorithm design," *Control Eng. Pract.*, vol. 71, pp. 1–9, 2018.

[112] U. Westerhoff, K. Kurbach, F. Lienesch, and M. Kurrat, "Analysis of Lithium-Ion Battery Models Based on Electrochemical Impedance Spectroscopy," *Energy Technol.*, vol. 4, no. 12, pp. 1620–1630, 2016.

[113] S. Gantenbein, M. Weiss, and E. Ivers-Tiffée, "Impedance based time-domain modeling of lithium-ion batteries: Part I," *J. Power Sources*, vol. 379, pp. 317–327, 2018.

[114] M. Gaberšček, "Understanding Li-based battery materials via electrochemical impedance spectroscopy," *Nat. Commun.*, vol. 12, no. 1, pp. 19–22, 2021.

[115] M.-T. von Srbik, M. Marinescu, R. F. Martinez-Botas, and G. J. Offer, "A physically meaningful equivalent circuit network model of a lithium-ion battery accounting for local electrochemical and thermal behaviour, variable double layer capacitance and degradation," *J. Power Sources*, vol. 325, pp. 171–184, 2016.

[116] S. Cui, Y. Wei, T. Liu, W. Deng, Z. Hu, Y. Su, H. Li, M. Li, H. Guo, Y. Duan, W. Wang, M. Rao, J. Zheng, X. Wang, and F. Pan, "Optimized Temperature Effect of Li-Ion Diffusion with Layer Distance in $Li(Ni_xMn_yCo_z)O_2$ Cathode Materials for High Performance Li-Ion Battery," *Adv. Energy Mater.*, vol. 6, no. 4, pp. 1–9, 2016.

[117] S. G. Marquis, V. Sulzer, R. Timms, C. P. Please, and S. J. Chapman, "An Asymptotic Derivation of a Single Particle Model with Electrolyte," *J. Electrochem. Soc.*, vol. 166, no. 15, pp. A3693–A3706, 2019.

[118] M. Heinrich, N. Wolff, N. Harting, V. Laue, F. Röder, S. Seitz, and U. Krewer, "Physico-Chemical Modeling of a Lithium-Ion Battery: An Ageing Study with Electrochemical Impedance Spectroscopy," *Batteries Supercaps*, vol. 2, no. 6, pp. 530–540, 2019.

[119] F. Röder, S. Sonntag, D. Schröder, and U. Krewer, "Simulating the Impact of Particle Size Distribution on the Performance of Graphite Electrodes in Lithium-Ion Batteries," *Energy Technol.*, vol. 4, no. 12, pp. 1588–1597, 2016.

[120] A. Schmidt, E. Ramani, T. Carraro, J. Joos, A. Weber, M. Kamlah, and E. Ivers-Tiffée, "Understanding Deviations between Spatially Resolved and Homogenized Cathode Models of Lithium-Ion Batteries," *Energy Technology*, vol. 9, no. 6, p. 2000881, 2021.

[121] M. Ender, J. Joos, T. Carraro, and E. Ivers-Tiffée, "Quantitative Characterization of $LiFePO_4$ Cathodes Reconstructed by FIB/SEM Tomography," *J. Electrochem. Soc.*, vol. 159, no. 7, pp. A972–A980, 2012.

[122] M. Doyle, T. F. Fuller, and J. Newman, "Modeling of Galvanostatic Charge and Discharge of the Lithium/Polymer/Insertion Cell," *J. Electrochem. Soc.*, vol. 140, no. 6, pp. 1526–1533, 1993.

[123] N. Legrand, S. Raël, B. Knosp, M. Hinaje, P. Desprez, and F. Lapicque, "Including Double-Layer Capacitance in Lithium-Ion Battery Mathematical Models," *J. Power Sources*, vol. 251, pp. 370–378, 2014.

[124] F. Röder, V. Laue, and U. Krewer, "Model Based Multiscale Analysis of Film Formation in Lithium-Ion Batteries," *Batteries Supercaps*, vol. 2, no. 3, pp. 248–265, 2019.

[125] N. Wolff, F. Röder, and U. Krewer, "Model Based Assessment of Performance of Lithium-Ion Batteries Using Single Ion Conducting Electrolytes," *Electrochim. Acta*, vol. 284, pp. 639–646, 2018.

[126] C. Mao, S. J. An, H. M. Meyer, J. Li, M. Wood, R. E. Ruther, and D. L. Wood, "Balancing formation time and electrochemical performance of high energy lithium-ion batteries," *J. Power Sources*, vol. 402, pp. 107–115, 2018.

[127] M. Kespe, M. Gleiß, S. Hammerich, and H. Nirschl, "Numerical optimization of the spatial conductivity distribution within cathode microstructures of lithium-ion batteries considering the cell performance," *Int. J. Energy Res.*, vol. 41, no. 14, pp. 2282–2296, 2017.

[128] M. Chouchane, A. Rucci, T. Lombardo, A. C. Ngandjong, and A. A. Franco, "Lithium ion battery electrodes predicted from manufacturing simulations: Assessing the impact of the carbon-binder spatial location on the electrochemical performance," *J. Power Sources*, vol. 444, p. 227285, 2019.

[129] D. Westhoff, I. Manke, and V. Schmidt, "Generation of virtual lithium-ion battery electrode microstructures based on spatial stochastic modeling," *Comput. Mater. Sci.*, vol. 151, pp. 53–64, 2018.

[130] J. Joos, A. Buchele, A. Schmidt, A. Weber, and E. Ivers-Tiffée, "Virtual Electrode Design for Lithium-Ion Battery Cathodes," *Energy Technol.*, vol. 9, no. 6, p. 2000891, 2021.

[131] P. R. Shearing, L. E. Howard, P. S. Jørgensen, N. P. Brandon, and S. J. Harris, "Characterization of the 3-dimensional microstructure of a graphite negative electrode from a Li-ion battery," *Electrochem. Commun.*, vol. 12, no. 3, pp. 374–377, 2010.

[132] M. Ender, J. Joos, A. Weber, and E. Ivers-Tiffée, "Anode microstructures from high-energy and high-power lithium-ion cylindrical cells obtained by X-ray nano-tomography," *J. Power Sources*, vol. 269, pp. 912–919, 2014.

[133] S. Komini Babu, A. I. Mohamed, J. F. Whitacre, and S. Litster, "Multiple imaging mode X-ray computed tomography for distinguishing active and inactive phases in lithium-ion battery cathodes," *J. Power Sources*, vol. 283, pp. 314–319, 2015.

[134] M. Ender, J. Joos, T. Carraro, and E. Ivers-Tiffée, "Three-dimensional reconstruction of a composite cathode for lithium-ion cells," *Electrochem. Commun.*, vol. 13, no. 2, pp. 166–168, 2011.

[135] J. R. Wilson, J. S. Cronin, S. A. Barnett, and S. J. Harris, "Measurement of three-dimensional microstructure in a $LiCoO_2$ positive electrode," *J. Power Sources*, vol. 196, no. 7, pp. 3443–3447, 2011.

[136] L. Zielke, T. Hutzenlaub, D. R. Wheeler, C. W. Chao, I. Manke, A. Hilger, N. Paust, R. Zengerle, and S. Thiele, "Three-phase multiscale modeling of a $LiCoO_2$ cathode: Combining the advantages of FIB-SEM imaging and X-ray tomography," *Adv. Energy Mater.*, vol. 5, no. 5, pp. 1–8, 2015.

[137] A. N. Mistry, K. Smith, and P. P. Mukherjee, "Secondary-Phase Stochastics in Lithium-Ion Battery Electrodes," *ACS Appl. Mater. Interfaces*, vol. 10, no. 7, pp. 6317–6326, 2018.

[138] Y. Li, M. Abdel-Monem, R. Gopalakrishnan, M. Berecibar, E. Nanini-Maury, N. Omar, P. van den Bossche, and J. Van Mierlo, "A quick on-line state of health estimation method for Li-ion battery with incremental capacity curves processed by Gaussian filter," *J. Power Sources*, vol. 373, pp. 40–53, 2018.

[139] C. Pastor-Fernández, K. Uddin, G. H. Chouchelamane, W. D. Widanage, and J. Marco, "A Comparison between Electrochemical Impedance Spectroscopy and Incremental Capacity-Differential Voltage as Li-ion Diagnostic Techniques to Identify and Quantify the Effects of Degradation Modes within Battery Management Systems," *J. Power Sources*, vol. 360, pp. 301–318, 2017.

[140] E. Peled, "The Electrochemical Behavior of Alkali and Alkaline Earth Metals in Nonaqueous Battery Systems—The Solid Electrolyte Interphase Model," *J. Electrochem. Soc.*, vol. 126, no. 12, pp. 2047–2051, 1979.

[141] Y. Ali, N. Iqbal, and S. Lee, "Role of SEI layer growth in fracture probability in lithium-ion battery electrodes," *Int. J. Energy Res.*, vol. 45, no. 4, pp. 5293–5308, 2021.

[142] S. Y. Luchkin, S. A. Lipovskikh, N. S. Katorova, A. A. Savina, A. M. Abakumov, and K. J. Stevenson, "Solid-electrolyte interphase nucleation and growth on carbonaceous negative electrodes for Li-ion batteries visualized with in situ atomic force microscopy," *Sci. Rep.*, vol. 10, no. 1, pp. 1–10, 2020.

[143] M. Leißing, F. Horsthemke, S. Wiemers-Meyer, M. Winter, P. Niehoff, and S. Nowak, "The Impact of the C-Rate on Gassing During Formation of NMC622 || Graphite Lithium-Ion Battery Cells," *Batteries Supercaps*, vol. 4, no. 8, pp. 1344–1350, 2021.

[144] Y. P. Stenzel, F. Horsthemke, M. Winter, and S. Nowak, "Chromatographic techniques in the research area of lithium ion batteries: Current state-of-the-art," *Separations*, vol. 6, no. 2, pp. 17–23, 2019.

[145] W. Huang, P. M. Attia, H. Wang, S. E. Renfrew, N. Jin, S. Das, Z. Zhang, D. T. Boyle, Y. Li, M. Z. Bazant, B. D. McCloskey, W. C. Chueh, and Y. Cui, "Evolution of the Solid–Electrolyte Interphase on Carbonaceous Anodes Visualized by Atomic-Resolution Cryogenic Electron Microscopy," *Nano Lett.*, vol. 19, no. 8, pp. 5140–5148, 2019.

[146] V. Ramadesigan, K. Chen, N. A. Burns, V. Boovaragavan, R. D. Braatz, and V. R. Subramanian, "Parameter Estimation and Capacity Fade Analysis of Lithium-Ion

Batteries Using Reformulated Models," *J. Electrochem. Soc.*, vol. 158, no. 9, p. A1048, 2011.

[147] F. M. Kindermann, J. Keil, A. Frank, and A. Jossen, "A SEI Modeling Approach Distinguishing between Capacity and Power Fade," *J. Electrochem. Soc.*, vol. 164, pp. E287–E294, 2017.

[148] F. Single, B. Horstmann, and A. Latz, "Theory of Impedance Spectroscopy for Lithium Batteries," *J. Phys. Chem. C*, vol. 123, no. 45, pp. 27 327–27 343, 2019.

[149] V. Laue, F. Röder, and U. Krewer, "Practical identifiability of electrochemical P2D models for lithium-ion batteries," *J. Appl. Electrochem.*, vol. 51, no. 9, pp. 1253–1265, 2021.

[150] J. Schmalstieg, C. Rahe, M. Ecker, and D. U. Sauer, "Full Cell Parameterization of a High-Power Lithium-Ion Battery for a Physico-Chemical Model: Part I. Physical and Electrochemical Parameters," *J. Electrochem. Soc.*, vol. 165, no. 16, pp. A3799–A3810, 2018.

[151] U. Krewer, M. Christov, T. Vidakovic', and K. Sundmacher, "Impedance spectroscopic analysis of the electrochemical methanol oxidation kinetics," *J. Electroanal. Chem.*, vol. 589, no. 1, pp. 148–159, 2006.

[152] A. A. Tahmasbi, T. Kadyk, and M. H. Eikerling, "Statistical Physics-Based Model of Solid Electrolyte Interphase Growth in Lithium Ion Batteries," *J. Electrochem. Soc.*, vol. 164, no. 6, pp. A1307–A1313, 2017.

[153] I. S. Sarpal, A. Bensmann, J. Mähliß, D. Hennefeld, and R. Hanke-Rauschenbach, "Characterisation of batteries with E–P-curves: Quantifying the impact of operating conditions on battery performance," *Int. J. Electr. Power Energy Syst.*, vol. 99, pp. 722–732, 2018.

[154] M. W. Hermanto, N. C. Kee, R. B. H. Tan, M.-S. Chiu, and R. D. Braatz, "Robust Bayesian estimation of kinetics for the polymorphic transformation of L-glutamic acid crystals," *AIChE J.*, vol. 54, no. 12, pp. 3248–3259, 2008.

[155] L. Su, J. Zhang, C. Wang, Y. Zhang, Z. Li, Y. Song, T. Jin, and Z. Ma, "Identifying main factors of capacity fading in lithium ion cells using orthogonal design of experiments," *Appl. Energy*, vol. 163, pp. 201–210, 2016.

[156] O. Rynne, M. Dubarry, C. Molson, D. Lepage, A. Prébé, D. Aymé-Perrot, D. Rochefort, and M. Dollé, "Designs of experiments for beginners—A quick start guide for application to electrode formulation," *Batteries*, vol. 5, no. 4, p. 72, 2019.

[157] F. Galvanin, M. Barolo, and F. Bezzo, "A framework for model-based design of experiments in the presence of continuous measurement systems," *IFAC Proc. Vol.*, vol. 43, no. 5, pp. 571–576, 2010.

[158] A. Chakrabarty, G. T. Buzzard, and A. E. Rundell, "Model-based design of experiments for cellular processes," *Wiley Interdiscip. Rev.: Syst. Biol. Med.*, vol. 5, no. 2, pp. 181–203, 2013.

[159] F. Galvanin, C. C. Ballan, M. Barolo, and F. Bezzo, "A general model-based design of experiments approach to achieve practical identifiability of pharmacokinetic and pharmacodynamic models," *J. Pharmacokinet. Pharmacodyn.*, vol. 40, no. 4, pp. 451–467, 2013.

[160] R. Schenkendorf, X. Xie, M. Rehbein, S. Scholl, and U. Krewer, "The Impact of Global Sensitivities and Design Measures in Model-Based Optimal Experimental Design," *Processes*, vol. 6, no. 4, p. 27, 2018.

[161] S. Curtarolo, G. L. Hart, M. B. Nardelli, N. Mingo, S. Sanvito, and O. Levy, "The high-throughput highway to computational materials design," *Nat. Mater.*, vol. 12, no. 3, pp. 191–201, 2013.

[162] J. E. Saal, S. Kirklin, M. Aykol, B. Meredig, and C. Wolverton, "Materials Design and Discovery with High-Throughput Density Functional Theory: The Open Quantum Materials Database (OQMD)," *JOM*, vol. 65, no. 11, pp. 1501–1509, 2013.

[163] R. Xiao, H. Li, and L. Chen, "High-throughput design and optimization of fast lithium ion conductors by the combination of bond-valence method and density functional theory," *Sci. Rep.*, vol. 5, no. 1, pp. 1–11, 2015.

[164] W. Fitzhugh, F. Wu, L. Ye, W. Deng, P. Qi, and X. Li, "A High-Throughput Search for Functionally Stable Interfaces in Sulfide Solid-State Lithium Ion Conductors," *Adv. Energy Mater.*, vol. 9, no. 21, p. 1900807, 2019.

[165] R. P. Cunha, T. Lombardo, E. N. Primo, and A. A. Franco, "Artificial Intelligence Investigation of NMC Cathode Manufacturing Parameters Interdependencies," *Batteries Supercaps*, vol. 3, no. 1, pp. 60–67, 2020.

[166] K. A. Severson, P. M. Attia, N. Jin, N. Perkins, B. Jiang, Z. Yang, M. H. Chen, M. Aykol, P. K. Herring, D. Fraggedakis, M. Z. Bazant, S. J. Harris, W. C. Chueh, and R. D. Braatz, "Data-driven prediction of battery cycle life before capacity degradation," *Nat. Energy*, vol. 4, no. 5, pp. 383–391, 2019.

[167] A. Turetskyy, V. Laue, R. Lamprecht, S. Thiede, U. Krewer, and C. Herrmann, "Artificial Neural Network enabled P2D Model Deployment for End-of-Line Battery Cell Characterization," in *2019 IEEE 17th International Conference on Industrial Informatics (INDIN)*, vol. 1, 2019, pp. 53–58.

[168] N. Dawson-Elli, S. B. Lee, M. Pathak, K. Mitra, and V. R. Subramanian, "Data Science Approaches for Electrochemical Engineers: An Introduction through Surrogate Model Development for Lithium-Ion Batteries," *J. Electrochem. Soc.*, vol. 165, no. 2, pp. A1–A15, 2018.

[169] V. Laue, O. Schmidt, H. Dreger, X. Xie, F. Röder, R. Schenkendorf, A. Kwade, and U. Krewer, "Model-Based Uncertainty Quantification for the Product Properties of Lithium-Ion Batteries," *Energy Technol.*, vol. 8, no. 2, p. 1900201, 2019.

[170] X. Xie, R. Schenkendorf, and U. Krewer, "Toward a comprehensive and efficient robust optimization framework for (Bio)chemical processes," *Processes*, vol. 6, no. 10, pp. 1–26, 2018.

[171] X. Xie and R. Schenkendorf, "Robust optimization of a pharmaceutical freeze-drying process under non-Gaussian parameter uncertainties," *Chem. Eng. Sci.*, vol. 207, pp. 805–819, 2019.

[172] M. Doyle and J. Newman, "The use of mathematical modeling in the design of lithium/polymer battery systems," *Electrochim. Acta*, vol. 40, no. 13, pp. 2191–2196, 1995.

[173] S. T. Taleghani, B. Marcos, K. Zaghib, and G. Lantagne, "The Effect of Structural Properties of a Two-Layered Electrode on the Li-Ion Battery Polarization," *J. Electrochem. Soc.*, vol. 166, no. 2, pp. A225–A235, 2019.

[174] C. Sangrós Giménez, B. Finke, C. Nowak, C. Schilde, and A. Kwade, "Structural and mechanical characterization of lithium-ion battery electrodes via DEM simulations," *Adv. Powder Technol.*, vol. 29, no. 10, pp. 2312–2321, 2018.

[175] R. Wang, "Sankey diagram," MATLAB Central File Exchange, 2020, accessed September 1, 2020. [Online]. Available: https://www.mathworks.com/matlabcentral/fileexchange/75813-sankey-diagram

[176] S. Golmon, K. Maute, and M. L. Dunn, "Multiscale design optimization of lithium ion batteries using adjoint sensitivity analysis," *Int. J. Numer. Methods Eng.*, vol. 92, no. 5, pp. 475–494, 2012.

[177] F. M. Kindermann, J. Keil, A. Frank, and A. Jossen, "A SEI Modeling Approach Distinguishing between Capacity and Power Fade," *J. Electrochem. Soc.*, vol. 164, no. 12, pp. E287–E294, 2017.

[178] V. Ramadesigan, R. N. Methekar, F. Latinwo, R. D. Braatz, and V. R. Subramanian, "Optimal Porosity Distribution for Minimized Ohmic Drop across a Porous Electrode," *J. Electrochem. Soc.*, vol. 157, no. 12, p. A1328, 2010.

[179] F. Baakes, D. Witt, and U. Krewer, "Impact of electrolyte impurities and SEI composition on battery safety," *Chem. Sci.*, vol. 14, no. 47, pp. 13 783–13 798, 2023.

[180] Y. Kamikawa, K. Amezawa, and K. Terada, "First-Principles Study on the Mechanical Properties of Polymers Formed by the Electrochemical Reduction of Fluoroethylene Carbonate and Vinylene Carbonate," *J. Phys. Chem. C*, vol. 124, no. 37, pp. 19 937–19 944, 2020.

[181] F. Single, B. Horstmann, and A. Latz, "Dynamics and morphology of solid electrolyte interphase (SEI)," *Phys. Chem. Chem. Phys.*, vol. 18, no. 27, pp. 17 810–17 814, 2016.

[182] Y. Li, K. Leung, and Y. Qi, "Computational Exploration of the Li-Electrode|Electrolyte Interface in the Presence of a Nanometer Thick Solid-Electrolyte Interphase Layer," *Acc. Chem. Res.*, vol. 49, no. 10, pp. 2363–2370, 2016.

[183] Q. Zhang, J. Pan, P. Lu, Z. Liu, M. W. Verbrugge, B. W. Sheldon, Y. T. Cheng, Y. Qi, and X. Xiao, "Synergetic Effects of Inorganic Components in Solid Electrolyte Interphase on High Cycle Efficiency of Lithium Ion Batteries," *Nano Lett.*, vol. 16, no. 3, pp. 2011–2016, 2016.

[184] J. Popovic, "The importance of electrode interfaces and interphases for rechargeable metal batteries," *Nat. Commun.*, vol. 12, no. 1, p. 6240, 2021.

[185] J. Lück and A. Latz, "Theory of reactions at electrified interfaces," *Phys. Chem. Chem. Phys.*, vol. 18, no. 27, pp. 17 799–17 804, 2016.

[186] J. Lück and A. Latz, "Modeling of the electrochemical double layer and its impact on intercalation reactions," *Phys. Chem. Chem. Phys.*, vol. 20, no. 44, pp. 27 804–27 821, 2018.

[187] J.-M. Chern and F. G. Helfferich, "Effective kinetic modeling of multistep homogeneous reactions," *AIChE J.*, vol. 36, no. 8, pp. 1200–1208, 1990.

[188] O. Borodin, G. V. Zhuang, P. N. Ross, and K. Xu, "Molecular dynamics simulations and experimental study of lithium ion transport in dilithium ethylene dicarbonate," *J. Phys. Chem. C*, vol. 117, no. 15, pp. 7433–7444, 2013.

[189] S. Shi, P. Lu, Z. Liu, Y. Qi, L. G. Hector, H. Li, and S. J. Harris, "Direct calculation of Li-ion transport in the solid electrolyte interphase," *J. Am. Chem. Soc.*, vol. 134, no. 37, pp. 15 476–15 487, 2012.

[190] S. Shi, Y. Qi, H. Li, and L. G. Hector, "Defect thermodynamics and diffusion mechanisms in Li_2CO_3 and implications for the solid electrolyte interphase in Li-ion batteries," *J. Phys. Chem. C*, vol. 117, no. 17, pp. 8579–8593, 2013.

[191] M. Steinhauer, S. Risse, N. Wagner, and K. A. Friedrich, "Investigation of the Solid Electrolyte Interphase Formation at Graphite Anodes in Lithium-Ion Batteries with Electrochemical Impedance Spectroscopy," *Electrochim. Acta*, vol. 228, pp. 652–658, 2017.

[192] R. Drees, F. Lienesch, and M. Kurrat, "Fast charging lithium-ion battery formation based on simulations with an electrode equivalent circuit model," *J. Energy Storage*, vol. 36, p. 102345, 2021.

[193] T. Lombardo, M. Duquesnoy, H. El-Bouysidy, F. Årén, A. Gallo-Bueno, P. B. Jørgensen, A. Bhowmik, A. Demortière, E. Ayerbe, F. Alcaide, M. Reynaud, J. Carrasco, A. Grimaud, C. Zhang, T. Vegge, P. Johansson, and A. A. Franco, "Artificial Intelligence Applied to Battery Research: Hype or Reality?" *Chem. Rev.*, vol. 122, no. 12, pp. 10 899–10 969, 2022.

[194] A. M. Colclasure and R. J. Kee, "Thermodynamically consistent modeling of elementary electrochemistry in lithium-ion batteries," *Electrochim. Acta*, vol. 55, no. 28, pp. 8960–8973, 2010.

[195] D. K. Karthikeyan, G. Sikha, and R. E. White, "Thermodynamic model development for lithium intercalation electrodes," *J. Power Sources*, vol. 185, no. 2, pp. 1398–1407, 2008.

[196] R. Hausbrand, G. Cherkashinin, H. Ehrenberg, M. Gröting, K. Albe, C. Hess, and W. Jaegermann, "Fundamental degradation mechanisms of layered oxide Li-ion battery cathode materials: Methodology, insights and novel approaches," *Mater. Sci. Eng. B*, vol. 192, pp. 3–25, 2015.

[197] A. M. Bizeray, D. A. Howey, and C. W. Monroe, "Resolving a Discrepancy in Diffusion Potentials, with a Case Study for Li-Ion Batteries," *J. Electrochem. Soc.*, vol. 163, no. 8, pp. E223–E229, 2016.

[198] X. Jin, A. Vora, V. Hoshing, T. Saha, G. Shaver, R. E. García, O. Wasynczuk, and S. Varigonda, "Physically-based reduced-order capacity loss model for graphite anodes in Li-ion battery cells," *J. Power Sources*, vol. 342, pp. 750–761, 2017.

[199] M. Gaberscek, J. Moskon, B. Erjavec, R. Dominko, and J. Jamnik, "The importance of interphase contacts in Li ion electrodes: The meaning of the high-frequency impedance arc," *Electrochem. Solid-State Lett.*, vol. 11, no. 10, pp. 170–174, 2008.

[200] T. P. Heins, N. Harms, L. S. Schramm, and U. Schröder, "Development of a new Electrochemical Impedance Spectroscopy Approach for Monitoring the Solid Electrolyte Interphase Formation," *Energy Technol.*, vol. 4, no. 12, pp. 1509–1513, 2016.

[201] K. Ushirogata, K. Sodeyama, Y. Okuno, and Y. Tateyama, "Additive effect on reductive decomposition and binding of carbonate-based solvent toward solid electrolyte interphase formation in lithium-ion battery," *J. Am. Chem. Soc.*, vol. 135, no. 32, pp. 11 967–11 974, 2013.

[202] W. Dreyer, J. Jamnik, C. Guhlke, R. Huth, J. Moškon, and M. Gaberšček, "The thermodynamic origin of hysteresis in insertion batteries," *Nat. Mater.*, vol. 9, no. 5, pp. 448–453, 2010.

[203] W. Mai, A. Colclasure, and K. Smith, "A Reformulation of the Pseudo2D Battery Model Coupling Large Electrochemical-Mechanical Deformations at Particle and Electrode Levels," *J. Electrochem. Soc.*, vol. 166, no. 8, pp. A1330–A1339, 2019.

[204] Y. Zhuang, Z. Zou, B. Lu, Y. Li, D. Wang, M. Avdeev, and S. Shi, "Understanding the Li diffusion mechanism and positive effect of current collector volume expansion in anode free batteries," *Chinese Phys. B*, vol. 29, no. 6, p. 068202, 2020.

[205] M. Ender, "An extended homogenized porous electrode model for lithium-ion cell electrodes," *J. Power Sources*, vol. 282, pp. 572–580, 2015.

[206] E. Prada, D. Di Domenico, Y. Creff, J. Bernard, V. Sauvant-Moynot, and F. Huet, "A Simplified Electrochemical and Thermal Aging Model of $LiFePO_4$-Graphite Li-ion Batteries: Power and Capacity Fade Simulations," *J. Electrochem. Soc.*, vol. 160, no. 4, pp. A616–A628, 2013.

[207] J. Maibach, F. Lindgren, H. Eriksson, K. Edström, and M. Hahlin, "Electric Potential Gradient at the Buried Interface between Lithium-Ion Battery Electrodes and the SEI Observed Using Photoelectron Spectroscopy," *J. Phys. Chem. Lett.*, vol. 7, no. 10, pp. 1775–1780, 2016.

[208] T. Momma, M. Matsunaga, D. Mukoyama, and T. Osaka, "Ac impedance analysis of lithium ion battery under temperature control," *J. Power Sources*, vol. 216, pp. 304–307, 2012.

[209] M. Ecker, S. Käbitz, I. Laresgoiti, and D. U. Sauer, "Parameterization of a Physico-Chemical Model of a Lithium-Ion Battery," *J. Electrochem. Soc.*, vol. 162, no. 9, pp. A1849–A1857, 2015.

[210] I. A. Gordon, S. Grugeon, H. Takenouti, B. Tribollet, M. Armand, C. Davoisne, A. Débart, and S. Laruelle, "Electrochemical Impedance Spectroscopy response study of a commercial graphite-based negative electrode for Li-ion batteries as function of the cell state of charge and ageing," *Electrochim. Acta*, vol. 223, pp. 63–73, 2017.

[211] W. Liu, P. Liu, and D. Mitlin, "Review of Emerging Concepts in SEI Analysis and Artificial SEI Membranes for Lithium, Sodium, and Potassium Metal Battery Anodes," *Adv. Energy Mater.*, vol. 10, no. 43, p. 2002297, 2020.

[212] L. Liu, J. Park, X. Lin, A. M. Sastry, and W. Lu, "A thermal-electrochemical model that gives spatial-dependent growth of solid electrolyte interphase in a Li-ion battery," *J. Power Sources*, vol. 268, pp. 482–490, 2014.

[213] R. D. Deshpande and D. M. Bernardi, "Modeling Solid-Electrolyte Interphase (SEI) Fracture: Coupled Mechanical/Chemical Degradation of the Lithium Ion Battery," *J. Electrochem. Soc.*, vol. 164, no. 2, pp. A461–A474, 2017.

[214] L. Bläubaum, P. Röse, L. Schmidt, and U. Krewer, "The Effects of Gas Saturation of Electrolytes on the Performance and Durability of Lithium-Ion Batteries," *ChemSusChem*, vol. 14, no. 14, p. cssc.202100845, 2021.

[215] C. H. Lee, J. A. Dura, A. LeBar, and S. C. DeCaluwe, "Direct, operando observation of the bilayer solid electrolyte interphase structure: Electrolyte reduction on a non-intercalating electrode," *J. Power Sources*, vol. 412, pp. 725–735, 2019.

[216] C. Stetson, T. Yoon, J. Coyle, W. Nemeth, M. Young, A. Norman, S. Pylypenko, C. Ban, C. S. Jiang, M. Al-Jassim, and A. Burrell, "Three-dimensional electronic resistivity mapping of solid electrolyte interphase on Si anode materials," *Nano Energy*, vol. 55, pp. 477–485, 2019.

[217] P. Verma, P. Maire, and P. Novák, "A review of the features and analyses of the solid electrolyte interphase in Li-ion batteries," *Electrochim. Acta*, vol. 55, no. 22, pp. 6332–6341, 2010.

[218] W. Huang, J. Wang, M. R. Braun, Z. Zhang, Y. Li, D. T. Boyle, P. C. McIntyre, and Y. Cui, "Dynamic Structure and Chemistry of the Silicon Solid-Electrolyte Interphase Visualized by Cryogenic Electron Microscopy," *Matter*, vol. 1, no. 5, pp. 1232–1245, 2019.

[219] D. R. Kim, J. W. Kang, T. H. Eom, J. M. Kim, J. Lee, and C. Y. Won, "An adaptive rapid charging method for lithium-ion batteries with compensating cell degradation behavior," *Appl. Sci.*, vol. 8, no. 8, pp. 1–12, 2018.

[220] K. Ushirogata, K. Sodeyama, Z. Futera, Y. Tateyama, and Y. Okuno, "Near-Shore Aggregation Mechanism of Electrolyte Decomposition Products to Explain Solid Electrolyte Interphase Formation," *J. Electrochem. Soc.*, vol. 162, no. 14, pp. A2670–A2678, 2015.

[221] F. Röder, R. D. Braatz, and U. Krewer, "Multi-Scale Simulation of Heterogeneous Surface Film Growth Mechanisms in Lithium-Ion Batteries," *J. Electrochem. Soc.*, vol. 164, no. 11, pp. E3335–E3344, 2017.

[222] M. Tang, S. Lu, and J. Newman, "Experimental and Theoretical Investigation of Solid-Electrolyte-Interphase Formation Mechanisms on Glassy Carbon," *J. Electrochem. Soc.*, vol. 159, no. 11, pp. A1775–A1785, 2012.

[223] Y. Wang, S. Nakamura, M. Ue, and P. B. Balbuena, "Theoretical studies to understand surface chemistry on carbon anodes for lithium-ion batteries: Reduction mechanisms of ethylene carbonate," *J. Am. Chem. Soc.*, vol. 123, no. 47, pp. 11 708–11 718, 2001.

[224] T. Osaka, T. Momma, D. Mukoyama, and H. Nara, "Proposal of novel equivalent circuit for electrochemical impedance analysis of commercially available lithium ion battery," *J. Power Sources*, vol. 205, pp. 483–486, 2012.

[225] S. Xia, L. Mu, Z. Xu, J. Wang, C. Wei, L. Liu, P. Pianetta, K. Zhao, X. Yu, F. Lin, and Y. Liu, "Chemomechanical interplay of layered cathode materials undergoing fast charging in lithium batteries," *Nano Energy*, vol. 53, pp. 753–762, 2018.

[226] Y. Shi, M. Zhang, D. Qian, and Y. S. Meng, "Ultrathin Al_2O_3 Coatings for Improved Cycling Performance and Thermal Stability of $LiNi_{0.5}Co_{0.2}Mn_{0.3}O_2$ Cathode Material," *Electrochim. Acta*, vol. 203, pp. 154–161, 2016.

[227] S. J. An, J. Li, Z. Du, C. Daniel, and D. L. Wood, "Fast formation cycling for lithium ion batteries," *J. Power Sources*, vol. 342, pp. 846–852, 2017.

[228] F. Schomburg, B. Heidrich, S. Wennemar, R. Drees, T. Roth, M. Kurrat, H. Heimes, A. Jossen, M. Winter, J. Y. Cheong, and F. Röder, "Lithium-ion battery cell formation: status and future directions towards a knowledge-based process design," *Energy Environ. Sci.*, vol. 17, pp. 2686–2733, 2024.

[229] V. Müller, R. Kaiser, S. Poller, and D. Sauerteig, "Importance of the constant voltage charging step during lithium-ion cell formation," *J. Energy Storage*, vol. 15, pp. 256–265, 2018.

[230] D. Lu, M. Xu, L. Zhou, A. Garsuch, and B. L. Lucht, "Failure Mechanism of Graphite/$LiNi_{0.5}Mn_{1.5}O_4$ Cells at High Voltage and Elevated Temperature," *J. Electrochem. Soc.*, vol. 160, no. 5, pp. A3138–A3143, 2013.

[231] P. M. Attia, S. J. Harris, and W. C. Chueh, "Benefits of Fast Battery Formation in a Model System," *J. Electrochem. Soc.*, vol. 168, no. 5, p. 050543, 2021.

[232] H. B. Son, M.-Y. Jeong, J.-G. Han, K. Kim, K. H. Kim, K.-M. Jeong, and N.-S. Choi, "Effect of reductive cyclic carbonate additives and linear carbonate co-solvents on fast chargeability of $LiNi_{0.6}Co_{0.2}Mn_{0.2}O_2$/graphite cells," *J. Power Sources*, vol. 400, pp. 147–156, 2018.

[233] V. A. Agubra and J. W. Fergus, "The formation and stability of the solid electrolyte interface on the graphite anode," *J. Power Sources*, vol. 268, pp. 153–162, 2014.

[234] D. M. Seo, D. Chalasani, B. S. Parimalam, R. Kadam, M. Nie, and B. L. Lucht, "Reduction reactions of carbonate solvents for lithium ion batteries," *ECS Electrochem. Lett.*, vol. 3, no. 9, pp. 3–6, 2014.

[235] S. K. Heiskanen, J. Kim, and B. L. Lucht, "Generation and Evolution of the Solid Electrolyte Interphase of Lithium-Ion Batteries," *Joule*, vol. 3, no. 10, pp. 2322–2333, 2019.

[236] M. Herstedt, A. M. Andersson, H. Rensmo, H. Siegbahn, and K. Edström, "Characterisation of the SEI formed on natural graphite in PC-based electrolytes," *Electrochim. Acta*, vol. 49, no. 27, pp. 4939–4947, 2004.

[237] A. M. Colclasure, K. A. Smith, and R. J. Kee, "Modeling detailed chemistry and transport for solid-electrolyte-interface (SEI) films in Li-ion batteries," *Electrochim. Acta*, vol. 58, no. 1, pp. 33–43, 2011.

[238] J. A. Gilbert, I. A. Shkrob, and D. P. Abraham, "Transition Metal Dissolution, Ion Migration, Electrocatalytic Reduction and Capacity Loss in Lithium-Ion Full Cells," *J. Electrochem. Soc.*, vol. 164, no. 2, pp. A389–A399, 2017.

[239] S. Solchenbach, M. Metzger, M. Egawa, H. Beyer, and H. A. Gasteiger, "Quantification of PF_5 and POF_3 from Side Reactions of $LiPF_6$ in Li-Ion Batteries," *J. Electrochem. Soc.*, vol. 165, no. 13, pp. A3022–A3028, 2018.

[240] C. Jayawardana, N. Rodrigo, B. Parimalam, and B. L. Lucht, "Role of Electrolyte Oxidation and Difluorophosphoric Acid Generation in Crossover and Capacity Fade in Lithium Ion Batteries," *ACS Energy Lett.*, vol. 6, no. 11, pp. 3788–3792, 2021.

[241] B. S. Parimalam, A. D. MacIntosh, R. Kadam, and B. L. Lucht, "Decomposition Reactions of Anode Solid Electrolyte Interphase (SEI) Components with $LiPF_6$," *J. Phys. Chem. C*, vol. 121, no. 41, pp. 22 733–22 738, 2017.

[242] N. Kaden, N. Schlüter, R. Leithoff, S. Savas, S. Grundmeier, and K. Dröder, "Influence of the lamination process on the wetting behavior and the wetting rate of lithium-ion batteries," *Processes*, vol. 9, no. 10, p. 1851, 2021.

[243] M.-T. F. Rodrigues, I. A. Shkrob, A. M. Colclasure, and D. P. Abraham, "Fast Charging of Li-Ion Cells: Part IV. Temperature Effects and "Safe Lines" to Avoid Lithium Plating," *J. Electrochem. Soc.*, vol. 167, no. 13, p. 130508, 2020.

[244] F. Schomburg, R. Drees, M. Kurrat, M. A. Danzer, and F. Röder, "Characterization of the Solid–Electrolyte Interphase Growth During Cell Formation Based on Differential Voltage Analysis," *Energy Technol.*, p. 2200688, 2022.

[245] J. Vatamanu, O. Borodin, and G. D. Smith, "Molecular Dynamics Simulation Studies of the Structure of a Mixed Carbonate/$LiPF_6$ Electrolyte near Graphite Surface as a Function of Electrode Potential," *J. Phys. Chem. C*, vol. 116, no. 1, pp. 1114–1121, 2012.

[246] P. Münster, M. Diehl, J. E. Frerichs, M. Börner, M. R. Hansen, M. Winter, and P. Niehoff, "Effect of Li plating during formation of lithium ion batteries on their cycling performance and thermal safety," *J. Power Sources*, vol. 484, p. 229306, 2021.

[247] A. Jetybayeva, N. Schön, J. Oh, J. Kim, H. Kim, G. Park, Y. G. Lee, R. A. Eichel, K. Kleiner, F. Hausen, and S. Hong, "Unraveling the State of Charge-Dependent Electronic and Ionic Structure-Property Relationships in NCM622 Cells by Multiscale Characterization," *ACS Appl. Energy Mater.*, vol. 5, no. 2, pp. 1731–1742, 2022.

[248] C.-H. Chen, F. Brosa Planella, K. O'Regan, D. Gastol, W. D. Widanage, and E. Kendrick, "Development of Experimental Techniques for Parameterization of Multi-scale Lithium-ion Battery Models," *J. Electrochem. Soc.*, vol. 167, no. 8, p. 080534, 2020.

[249] T. N. Kröger, M. J. Wölke, P. Harte, T. Beuse, M. Winter, S. Nowak, and S. Wiemers-Meyer, "State-of-Charge Distribution of Single-Crystalline NMC532 Cathodes in Lithium-Ion Batteries: A Critical Look at the Mesoscale," *ChemSusChem*, vol. 15, no. 21, pp. 36–39, 2022.

[250] S. Frisco, A. Kumar, J. F. Whitacre, and S. Litster, "Understanding Li-Ion Battery Anode Degradation and Pore Morphological Changes through Nano-Resolution X-ray Computed Tomography," *J. Electrochem. Soc.*, vol. 163, no. 13, pp. A2636–A2640, 2016.

[251] A. L. Michan, G. Divitini, A. J. Pell, M. Leskes, C. Ducati, and C. P. Grey, "Solid Electrolyte Interphase Growth and Capacity Loss in Silicon Electrodes," *J. Am. Chem. Soc.*, vol. 138, no. 25, pp. 7918–7931, 2016.

[252] S. Müller, M. Lippuner, M. Verezhak, V. De Andrade, F. De Carlo, and V. Wood, "Multimodal Nanoscale Tomographic Imaging for Battery Electrodes," *Adv. Energy Mater.*, vol. 10, no. 28, p. 1904119, 2020.

[253] O. Schmidt and F. Röder, "Conductive Networks and Their Impact on Uncertainty, Degradation, and Failure of Lithium-Ion Battery Electrodes," *ACS Appl. Energy Mater.*, vol. 4, no. 5, pp. 4845–4860, 2021.

[254] T. Liu, L. Lin, X. Bi, L. Tian, K. Yang, J. Liu, M. Li, Z. Chen, J. Lu, K. Amine, K. Xu, and F. Pan, "In situ quantification of interphasial chemistry in Li-ion battery," *Nat. Nanotechnol.*, vol. 14, no. 1, pp. 50–56, 2019.

[255] Z. Liu, P. Lu, Q. Zhang, X. Xiao, Y. Qi, and L. Q. Chen, "A Bottom-Up Formation Mechanism of Solid Electrolyte Interphase Revealed by Isotope-Assisted Time-of-Flight Secondary Ion Mass Spectrometry," *J. Phys. Chem. Lett.*, vol. 9, no. 18, pp. 5508–5514, 2018.

[256] X. He, H. Sun, X. Ding, and K. Zhao, "Grain Boundaries and Their Impact on Li Kinetics in Layered-Oxide Cathodes for Li-Ion Batteries," *J. Phys. Chem. C*, vol. 125, no. 19, pp. 10 284–10 294, 2021.

[257] D. Goldbach, J. Gluch, T. Graf, M. Gaus, S. Käbitz, M. Zillmer, and U. Krewer, "An Efficient Approach for Quantifying the Mechanical Degradation of Ni-Rich NMC-based Cathodes for Lithium-Ion Batteries using Nano-XCT Analysis," *ChemElectroChem*, vol. 202300353, 2023.

[258] Y. Xie, H. Gao, J. Gim, A. T. Ngo, Z. F. Ma, and Z. Chen, "Identifying Active Sites for Parasitic Reactions at the Cathode-Electrolyte Interface," *J. Phys. Chem. Lett.*, vol. 10, no. 3, pp. 589–594, 2019.

[259] S. P. Kühn, K. Edström, M. Winter, and I. Cekic-Laskovic, "Face to Face at the Cathode Electrolyte Interphase: From Interface Features to Interphase Formation and Dynamics," *Adv. Mater. Interfaces*, vol. 9, no. 8, p. 2102078, 2022.

[260] J.-N. Zhang, Q. Li, Y. Wang, J. Zheng, X. Yu, and H. Li, "Dynamic evolution of cathode electrolyte interphase (CEI) on high voltage LiCoO2 cathode and its interaction with Li anode," *Energy Storage Mater.*, vol. 14, no. 36, pp. 1–7, 2018.

[261] H. Seng Chan, L. Bläubaum, D. Vijayshankar, F. Röder, C. Nowak, A. Weber, A. Kwade, and U. Krewer, "Revealing the Impact of Particle Size Distribution on Ageing of Lithium-Ion Batteries with Frequency Response Analysis," *Batteries Supercaps*, vol. 6, no. 10, p. e202300203, 2023.

[262] S. F. Schuster, T. Bach, E. Fleder, J. Müller, M. Brand, G. Sextl, and A. Jossen, "Nonlinear aging characteristics of lithium-ion cells under different operational conditions," *J. Energy Storage*, vol. 1, pp. 44–53, 2015.

[263] B. L. Rinkel, D. S. Hall, I. Temprano, and C. P. Grey, "Electrolyte oxidation pathways in lithium-ion batteries," *J. Am. Chem. Soc.*, vol. 142, no. 15058–15074, pp. 15 058–15 074, 2020.

[264] R. Stockhausen, L. Gehrlein, M. Müller, T. Bergfeldt, A. Hofmann, F. J. Müller, J. Maibach, H. Ehrenberg, and A. Smith, "Investigating the dominant decomposition mechanisms in lithium-ion battery cells responsible for capacity loss in different stages of electrochemical aging," *J. Power Sources*, vol. 543, p. 231842, 2022.

[265] J. C. Burns, N. N. Sinha, D. J. Coyle, G. Jain, C. M. VanElzen, W. M. Lamanna, A. Xiao, E. Scott, J. P. Gardner, and J. R. Dahn, "The Impact of Varying the Concentration of Vinylene Carbonate Electrolyte Additive in Wound Li-Ion Cells," *J. Electrochem. Soc.*, vol. 159, no. 2, pp. A85–A90, 2011.

[266] "Investigating electrode calendering and its impact on electrochemical performance by means of a new discrete element method model: Towards a digital twin of Li-Ion battery manufacturing," *J. Power Sources*, vol. 485, p. 229320, 2021.

[267] E. W. C. Spotte-Smith, R. L. Kam, D. Barter, X. Xie, T. Hou, S. Dwaraknath, S. M. Blau, and K. A. Persson, "Toward a Mechanistic Model of Solid–Electrolyte Interphase Formation and Evolution in Lithium-Ion Batteries," *ACS Energy Lett.*, vol. 7, no. 4, pp. 1446–1453, 2022.

[268] T. L. Kulova, A. M. Skundin, E. A. Nizhnikovskii, and A. V. Fesenko, "Temperature effect on the lithium diffusion rate in graphite," *Russ. J. Electrochem.*, vol. 42, no. 3, pp. 259–262, 2006.

[269] P. Yu, B. N. Popov, J. A. Ritter, and R. E. White, "Determination of the Lithium Ion Diffusion Coefficient in Graphite," *J. Electrochem. Soc.*, vol. 146, no. 1, pp. 8–14, 1999.

[270] S. Marelli and B. Sudret, "UQLab: A Framework for Uncertainty Quantification in Matlab," in *Vulnerability, Uncertainty, Risk*. Reston, VA: American Society of Civil Engineers, 2014, pp. 2554–2563.

[271] S. Marelli, C. Lamas, K. Konakli, C. Mylonas, P. Wiederkehr, and B. Sudret, "UQLab user manual – Sensitivity analysis," Chair of Risk, Safety and Uncertainty Quantification, ETH Zurich, Switzerland, Tech. Rep., 2022, report UQLab-V2.0-106.

[272] M. Nie, J. Demeaux, B. T. Young, D. R. Heskett, Y. Chen, A. Bose, J. C. Woicik, and B. L. Lucht, "Effect of Vinylene Carbonate and Fluoroethylene Carbonate on SEI Formation on Graphitic Anodes in Li-Ion Batteries," *J. Electrochem. Soc.*, vol. 162, no. 13, pp. A7008–A7014, 2015.

List of Figures

List of Tables

List of Equations

List of Symbols and Abbreviations

Symbols

A_m	Redlich-Kister coefficients	-
a	activity	-
a_s	specific surface area	m^{-1}
$\tilde{C}$	ratio between electrode layer and total electrode capacity	-
C_theo	theoretical areal electrode capacity	$\mathrm{Ah\,m}^{-2}$
C_DL	double-layer capacitance	$\mathrm{C\,m}^{-2}$
c_0	initial lithium-ion concentration	$\mathrm{mol\,m}^{-3}$
c_e	lithium-ion concentration in electrolyte phase	$\mathrm{mol\,m}^{-3}$
c_s	lithium-ion concentration in solid phase	$\mathrm{mol\,m}^{-3}$
D_e	lithium-ion diffusion coefficient in electrolyte phase	$\mathrm{m}^2\,\mathrm{s}^{-1}$
D_s	lithium-ion diffusion coefficient in solid phase	$\mathrm{m}^2\,\mathrm{s}^{-1}$
d	thickness	m
E_a	activation energy	$\mathrm{J\,mol}^{-1}$
G^0	standard Gibbs free energy	$\mathrm{J\,mol}^{-1}$
I	electric current	A
J_e	flux of lithium ions in electrolyte phase	$\mathrm{A\,m}^{-2}$
J_s	flux of lithium ions in solid phase	$\mathrm{A\,m}^{-2}$
j^DL	volumetric double-layer lithium-ion current density	$\mathrm{A\,m}^{-3}$
j^tot	total volumetric lithium-ion current density	$\mathrm{A\,m}^{-3}$
j^Li	volumetric lithium-ion reaction current density	$\mathrm{A\,m}^{-3}$
j_0	exchange current density	$\mathrm{A\,m}^{-2}$
$k_{0,\mathrm{a}}$	reaction rate constant anode	s^{-1}
$k_{0,\mathrm{c}}$	reaction rate constant cathode	$\mathrm{m\,s}^{-1}$
$\dot{n}$	volumetric lithium-ion flux	$\mathrm{mol\,m}^{-3}\,\mathrm{s}^{-1}$

Q_{ICL}	irreversible initial capacity loss	$\mathrm{C\,m^{-3}}$
R_{s}	active material particle radius	m
r	radial coordinate in active material particles	m
r_{i}	volumetric reaction rate of reaction i	$\mathrm{mol\,m^{-3}\,s^{-1}}$
T	temperature	K
t	time	s
$t_{\mathrm{p,SEI}}$	transference number of $\mathrm{Li^+}$ in SEI	-
t_{p}	transference number of $\mathrm{Li^+}$ in electrolyte phase	-
$\tilde{V}$	molar volume	$\mathrm{m^3\,mol^{-1}}$
x	coordinate in direction of cell thickness	m
α	charge transfer coefficient	-
β	Bruggeman exponent	-
γ	activity coefficient	-
δ	width	m
ε_{e}	electrolyte volume fraction	-
ε_{s}	active material volume fraction	-
Γ	surface site density	$\mathrm{mol\,m^{-2}}$
κ_{SEI}	ionic conductivity of the SEI	$\mathrm{S\,m^{-1}}$
μ^0	standard chemical potential	$\mathrm{J\,mol^{-1}}$
η	reaction overpotential	V
$\Delta\phi$	potential difference	V
ϕ	electrical potential	V
φ_{s}	lithium flux in solid phase	$\mathrm{mol\,m^{-2}\,s^{-1}}$
σ_{e}	ionic conductivity	$\mathrm{S\,m^{-1}}$
σ_{s}	electrical conductivity	$\mathrm{S\,m^{-1}}$
θ	surface coverage	-

Indices

a	anode
b	backward
CBD	carbon-binder domain

c	cathode
cc	current collector
DL	double-layer
e	electrolyte phase
eff	effective
eq	equilibrium
f	forward
max	maximum value
SEI	solid electrolyte interphase
SEIe	interface between SEI and electrolyte phase
SEIe/e	transition between SEIe and e
s	solid phase
s/sSEI	transition between s and sSEI
sep	separator
sSEI	interface between active material and SEI
sSEI/SEIe	transition between sSEI and SEIe
tot	total

Constants

F	Faraday constant, 96485.3	$\mathrm{C\,mol^{-1}}$
R	universal gas constant, 8.3145	$\mathrm{J\,mol^{-1}\,K^{-1}}$

Abbreviations

AM	active material
CC	constant current
CV	constant voltage
DOE	design of experiments
EC	ethylene carbonate
EIS	electrochemical impedance spectroscopy
EMC	ethyl methyl carbonate
FIB	focused ion beam
LEDC	lithium ethylene dicarbonate

NMC	nickel manganese cobalt oxide
OCP	open circuit potential
P2D	pseudo-two-dimensional
SEI	solid electrolyte interphase
SEM	scanning electron microscopy
SOC	state of charge
SPM	single particle model
TEM	transmission electron microscopy
V	vacancy
VC	vinylene carbonate

A Publications Within the Scope of This Thesis

Journal Publications

1. D. Witt, D. Wilde, F. Baakes, F. Belkhir, F. Röder, and U. Krewer, “Myth and Reality of a Universal Lithium-Ion Battery Electrode Design Optimum: A Perspective and Case Study,” Energy Technol., vol. 9, no. 6, 2000989, 2021.
2. D. Witt, F. Röder, and U. Krewer, “Analysis of Lithium-Ion Battery State and Degradation via Physicochemical Cell and SEI Modeling,” Batteries Supercaps, vol. 5, no. 7, e202200067, 2022.
3. D. Witt, L. Bläubaum, F. Baakes, and U. Krewer, "Origin of Performance Improvements in Lithium-Ion Cells after Fast Formation", Batteries Supercaps, e202400023, 2024.

Conference Contributions

1. D. Witt, F. Röder, U. Krewer, “Physicochemical SEI model for cell diagnosis with C-rate and EIS data”, oral presentation at the 17th Symposium on Modeling and Experimental Validation of Electrochemical Energy Technologies (April 20-22, 2021, online).
2. D. Witt, D. Wilde, F. Baakes, F. Belkhir, F. Röder, U. Krewer, “Model-based screening of electrode designs for charge and discharge”, oral presentation at the 13th Advanced Battery Power Conference (April 28-29, 2021, online).
3. D. Witt, F. Baakes, F. Röder, U. Krewer, “Physicochemical SEI Modeling for a Holistic Understanding of Lithium-Ion Battery Behavior”, oral presentation at the 72nd Annual Meeting of the International Society of Electrochemistry (August 29 - September 3, 2021, online).
4. D. Witt, L. Bläubaum, F. Baakes, U. Krewer, “In-Depth Analysis of the Substantial Effect of Fast Formation on Lithium-Ion Cell Characteristics”, oral presentation at the 242nd ECS Meeting in Atlanta, Georgia, USA (October 9-13, 2022).
5. D. Witt, L. Bläubaum, F. Baakes, U. Krewer, “Detailed Model-based Lithium-Ion Cell Diagnosis after Fast Formation”, oral presentation at the International Battery Production Conference in Braunschweig, Germany (November 7-8, 2022).

B Supporting Information for Model-Based Cell Design Study[1]

[1] Parts of this chapter have been published in Witt, Wilde, Baakes, Belkhir, Röder, Krewer, Energy Technol., 9(6):2000989, 2021 (doi: 10.1002/ente.202000989, CC BY 4.0 [15]).

Table B.1: Complementary equations for the employed model. Variables with a tilde are dimensionless.

Equations			References
$j^{\mathrm{Li}}(x)$	=	$a_\mathrm{s} i_0 \left(\exp\left(\alpha \frac{\eta F}{RT}\right) - \exp\left((1-\alpha)\frac{\eta F}{RT}\right)\right)$	[122]
η	=	$\Phi_\mathrm{s}(x) - \Phi_\mathrm{e}(x) - U_\mathrm{OCP}$	[122]
ε_CBD	=	$r_\mathrm{CBD} \cdot \varepsilon$	[75]
ε_e	=	$1 - \varepsilon - \varepsilon_\mathrm{CBD}$	[75]
ε_e^*	=	$\frac{1-\varepsilon-\varepsilon_\mathrm{CBD}-\varepsilon_\mathrm{crit,liq}}{1-\varepsilon_\mathrm{crit,liq}}, \ \forall \varepsilon_\mathrm{e} : \varepsilon_\mathrm{e} > \varepsilon_\mathrm{crit,liq}$	[75]
ε^*	=	$\frac{\varepsilon-\varepsilon_\mathrm{crit,s}}{1-\varepsilon_\mathrm{crit,s}}, \ \forall \varepsilon : \varepsilon > \varepsilon_\mathrm{crit,s}$	[75]
$\varepsilon_\mathrm{CBD}^*$	=	$\varepsilon_\mathrm{CBD} \frac{\varepsilon_\mathrm{CBD}+\varepsilon-\varepsilon_\mathrm{crit,s}}{1-\varepsilon_\mathrm{crit,s}}, \ \forall \varepsilon_\mathrm{CBD} : \varepsilon_\mathrm{CBD} + \varepsilon > \varepsilon_\mathrm{crit,s}$	[75]
d^cc	=	$\frac{C_\mathrm{theo}}{F c_\mathrm{max} \varepsilon} \cdot \tilde{C}^\mathrm{cc}$	
a_s	=	$\left(1 - \nu_4 \cdot \frac{\varepsilon_\mathrm{CBD}^{\nu_5}}{\varepsilon}\right) \cdot \nu_6 \cdot \frac{1-4(0.75-\varepsilon)^2 \cdot \varepsilon_e}{R}$	[75]
β_2	=	$\varepsilon_\mathrm{CBD}^{\nu_1}$	[75]
τ_a	=	$\varepsilon_e^{-\beta}$	[39]
τ_c	=	$(\varepsilon_\mathrm{e}^*)^{\beta_1+\beta_2} \cdot \varepsilon_\mathrm{e}$	[75]
$\tilde{c}_\mathrm{s}$	=	$\frac{c_\mathrm{s}}{c_\mathrm{s,max}}$	
$\tilde{c}_\mathrm{e}$	=	$\frac{c_\mathrm{e}}{c_\mathrm{e,0}}$	
$\sigma_\mathrm{s,eff,a}$	=	$\varepsilon \cdot \sigma_\mathrm{AM}$	[75]
$\sigma_\mathrm{s,eff,c}$	=	$\varepsilon \cdot \sigma_\mathrm{CBD} \cdot \left(\varepsilon_\mathrm{CBD}^*\right)^{\beta_3} \cdot \frac{1}{2}\left(1 + \tanh\left(\frac{1}{\nu_2}\varepsilon_\mathrm{CBD}^* - \nu_3\right)\right)$ $+ \left(\frac{1}{\sigma_\mathrm{CBD} \cdot \left(\varepsilon_\mathrm{CBD}^*\right)^2 + 2\sigma_\mathrm{c} \cdot (\varepsilon^*)^{1.5}} + \frac{1}{2\sigma_\mathrm{c} \cdot (\varepsilon^*)^{1.5}}\right)^{-1}$	[75]
σ_e	=	$0.0521 \cdot (1 + (\frac{T}{\mathrm{K}} - 228)) \cdot \tilde{c}_\mathrm{e} \cdot \frac{\left(1-1.06\cdot\sqrt{\tilde{c}_\mathrm{e}}+0.353\cdot\left(1-3.59^{-3}\cdot\exp\left(\frac{1000\ \mathrm{K}}{T}\right)\right)\cdot\tilde{c}_\mathrm{e}\right)}{1+\tilde{c}_\mathrm{e}^4\cdot\left(1.48^{-3}\cdot\exp\left(\frac{1000\ \mathrm{K}}{T}\right)\right)}$	[50]
$\sigma_\mathrm{e,eff}$	=	$\frac{\varepsilon_\mathrm{e}}{\tau} \cdot \sigma_\mathrm{e}$	[75]
D_e	=	$1.01 \cdot 10^3 \exp(1.01 \cdot \tilde{c}_\mathrm{e}) \cdot \exp\left(\frac{-1.56^3\ \mathrm{K}}{T}\right) \cdot \exp\left(\frac{-487\ \mathrm{K}}{T} \cdot \tilde{c}_\mathrm{e}\right) \cdot 10^{-10}$	[50]
$D_\mathrm{e,eff}$	=	$\frac{\varepsilon_\mathrm{e}}{\tau} \cdot D_\mathrm{e}$	[50]
$U_\mathrm{OCP,a}$	=	$8.03914 + 5.08225 \cdot \tilde{c}_\mathrm{s} - 12.56166 \cdot \sqrt{\tilde{c}_\mathrm{s}} + 0.44842 \cdot 10^{-5} \cdot \sqrt{\tilde{c}_\mathrm{s}^3}$ $-0.09620 \cdot \exp(15.0006 \cdot (0.1684 - \tilde{c}_\mathrm{s})) - 0.4599 \cdot \exp(2.3166 \cdot (0.5856 - \tilde{c}_\mathrm{s}))$ $-0.9575 \cdot \exp(2.4033 \cdot (0.5124 - \tilde{c}_\mathrm{s})) - 0.0114 \cdot (0.0317 + \tilde{c}_\mathrm{s})^{-1}$	[75]
$U_\mathrm{OCP,c}$	=	$-2.46444 \cdot \tilde{c}_\mathrm{s}^6 + 2.20077 \cdot \tilde{c}_\mathrm{s}^5 + 3.32765 \cdot \tilde{c}_\mathrm{s}^4 - 5.71320 \cdot \tilde{c}_\mathrm{s}^3 + 3.91673 \cdot \tilde{c}_\mathrm{s}^2$ $-2.09035 \cdot \tilde{c}_\mathrm{s} + 4.19975 \cdot \exp\left(-0.03988 \cdot \tilde{c}_\mathrm{s}^{414.66769}\right) + 0.18614$	[75]

Table B.2: The parameter set utilized in the employed model is adopted from Laue et al. [75]. Derived variables can be calculated with equations in Table B.1 and corresponding parameter variations that are defined in Table 3.1. Fitting parameters relate to the equations in Table B.1.

Parameter	Symbol	Anode	Separator	Cathode
Ratio between CBD and AM volume fraction / -	r_{CBD}	0.1	-	0.2273
CBD volume fraction / -	$\varepsilon_{\mathrm{CBD}}$	Table B.1→3.1	-	Table B.1→3.1
Electrolyte volume fraction / -	ε_{e}	Table B.1→3.1	0.5	Table B.1→3.1
Active material volume fraction / -	ε	Table 3.1	-	Table 3.1
Specific surface area / m^{-1}	a_{s}	Table B.1→3.1	-	Table B.1→3.1
Particle radius / µm	R	Table 3.1	-	Table 3.1
Discretization elements in particle / -	n_{P}	4	-	4
Discretization elements in cell / -	n_{cell}	5 & 5	5	5 & 5
Layer thickness / µm	d	Table B.1→3.1	20	Table B.1→3.1
Diffusion coefficient in AM / $\mathrm{m}^2\,\mathrm{s}^{-1}$	D_{s}	$1.18 \cdot 10^{-14}$	-	$4.98 \cdot 10^{-12}$
Diffusion coefficient in electrolyte / $\mathrm{m}^2\,\mathrm{s}^{-1}$	D_{e}	Table B.1→3.1	-	Table B.1→3.1
Bruggeman coefficient / -	β	1.5	-	-
Tortuosity / -	τ	Table B.1→3.1	1	Table B.1→3.1
Electrolyte conductivity / $\mathrm{S\,m}^{-1}$	σ_{e}	Table B.1→3.1	Table B.1→3.1	Table B.1→3.1
Active material conductivity / $\mathrm{S\,m}^{-1}$	σ_{AM}	10	-	0.0161
Carbon-binder domain conductivity / $\mathrm{S\,m}^{-1}$	σ_{CBD}	-	-	760
Charge transfer coefficient / -	α	0.5	-	0.5
Exchange current density / $\mathrm{A\,m}^{-2}$	i_0	0.4935	-	$1.2298 \cdot 10^3$
Double-layer capacitance / $\mathrm{F\,m}^{-2}$	C_{DL}	0.2	-	0.2
Transference number / -	t_{p}	0.24	0.24	0.24
Reference electrolyte concentration / $\mathrm{mol\,L}^{-1}$	$c_{\mathrm{e,ref}}$	1	1	1
Initial electrolyte concentration / $\mathrm{mol\,L}^{-1}$	$c_{\mathrm{e},0}$	1	1	1
Theoretical electrode capacity / $\mathrm{mAh\,cm}^{-2}$	C_{theo}	5.5[d]	-	5[d]
Maximum active material concentration / $\mathrm{mol\,m}^{-3}$	$c_{\mathrm{s,max}}$	24591	-	25429
Initial concentration for charge / $\mathrm{mol\,m}^{-3}$	$c_{\mathrm{s},0,\mathrm{charge}}$	3331	-	25427
Initial concentration for discharge / $\mathrm{mol\,m}^{-3}$	$c_{\mathrm{s},0,\mathrm{discharge}}$	24564	-	1273.3
Temperature / K	T	298.15	298.15	298.15
Fitting parameter for $\sigma_{\mathrm{s,eff,c}}$ / -	$\varepsilon_{\mathrm{crit,liq}}$	-	-	0.075[a]
Fitting parameter for $\sigma_{\mathrm{s,eff,c}}$ / -	$\varepsilon_{\mathrm{crit,s}}$	-	-	0.2[a]
Fitting parameter for τ_{c} / -	β_1	-	-	2.4049[a]
Fitting parameter for τ_{c} / -	β_2	-	-	Table B.1→3.1
Fitting parameter for $\sigma_{\mathrm{s,eff,c}}$ / -	β_3	-	-	2[a]
Fitting parameter for $\sigma_{\mathrm{s,eff,c}}$ / -	β_4	-	-	1.5[a]
Fitting parameter for $\sigma_{\mathrm{e,eff}}$ / -	ν_1	-	-	0.9499[a]
Fitting parameter for $\sigma_{\mathrm{s,eff,c}}$ / -	ν_2	-	-	0.0228[a]
Fitting parameter for $\sigma_{\mathrm{s,eff,c}}$ / -	ν_3	-	-	0.1[a]
Fitting parameter for a_{s} / -	ν_4	0.9037	-	0.9037
Fitting parameter for a_{s} / -	ν_5	1.1270	-	1.1270
Fitting parameter for a_{s} / -	ν_6	4.9118	-	4.9118

[a] adjusted
[d] defined

Table B.3: Identified parameter values in the full-cell parameter study for highest volumetric capacity for the four different operating modes with two-layer electrodes. The best cell configurations are the same for both the initial parameter screening, which did not control for lithium plating, and the subsequent parameter screening, which terminated charging below 0 V vs. Li/Li^+ to prevent lithium plating.

Parameters	**Discharge @ C/10**	**Charge @ C/10**	**Discharge @ 1C**	**Charge @ 1C**
ε_a^{cc} / -	0.65	0.65	0.65	0.45
ε_a^{sep} / -	0.65	0.65	0.55	0.45
ε_c^{sep} / -	0.55	0.65	0.45	0.45
ε_c^{cc} / -	0.65	0.65	0.55	0.55
R_a^{cc} / µm	3	3	3	3
R_a^{sep} / µm	9	9	9	9
R_c^{sep} / µm	3	3	3	9
R_c^{cc} / µm	3	3	3	9
$\tilde{C}_a^{cc}$ / %	75	25	75	75
$\tilde{C}_c^{cc}$ / %	75	25	25	75

Table B.4: Identified parameter values in the full-cell parameter study for highest volumetric capacity for the four different operating modes with single-layer electrodes. The best cell configurations are the same for both the initial parameter screening, which did not control for lithium plating, and the subsequent parameter screening, which terminated charging below 0 V vs. Li/Li^+ to prevent lithium plating.

Parameters	**Discharge @ C/10**	**Charge @ C/10**	**Discharge @ 1C**	**Charge @ 1C**
ε_a / -	0.65	0.65	0.55	0.45
ε_c / -	0.65	0.65	0.45	0.55
R_a / µm	3	3	9	3
R_c / µm	3	9	3	9

C Supporting Information for Model-Based Cell Diagnostics[1]

C.1 Loss of Lithium Inventory due to SEI Growth

The unlithiated graphite active material starts with a relatively high potential vs. Li/Li$^+$. The required amount of lithium to reduce the anode potential to practical values requires a shift in the state of charge (SOC) of the anode. During normal operation, this reversible shift in SOC may seem indistinguishable from an irreversible lithium loss due to SEI growth. However, for a sound estimation of the SEI thickness, only the irreversible loss of lithium inventory should be considered.

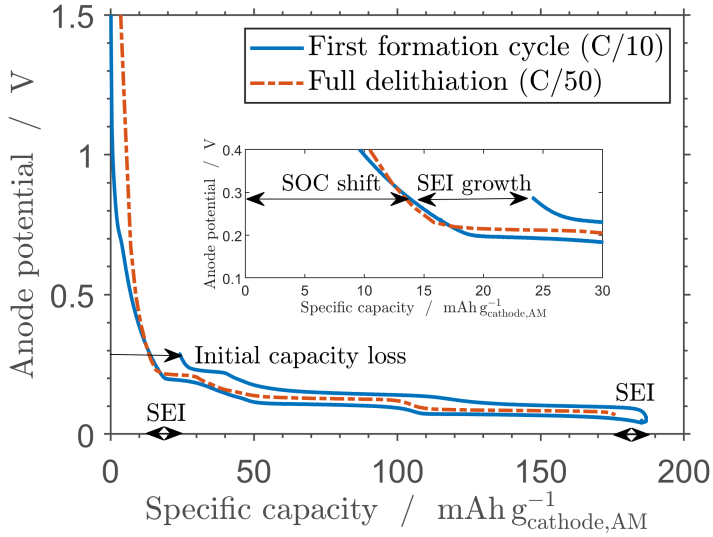

Figure C.1: Comparison of the anode potential during the first formation cycle in a three-electrode setup with an open circuit potential measurement that fully delithiates the anode. The inset shows the deconvolution of the initial capacity loss into a reversible SOC shift and an irreversible capacity loss due to SEI growth.

[1] Parts of this chapter have been published in Witt, Röder, Krewer, Batteries Supercaps, 5(7):e202200067, 2022 (doi: 10.1002/batt.202200067, CC BY 4.0 [16]).

Figure C.1 illustrates the difference between a reversible shift in SOC and irreversible SEI growth. It compares the first formation cycle, including charge and discharge at a C-rate of C/10, with a C/50 discharge after formation. The latter measurement is performed until full delithiation of the anode, which allows to identify irreversible loss of lithium inventory. The blue curve clearly shows that the initially charged capacity during formation cannot be fully recovered during discharge. However, the difference between the charged capacity during formation (blue line) and the discharge capacity during full delithiation (dashed orange line) is much smaller than the observed initial capacity loss. In fact, it is strikingly similar to the highlighted capacity difference in the inset, which is observed for the first formation cycle at the anode potential at the end of discharge. From this, it is concluded that the initial capacity loss originates from a combination of irreversible SEI growth and a theoretically reversible but practically not usable SOC shift within the anode active material. To differentiate between these two aspects, the anode potential at the end of the first discharge is used as a reference point for the estimation of the lithium loss due to SEI growth.

C.2 Objective Functions for Parameterization

In the following, the objective functions are described, which are necessary for the parameterization strategy depicted in Figure 4.3. Parameterization steps I to III employ a mathematical optimization routine based on the MATLAB-function lsqnonlin. It is used to identify those parameter values, which minimize the difference between experiment and simulation. The following equation describes the general optimization problem of the parameter vector X based on a given measurement type

$$X^* : F(X^*) = \min_{X \in \mathbb{R}^N} (|F(X)|) \tag{C.1}$$

with the identified parameter vector X^* and the objective function F. In step I, the initial and maximum lithium concentrations in the anode and cathode active material are identified from the discharge curve at C/10. The objective function contains the squared relative difference between experiment and simulation regarding the total discharge time and the experimentally observed as well as simulated anode and cathode potential at the end of discharge:

$$F_{\text{discharge}}(X) = \sum_{j \in \{a,c\}} \left(\frac{\left(t_{\text{exp,j}}(\text{end}) - t_{\text{sim,j}}(\text{end})\right)^2}{t_{\text{exp,j}}(\text{end})^2} + \frac{\left(V_{\text{exp,j}}(\text{end}) - V_{\text{sim,j}}(\text{end})\right)^2}{\max\left(V_{\text{exp,j}}\right)^2} \right). \tag{C.2}$$

Parameterization step II employs the same objective function. It is used to identify mass transport-related parameters, i.e., anode and cathode tortuosities, as well as solid diffusion coefficients, using discharge curves at C-rates of 1C and 2C. The objective function for this joint parameterization of both C-rates is the sum of the objective functions for each individual C-rate.

Parameterization step III uses a different objective function. Here, the squared relative differences between experimental and simulated real $Z^{'}(k)$ and imaginary part $Z^{''}(k)$ of the impedance response at excitation frequency k are calculated for n frequencies. Anode and cathode differences are added:

$$F_{\mathrm{EIS}}(X) = \sum_{j\in\{a,c\}} \left(\sum_{k=1}^{n} \left(\frac{\left(Z'_{\mathrm{exp,j}}(k) - Z'_{\mathrm{sim,j}}(k)\right)^2}{\max\left(Z'_{\mathrm{exp,j}}\right)^2} + \frac{\left(Z''_{\mathrm{exp,j}}(k) - Z''_{\mathrm{sim,j}}(k)\right)^2}{\max\left(Z''_{\mathrm{exp,j}}\right)^2} \right) \right). \tag{C.3}$$

Importantly, the chosen frequency range was tailored to the available experimental data to avoid the analysis of artifacts, which are inherent to the utilized three-electrode setup. Future studies may need to adjust this frequency range to enable a meaningful parameter identification.

C.3 Identifiability of Initial Parameter Set

The assessment of the parameter identifiability was done primarily via physical considerations and individual parameter studies, as shown in Chapter 4 for four SEI parameters (see Figure 4.5 and 4.6). In the following, the reasoning behind the employed three-step parameterization strategy from Table 4.1 for the initial model parameterization is explained.

Before any mathematical optimization of model parameters is performed, all available parameter values from manufacturer specifications and literature are fixed (see Table C.4). Here, the initial SEI thickness is calculated directly from the initial capacity loss during cell formation. Due to the low C-rate of C/10, the estimation of the SEI thickness is not substantially affected by any overpotentials.

In the first parameterization step, a starting point for the initial and maximum lithium concentrations in the active materials is calculated based on cycle 0, using the initial and final half-cell potentials at a C-rate of C/10. With these estimates, the mathematical optimization must compensate only for the neglected kinetic and transport losses at this fairly low C-rate. Considering the close link between the four concentrations and the two half-cell potentials at the beginning and at the end of C/10 discharge, the identifiability of these parameters is deemed sufficient.

At C-rates of 1C and 2C, substantial overpotentials can be observed in the experimental data. For both anode and cathode, the electrode tortuosity, i.e., the effective transport properties in the

electrolyte phase, and the solid diffusion in the active material are parameterized. At first sight, these two parameters for each electrode may have the same effect: they both increase voltage losses by inducing concentration gradients in the electrolyte and solid phase, respectively. The sensitivity analysis in Figure C.2 illustrates the effect of these four parameters on the discharge behavior at 1C and 2C. From the total Sobol indices, it can be seen that the anode tortuosity is the most sensitive parameter, followed by the cathode solid diffusion coefficient, the cathode tortuosity, and finally the anode solid diffusion coefficient. Here, the first-order Sobol index of the anode solid diffusion coefficient is practically zero, indicating strong multivariate dependence. In the end, the estimated parameter value for the anode solid diffusion coefficient remains within the range of reported values from other studies [268, 269].

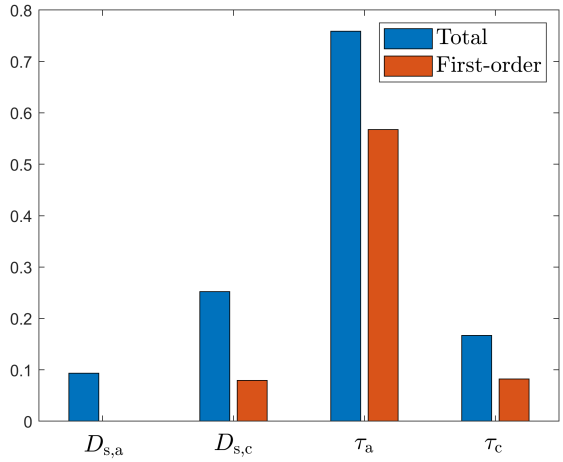

Figure C.2: Polynomial-Chaos-Expansion-based Sobol sensitivity analysis for the initial parameter estimation described in Table 4.1 based on discharge curves at C-rates of 1C and 2C. Both the total and the first-order Sobol indices are shown for the anode and cathode solid diffusion coefficients and tortuosities. The sensitivity analysis was performed with the UQLab framework, using gaussian distributions for the investigated model parameters [270, 271].

Finally, thirteen parameters are optimized based on EIS. To achieve reasonable parameter identifiability, the number of unknown model parameters must be matched by an equal number of features in the experimental data. For impedance data, the amplitude and the phase shift of the impedance response contain various features as a function of frequency. As typically two arcs are seen in the anode half-cell impedance spectrum and a single arc for the cathode, this allows for the identification of six model parameters, i.e., one rate constant and one double-layer capacitance for each arc. As discussed in the main manuscript, the sensitivity of the contact resistances and the corresponding double-layer capacitances at the current collectors is not as high as for the earlier mentioned interfacial processes. The data does not show a clear semicircle at high

frequencies, which could be clearly attributed to the current collectors. For this reason, the interpretation of the current collector-related parameters should be done with caution. This leaves three model parameters: the ionic conductivity of the SEI and the electrical conductivity of anode and cathode. Since the electrolyte properties were adopted from measurements by Landesfeind et al., the electrical conductivities of anode and cathode define the ohmic contribution at high frequencies [50]. These conductivities are directly related to a shift of the real part of the anode and cathode half-cell impedance responses. Here, the ionic conductivity of the SEI can also cause a shift of the impedance response to higher or lower ohmic values. However, this parameter additionally changes the shape of the impedance response as shown in Figure 4.6b, enabling a differentiation between these two parameters. Moreover, the anode impedance could only be reproduced with a high electrical conductivity, which is likely for a graphite-based anode. At the same time, this reduces the parameter sensitivity as a result of the diminishing impedance changes upon a further parameter improvement. This highlights that the estimated ionic conductivity of the SEI is at least as high as reported. It further supports the conclusion that the SEI ionic conductivity could not limit the performance in the examined cell.

C.4 Identifiability of Aging-Related Parameter Changes

Along aging, most of the initially optimized model parameters were fixed to their initial values. The initial and maximum lithium concentrations in the anode and cathode are fixed as inherent properties of the active material. The SEI thickness is adjusted to account for changes in the cyclable lithium inventory in the cell. However, it was observed that the sole adjustment of the SEI thickness along aging could not capture the half-cell potentials and the capacity at the end of discharge accurately. Loss of cathode active material could be ruled out as this would also change the cathode potential along discharge rather than exclusively altering the electrode's behavior at the end of discharge. Due to the fast diffusion in the electrolyte phase compared to the cathode active material, the cathode tortuosity could not change the cathode potential profile. With a slight improvement of the cathode solid diffusion coefficient, both anode and cathode potential profiles could be described accurately. For this reason, both the SEI thickness and the solid diffusion coefficient in the cathode active material were optimized based on C/10 discharge.

For discharge at C-rates of 1C and 2C, the anode solid diffusion coefficient and the cathode tortuosity are fixed to their initial values due to their comparably low sensitivity as evident from the sensitivity analysis in Figure C.2.

Based on impedance data, six model parameters are updated. The electrical electrode conductivities are assumed to remain unchanged during the first 100 cycles. However, substantial changes

may be expected for long-term aging due to the degradation of the conductive network [253]. As the experimental data did not show distinctive features at high frequencies, the two contact resistances and double-layer capacitances for the dynamics at the anode and cathode current collectors are fixed. Any change to the ohmic part of the anode half-cell impedance at high frequencies is attributed to the ionic conductivity of the SEI. The rate constants for the two interfacial processes at the SEI are kept constant and the surface site density is adjusted. However, the cell behavior could also be described with changes in the two rate constants. Without knowledge of the interfacial structure and composition of the SEI along aging, a change in the available surface sites and a change in the reactivity of the available sites are both possible. In addition to the surface site density, the two interfacial double-layer capacitances of the SEI are adjusted. The SEI diffusion coefficient is kept constant along aging since the feature from the parameter study in Figure 4.6c could not be observed in the experiment. Finally, changes in the cathode half-cell impedance are attributed to changes in its reaction rate constant and double-layer capacitance.

C.5 Tables

Table C.1: Complementary equations for the SEI-extended P2D model.

Description	Equation
Reaction current density (cathode)	$j^{\mathrm{Li}} = 2 j_0 a_\mathrm{s} \sinh\left(\frac{\alpha \mathrm{F}}{\mathrm{R}T}\eta\right)$
Overpotential (cathode)	$\eta = \phi_\mathrm{s} - \phi_\mathrm{e} - E^\mathrm{eq}$
Exchange current dens. (cathode)[194, adj.]	$j_0 = k_0 F c_{\mathrm{s,max}} \left(1 - X_{\mathrm{Li(s)}}\right)^\alpha \left(a_{\mathrm{Li(e)}}\right)^\alpha \left(X_{\mathrm{Li(s)}}\right)^{1-\alpha}$
Degree of lithiation	$X_{\mathrm{Li(s)}} = \frac{c_\mathrm{s}}{c_{\mathrm{s,max}}}$
Activity in electrolyte phase	$a_{\mathrm{Li(e)}} = \frac{c_\mathrm{e}}{c_{\mathrm{e},0}}$
Equilibrium potential[194]	$E^\mathrm{eq} = \frac{\Delta G^0_{\mathrm{Li(s)}=\mathrm{V(s)}+\mathrm{Li}^0+\mathrm{e}^-}}{F} + \frac{\mathrm{R}T}{\mathrm{F}} \ln\left(\frac{a_{\mathrm{V(s)}}}{a_{\mathrm{Li(s)}}}\right)$
Activity intercalated lithium[194]	$\mathrm{a}_{\mathrm{Li(s)}} = \gamma_{\mathrm{Li(s)}} X_{\mathrm{Li(s)}}$
	$\ln\left(\gamma_{\mathrm{Li(s)}}\right) = \frac{1 - {X_{\mathrm{Li(s)}}}^2}{RT} \sum_{\mathrm{m}=0}^{\mathrm{N}} A_\mathrm{m} \left(2X_{\mathrm{Li(s)}} - 1\right)^\mathrm{m} \left(1 + \frac{2\mathrm{m}X_{\mathrm{Li(s)}}}{2X_{\mathrm{Li(s)}} - 1}\right)$
Activity lithium vacancy[194]	$\mathrm{a}_{\mathrm{V(s)}} = \gamma_{\mathrm{V(s)}} \left(1 - X_{\mathrm{Li(s)}}\right)$
	$\ln\left(\gamma_{\mathrm{V(s)}}\right) = \frac{{X_{\mathrm{Li(s)}}}^2}{RT} \sum_{\mathrm{m}=0}^{\mathrm{N}} A_\mathrm{m} \left(2X_{\mathrm{Li(s)}} - 1\right)^\mathrm{m} \left(1 - \frac{2\mathrm{m}\left(1 - X_{\mathrm{Li(s)}}\right)}{2X_{\mathrm{Li(s)}} - 1}\right)$
Active surface area	$a_\mathrm{s} = \frac{3\varepsilon_\mathrm{s}}{R_\mathrm{s}}$
Effective electrical conductivity	$\sigma_{\mathrm{s,eff}} = \varepsilon_\mathrm{s} \sigma_\mathrm{s}$
Effective diffusion coefficient	$D_{\mathrm{e,eff}} = \frac{\varepsilon_\mathrm{e}}{\tau} D_\mathrm{e}$
Diffusion coefficient electrolyte[50]	$D_\mathrm{e} = 1.01 \cdot 10^{-7} \exp\left(1.01\tilde{c}_\mathrm{e}\right) \exp\left(\frac{-1.56 \cdot 10^3\ \mathrm{K}}{T}\right) \exp\left(\frac{-487\ \mathrm{K}}{T}\tilde{c}_\mathrm{e}\right)$
Effective ionic conductivity	$\sigma_{\mathrm{e,eff}} = \frac{\varepsilon_\mathrm{e}}{\tau} \sigma_\mathrm{e}$
Effective diffusive ionic conductivity	$\sigma_{\mathrm{De,eff}} = 2\frac{\mathrm{R}T}{\mathrm{F}} \left(t_\mathrm{p} - 0.5\right) \sigma_{\mathrm{e,eff}}$
Ionic conductivity electrolyte[50]	$\sigma_\mathrm{e} = 0.0521(1 + (\frac{T}{\mathrm{K}} - 228))\tilde{c}_\mathrm{e} \frac{1 - 1.06\sqrt{\tilde{c}_\mathrm{e}} + 0.353\left(1 - 3.59 \cdot 10^{-3} \exp\left(\frac{1000\ \mathrm{K}}{T}\right)\right)\tilde{c}_\mathrm{e}}{1 + {\tilde{c}_\mathrm{e}}^4 1.48 \cdot 10^{-3} \exp\left(\frac{1000\ \mathrm{K}}{T}\right)}$

Table C.2: Chemical potentials with unit of $\mathrm{J\,mol^{-1}}$ used in the employed model.

Parameter	Value	Source
$\mu^0_{\mathrm{a,Li(s)}}$	$-1.77 \cdot 10^4$	fit
$\mu^0_{\mathrm{a,V(s)}}$	0	[124]
$\mu^0_{\mathrm{a,Li(sSEI)}}$	0	defined
$\mu^0_{\mathrm{a,V(sSEI)}}$	0	defined
$\mu^0_{\mathrm{a,Li(SEIe)}}$	0	[124]
$\mu^0_{\mathrm{a,V(SEIe)}}$	0	defined
$\mu^0_{\mathrm{c,Li(s)}}$	$-3.70 \cdot 10^5$	fit
$\mu^0_{\mathrm{Li^+(e)}}$	0	[194]
$\mu^0_{\mathrm{electron,s}}$	0	[194]

Table C.3: Redlich-Kister coefficients with unit of $\mathrm{J\,mol^{-1}}$ obtained from parameterization for the graphite anode and the NMC622 cathode.

Coefficient	Anode	Cathode
A_0	-11037	-26675
A_1	10893	10521
A_2	-12560	-8374
A_3	39184	-10336
A_4	37543	12414
A_5	-131057	14013
A_6	-317290	-18154
A_7	517539	-27294
A_8	820354	-11514
A_9	-1107077	35838
A_{10}	-946972	50617
A_{11}	1210798	-27031
A_{12}	333686	-40315
A_{13}	-443283	0

Table C.4: Initial parameter set utilized in the employed model. The parameter values are obtained from three different sources: adjusted by model parameterization, given by manufacturer specifications, or adopted from literature. For parameters that relate to two SEI interfaces, the value for the interface sSEI is shown first, followed by the value for the SEIe interface.

Parameter	**Symbol**	**Anode**	**Sep.**	**Cathode**
Electrolyte volume fraction[s] / -	ε_e	0.37	0.74	0.24
Active material volume fraction[s] / -	ε_s	0.59	-	0.71
Particle radius[s] / µm	R_s	9.5	-	5.1
Layer thickness[s] / µm	d	84	220	68
Tortuosity[a] / -	τ	14.5	1.4	3.6
Transference number[123] / -	t_p	0.24	0.24	0.24
Diffusion coefficient active material[a] / $m^2\,s^{-1}$	D_s	$1.80 \cdot 10^{-14}$	-	$2.85 \cdot 10^{-15}$
Active material conductivity[a] / $S\,m^{-1}$	σ_s	1346	-	0.08
Reaction rate constant anode[a] / s^{-1}	$k_{0,a}$	40.59, $2.83 \cdot 10^6$	-	-
Reaction rate constant cathode[a] / $m\,s^{-1}$	$k_{0,c}$	-	-	$1.56 \cdot 10^{-9}$
Activation energy[a,124] / $kJ\,mol^{-1}$	E_a	2.89, 28.95	-	-
Double-layer capacitance[a] / $F\,m^{-2}$	C_{DL}	1.28, 1.67	-	0.30
Double-layer capacitance current collector[a] / $F\,m^{-2}$	$C_{DL,cc}$	1.01	-	8.07
Contact resistance[a] / $\Omega\,m^2$	R_{cc}	$1.56 \cdot 10^{-4}$	-	$8.12 \cdot 10^{-5}$
Initial electrolyte concentration[s] / $mol\,L^{-1}$	$c_{e,0}$	1	1	1
Maximum active material concentration[a] / $mol\,m^{-3}$	$c_{s,max}$	22930	-	21836
Initial active material concentration[a] / $mol\,m^{-3}$	$c_{s,0}$	21183	-	914
SEI diffusion coefficient[a,189] / $m^2\,s^{-1}$	D_{SEI}	$1 \cdot 10^{-11}$	-	-
SEI ionic conductivity[a] / $S\,m^{-1}$	κ_{SEI}	$8.35 \cdot 10^{-4}$	-	-
SEI surface site density[a,124] / $mol\,m^{-2}$	Γ	$1 \cdot 10^{-5}$	-	-
SEI thickness[a] / nm	d_{SEI}	85.8	-	-
SEI transference number[148] / -	$t_{p,SEI}$	0.97	-	-
Molar SEI volume[237] / $m^3\,mol^{-1}$	$\tilde{V}_{Li_2CO_3}$	$3.50 \cdot 10^{-5}$	-	-
Temperature / K	T	293.15	293.15	293.15

[a] adjusted

[s] specified by manufacturer

Table C.5: Measurement parameters for cell formation, characterization, and cycling. The capacity test is used to set the currents for the respective C-rates after formation. The cell characterization and cycling procedure alternate up to a total of 100 cycles, ending with a final cell characterization. For simplicity, this cycle count omits all cycles from the cell characterization procedure.

Procedure	Parameter	Value
General	Temperature	20 °C
	CV-step current-cutoff	C/20
	Cutoff voltages	2.9 V, 4.2 V
	Rest times	1 min / 10 min after charge/discharge
Initial rest time		12 h
Cell formation		2 cycles C/10 (charge with CV step)
Capacity test		C/10 (charge/discharge with CV step)
Cell characterization	Voltage adjustment	3.7 V, 1C charge with CV step
	Rest time	2 h
	Current pulse	1C charge for 1 s
	Rest time	2 h
	Current pulse	1C discharge for 1 s
	Rest time	2 h
	EIS	see Table C.6
	Voltage adjustment	2.9 V, 1C CC-CV discharge
	Symmetric C-rate test	1× C/10 CC-CV charge/discharge
	Symmetric C-rate test	2× [1C, 2C, 3C, 4C, 5C] CC-CV charge/discharge
Cell cycling	50 cycles	2C (charge with CV step)

Table C.6: Parameters for electrochemical impedance spectroscopy measurements. Each frequency range has a different number of measurement points per decade.

Parameter	Value
Temperature	20 °C
Mode	galvanostatic
Current amplitude	C/10
Frequency ranges	10^6 Hz to 1 Hz, 1 Hz to 0.1 Hz, 0.1 Hz to 0.01 Hz
Data points/decade	20, 10, 5

D Supporting Information for Cell Formation Study[1]

D.1 Analysis of Experimental Data

D.1.1 Further Analysis of Formation Procedures at 20 °C

Figure D.1 shows the full-cell impedance spectra for all three formation procedures at 20 °C. It can be seen that the reference formation F@C/10 features the highest impedance response. Considering similar anode half-cell impedance spectra for all these cells, the formation procedure must affect the cathode reaction kinetics. However, reaction kinetics alone cannot explain the observed differences in the cathode half-cell potentials during discharge (see Section D.2.1).

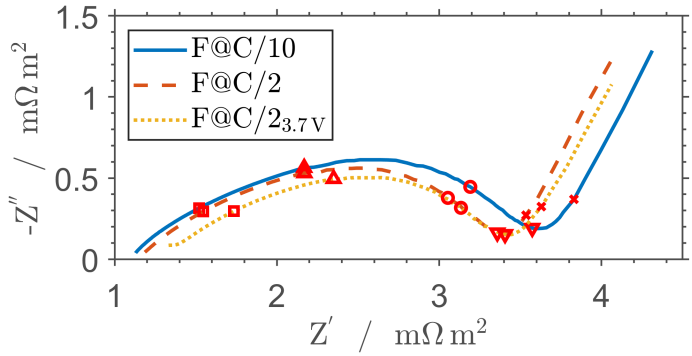

Figure D.1: Full-cell impedance spectra directly after formation for all three formation variations at 20 °C and a cell voltage of 3.7 V. Five frequencies are highlighted with red markers: 1 kHz (□), 100 Hz (Δ), 10 Hz (○), 1 Hz (∇), and 0.1 Hz (×).

Figure D.2 displays the differential voltage analysis of the C/10 discharge data directly after formation. Herein, F@C/$2_{3.7\,V}$ consistently demonstrates a higher capacity across both anode

[1] Parts of this chapter have been published in Witt, Bläubaum, Baakes, Krewer, Batteries Supercaps, e202400023, 2024 (doi: 10.1002/batt.202400023, CC BY 4.0 [17]).

and cathode compared to the reference formation F@C/10. Given that the characteristic features still occur, but at shifted positions, a change in the accessible active material of anode and cathode is expected [29, 139].

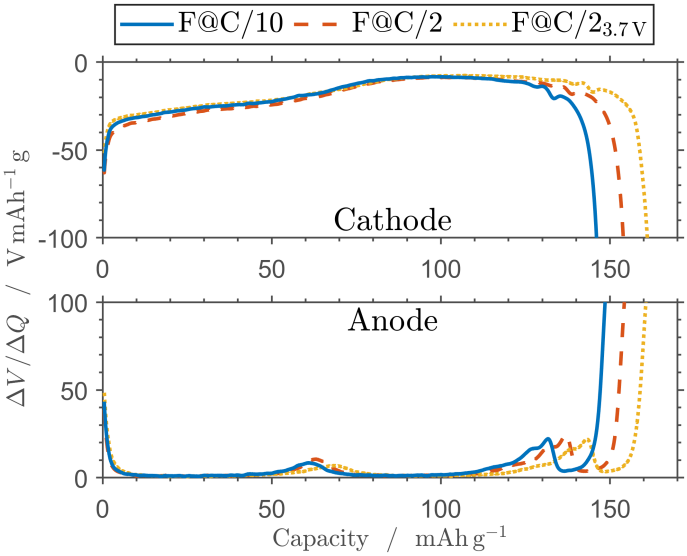

Figure D.2: Differential voltage analysis of C/10 half-cell discharge data directly after formation for all three formation procedures at 20 °C.

Figure D.3 depicts the reproducibility of the full-cell and anode half-cell impedance spectra after formation for all three formation procedures at 20 °C. The data show small cell-to-cell variations with one exception: the full-cell impedance F@C/2$_{3.7\,\mathrm{V}}$ has a notable ohmic offset. Nonetheless, the anode half-cell impedance is very similar between the cells, which indicates a poor electrical contact of the three-electrode cell during the EIS measurement. After reconnecting this cell for further cycling and characterization, this offset is no longer observable. Figure D.4 shows the full-cell and anode half-cell impedance spectra after 100 cycles for all three formation procedures at 20 °C. In this instance, an artifact is observable in the anode half-cell impedance of F@C/2 (cell 2), characterized by a loop preceding the transition into the diffusion tail. For meaningful model-based cell diagnostics, it is crucial to select data without such clear distortions.

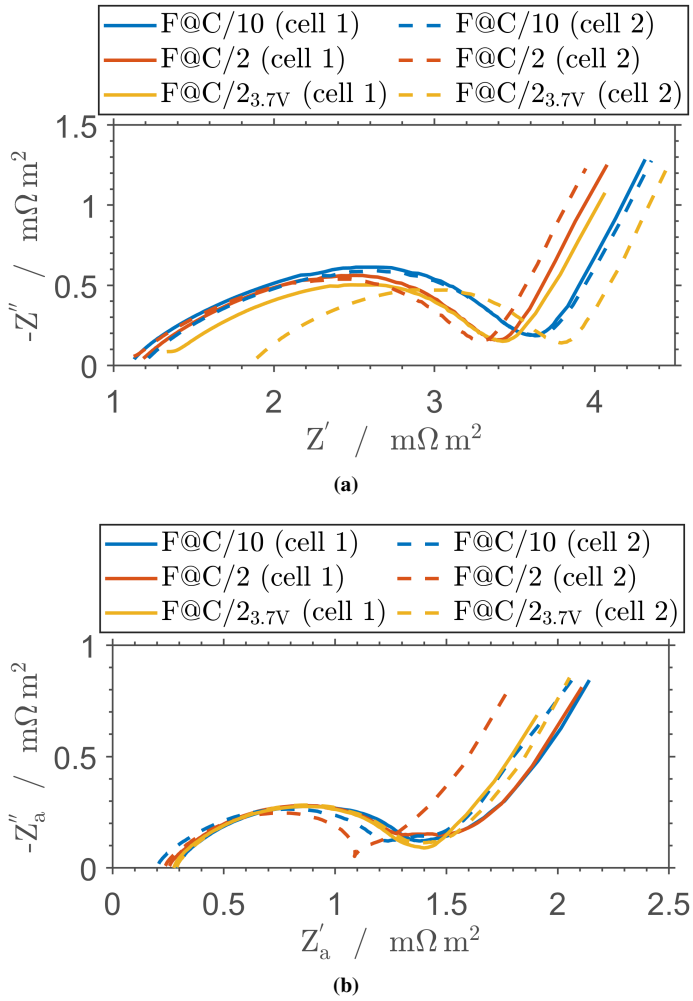

Figure D.3: Comparison of experimental cell-to-cell variations of (a) full-cell and (b) anode half-cell impedance spectra directly after formation for all three formation variations at 20 °C and a cell voltage of 3.7 V. For the model-based analysis of the formation procedures, always the first cell was considered.

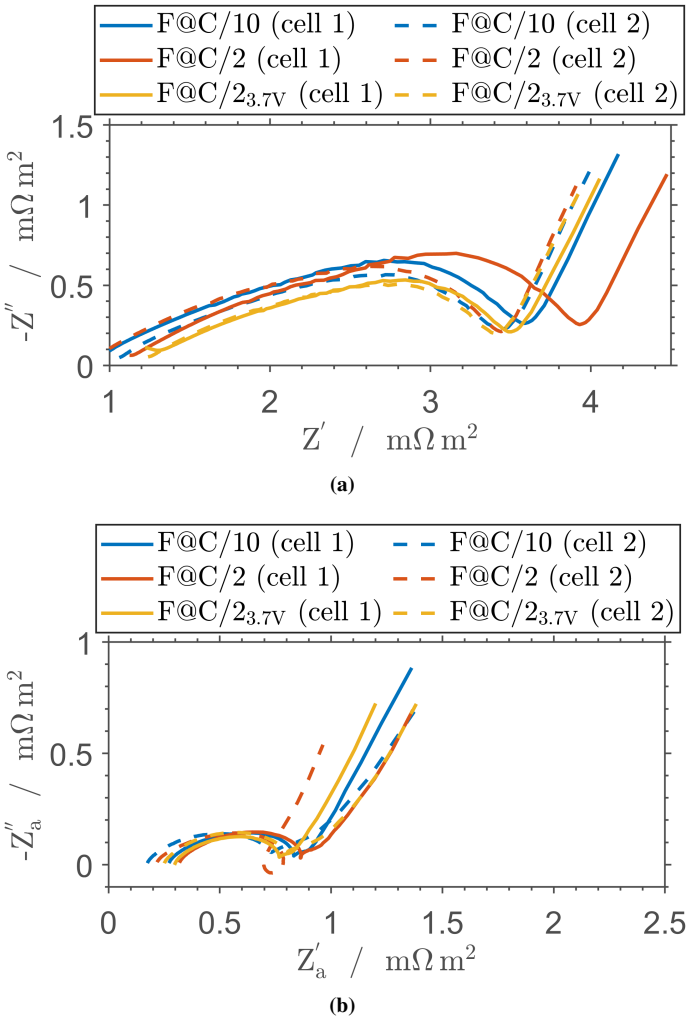

Figure D.4: Comparison of experimental cell-to-cell variations of (a) full-cell and (b) anode half-cell impedance spectra after 100 cycles for all three formation variations at 20 °C and a cell voltage of 3.7 V. For the model-based analysis of the formation procedures, always the first cell was considered.

D.1.2 Anode Half-Cell Potentials during Formation at 35 °C and 50 °C

In Chapter 5, it was observed that cells had a reduced fast charge capability, when the formation was done at 35 °C or 50 °C. Although they could match or even outperform the benchmark F@C/10 at 20 °C in terms of 2C discharge capacity, they still lagged behind the best-performing

cell F@C/$2_{3.7\,V}$ at 20 °C. Analyzing existing research already offered insights into possible reasons for the underperformance of cells undergoing formation at elevated temperatures. The following examination of the anode potentials during formation adds weight to the suggested major causes, i.e., faster kinetics for parasitic side reactions and thermally-induced decomposition of SEI components.

Figure D.5a shows the anode potentials during cell formation at 35 °C. The curves resemble the ones for 20 °C (see Figure 5.4a). This suggests similar electrochemical conditions for SEI formation. Yet, it is essential to bear in mind that also chemical reactions take place. These are affected by both the increased diffusivity and reactivity of reaction products at elevated temperatures. For instance, the electrochemical reduction of the additive vinylene carbonate can form radicals, triggering a purely chemical chain polymerization [272]. This goes hand-in-hand with reactions between SEI components and electrolyte, which become increasingly relevant at elevated temperatures [241]. Overall, this could lead to a different surface film structure despite a comparable initial capacity loss.

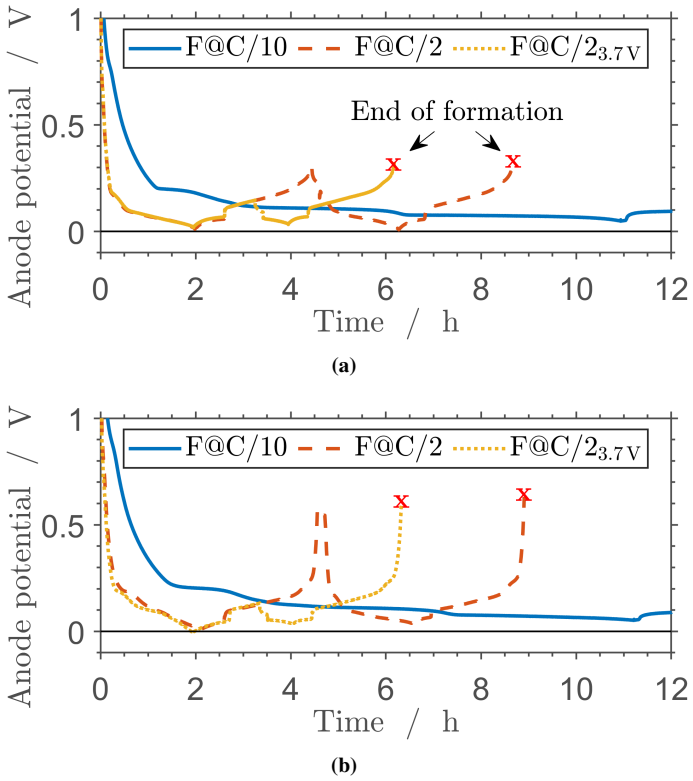

Figure D.5: Anode half-cell potentials during formation at (a) 35 °C and (b) 50 °C. The end of the formation procedures F@C/2 and F@C/$2_{3.7\,V}$ is highlighted with red markers.

Figure D.5b shows the anode potentials during cell formation at 50 °C. Here, the shape of the potential curves changes. This is especially evident from the anode potentials for F@C/2 and F@C/$2_{3.7\,V}$ at the end of discharge, which are elevated by about 0.2 V compared to the formation procedures at both 20 °C and 35 °C. This is most likely related to the cathode. Here, the faster solid diffusion at elevated temperatures reduces concentration gradients within the active material, slightly delaying the cathode voltage drop at the end of discharge and shifting it to the anode. Eventually, this leads to a higher anode potential due to the extended delithiation. This effect of the cathode solid diffusion coefficient on the voltage drop toward the end of discharge is also discussed in Section D.2.1 in the context of model parameter identifiability.

Nonetheless, an effect of the formation temperature on the initial capacity loss is still very much relevant for the shallow formation cycling F@C/$2_{3.7\,V}$. In this case, the extended duration at low anode and high cathode potentials seems overall detrimental. The combination of thermally-induced SEI decomposition and its rapid new formation could form a vicious cycle, especially due to the higher reactivity of the nascent SEI [254]. The negative impact is evident from both the higher initial capacity loss and the poor fast charge and fast discharge performance.

D.1.3 EIS Data for all Formation Variations

As discussed before, the overall performance disadvantage of elevated formation temperatures may be related to the thermally-induced decomposition of SEI components like LEDC and inorganic lithium carbonate [241]. If the initial SEI could decompose already during formation, a well-protective surface film may not be formed. The result could be ongoing SEI growth after formation, potentially creating unfavorable SEI structures. The poor performance at elevated C-rates already suggested an adverse effect on transport processes and reaction kinetics in the cell. The EIS data in Figure D.6 support this. They show a straightforward trend, independent of the formation procedure: the higher the temperature, the larger the impedance response. This indicates changes in reaction kinetics, which may be related to a different surface structure or composition on both anode and cathode active material.

Figure D.7 shows the EIS data after 100 cycles. Here, the initial trend almost inverts. The highest formation temperature features the smallest impedance response for all formation procedures. This may originate from a restructuring of the SEI. The shift to higher ohmic values could arise from a lower ionic conductivity of the SEI, whereas the shrinkage of the semicircle may be attributed to a larger electrochemically active surface area, e.g., due to particle cracking, or a different surface composition, which may improve reaction kinetics. However, these changes are not expected to result in substantial performance differences. For instance, the shallow formation cycling F@C/$2_{3.7\,V}$ features fairly similar impedance spectra for formation at 20 °C and 50 °C. Yet, their fast charge and fast discharge behavior differs substantially. Hence, additional changes

at the electrode or particle level must exist that EIS cannot precisely identify. These changes may include deteriorated transport within the pore volume due to surface film formation and pore blocking [250]. Additionally, the effective solid diffusion within the active material particles could be altered, e.g., by their surface composition and structure [48, 226].

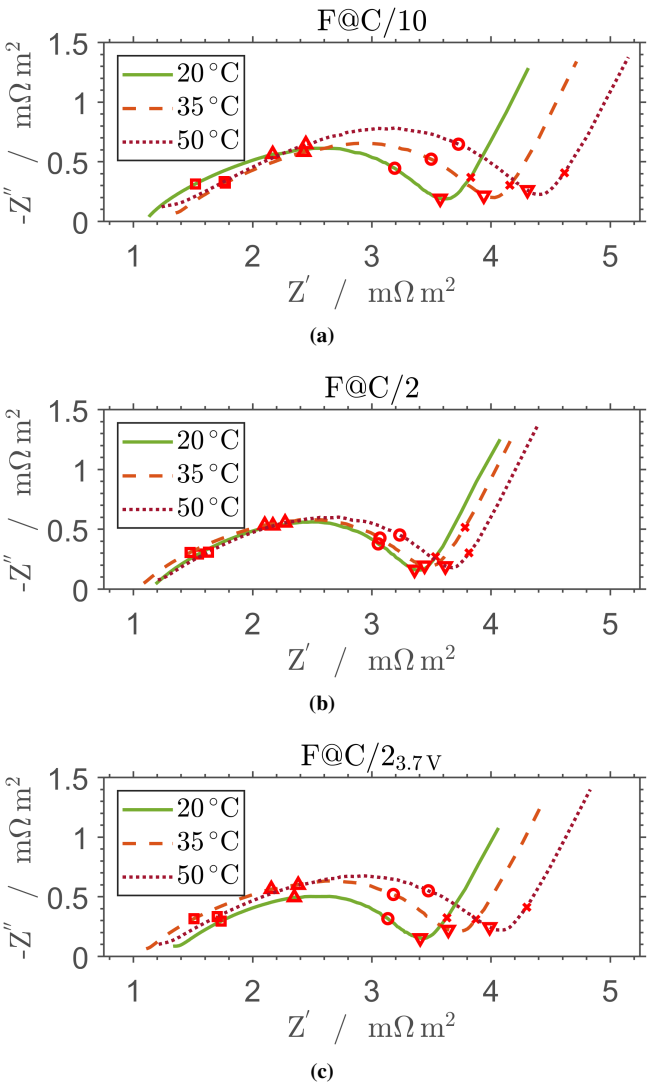

Figure D.6: Comparison of full-cell impedance spectra directly after formation for formation procedures (a) F@C/10, (b) F@C/2, and (c) F@C/$2_{3.7\,V}$ at a cell voltage of 3.7 V. Each plot compares the impedance response for formation temperatures of 20 °C, 35 °C, and 50 °C. Five frequencies are highlighted with red markers: 1 kHz (□), 100 Hz (Δ), 10 Hz (○), 1 Hz (∇), and 0.1 Hz (×).

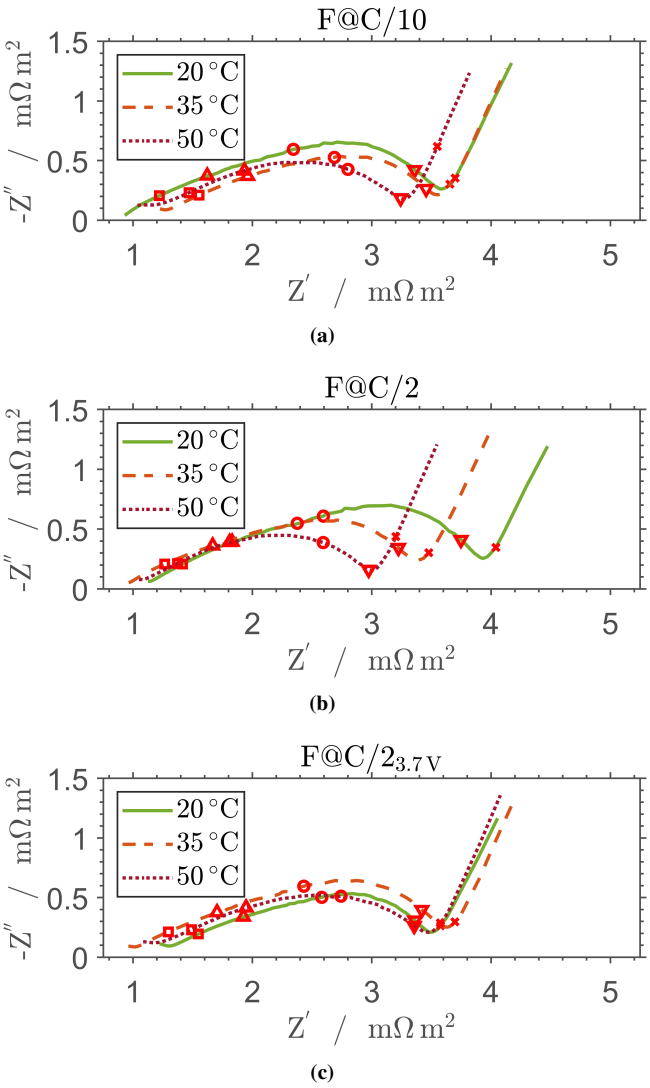

Figure D.7: Comparison of full-cell impedance spectra after 100 cycles for formation procedures (a) F@C/10, (b) F@C/2, and (c) F@C/$2_{3.7\,V}$ at a cell voltage of 3.7 V. Each plot compares the impedance response for formation temperatures of 20 °C, 35 °C, and 50 °C. Five frequencies are highlighted with red markers: 1 kHz (□), 100 Hz (Δ), 10 Hz (○), 1 Hz (∇), and 0.1 Hz (×).

D.1.4 Effect of Formation on Cell Performance at 3C

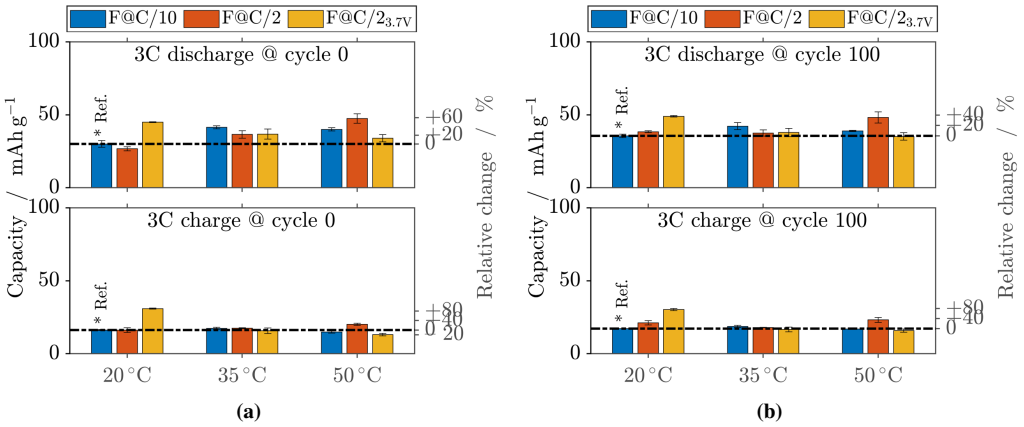

Figure D.8: Comparison of 3C discharge and charge capacities (a) directly after formation and (b) after 100 cycles as a function of formation procedure and formation temperature. The indicated standard deviations are based on two cells for each formation variation. The dashed-dotted line indicates the performance of the formation F@C/10 at 20 °C, which is used as the reference (marked by *).

D.2 Model-Based Cell Diagnosis

D.2.1 Performance-Sensitive Model Parameters

To accurately interpret parameter estimates and their evolution with aging, it is essential to grasp how these parameters affect cell performance. Furthermore, it helps to develop a meaningful parameterization strategy in the first place. For instance, concurrently estimating model parameters that affect the same feature in the experimental data is problematic. If parameters are closely intertwined, both the absolute parameter estimates and their trend along aging may be distorted, potentially leading to false narratives in their interpretation. To truly add value to the analysis of experimental data through model-based cell diagnostics, this kind of uncontrolled interdependence between the model parameters should be avoided during parameterization. A thorough understanding of the effects of individual model parameters on the cell behavior helps with this.

The following analysis showcases two active material-related parameters, four transport-related parameters, and four kinetics-related parameters, including the effect of the SEI. The parameters are varied individually, i.e., all other model parameters are kept constant, and the actual parameter variations are defined individually for each parameter to reflect realistic parameter ranges. The

medium values correspond to the estimated parameter values for the reference formation F@C/10 at 20 °C directly after formation, i.e., cycle 0 in Table D.2. The discharge simulations comprise C-rates of C/10, 1C, and 2C.

A variation of the maximum lithium concentration scales the lithium storage capability of the active material, effectively scaling the capacity of the whole electrode. In a real cell, changes in this parameter may result from variations in the actual active material volume fraction compared to the intended electrode formulation. Another significant factor is loss of active material, which affects the amount of material that remains electrically connected and in contact with the electrolyte phase.

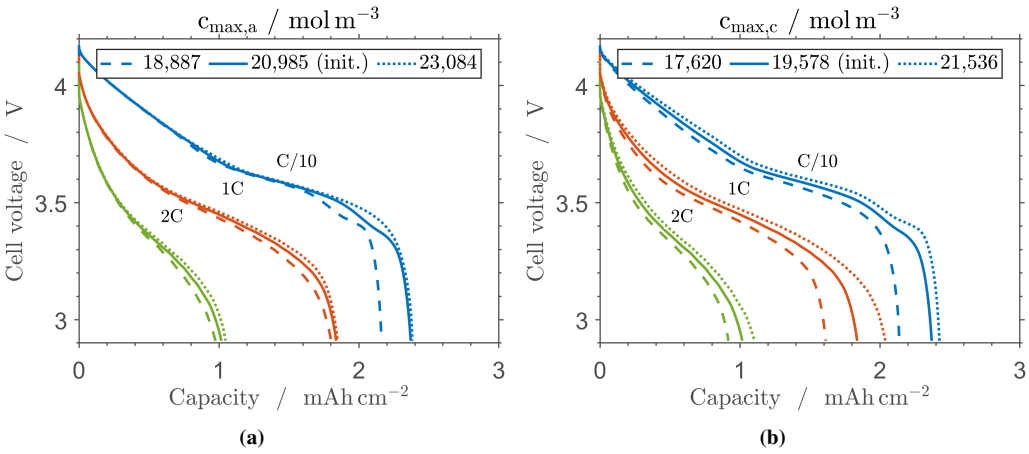

Figure D.9: Simulated discharge curves at C/10, 1C, and 2C for a ±10% variation of the maximum lithium concentration in (a) anode and (b) cathode active material. To maintain the same cell voltage at the beginning of discharge, the initial lithiation degree of the active materials is kept constant. The solid line represents the simulation of the parameterized reference cell F@C/10 at cycle 0.

Figure D.9a and Figure D.9b depict the effect of the maximum lithium concentration in the anode and cathode active material particles, respectively. For the sake of better comparability, the initial lithiation degree at the beginning of discharge, and thus the initial cell voltage, are kept constant. It can be seen that an increase in this parameter for either the anode or the cathode has only a small effect on the C/10 discharge capacity. This is related to the rapid change of both half-cell potentials toward the end of discharge, which shifts the limitation from one electrode to the other with a minimal impact on the discharge capacity. However, the effect on the cell voltage is more pronounced for a variation of the maximum lithium concentration of the cathode active material. A decrease of either of the two parameters results in an almost proportional decrease of the C/10 discharge capacity. In contrast, the 1C and 2C discharge capacity are primarily affected by the cathode. An improvement on the anode side has almost no effect on the discharge capacity and cell voltage. For 2C discharge, a 10% deterioration has no substantial effect on the discharge

capacity, though a decrease of the cell voltage can be observed. In contrast, both a deterioration and an improvement on the cathode side have a notable effect on the end of discharge and the cell voltage. Overall, an unambiguous determination of these parameters is possible due to their unique effect on the C/10 discharge capacity and the corresponding half-cell potentials.

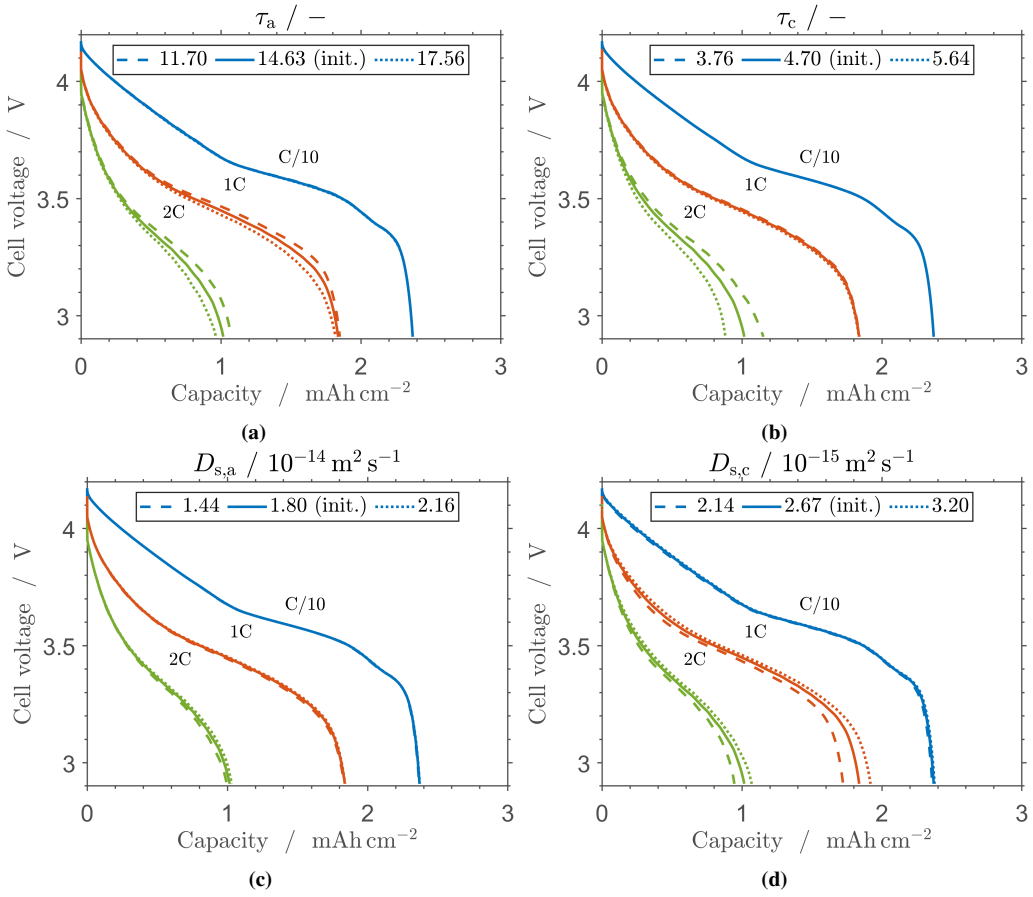

Figure D.10: Simulated discharge curves at C/10, 1C, and 2C for a ±20% variation of (a) anode tortuosity, (b) cathode tortuosity, (c) anode solid diffusion coefficient, and (d) cathode solid diffusion coefficient. The solid line represents the simulation of the parameterized reference cell F@C/10 at cycle 0.

Figure D.10a and Figure D.10b show the effect of the anode and cathode tortuosity, respectively. It can be seen that the ±20% variations of these parameters have no notable effect on the C/10 discharge behavior, but they have a notable effect on 2C discharge. This can be explained with increasing concentration gradients in the electrolyte phase at high C-rates. A higher tortuosity effectively elongates transport pathways in the electrolyte phase. This intensifies concentration

gradients and causes a less uniform electrode utilization. The parameter variation further shows that the effect of the cathode tortuosity on the 2C discharge behavior is more pronounced than the effect of the anode tortuosity. This can be attributed to the lithium-ion depletion in the cathode electrolyte phase during fast discharge. Low lithium-ion concentrations in the cathode electrolyte phase are more critical in terms of overpotentials than high concentrations in the anode electrolyte phase. Furthermore, the positive effect of an improved anode tortuosity on the discharge capacity is limited by the sharp drop of the cathode half-cell potential toward the end of discharge. Nonetheless, a higher cell voltage during 1C and 2C discharge still illustrates the effect of this parameter.

Figure D.10c and Figure D.10d show the effect of the $\pm 20\%$ variations of the anode and cathode solid diffusion coefficients, respectively. The anode solid diffusion has a small influence on the 1C and 2C discharge behavior. Compared to the anode tortuosity, the effect is smaller in terms of the overpotential during discharge and the final discharge capacity. Nonetheless, the qualitative effect on the discharge curves seems similar, which prevents the estimation of both parameters. Overall, a change in the anode tortuosity due to cell formation and cycling is deemed more likely due to the expected effect of the SEI on the microstructure of the anode.

While the effect of the cathode solid diffusion may initially appear similar to that of cathode tortuosity, closer examination reveals distinct differences. The cathode solid diffusion has a significant effect on 1C and 2C discharge, with a subtle effect also on C/10 discharge. Expanding on this, the cathode tortuosity does not markedly influence the 1C discharge capacity, but it significantly affects the 2C discharge capacity. This highlights the unique role of each parameter and underscores the intricate interplay between transport in the electrolyte and solid phase. During the discussion of the half-cell data in Figure 5.3 for the shallow formation F@C/$2_{3.7\,\mathrm{V}}$ versus the reference formation F@C/10, changes in transport processes in the anode and cathode were expected. When combined with this sensitivity analysis, it is evident that merely enhancing the cathode tortuosity could not capture the observed changes in the experimental data as not only 2C discharge but also 1C discharge show an improvement. Similarly, the sole improvement of the cathode solid diffusion is unlikely as the absolute improvement of the 2C discharge capacity exceeds the improvement at 1C. For this reason, the joint optimization of cathode solid diffusion and cathode tortuosity seems necessary. Given the different effects of these parameters on the 1C and 2C discharge curves, a joint parameter identification without substantial parameter correlation appears feasible.

Importantly, an estimate of the cathode solid diffusion coefficient derived from a C/10 discharge curve can only serve as an initial reference for subsequent optimization based on 1C and 2C discharge data. Considering the dependence of the solid diffusion coefficient on the lithiation degree and its substantial deterioration at high lithiation degrees, extracting this parameter from

the end of a C/10 discharge can introduce a significant bias [247]. This is especially relevant when using it as an effective parameter for the entire range of operation, as done in this work.

Besides parameter identifiability, the question arises if changes in anode tortuosity, cathode tortuosity, and cathode solid diffusion are physically sound and backed by observations in literature. As discussed in Chapter 5, changes in the anode tortuosity are expected due to cell formation, i.e., initial SEI growth, and due to changes in SEI structure and composition during aging. The surface film on the cathode side is generally assumed to be much thinner. Thus, only small changes in this parameter due to formation would be anticipated. Changes in tortuosity or electrode microstructure due to mechanical degradation would be expected on longer timescales [46, 47]. However, cross-talk between the anode and cathode is possible, such as the diffusion of side-reaction products from the anode to the cathode and vice versa [240]. The apparent cathode solid diffusion coefficient depends on the species at the particle surface and at the highly reactive grain boundaries [48], which are crucial for fast diffusion into the depth of a polycrystalline active material particle before changing to the comparably slow bulk diffusion [256].

Figure D.11a depicts the effect of the SEI thickness on the discharge behavior, comparing 50 nm and 150 nm to the initial parameter estimate of 80 nm. Importantly, the SEI thickness decreases the electrolyte volume fraction. For simplicity, the tortuosity is kept constant, considering that porosity changes usually correlate non-linearly with tortuosity [37]. It can be seen that the SEI thickness has a notable effect on C/10 discharge, but only a small effect at higher C-rates. Due to the assumed SEI growth reaction, the SEI thickness is directly linked to the loss of lithium inventory and does not cause a notable change in the anode porosity. Even for an SEI thickness of 150 nm, the SEI-free pore volume is only reduced by about 8%. As such, this parameter has more resemblance to $c_{\mathrm{max,a}}$ than to the anode tortuosity τ_{a} and can be best identified from the capacity loss during formation or, for its update along aging, from C/10 discharge. Nonetheless, the assumed SEI growth reaction of ethylene carbonate to lithium carbonate is a strong simplification of the multi-component nature of both the electrolyte and the SEI. If more information on the electrode porosity after SEI formation or detailed information on the SEI composition were available, the SEI thickness could have a stronger effect on electrolyte-level transport.

Figure D.11b shows a variation of the ionic conductivity of the SEI by a factor of 0.2 and 5, respectively. This parameter clearly does not affect the discharge behavior. In impedance data, this parameter also has a comparably small effect. This highlights again that the ionic conductivity of the SEI does not seem to be performance-limiting for the investigated cell design and chemistry, as already discussed in Chapter 4. In contrast, the surface site density of the SEI, which captures anode reaction kinetics, influences the cell voltage at elevated C-rates, as illustrated in Figure D.11c. However, a substantial 5-fold decrease is required to reveal this effect. Given the prominent effect of this parameter on the anode half-cell impedance, it can be estimated from EIS data, thereby preventing a direct correlation with the anode tortuosity.

Figure D.11d displays a variation of the cathode reaction rate constant by ±50%. Similar to anode reaction kinetics, this parameter demonstrates a small effect on the cell voltage at elevated C-rates. It can be estimated from the cathode half-cell impedance data.

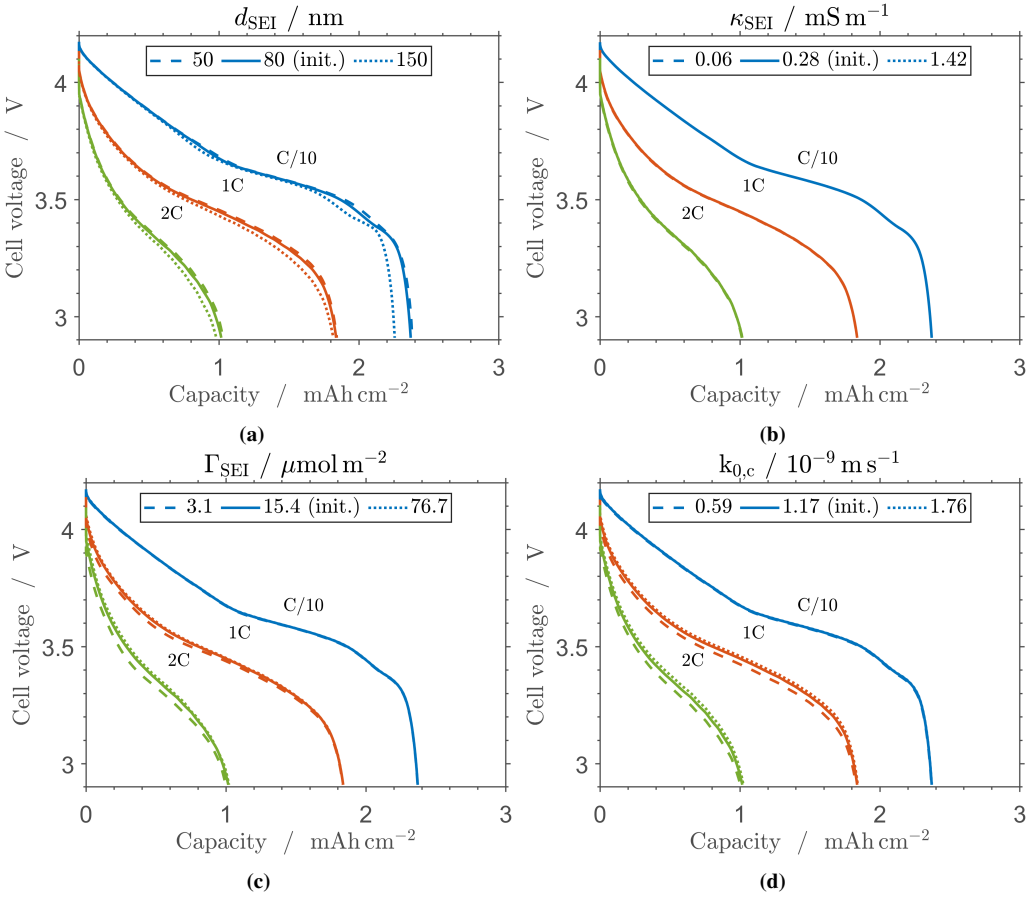

Figure D.11: Simulated discharge curves at C/10, 1C, and 2C for a variation of (a) SEI thickness to 50 nm and 150 nm, (b) SEI ionic conductivity by a factor of 0.2 and 5, (c) surface site density of the SEI, which captures anode reaction kinetics, by a factor of 0.2 and 5, and (d) cathode reaction rate constant by ±50%. The solid line represents the simulation of the parameterized reference cell F@C/10 at cycle 0.

D.2.2 Parameterization Quality

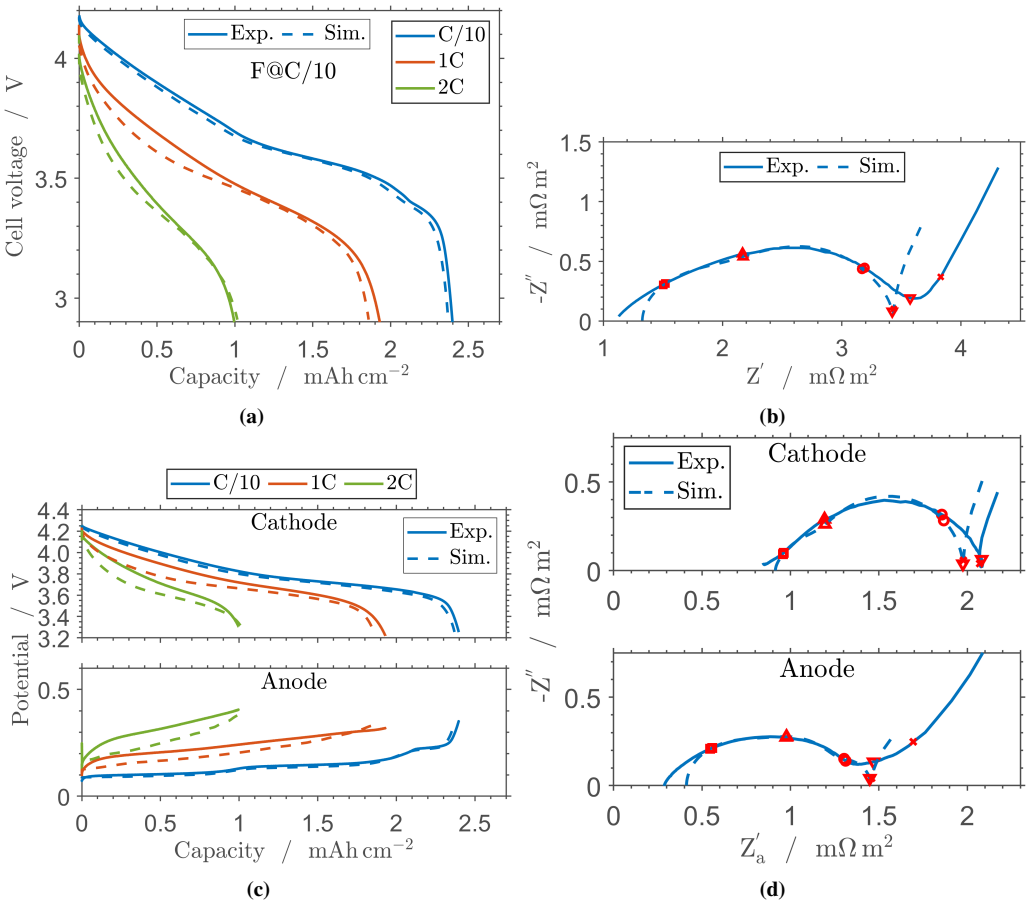

Figure D.12: Comparison of experimental data (solid lines) and simulations (dashed lines) of F@C/10 at 20 °C after the initial cell state estimation. (a) Full-cell and (c) half-cell discharge curves at C-rates of C/10, 1C, and 2C. (b) Full-cell and (d) half-cell impedance spectra at 3.7 V. Five frequencies are highlighted with red markers: 1 kHz (□), 100 Hz (Δ), 10 Hz (○), 1 Hz (∇), and 0.1 Hz (×).

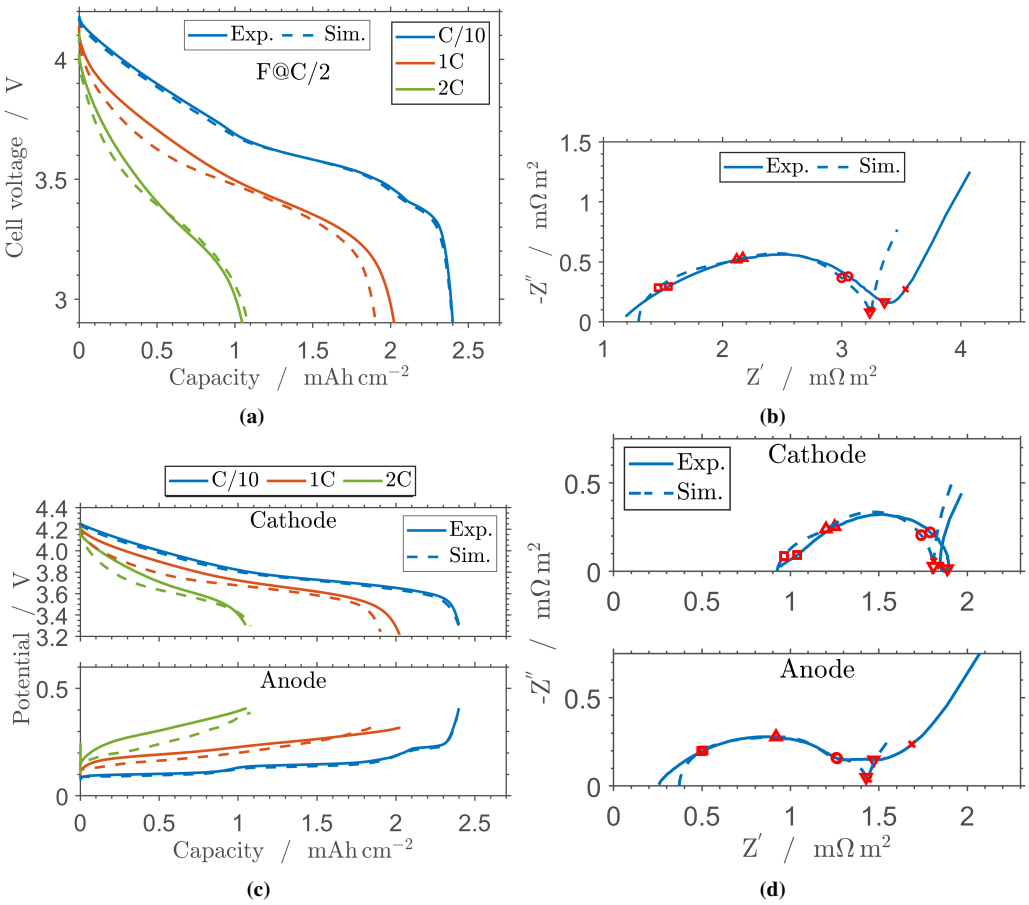

Figure D.13: Comparison of experimental data (solid lines) and simulations (dashed lines) of F@C/2 at 20 °C after the initial cell state estimation. (a) Full-cell and (c) half-cell discharge curves at C-rates of C/10, 1C, and 2C. (b) Full-cell and (d) half-cell impedance spectra at 3.7 V. Five frequencies are highlighted with red markers: 1 kHz (□), 100 Hz (Δ), 10 Hz (○), 1 Hz (▽), and 0.1 Hz (×).

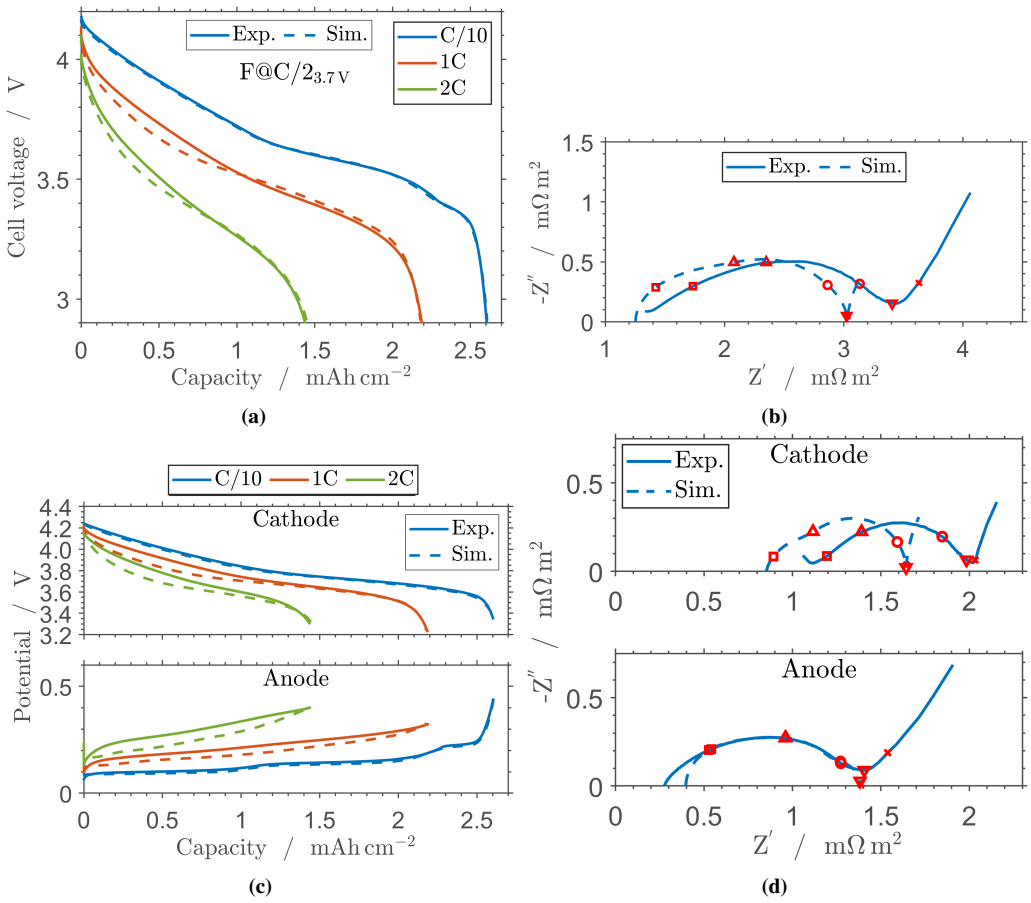

Figure D.14: Comparison of experimental data (solid lines) and simulations (dashed lines) of F@C/$2_{3.7\,V}$ at 20 °C after the initial cell state estimation. (a) Full-cell and (c) half-cell discharge curves at C-rates of C/10, 1C, and 2C. (b) Full-cell and (d) half-cell impedance spectra at 3.7 V. Five frequencies are highlighted with red markers: 1 kHz (□), 100 Hz (Δ), 10 Hz (○), 1 Hz (∇), and 0.1 Hz (×).

Figure D.14 compares the experimental data of F@C/$2_{3.7\,V}$ at 20 °C with the simulation results after the model parameterization. The anode and cathode half-cell discharge curves and the anode impedance response can be accurately described. The shape of the cathode half-cell impedance spectrum is also reproduced successfully, but there is a discrepancy in the magnitude of the impedance values. This could be due to the simplified modeling of the cathode side. As shown in Chapter 4, the ionic conductivity of the SEI has almost no effect on the discharge performance, even for a five-fold reduction compared to the parameterized value. Nonetheless, it can change the onset of the impedance response. For this reason, an extension of the employed model by a cathode surface film could potentially solve the poor representation of the cathode half-cell,

and thus, also the full-cell impedance. However, even without a model adjustment, this indicates that the interfacial properties of the cathode active material particles may have changed for F@C/$2_{3.7\,V}$ at 20 °C.

D.3 Tables

Table D.1: Measurement parameters for cell formation, characterization, and cycling. C-rates are defined based on the theoretical capacity of the cathode. The cell characterization and aging procedure alternate up to a total of 100 cycles, ending with a final cell characterization. For simplicity, this cycle count omits all cycles from the cell characterization procedure.

Procedure	**Parameter**	**Value**
General	Temperature after formation	20 °C
	CV step current cutoff	C/20
	Cutoff voltages	2.9 V, 4.2 V
	Rest times	1 min / 10 min after charge/discharge
Initial rest time		12 h
Cell formation		2 cycles (charge with CV step)
Capacity test		C/10 (charge/discharge with CV step)
Cell characterization	Voltage adjustment	3.7 V, 1C charge with CV step
	Rest time	2 h
	Current pulse	1C charge for 1 s
	Rest time	2 h
	Current pulse	1C discharge for 1 s
	Rest time	2 h
	EIS	see Table C.6
	Voltage adjustment	2.9 V, 1C CC-CV discharge
	Symmetric C-rate test	1× C/10 CC-CV charge/discharge
	Symmetric C-rate test	2× [1C, 2C, 3C, 4C, 5C] CC-CV charge/discharge
Cell aging	50 cycles	2C (charge with CV step)

Table D.2: Parameter estimates for all three formation procedures at 20 °C along aging. Parameter values that are given for only one cycle are kept constant for all other cycles. The changes in the initial lithium concentration in the anode active material along aging are directly related to the estimated SEI thicknesses.

	Formation:	**F@C/10**			**F@C/2**			**F@C/2$_{3.7\,V}$**		
Parameters	**Cycle:**	**0**	**50**	**100**	**0**	**50**	**100**	**0**	**50**	**100**
$\sigma_{s,a}$ / S m^{-1}		136	-	-	-	-	-	-	-	-
$\sigma_{s,c}$ / S m^{-1}		0.07	-	-	-	-	-	-	-	-
$c_{0,a}$ / mol m^{-3}		19,514	19,049	18,893	19,595	18,156	18,151	21,170	19,419	19,086
$c_{0,c}$ / mol m^{-3}		738	-	-	741	-	-	907	-	-
$c_{max,a}$ / mol m^{-3}		20,985	-	-	21,292	-	-	22,348	-	-
$c_{max,c}$ / mol m^{-3}		19,578	-	-	19,849	-	-	21,721	-	-
d_{SEI} / nm		80.4	106.15	114.8	92.9	172.6	172.9	64.0	161.1	179.5
$D_{s,c}$ / 10^{-15} m^2 s^{-1}		2.67	3.30	3.33	2.58	2.63	2.75	3.02	2.63	2.50
τ_a / -		14.63	13.79	13.72	14.82	12.41	11.82	11.61	9.84	10.35
τ_c / -		4.70	4.09	4.03	4.87	4.37	4.10	3.86	3.40	3.16
κ_{SEI} / µS m^{-1}		0.28	0.49	0.58	0.49	0.66	0.59	0.24	0.63	0.93
Γ_{SEI} / µmol m^{-2}		15.35	33.62	55.45	14.44	34.64	47.72	13.75	38.28	54.74
$C_{DL,sSEI}$ / F m^{-2}		0.66	2.28	4.04	0.88	1.82	3.47	0.72	2.33	6.47
$C_{DL,SEIe}$ / F m^{-2}		0.99	2.26	2.90	1.20	1.90	2.25	0.82	2.30	3.26
$C_{DL,c}$ / F m^{-2}		0.28	0.43	0.53	0.32	0.33	0.41	0.32	0.36	0.39
$k_{0,c}$ / 10^{-9} m s^{-1}		1.17	0.93	0.87	1.49	0.93	0.85	1.55	1.08	0.96